Development Of A Cold Atoms Platform For A DQC1 Implementation

Thesis

Development of a cold atoms platform for a DQC1 implementation

Author:
Katarzyna KRZYZANOWSKA

Supervisor:
Dr. Silvia BERGAMINI
Dr. Jim HAGUE
Prof. Edward HINDS

A thesis submitted in fulfillment of the requirements for the degree of Doctor of Philosophy

in the

School of Physical Sciences
Faculty of Science, Technology, Engineering and Mathematics

Milton Keynes
December 18, 2017

Abstract

In this work we report on the development progress of a cold atoms platform to demonstrate a model of quantum computation known as deterministic Quantum computing with One Clean Qubit (DQC1). This is a novel class of algorithms where interactions between qubits enable nonclassical correlations other than entanglement, namely discord. We aim to demonstrate the DQC1 protocol using a scheme in which the information processing is realized on cold neutral rubidium atoms through the cNOT gate based on a Rydberg blockade. The implementation of this protocol imposes very stringent requirements on the cloud of atoms: to realise the cNOT gate with high fidelity it is required that a full Rydberg blockade is operating throughout the extent of the ensemble. This means that a cloud of atoms needs to have a radius below approximately $5\,\mu\mathrm{m}$ (for Rydberg states of atoms $n = 43$).

A dipole trap system was designed and implemented during the course of this PhD with the aim of satisfying these experimental constraints. In our setup, a vapour of ^{87}Rb is first trapped in a Magneto-Optical Trap (MOT) and cooled to sub-Doppler temperatures. The atoms are then subsequently trapped in the dipole trap. Our dipole trapping setup is based on a high numerical aperture lens (NA=0.53) to achieve a sub-micron trapping potential and simultaneously observe trapped atoms with a micrometre resolution. According to the design and the optical tests, the system is capable of creating the trapping potential with about $1\,\mu\mathrm{m}$ waist and $4\,\mu\mathrm{m}$ Rayleigh length.

The aim of this work was to examine and optimise experimental conditions under which the dipole trap should be operated, so that the sufficiently small trap for the DQC1 algorithm can be obtained in the future. For characterisation, a trap of a bigger volume (about $6\,\mu\mathrm{m}$ waist and $28\,\mu\mathrm{m}$ length) was setup instead of using the full capacity of the system. This enhanced the atom loading procedure and provided more convenient conditions for experiments. The temperature of atoms was typically around $250\,\mu\mathrm{K}$, and the trap lifetime ($2.5\,\mathrm{s}$) was limited by the background collisions, which indicates that the vacuum was maintained on the expected level of 10^{-9} Torr. The key findings of the thesis are that the properties of the atoms reservoir (MOT temperature and density), and the loading processes (intensity of MOT beams), need to be optimised to be able to load a micrometre size trap. These findings are instrumental for the future implementation of the DQC1 protocol and also have implications for other protocols founded on the use of a Rydberg blockade.

Acknowledgements

Before I delve into the explanation of what my work over past three years was about, first I would like to take the opportunity to thank people who helped me to complete the project and finish my dissertation.

I have been fortunate to receive the guidance of my very supportive supervisor Dr Silvia Bergamini. She was the one who shaped the ambitious project in which I had the honour to participate, learn and develop new skills required for my further career. Thanks to her profound commitment all issues could be always neatly solved, whether it was a broken piece of equipment or thesis corrections. Most of all, I am grateful to Dr Bergamini for giving me the independence in planning my work and setting up scientific goals to achieve. I would also like to thank the rest of my supervisory team, Dr Jim Hague and professor Edward Hinds for advice and encouragement. Many thanks to Dr Calum MacCormick, who was mainly responsible for the design and building up the equipment, for introducing me to the lab work, teaching the essentials of know-how in our field, patiently answering *all* my questions, and for *always* having time to help. Working with him was an enjoyable and valuable experience. I would also like to thank my coworkers: Rudy Romain for a great work we did in a cheerful atmosphere - it was a real pleasure to work together, and Michael Copley-May with whom I shared the lab and faced experimental difficulties with for over two years.

I would also like to acknowledge the help of other researchers: professor Nicholas Braithwaite and Dr Sam Eden who shared their equipment while I was battling the faulty vacuum chamber, and Professor Andrew Murray from Manchester university for advice and help in electrodes design. Let me additionally mention Dr Michal Ryszka, a colleague who was such a great help and friend to me during my first year. I also appreciate the support of Chris Hall and the entire team of the mechanical workshop while building for us custom parts of the experiment.

I owe a great deal to my friends for their patience when I used to disappear into the abyss of the dark lab for weeks and months with minimal contact. Special thanks to Nathan Bush, with whom in parallel I finished my dissertation, for long memorable evenings in the office, the 'who-submits-first-race', encouragement and proofreading. I am deeply grateful for my family for the support that they have given me. They always have words of encouragement and have been there to listen to all of my ups and downs.

Contents

List of Figures

List of Tables

List of Abbreviations

AOM	**A**cousto-**O**ptic **M**odulator
APD	**A**valanche **P**hoto **D**iode
BFL	**B**ack **F**ocal **L**ength
CCD	**C**harge-**C**oupled **D**evice
CNOT	**C**ontrol **NOT** (gate)
DQC1	**D**eterministic **Q**uantum **C**omputing with one clean qubit
DOF	**D**epth **o**f **F**ield
EIT	**E**lectromagnetically **I**nduced **T**ransparency
FORT	**F**ar **o**f **R**esonance **T**rap
FWHM	**F**ull **W**idth at **H**alf **M**aximum
ICCD	**I**ntensified **C**harge-**C**oupled **D**evice
MCP	**M**icro**c**hannel **P**late
MOT	**M**agneto-**O**ptical **T**rap
MTF	**M**odulation **T**ransfer **F**unction
NA	**N**umerical **A**perture **F**unction
OBE	**O**ptical **B**loch **E**quations
PBS	**P**olarization **B**eam **S**plitter
POP	**P**hysical **O**ptics **P**ropagation
PZT	**P**ie**z**oelec**t**ric
RGA	**R**esidual **G**as **A**nalyzer
RWA	**R**otating **W**ave **A**pproximation
SLM	**S**patial **L**ight **M**odulator
SNR	**S**ignal to **N**oise **R**atio
SPDC	**S**pontaneous **P**arametric **D**own-**C**onversion
STIRAP	**St**imulated **R**aman **A**diabatic **P**assage
TOF	**T**ime-**o**f-**f**light
QED	**Q**uantum **E**lectro**d**ynamics

QC	**Q**uantum **C**omputing
UHV	**U**ltra **H**igh **V**acuum

Physical Constants

Speed of light	$c_0 = 2.997\,924\,58 \times 10^{8}\,\mathrm{m\,s^{-1}}$
Fine-structure constant	$\alpha = \frac{1}{4\pi\epsilon_0}\left(\frac{e^2}{\hbar c}\right) = \frac{1}{137}$
Reduced Planck constant	$\hbar = 1.054\,571\,8 \times 10^{-34}\,\mathrm{J\,s}$
Boltzmann's constant	$k_B = 1.380\,650\,3 \times 10^{-23}\,\mathrm{J\,K^{-1}}$
Bohr Magneton	$\mu_B = 9.274\,008\,993\,7\,\mathrm{J\,T^{-1}}$
Rydberg constant	$R_\infty = 1.097\,373\,156\,850\,865 \times 10^{7}\,\mathrm{m^{-1}}$

Chapter 1

Introduction

1.1 Motivation

Quantum technology is a cutting-edge research field focused on the development of tools and devices which can potentially revolutionize modern society in many aspects. It consists of four main research areas: quantum sensors, computing, metrology and cryptography. A quantum computer could potentially threaten internet security systems in the future, while quantum cryptography would establish a new unbreakable method for data encryption[1]. In fact, the impact of quantum technologies on modern science is well-established. For instance, in 2015 the interferometer with an enhanced sensitivity[2] [1] (LIGO) was able to detect gravitational waves for the very first time in history [2]. An interest in quantum technologies goes far beyond their academic scope, as there are already attempts toward commercialized solutions, such as highly sensitive gravimeters [3, 4] and atomic clocks [5]. Gravimeters based on atomic fountains could have applications in numerous fields, from fundamental physics to navigation and geophysics. Atomic clocks, on the other hand, could be used in applications requiring time synchronization over short periods, such as GPS receivers. These and many other applications are covered by the broad term *Quantum technologies*.

Regarding quantum computing, the field still requires thorough investigation and development of new experimental methods to overcome the technological difficulties. Even commercial companies such as Google, NASA and IBM have invested heavily in this area. In 2015, D-wave proudly announced a processor based on over one thousand qubits that gave

[1] Quantum cryptography is a method to establish secure, private encryption keys. Quantum cryptography assumes that a sender and receiver establish a private key for data encryption using both a public and quantum channel. The information transmitted through the quantum channel is encoded by quantum particles, whereas the public channel is used to exchange instructions that allow the interpretation of the quantum channel. Due to the no-cloning theorem, one cannot eavesdrop the quantum channel without being noticed. In this sense, it is an unbreakable method for data encryption.

[2] Sensitivity of LIGO (Laser Interferometer Gravitational-Wave Observatory) was enhanced using squeezed states of light allowing to pass standard quantum limit. This belongs to a domain of quantum metrology.

an answer for an NP-hard[3] computational task and beat the best known classical solvers [6]. However, its architecture is such that this powerful computer is not universal and limited only to certain specific optimization problems, namely Ising models or clause problems [7]. Another attempt from IBM created a device consisting of 5 qubits, and the company shared its resource with users around the world via the cloud. This was beneficial in so far as testing and developing quantum algorithms [8, 9], but even though the device is quite flexible, 5 qubits do not provide sufficient computational power for practical applications. Simultaneously, work on a 5 qubits computer based on ions was reported in 2016 [10], with a potential to expand the system further. To give an insight into current state-of-the-art applications, three distinctive platforms and their challenges are briefly introduced in following paragraphs.

Photonics is an approach based on encoding qubits in the quantum state of single photons, typically their polarization or phase. Encoding and manipulating qubit in photons is relatively easy using linear optics, while controlled gates are challenging due to the lack of interactions between single photons. The solution to this problem was proposed in [11] where ancilla photons and post-selection of events are used to perform controlled gates which exploits only linear optics. Ancilla photons can be obtained in nonlinear processes, such as spontaneous parametric down-conversion (SPDC) [12]. This concept was successfully demonstrated on a small reprogrammable optical circuit with 6 qubits [13]. Even though photonics proved itself to be useful in testing the fundamental principles of quantum computing, scalability appears to be a fundamental challenge due to the low efficiency in creating ancilla photons.

Cold ions are arguably considered the most advanced platform to implement quantum information processing. This platform benefits from high experimental standards since ions are well studied and commonly used in mass spectrometry and atomic clocks. Typically, ions are trapped in Paul trap [14], which emerges from a combination of static and oscillating electric potentials. The linear Paul trap provides harmonic potential, in which ions form a 1D array, with spacing determined by repulsive Coulomb force between individual ions [15]. In this configuration, ions are individually addressed by lasers which encode qubits in the hyperfine structure of the ion's ground state. The proposal to use coulomb interactions between (not necessarily neighbouring) ions in order to perform conditional two-qubit gates

[3] NP stands for nondeterministic polynomial time. NP is a complexity class of all decision problems, whose answer can be verified in polynomial time if an instance of the problem is given. NP-hard is a class of NP decisions problems.

was introduced in [16], demonstrated in [17] and is now a leading technique to perform high fidelity gates [18]. Scalability of this system is limited by the number of ions which can be achieved in a single linear Paul trap, typically less than ten ions. One of the possible solutions regarding expanding the system is ions shuttling through space between separate Paul traps. Development of this technique is based on microfabrication of segmented Paul traps [19–21] and might allow scaling of the system up to one thousand qubits before ion shuttling at long distances destroys the coherence of the system. Another approach towards scalability is based on the entanglement of selected ions from any two traps using photonics [22] and entanglement swapping [23]. In this technique, an ion pumped with an appropriate pulse laser emits a single photon which is entangled with ion's internal state. Then, two such prepared photons from different ions are combined on a 50:50 beam splitter and measured with single-photon detectors. The detection heralds Bell states of photons and creates an entanglement of ions [24, 25]. In practice it is likely that both methods, photonic and ion shuttling, will have to be combined in order to reliably scale up an ion-based quantum computer.

The platform which is discussed in this thesis, cold neutral atoms, is another advanced approach toward quantum information processing [26]. Neutral atoms, similarly to ions, benefit from excellent frequency standards and therefore are a popular platform in quantum technologies, especially quantum sensors. Due to their polarizability, neutral atoms are usually stored in the optical traps formed by the oscillating electric field of laser beams far detuned from the atomic transitions. An optical trap can be made in a form of optical lattice [27, 28], where the periodic potential is produced by the interference of coherent light. This enables the creation of a well-defined 3D structure of densely packed single atoms with approximately $5\,\mu\mathrm{m}$ distance between them [29]. Another approach is known as dipole traps [30], also called *optical tweezers*, which are typically achieved by focusing a high power laser beam. With optical tweezers it is possible to create a two dimensional array of traps (Figure 1.1) with a micrometer precision in a relatively convenient way, using programmable phase modulator [31, 32]. The opportunity to create a 2D or 3D arrays of traps is very interesting, as many quantum protocols require special geometries of traps to enhance the correlations between qubits [33, 34]. Both techniques, optical lattices and dipole traps, allow the accurate manipulation of neutral atoms through the laser-induced dipole moment and due to a low interaction of neutral atoms with the environment [35] provide long coherence

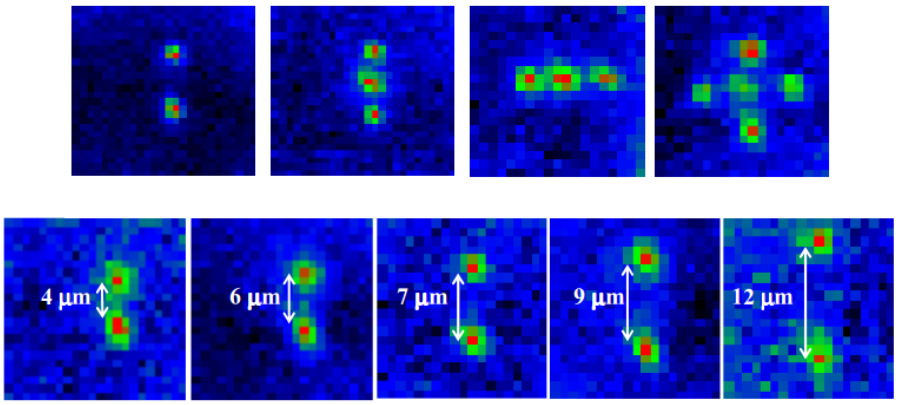

FIGURE 1.1: The first experiment showing single atoms trapping using dipole trap method and SLM (Spatial Light Modulator). Source [31]

time of a few seconds [36]. The typical trap depth of optical tweezers is in the range of millikelvin, and the main advantage of this method is that the trapping does not depend on the internal structure of the ground state. It is very convenient, because the hyperfine structure may then be easily exploited in experiments for encoding quantum information. Therefore, qubits are typically encoded in the ground state of alkali atom, while their initialization and detection are performed by optical pumping and fluorescence detection [37, 38]. One-qubit gates can be performed with very high fidelity [39, 40] using microwaves [41, 42], stimulated Raman transitions[43, 44], or a combination of microwaves with Stark shifting light [45–49]. Two-qubits gates are still a challenge in the platform, and their fidelity still remains insufficient for quantum error correction. Controlled gates can be realised by a photon exchange between atoms [50] or exploiting collisional interactions [51–53], but the most successful so far were Rydberg interaction mediated gates [54–60] achieving up to 0.81 fidelity. Even though the fidelity of controlled gates remains the main issue to address, the scalability of the system is promising and systems with hundreds of qubits have now been successfully implemented [29, 32, 61]. The number of qubits implemented with optical traps is limited mostly by the available laser power, but this difficulty can be solved by the appropriate development of laser techniques, potentially scaling up the system up to thousands of qubits. However, the loading time of an array of single atoms rises exponentially with the number of traps, and increasing the number of traps soon becomes unfeasible. This issue is typically addressed through appropriate laser cooling which increases loading efficiency [62], or by

spatial rearrangement of a semi-loaded lattice using atoms shuttling [63]. Nonetheless, scaling up the system by simply extending the size of the lattice may not be sufficient for many computational tasks, therefore hybrid solutions need to be sought. For instance, two qubits from two distinctive traps can be coupled with each other through cavity quantum electrodynamics (QED) [64], which is considered to be a separate platform for quantum computing and is not covered in this review.

These and many other examples show that quantum computing has just entered the next research phase known as the second quantum revolution. This means that scientists have managed to prepare and control well-defined qubits and to implement a set of universal gates with fidelity high enough to perform quantum computations. These quantum computing models are generally based on the manipulation of qubits in pure states and the exploitation of entanglement to implement logic gates. However, even if these conditions are satisfied for a small number of qubits, scalability remains a challenge and the computational power is usually limited by the system architecture. There are however non-standard approaches toward quantum computing which are also in the scope of current research, which unlike in standard approach, do not operate with pure qubits and entanglement. Deterministic Quantum Computing with One Clean Qubit (DQC1) [65] is a novel class of algorithms where only one control qubit is required to be in an almost pure state, while the target ensemble of qubits is initially prepared in a mixed state. In this case, interactions between atoms enable non-classical correlations other than entanglement, namely *discord*. In [66] it was proposed that discord would provide sufficient quantum enhancement to solve a particular class of classically-intractable computations. Although DQC1 does not provide universal computation, it can provide exponential speedup for specific classically intractable computational tasks. While having a suitable platform to implement DQC1, this protocol creates the opportunity to be easily extended by additional qubits in ensembles, and hence a scaling up of the computational power is much more easily obtained. Interestingly, the increase in speed offered by this algorithm is not affected by reducing the purity of the control qubit, until it reaches a threshold (purity $\alpha \geq 0.5$) when the protocol fails [65].

In [67] the concept of DQC1 was applied to a trivial case, with only one qubit in the target ensemble using photon-based architecture. The result of the experiment was enough to prove the computational utility of mixed states. Although this was a very important step, it was not sufficient to prove that the protocol would also work with a large number of qubits in a target ensemble. This research was limited by the physical properties of the system that

was used [68]. Nevertheless, there exist systems which are a more natural choice for the DQC1 protocol, where it is easier to increase the number of qubits, for instance NMR [69] or cold neutral atoms [70]. As an example, the Jones polynomial was approximated using the architecture based on four liquid state NMR qubits exploiting carbon nuclei structure [71]. Although the algorithm was successfully performed with four qubits, the question of where the limit on scaling up the system is, before noise and control errors of the system destroy the computational advantage, remained unanswered.

Our project is the first attempt to use atoms to demonstrate and scale up the DQC1 protocol. Initially, we aim to demonstrate the DQC1 protocol for just a few atoms in the target ensemble to verify the model's prediction from [70], using a scheme in which the information processing is realised through a $cNOT$ gate based on Rydberg blockade [55]. This proposal imposes highly stringent requirements on the experimental realization: a full Rydberg blockade operating throughout the extent of the ensemble is necessary to perform $cNOT$ gate with high fidelity (Figure 1.2a). Although a local Rydberg blockade has been already observed in a magneto-optical trap (MOT), the sample size exposed to laser light was much bigger than the blockade radius and hence only partial blockade could be achieved [72, 73]. Dipole traps are a possible solution to that problem, as they benefit from tight confinement [30]. Recently, a full Rydberg blockade was demonstrated on two [56, 74] and three atoms [75] and also on three ensembles consisting of many atoms [76] proving the utility of dipole traps to implement schemes for fast quantum gates based on neutral atoms [54, 55]. Cold Rubidium atoms in dipole traps seem a good and effective approach, as it is possible to load micrometre-size dipole traps with a controllable number of atoms, ranging from one to many, by varying the trap's parameters and loading rate [77–79]. In this way, a cloud of atoms in a dipole trap can be easily extended by adding atoms and hence increasing the computational power of DQC1.

Cold atoms are therefore a natural platform to perform DQC1 and test when the experimental noise limits the protocol while expanding the system with many qubits. In our proposal, atoms are first cooled down and trapped in a vacuum chamber using a Magneto-Optical Trap playing the role of a reservoir from which a dipole trap containing N atoms can be loaded. Two individually addressable traps for the control and target ensemble can be created either by combining two optical tweezers or by using a Spatial Light Modulator. A $cNOT$ gate on the atom in dipole traps can then be performed by Raman beams and a very strong blue laser light, using a scheme that involves Electromagnetically Induced

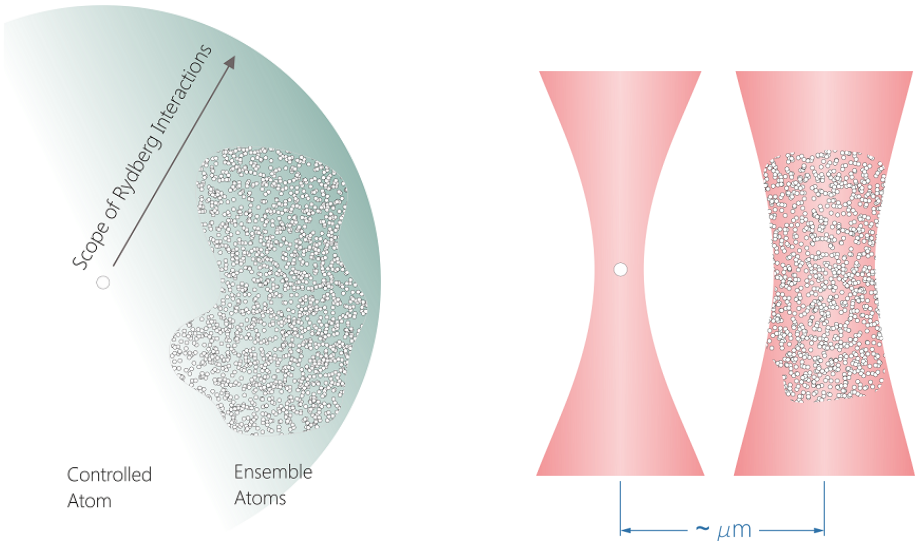

(a) Rydberg blockade (b) Pair of optical tweezers

FIGURE 1.2: Pattern of dipole traps with a single atom loading and many atoms loading. (a) All of atoms in the ensemble need to be within the scope of Rydberg blockade to implement DQC1. (b) The confinement of atoms into the desirable pattern of a single atom in the control and multiple atoms in the ensemble is realised by two dipole traps. Dipole traps are depicted here as a two (far detuned) focused laser beams, which attract atoms in vicinity of the focal plane where the laser intensity is the highest. Two dipole traps are in the distance of few micrometers to ensure that the Rydberg blockade mechanism works.

Transparency.

Since this proposal is very ambitious and requires many different experimental stages to be integrated, the work presented in this thesis is focused only on the development of the experimental apparatus for dipole trapping. The aim is to achieve the optical tweezers which satisfy the requirement of the DQC1 protocol, namely to trap a cloud of atoms with a controllable number of atoms to provide enough confinement to enable a Rydberg Blockade. The first step consists of creating an appropriate reservoir of atoms (MOT), which is dense and cold enough for loading a dipole trap. The next step is to design and implement an optical system dedicated to the dipole trapping with an embedded imaging system for detection of atoms. The design needs to then be implemented and merged with the existing apparatus and tested to confirm the design predictions. Finally, the physical properties of the dipole trap should be tested to assess its utility for the protocol processing, such as the temperature of trapped atoms, atomic cloud's size, and cloud lifetime. These measurements will give the ultimate answer whether the dipole trapping is suitable for the DQC1 protocol or whether it requires further improvements.

1.2 Thesis outline

The thesis is divided into five main sections.

- The following chapter 2 is a theoretical introduction to the physics behind the project: how can the DQC1 protocol be implemented with cold atoms. It starts with basics of quantum computing theory and an explanation of the DQC1 algorithm in detail. Then, the atomic structure, light matter interactions exploited in laser cooling and dipole trapping of rubidium atoms are presented. The chapter is concluded with a detailed proposal of the DQC1 realization with cold atoms.

- In chapter 3 the experimental apparatus and the underlying physics principles are thoroughly explained. It covers the cooling method and vacuum system description, including schemes of the laser system and an ultimate MOT diagnostics.

- In chapter 4 the design of the dipole trapping system with embedded imaging system is presented. The chapter includes first a consideration over the technical requirements of the design enriched by the theoretical introduction to optics design. Then, a full scheme of optical components is proposed along with the analysis of the expected system performance. Finally, the chapter 4 provides a description of implementation in the laboratory on the optical bench, testing procedure and measurements of the optical system quality.

- The last experimental chapter 5 shows the way from dipole trap implementation to characterization of its properties. It starts with remarks on the experimental approach toward dipole trap detection and imaging system signal calibration. When the procedure of dipole trap detection is established, the main interesting features of the dipole trap are measured: atoms temperature, number of atoms in the trap, estimation of trap depth, trap lifetime and losses mechanism.

- chapter 6 provides the discussion of our results and an outlook into the future work based on the results obtained in this thesis.

Chapter 2

Theoretical background

2.1 Theoretical background of quantum computation

In 1965, a co-founder of Intel, Gordon Moore, predicted that the computational power, based on number of transistors on a silicon chip, would double every 18 months. His predictions were not too far from the truth, as the computational speed has doubled approximately every two years. The increase in transistor numbers etched into a silicon wafer was accompanied by a decrease in size of transistors. Although, transistors of size $5\,\mathrm{nm}$ have already been achieved, $(14 \text{ to } 20)\,\mathrm{nm}$ transistors are used today in commercially available devices. If the progress in information technology continues at the same speed, by 2020 the size of a processing unit will reach the theoretical limit[1], beyond which quantum effects will become significant. This is one of many reasons why research in quantum computing deserves special attention.

Initially the term quantum computation was used to refer to classical computers based on quantum mechanical systems. The current concept of quantum computation was developed about thirty years ago, when a few scientists (Manin, Yu. I. 1980, Feynman, R. P. 1982, Deutsch, David 1992) considered theoretically the possibility of employing quantum systems as platforms for computation. This idea may be successfully summed up by a quote from Richard Feynman *'Because nature isn't classical...'*. The idea of quantum computing remained almost unnoticed up until 1994 when mathematician Peter Shor presented a quantum algorithm for integer factorization. This big breakthrough increased interest in quantum information and triggered more theoretical research. It was shown that for some

[1]Current technology is limited by the length of channel in transistor. The atom-to-atom spacing on a crystalline silicon surface is on the order of $0.5\,\mathrm{nm}$. That puts a theoretical limit on the channel length of about $1\,\mathrm{nm}$. Moreover, if the channel is shorter than approximately $6\,\mathrm{nm}$ quantum effect such as quantum tunnelling impact the behaviour of transistors.

complex computational tasks a significant speed up can be obtained using quantum algorithms [80]. Moreover, there are theoretical proofs that some computational tasks can only be solved by quantum resources[81–85], in other words they are classically intractable. Such a development immediately resulted in the understanding of the great advantages of quantum information theory and showed how important further experimental research in this direction can be.

The aim of this section is to introduce and discuss the concept of the DQC1 protocol. A summary of the mathematical basics of quantum computing, which is important for the discussion, will be introduced first. Therefore the concepts of quantum computing, qubits, quantum gates for one and more qubits, and eventually quantum algorithm will be covered in following sections.

2.1.1 Quantum computing

The concept of a quantum computing (QC) device is in some way analogous to a classical computer, but the difference lies in the principles of quantum operations and information theory, as well as in the properties of the physical system in which the information is encoded. In classical information, data are represented by binary digits that are called bits. Information bits, (it is '1' or '0' logic unit), are associated with the state of some physical system, such as high and low voltage in a circuit. The memory which stores the value of a bit is called register. The computing unit needs to process information by performing a sequence of logical operations (gates).

In a quantum computer, any two level quantum systems can be exploited as a quantum bit. However, not all physical systems can become good computing units. In 2000 David DiVincenzo identified the criteria [86] that identify possible and viable resources for quantum computing. According to his work, there are five main requirements for quantum computation:

- Scalability - capability of a system of qubits accompanied with suitable processing tools to be extended (scaled up).
- Initialization - the ability to initialize the state of the qubits to a pure state.
- Coherence - the coherence time of the state of physical system should be much longer than the gate-operation time.

- Universality - a set of logic operations (quantum gates) which will enable to perform universal computation.
- Read out - a possibility of qubit-specific measurement.

and also two additional requirements related to linking two independent, spatially separated systems, which are called 'quantum computing networkability':

- Transmit - creating movable qubits which will transport information among immobile qubits.
- Interconvert - capability to exchange the state of movable qubits with immobile ones.

Table 2.1 presents a short summary of different physical systems and their utility for QC. The approach to the topic which DiVincezo presented has become an unofficial set of requirements which are widely used by scientist in QC. This acceptance of DiVincenzo's proposition is based on the belief that only pure entanglement can be a useful resource of computational power. However, there are also 'unconventional' algorithms that could perform specific computation without entanglement, exploiting other non-classical correlations, such as quantum discord. These non-classical algorithms are very interesting, promising and yet very controversial, as the role of non-classical correlations in quantum information is still not well understood. However, before delving into the topic of non-conventional quantum algorithms, a few definitions from quantum information theory need to be introduced.

Physical System	Quantum Computation					QC Networkability	
	Scalability	Initialisation	Coherence	Universality	Read Out	Interconvert	Transmit
NMR		✓	✓	✓✓	✓		
Trapped Ions	✓	✓✓	✓	✓✓	✓✓	✓	✓
Neutral Atoms	✓	✓✓	✓	✓	✓	✓	✓
Cavity QED	✓	✓✓	✓	✓	✓✓	✓	✓
Optical Systems	✓	✓	✓✓	✓	✓	✓	✓✓
Solid State	✓	✓	✓	✓	✓		
Superconducting	✓	✓✓	✓	✓	✓		

TABLE 2.1: Miscellaneous physical systems and their utility to perform QC. Empty space denotes that there are no known viable approaches; ✓denotes that a potentially viable approach has been proposed but there is no known sufficient proof of principle; ✓✓means that potentially viable approach has achieved sufficient proof of principle

2.1.2 Mathematical formalism of quantum computing

Qubit

The most fundamental unit of a quantum processor is a quantum memory unit called qubit, which is the analogue to the classical bit. A qubit is described by a *pure* state

$$|\Psi\rangle = \alpha\,|0\rangle + \beta\,|1\rangle \tag{2.1}$$

where the complex amplitudes satisfy $\alpha^2 + \beta^2 = 1$ and the vector basis is

$$|0\rangle = \begin{pmatrix} 1 \\ 0 \end{pmatrix} \tag{2.2a}$$

$$|1\rangle = \begin{pmatrix} 0 \\ 1 \end{pmatrix}. \tag{2.2b}$$

The state of a system of N qubits is represented by the tensor product

$$\begin{aligned} |\Psi\rangle &= |\Psi_1\rangle \otimes |\Psi_2\rangle \otimes \ldots \otimes |\Psi_N\rangle \\ &= c_{00\ldots00}\,|00\ldots00\rangle + c_{00\ldots01}\,|00\ldots01\rangle + \ldots + c_{11\ldots11}\,|11\ldots11\rangle \end{aligned} \tag{2.3}$$

To understand what the advantage of a quantum memory is, one needs to compare it to the classical bit. N classical bits give the opportunity to store 2^N combinations of zeros and ones, but N classical bits will encode only one from all of these possibilities. According to equation (2.3), where the state of qubit is described by 2^N terms, N qubits can encode all from 2^N possibilities simultaneously.

However, another more general concept will be used further in DQC1 for states description. Since the DQC1 exploits *pure* and *mixed*[2] quantum states, a so called *density matrix* is introduced as it is able to describe not only pure quantum states, but also mixed states. It is defined as

$$\rho = |\Psi\rangle\langle\Psi| = p_1\,|\Psi_1\rangle\langle\Psi_1| + p_2\,|\Psi_2\rangle\langle\Psi_2| + \ldots + p_N\,|\Psi_N\rangle\langle\Psi_N|\,. \tag{2.4}$$

where the probability of measurement of the given state $|\psi\rangle$ is given by $P(|\psi\rangle) = \mathrm{Tr}\,[\rho\,|\phi\rangle\langle\phi|]$. Every pure state can be expressed by the density matrix, but not every density matrix can

[2] Mixed quantum state is a statistical ensemble of pure states.

be described by pure states. It will be shown later that in DQC1, where one qubit is pure and the rest is in mixed states, the density matrix is an essential concept to describe the algorithm.

Entanglement and quantum discord

If the state $|\Psi\rangle$ of N qubits can be separated into a tensor product of independent pure states, as shown in equation (2.3), the correlation between qubits is recognized to be purely *classical*. Otherwise, when the state can not be decomposed the correlations are *non-classical*. The most 'popular' and very special case of non-classical correlation is the (pure/maximum) entanglement. It is easy to define entanglement for the bipartite state (two qubits) via so called *concurrence* [87], but it is not very obvious for more qubits and is currently best defined by the *von Neuman entropy* [88]. Entanglement is a feature of quantum systems that is usually recognized as a computational resource [89] and it requires the purity of the system to be maintained. Quantum Discord instead, is a measure of non-classicality of a given quantum system that does not imply purity or entanglement. It is based on measurement of mutual information between two parts of a system, it is maximum when there is entanglement and it can be nonzero even for separable mixed states.

Quantum gates

Logic gates, which are the basics of an information processing unit, perform operations on one or more logical inputs that results in a single logical output. The states of qubits can be manipulated in such a way that, depending on the initial state, a deterministic output will be produced. In quantum formalism, gates are represented by unitary operators in matrix form. The effect of applying a quantum gate on a system of qubits is a change in the complex amplitudes of their wave function. The most 'famous' examples of a one-qubit gates are the Hadamard gate H and the swap gate denoted here as NOT:

$$H = \frac{1}{\sqrt{2}} \begin{pmatrix} 1 & 1 \\ 1 & -1 \end{pmatrix}, NOT = \begin{pmatrix} 0 & 1 \\ 1 & 0 \end{pmatrix} \tag{2.5}$$

The Hadamard gate is one of the most handy gates, because it prepares a qubit, that was previously in one of $|0\rangle$ or $|1\rangle$ state, in a superposition of states. The swap gate, which changes a state $|\Psi\rangle = \alpha|0\rangle + \beta|1\rangle$ into the state $|\Psi'\rangle = \beta|0\rangle + \alpha|1\rangle$, is the quantum equivalence to the NOT gate of classical information. If we have a system of two or more qubits, a single

qubit gate that still performs operation on only one of qubit must be written in the basis of Hilbert space that describes the whole system. For instance the negation gate for two qubit system which acts only on the second qubit is

$$NOT^{(2)} = \begin{pmatrix} 0 & 1 & 0 & 0 \\ 1 & 0 & 0 & 0 \\ 0 & 0 & 0 & 1 \\ 0 & 0 & 1 & 0 \end{pmatrix} \tag{2.6}$$

and applied to the state $|\Psi_1\rangle \otimes |\Psi_2\rangle = \alpha_1\alpha_2 |00\rangle + \alpha_1\beta_1 |01\rangle + \beta_1\alpha_2 |10\rangle + \beta_1\beta_2 |11\rangle$ results in $|\Psi_1\rangle + NOT |\Psi_1\rangle$ as follows

$$\begin{pmatrix} 0 & 1 & 0 & 0 \\ 1 & 0 & 0 & 0 \\ 0 & 0 & 0 & 1 \\ 0 & 0 & 1 & 0 \end{pmatrix} \begin{pmatrix} \alpha_1\alpha_2 \\ \alpha_1\beta_2 \\ \beta_1\alpha_2 \\ \beta_1\beta_2 \end{pmatrix} = \begin{pmatrix} \alpha_1\beta_2 \\ \alpha_1\alpha_2 \\ \beta_1\beta_2 \\ \beta_1\alpha_2 \end{pmatrix} = (\alpha_1 |0\rangle + \beta_1 |1\rangle) \otimes (\beta_2 |0\rangle + \alpha_2 |1\rangle) .$$

One of the fundamental logic operations, which are not mentioned yet, performs the conditional change of the state of second qubit, depending on the state of the first one. The example of such a two qubit gate is a controlled negation gate,

$$cNOT^{(2)} = \begin{pmatrix} 1 & 0 & 0 & 0 \\ 0 & 1 & 0 & 0 \\ 0 & 0 & 0 & 1 \\ 0 & 0 & 1 & 0 \end{pmatrix} \tag{2.7}$$

which swaps the state of second qubit, if the first one is in state $|1\rangle$ (this is obviously very naive explanation, as the first qubit can be in a superposition of $|0\rangle$ and $|1\rangle$.) This is the common notation of the quantum gates for more than one qubit, which will be used further in this work.

Quantum circuits

For each input size N, a quantum circuit C_N can be defined as a prescribed sequence of computational steps. Here, a sequence of qubits $|\Psi_1\rangle, |\Psi_2\rangle, \ldots, |\Psi_N\rangle$ is an input, and a single computational step corresponds to a single application of a quantum logic gate. The

quantum circuit model is a straightforward generalization of circuit model from classical information theory. In classical computation it can be shown that a set of three (two single-bit and one two-bit) reversible gates is universal. Since quantum gates are unitary, they are also reversible by definition and so the proof of universality remains valid. There are three methods of presenting quantum algorithms, but the most common is a pictorial representation. In this representation, horizontal lines represent single qubits on which sequence of steps in time is marked from left to right. Operations related to particular qubits are usually marked as boxes attached to qubits lines. The example of such a graph is presented in Figure 2.1.

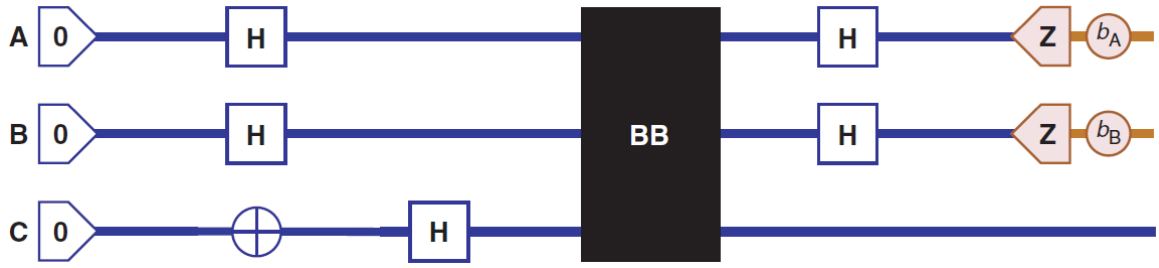

FIGURE 2.1: Example of quantum circuit pictorial representation: quantum network for solving the parity problem. A quantum network has a line (horizontal in this case) for each qubit. The line can be thought of as the timeline for the qubit and is shown in blue. Each gate is drawn as a box, circle, or other element intercepting the lines of the qubits it acts on. In this case, time runs from left to right. Each qubit's timeline starts at the point where it is added. In this example, the qubits' timelines end when they are measured, at which point a classical bit (brown timeline) containing the measurement outcome is introduced. The operation BB is illustrated as a black box. Source [90]

2.1.3 DQC1 protocol

Deterministic Quantum Computations with one Clean qubit (DQC1) is a recently developed quantum protocol based on mixed states. The idea of using non-classical correlations for computing was introduced in 1998 [66], however only in 2008 [67] the first experimental demonstration of this protocol exploiting discord was published. In DQC1 the information is stored in one well-controlled pure qubit and an ensemble of qubits in mixed states. As shown in the circuit model (Figure 2.2), the control qubit is prepared in state $\rho_c = |0\rangle\langle 0|$ and a register ensemble (target ensemble) of qubits is prepared in highly mixed state $\rho_e = \frac{1}{2^N}\mathbb{1}_N$. The control qubit is then prepared in the superposition state using a Hadamard gate. Then, a $N+1$ unitary qubit gate is applied, which performs or not the operation on the target qubits conditionally depending on the state of the control qubit. Since the control register

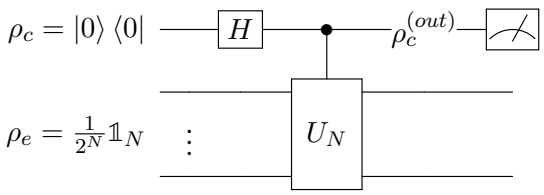

FIGURE 2.2: Circuit model of DQC1 algorithm.

is in a superposition state, performing a controlled unitary operation creates non-classical correlations among all qubits, which can be quantified as *discord*. Here discord is a result of the interaction of the control qubit individually with each qubit in the ensemble during the conditional gate. Even though the target ensemble is initially in the highly mixed state with no quantum correlations between the ensemble qubits, the correlations between the ensemble qubits are introduced via the target qubit. The output state of control qubit $\rho_c^{(out)}$ just after the controlled gate can be written as:

$$\rho_c^{(out)} = \frac{1}{2}\begin{pmatrix} 1 & \frac{Tr\left[U_N^\dagger\right]}{2^N} \\ \frac{Tr[U_N]}{2^N} & 1 \end{pmatrix}. \tag{2.8}$$

At the final stage of the algorithm only a state of the control qubit is measured (Figure 2.2). The trace of unitary operation can be retrieved after measuring the expectation values of the Pauli operators (X or Y) on the control qubit.

$$\langle X\rangle = \frac{Re\left(Tr\left[U_N\right]\right)}{2^N} \tag{2.9a}$$

$$\langle Y\rangle = -\frac{Im\left(Tr\left[U_N\right]\right)}{2^N} \tag{2.9b}$$

According to the central limit theorem, the measurement of the expectation values of $|X\rangle$ and $|Y\rangle$ must be repeated many times to ensure that the collected statistical data gives a good accuracy. Here, the measurement operation is applied only to the control qubit which is described by a two dimensional Hilbert space, hence the repetition number does not depend on the number of ensemble qubits. This is the most important feature of DQC1, that regardless of what is the size of a computational task, the accuracy of the measurement of

the trace of unitary depends only on the number of experiment repetitions N_{Rep}

$$\text{accuracy} = \frac{1}{\sqrt{N_{\text{Rep}}}}. \tag{2.10}$$

In other words, the number of repetitions needed to achieve a certain accuracy is independent on the size of the problem. This makes the algorithm computationally efficient even for complex computational tasks.

One remark about the nature of quantum resources exploited by DQC1 protocol needs to be discussed. When the purity of a quantum state is not preserved and the state of the system becomes mixed, which is the case for DQC1, interactions within the system can still build correlations beyond classical. The main question regarding the DQC1 protocol is whether quantum correlations other than entanglement (discord) can be a computational resource. Since ensemble qubits are in a highly mixed state, it is unknown how the mutual information of the system is spread across the ensemble qubits. In [65] the authors investigate an impact of the purity of the control qubit on the system, assuming that the state of the control qubit is $\rho_c = 0.5\,(\mathbb{1}_1 + \alpha_p Z)$, where Z is the Pauli operator. Here the factor α_p determines the purity of the qubit and takes values between 0 and 1. For the extreme cases, when the $\alpha_p = 0$ the control qubit is in the fully mixed state, whereas it is in maximally pure state for $\alpha_p = 1$. It was derived [65], that for a general case the output of the algorithm is just scaled by the factor α_p

$$\rho_c^{(out)} = \frac{\alpha_p}{2} \begin{pmatrix} 1 & \frac{Tr\left[U_N^\dagger\right]}{2^N} \\ \frac{Tr[U_N]}{2^N} & 1 \end{pmatrix},$$

while the accuracy remains unaffected. Moreover, entanglement does not occur in the system at all if the purity $\alpha_p < 0.5$. According to these results, authors speculate that the speed-up of the DQC1 algorithm is independent from the total amount of entanglement in the system, but arises due to the distribution of quantum correlations among individual qubits. Nevertheless, this still requires further investigation, therefore it is interesting to implement DQC1 eventually on a system with many qubits in ensemble and investigate quantum discord as a computational resource for quantum computing.

2.2 Physics of cold atoms

In quantum optics experiments, alkali atoms are usually employed due to their relatively simple hydrogen-like structure, which enables an easy manipulation of their internal state. It allows, for instance, to apply cooling of atoms (see chapter 3) or to encode a qubit in its stable electronic ground state. In our experiment rubidium is used, since the wavelength required for excitation from the ground state to the first excited state ($780\,\mathrm{nm}$) can be provided by commercial semiconductor laser diodes[3] (described further in chapter 3). Therefore, in this section the theoretical background for manipulation of rubidium atoms with laser light will be introduced. It will cover a discussion of the internal electronic structure of rubidium, its properties in external fields, and the general theory of light-matter interactions. Finally, a detailed description of the implementation of DQC1 with cold rubidium atoms is presented.

2.2.1 Atomic structure of rubidium

Alkali atoms from the first group of the periodic table have only one valence electron, and the remaining ground state shells are closed. Hydrogen-like atoms can be considered as a system composed of a single electron interacting with the nuclei via a potential $V(r)$, and described by the stationary Schrödinger equation as follows

$$\left(-\frac{i\hbar^2}{2\mu}\nabla^2 + V(\mathbf{r})\right)\psi(\mathbf{r}) = E\psi(\mathbf{r})$$

where $\mu = \frac{Mm_e}{M+m_e}$ is a reduced mass, m_e and M are electron and nucleon masses respectively. Since the reduced mass does not differ much from the electron mass[4], and a size of the nuclei is about 5 times smaller than the size of an atom, it can be assumed that the core with a total charge Ze originates the Coulomb potential $V(\mathbf{r}) = \frac{(Ze)^2}{4\pi\epsilon_0 r}$.

Expressing the Laplacian ∇^2 in spherical coordinates, the Schrödinger equation takes the form

$$\left[-\frac{\hbar^2}{2\mu r^2}\frac{\partial}{\partial r} + \frac{\mathbf{L}^2}{2\mu^2} - \frac{(Ze)^2}{4\pi\epsilon_0 r}\right]\psi(\mathbf{r}) = E\psi(\mathbf{r})$$

where part of the Laplacian is expressed through the orbital angular momentum

$$\mathbf{L}^2 = -\hbar^2\left[\frac{1}{sin\theta}\frac{\partial}{\partial\theta}\left(sin\theta\frac{\partial}{\partial\theta}\right) + \frac{1}{\sin^2\theta}\frac{\partial^2}{\partial\varphi^2}\right]$$

[3] Other commonly used chemical elements in cold atoms platforms are: cesium ($852\,\mathrm{nm}$), potassium ($766\,\mathrm{nm}$) and sodium ($590\,\mathrm{nm}$).

[4] An electron is about 2000 times lighter than the mass of a nucleon leading to $\mu \approx m_e\left(1 - \frac{m_e}{M}\right)$

Solving the Schrödinger equation leads to the expression for the energy levels

$$E_n = -\frac{\mu Z^2 e^4}{2(4\pi\epsilon_0\hbar)^2}\frac{1}{n^2} = \frac{E_{\text{ion}}}{n^2}, \tag{2.11}$$

where E_{ion} is the ionization energy. Here, $n = m + l \geq 1$ is the main quantum number and consists of constants $m, l \in \mathbb{Z}$, where l is the orbital quantum number and m is the magnetic quantum number. Even though the relativistic approach should be used for big Z to obtain accurate results, this model is very important as it shows that for each n there are $l \in \{0, 1, \ldots, n\}$ orbital sub-levels. Since the energy depends only on the main quantum number, each of the levels is n^2 times degenerated.

Fine structure

The atomic spectrum or rubidium was measured in [91], where spectral structure and ionization energies for alkali metals were determined. The electronic configuration of ^{87}Rb ground state was determined to be $1s^2 2s^2 2p^6 3s^2 3p^6 3d^{10} 4s^2 4p^6 5s^1$ with the ionization energy $33\,690.81\,\text{cm}^{-1}$ ($4.177\,128\,\text{eV}$). According to the results, the sublevels $P, D, \ldots$[5] are split further, as shown on Figure 2.3 where D line can be decomposed into two lines ($D1$ and $D2$). This is the fine structure of an atom and can be optically measured, since the split is larger than the linewidth of many lasers.

The expression for energy levels of a hydrogen-like atom in (2.11) hides the fine structure in the degeneracy of the energy levels. Therefore, in reality, the hydrogen-like model is not sufficient to fully describe the atomic structure of rubidium. The first improvement to the model can be obtained by taking relativistic effects into account, since the nuclei of rubidium is rather heavy. Moreover, a more accurate solution to the problem can be obtained using the Hartree-Fock approach which includes all interactions among protons and electrons. For many measurements the Hartree-Fock method gives results which are close to the measurements, as in [92]. Additionally, the observed fine structure comes from the coupling of the valence electron's spin angular momentum $\mathbf{S}$ with its orbital angular momentum $\mathbf{L}$. The split due to the coupling between $\mathbf{S}$ and $\mathbf{L}$ gives a total angular momentum $\mathbf{J} = \mathbf{S} + \mathbf{L}$ with the corresponding quantum number $|l - s| \leq J \leq l + s$. By adding all terms to the Hamiltonian and solving the Schrödinger equation using the perturbation theory, a full

[5] Naming sublevels with letter $S, P, D, F, \cdots$ is due to the spectroscopy notation, which comes from the times before atomic orbitals were understood. Initially, a distinct properties of the spectral series observed in alkali metals were the basis for energy levels classification. And hence, $S, P, D, F, \cdots$ comes from *sharp*, *principal*, *diffuse* and *fundamental* spectral lines.

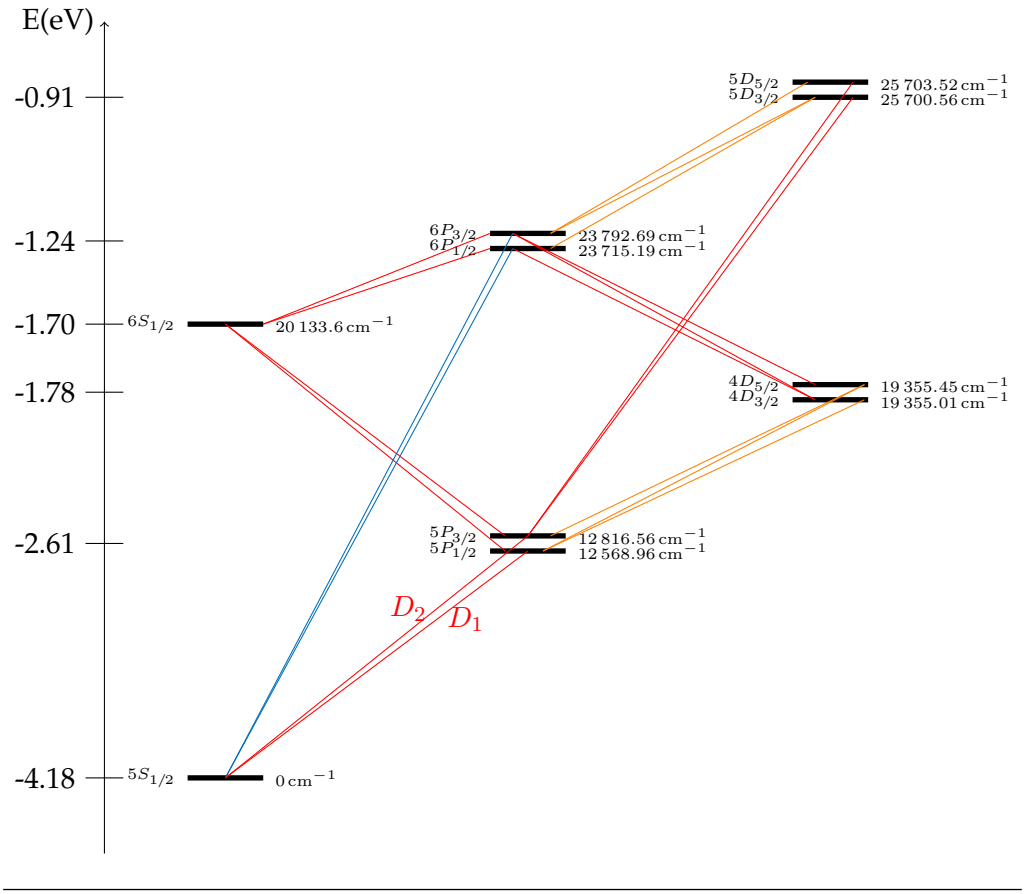

FIGURE 2.3: Fine structure of ^{87}Rb. Atomic transitions are shown by the solid lines and obeys selection rules as follows: $\Delta J = 0, \pm 1$ amd $\Delta l = \pm 1$.

picture of the fine structure can be obtained. The structure of ^{87}Rb is shown on Figure 2.3, where the ground state $\left|5^2S_{1/2}\right\rangle$ is a singlet and the first excited state is a doublet with two sublevels $\left|5^2P_{1/2}\right\rangle$ and $\left|5^2P_{3/2}\right\rangle$ corresponding to $J = \frac{1}{2}$ and $J = \frac{3}{2}$.

Hyperfine structure

A further split of the fine levels, so called hyperfine structure, was observed for the very first time in 1896 by Zeeman [93][6], for an atomic vapour placed in an external magnetic field.

The hyperfine structure arises from the coupling of nuclear spin $\mathbf{I}$ with the total angular momentum of a valence electron $\mathbf{J}$, resulting in a total atomic angular momentum $\mathbf{F} = \mathbf{J} + \mathbf{I}$. Therefore, the new quantum number describing the state takes values $|J - I| \leq F \leq J + I$.

[6] In fact, Zeeman noticed only broadening of spectral lines instead of a clear splitting, suggesting that there are two components. Although the effect was first observed in the presence of a magnetic field, the hyperfine structure is an intrinsic feature of atoms and occurs even in the absence of any external fields. Since the energy splitting is very small and hence difficult to be resolved, intense research on the hyperfine structure was conducted in the mid-twentieth century leading to a good understanding of the underlying principles [94]. A precise measurements of hyperfine structure[7] for D line ^{87}Rb were conducted only in the 1990s [95] [96] [97].

It means that in case of ^{87}Rb whose nuclear spin is equal $I = \frac{3}{2}$, the states $\left|5^2S_{1/2}\right\rangle$ and $\left|5^2P_{1/2}\right\rangle$ are split into two sublevels $F = 1, 2$, while state $\left|5^2P_{3/2}\right\rangle$ into $F = 0, 1, 2, 3$, as shown on Figure 2.4. Each of the hyperfine energy levels (F) is degenerated $2F + 1$ times in the absence of external fields, and the degeneracy is depicted on the Figure 2.4 as a separate level described by the m_F quantum number.

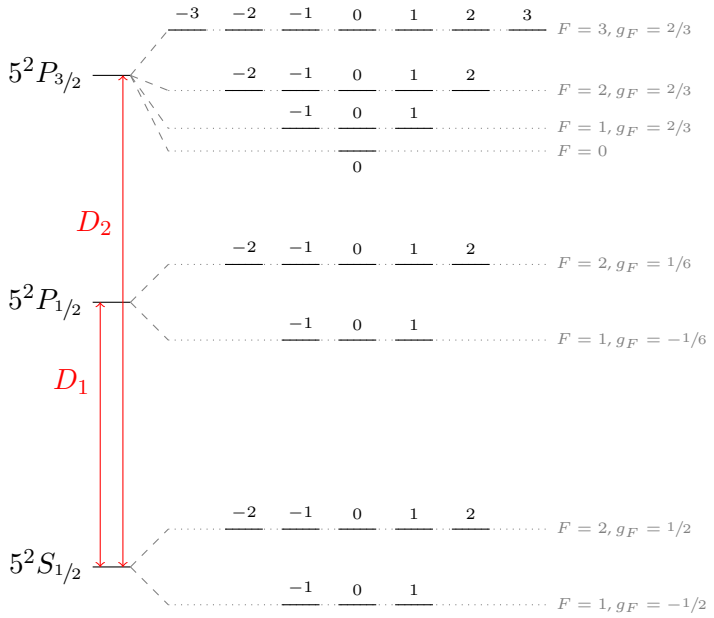

FIGURE 2.4: Hyperfine structure of ^{87}Rb. The small numbers denote the m_F number. Here g_F is a *Landé g-factor*.

2.2.2 Zeeman effect

The degeneracy of the energy levels in hyperfine structure is broken when an atom is placed in the external magnetic field. There are two regimes of the energy shifts regarding the strength of the magnetic field: *normal Zeeman effect* when the energy shifts are bigger than the hyperfine structure, and *anomalous Zeeman effect* otherwise. The general interaction Hamiltonian for *anomalous Zeeman effect*, which is typically exploited in cold atoms platform, can be expressed as

$$H_B = \frac{\mu_B}{\hbar} \left(g_J J_Z + g_I I_z\right) B_z$$

where $g_{J,I}$ are gyromagnetic factors, B_z is the magnetic field along the quantization axis, J_Z and I_z are z components of the total angular momentum $\mathbf{J}$ and the nuclear spin $\mathbf{I}$ respectively, see [94] for details. For a weak field, the energy shifts can be calculated using the first

order of perturbation theory with the explicit result

$$\delta E_{|F,m_F\rangle} = \mu_B g_F \mathrm{m_F} B_z \tag{2.12}$$

where μ_B is Bohr Magneton and $g_F(F, I, J)$ is a *Landé g-factor* (see Figure 2.4). In this regime the splitting is linear and proportional to the magnetic field.

2.2.3 Rydberg states of alkali atoms

Rydberg atoms are atoms in an excited electronic state of high quantum number n, typically in range from twenty to a few hundred. In the case of alkali atoms, the quantum-mechanical picture may be well approximated to the hydrogen-like model. The valence electron, interacting via Columb's potential with the nuclei, feels an effective potential field which is suppressed ('screened') by the inner shell electrons. In highly excited states hydrogen-like model can be justified by the large separation between valence electron and the last occupied closed shell.

However, if the angular momentum of the valence electron state is small, then the orbit becomes extremely elliptic and the electron can penetrate the inner shells. During this time the electron is exposed to unscreened Coulomb potential and additionally interacts with other electrons, which results in polarisation of the inner shells. The energy of the system can be described by an hydrogen-like atom model where a correction is applied by introducing the quantum defect $\delta(n)_{LJ}$, which is a function of the principal quantum number n and depends on the orbital **L** and the total angular momentum **J**. The measurement of quantum defect is the subject of research work [98–101].

The quantum defect is used to introduce an effective principal quantum number $n^* = n - \delta(n)_{LJ}$ which is the approximation of the main quantum number n in (2.11). The properties of atoms in a particular state are described by all quantum numbers, however since the principal quantum number is very high, it can dominate in defining the most important properties of Rydberg atoms [102], such as:

- large radius of the valence electron orbit obtained directly from Bohr's theory

$$r = \frac{(4\pi\epsilon_0)\hbar^2}{Ze^2 m_e} (n^*)^2 ,$$

- energy level structure proportinal to $(n^*)^{-2}$ and the Rydberg constant R_∞

$$E_n = -\frac{R_\infty}{(n^*)^2},$$

- small energy spacing between adjacent states $\Delta E_n = E_n - E_{n-1} \sim (n^*)^{-3}$,
- large polarizability described by relation

$$\alpha_n = -2\sum \frac{\mathbf{d}^2}{\Delta E_n} \sim (n^*)^7,$$

  where $\mathbf{d}$ is the electric dipole matrix element

- long radiative lifetime proportional to $\sim (n^*)^3$.

There are several methods for exciting atoms to such high energy levels. In our experiment, photo-excitation is the most efficient and accurate method that allows the laser light to be tuned to the specific transitions, thus controlling the excitation to the particular Rydberg state.

2.2.4 Interactions between Rydberg atoms

Because of the large polarizabilities, an electric field acting on Rydberg atoms induces significant dipole moments [103]. Although Rydberg atoms do not have a permanent dipole moment in the absence of an external electric field, their enhanced polarizability can result in fluctuating induced dipole moments leading to the time-varying van der Waals and dipole-dipole interactions between atoms. Additionally, the strength of the interactions can be enhanced by choosing appropriate states and deliberately applying an external field leading to so called Föster resonance [104].

If the atoms are in the vicinity of each other and interact via temporal dipole moments, a quantum system of two atoms has to be described by a single wave function. Then, the internal atomic structure is modified compared to the structure of non-interacting atoms. According to the semi-classical model, the dipole interaction between two atoms A and B can be described by the formula

$$V_{dd} = \frac{R^2 \mathbf{d}_A \cdot \mathbf{d}_B - 3\,(\mathbf{d}_A \cdot \mathbf{R})\,(\mathbf{d}_B \cdot \mathbf{R})}{R^5} \tag{2.13}$$

where R describes distance between dipoles and $\mathbf{d}$ is a quantum model of dipole moment defined by the equation (A.2). The Energy levels of two atoms excited to the same Rydberg state

$$|\Psi_{AB}\rangle = |\Psi_A(n,l,J)\Psi_B(n,l,J)\rangle$$

are $(2j+1)^2$ times degenerated when atoms are at infinite distance and in absence of external field. When the distance is finite the dipole-dipole V_{dd} interaction couples $|\Psi_{AB}\rangle$ to a different state:

$$\left|\Psi'_{AB}\right\rangle = \left|\Psi'_A(n_A,l_A,J_A)\Psi'_B(n_B,l_B,J_B)\right\rangle$$

which differs from the original state by the energy defect $\Delta = E(n_A,l_A,J_A)+E(n_B,l_B,J_B)-2E(n,l,J)$. This coupling is responsible for an energy shift of the $|\Psi_{AB}\rangle$ state, thus breaking its degeneracy.

Solving the time-independent Schrödinger equation, the energy shift [103] is given by the expression

$$\delta E(R) = \frac{\Delta}{2} - \frac{\Delta}{2}\sqrt{1+\frac{4}{\Delta}\frac{C_3^2}{R^6}} \tag{2.14}$$

with the dipole matrix elements $C_3 \propto \langle\Psi_A|\, e\mathbf{r_A}\, |\Psi'_A\rangle \langle\Psi_B|\, e\mathbf{r_B}\, |\Psi'_B\rangle$. Two regimes can be distinguished for $\delta E(R)$ regarding the distance between two Rydberg atoms. Van der Waals regime arise for long distances, when the energy shift is very small and depends mostly on $\delta E(R) \approx \frac{1}{\Delta}\frac{C_3}{R^3}$. Then, breaking the degeneracy is almost invisible as shown on Figure 2.5. On the other side, the dipole-dipole type of interactions is dominant for small R when the

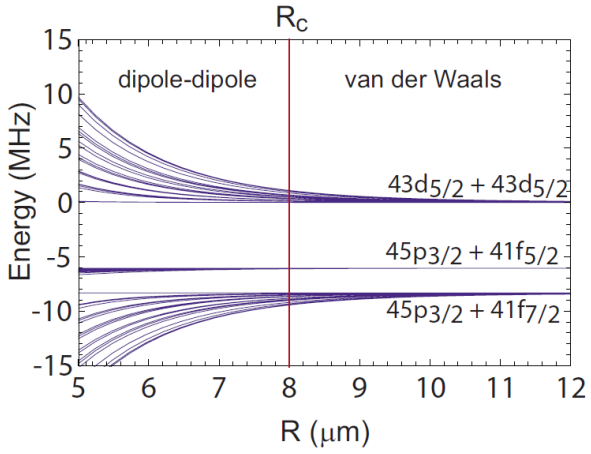

FIGURE 2.5: Interaction potentials for $\left|43D_{5/2}, 43D_{5/2}\right\rangle$, $\left|45P_{3/2}, 41F_{5/2}\right\rangle$ and $\left|45P_{3/2}, 41F_{7/2}\right\rangle$ Rydberg states of rubidium atoms. The cutoff radius Rc represents the distance scale for the transition from resonant dipole- dipole to van der Waals behavior. Source [104].

shift is much stronger and scales as $\delta E(R) \approx \frac{C_3}{R^3}$. In general the shift depends on the relation between the strength of dipole-dipole coupling C_3 and energy defect Δ. Usually $\Delta \neq 0$, however for some states $|\Psi_{AB}\rangle$ (e.g. $\left|58D_{3/2}, 58D_{3/2}\right\rangle$) it almost becomes zero and the dipole-dipole interaction is enhanced, referred to as a Föster resonance.

2.2.5 Light-atom interaction

Coupling between the electromagnetic field (laser light) and the atom may lead to two different effects depending on the light frequency, polarisation and the shape of the wavefront. As it will be shown in this chapter, when laser light is close to the atomic resonance the main contribution to interactions is given by absorption, spontaneous and stimulated emission of photons, which can also result in the cooling down of atoms. A different phenomenon dominates if a Gaussian laser beam is detuned from resonance and highly focused. In this case, the atoms are subject to the dipole trap force that arises because of the coupling of induced dipole moment and electromagnetic field.

Due to the fact the that the intensities of the laser beams used in optical trapping are usually high, the problem can be simplified by considering a semi-classical approach. In this model the atom is treated in a quantum mechanical way while the incident light is classically treated.

Hamiltonian in the interaction picture

The coupling of atoms and the electromagnetic field is a dynamic process[8], hence it is convenient to use the interaction picture to describe the system, following the approach presented in [105]. This example considers the general case of a group of atoms with separated N_g ground states $|g_j\rangle$ and N_e excited states $|e_j\rangle$.

The Hamiltonian describing an atom interacting with an electromagnetic wave can be expressed as

$$H = H_0 + H_{LA} \tag{2.15}$$

[8] Unlike a stationary interaction with electric and magnetic fields described by dc Stark shift or Zeeman Effect.

where H_0 is time independent non-perturbed Hamiltonian of the atom and H_{LA} is the dynamic light-atom interaction Hamiltonian. The part of Hamiltonian responsible for light-atom interaction is defined as

$$H_{LA}(\mathbf{R},t) = -\sum_{j=1}^{N_g}\sum_{l=1}^{N_e} \mathbf{D}_{g_j e_l} \cdot \mathbf{E}_L(\mathbf{R},t). \tag{2.16}$$

where $\mathbf{D}$ denotes *dipole moment operator*[9], $\mathbf{R}$ is the centre of mass of an atom, and the electric field of monochromatic laser light is given by

$$\mathbf{E}_L(\mathbf{r},t) = \frac{1}{2}\mathbf{E_0}\left(e^{-i(\omega_L t - \mathbf{k}_L \mathbf{r})} + c.c.\right).$$

Here, $\mathbf{E_0}$ is a vector field describing the amplitude and the polarisation of the field, ω_L is laser's anguar frequency and $\mathbf{k}_L$ is wavenumber.

The explicit form of interaction Hamiltonian can be obtained by using the *rotating wave approximation* (RWA). This approximation is valid if the electric field is close to resonance, which means if $\omega_L - \delta\omega_{g_j e_l} \ll \omega_L + \delta\omega_{g_j e_l}$ where $\delta\omega_{g_j e_l}$ is the frequency of atomic transition. For the Rubidium D_2 line, which is at 780 nm, laser wavelengths of up to $900\,\mathrm{nm}$ satisfy the assumption. It allows the rejection of terms with fast oscillation $\omega_L + \delta\omega_{g_j e_l}$ and simplify expression for H_{LA} to

$$H_{LA}(\mathbf{R},t) = \sum_{j=1}^{N_g}\sum_{l=1}^{N_e} \frac{1}{2}\hbar\Omega_{g_j e_l}(\mathbf{R}) \left|g_j\right\rangle \left\langle e_l\right| e^{-i(\omega_L t - \mathbf{k}_L \mathbf{R})} + h.c. \tag{2.17}$$

where the *Rabi frequency* was introduced in the form

$$\hbar\Omega_{g_j e_l}(\mathbf{r}) = -\left(\mathbf{d}_{g_j e_l} \cdot \mathbf{E}_0(\mathbf{r})\right). \tag{2.18}$$

All possible transitions between ground and excited states are taken into consideration in equation (2.17) by double summation $\sum_{j=1}^{N_g}\sum_{l=1}^{N_e}$, while the selection rules are included in Rabi frequency by the elements which are equal to zero.

[9] Definition and properties of dipole moment operator are in appendix A.1

Main radiative forces

The effective motion of an atom should be taken into account as a motion of the whole atomic wave packet. This means, that the average force[10] taken over the entire atomic wave function is

$$\langle \mathbf{F}(\mathbf{R},t)\rangle_{int} = -\langle \nabla H_{LA}(\mathbf{R},\mathbf{t})\rangle_{int}\,. \tag{2.19}$$

The evaluation of this expression requires assuming that the atomic wave packet is small in comparison to the optical wavelength, so called Small Atomic Wave Packet Limit (see appendix A.2). The effective force acting on an atom is derived by taking the average over an optical period and leads to

$$\mathbf{F}(\mathbf{R}) = -\hbar\sum_{j=1}^{N_g}\sum_{l=1}^{N_e}\left(\frac{\tilde{\rho}_{g_je_l}+\tilde{\rho}_{e_lg_j}}{2}\nabla\left(\Omega_{g_je_l}(\bar{\mathbf{R}})\right) - \frac{\tilde{\rho}_{g_je_l}-\tilde{\rho}_{e_lg_j}}{2i}\Omega_{g_je_l}\nabla(\mathbf{k}_L\bar{\mathbf{R}})\right), \tag{2.20}$$

where state of an atom is given by $\rho_{g_je_l}$ and the transition probability between states oscillates with a driving frequency $\rho_{g_je_l} = \tilde{\rho}_{g_je_l}e^{-i\left(\omega_L t-\mathbf{k}_L\bar{\mathbf{R}}\right)}$. In the equation (2.20) two forces appear. The first term which is proportional to the gradient of amplitude of field is responsible of the so called dipole trap force. The second term proportional to the phase gradient results in scattering forces which are used in Magneto-Optical Traps.

2.2.6 Scattering force

The temporal evolution of the system is described by the Louville equation for a dissipative system

$$\frac{d\rho}{dt} = -\frac{i}{\hbar}\left[H,\rho\right] + \chi_{dec} \tag{2.21}$$

where ρ is density matrix of the quantum system, H represents interaction Hamiltonian and χ_{dec} is responsible for the decoherence of the system. Inserting explicit forms of Hamiltonian and decoherence term into equation (2.21) leads to the Optical Bloch Equations (OBE), which will be used to obtain the explicit expressions for density matrix ρ elements.

The Hamiltonian describing coupling between all possible ground and excited states may be very complicated, but for rubidium in an almost resonant light to the atomic transition (with detuning smaller that the hyperfine structure splitting), a two level system can

[10] Regarding quantum mechanics and the Heisenberg point of view, the expression for the force takes the following form: $\mathbf{F} = \frac{d\mathbf{P}}{dt} = \frac{i}{\hbar}\left[H,\mathbf{P}\right] = -\nabla H$.

be considered as follows. Transitions between ground and excited states are driven by Rabi frequency $\Omega_{ge} \equiv \Omega$ but additionally the excited state can spontaneously decay back to the ground state with rate Γ. A set of differential OBE equations describe the system [106]:

$$\frac{d\rho_{gg}}{dt} = \frac{i}{2}\left(\Omega\tilde{\rho}_{eg} - \Omega\tilde{\rho}_{ge}\right) + \Gamma\rho ee \tag{2.22a}$$

$$\frac{d\rho_{ee}}{dt} = \frac{i}{2}\left(\Omega\tilde{\rho}_{ge} - \Omega\tilde{\rho}_{eg}\right) - \Gamma\rho ee \tag{2.22b}$$

$$\frac{d\tilde{\rho}_{ge}}{dt} = \frac{i}{2}\Omega\left(\rho_{ee} - \rho_{gg}\right) - \left(\frac{\Gamma}{2} + i\Delta\right)\tilde{\rho}_{ge} \tag{2.22c}$$

$$\frac{d\tilde{\rho}_{eg}}{dt} = \frac{i}{2}\Omega\left(\rho_{ee} - \rho_{gg}\right) - \left(\frac{\Gamma}{2} - i\Delta\right)\tilde{\rho}_{ge} \tag{2.22d}$$

where $\Delta = \omega_L - \delta\omega_{ge}$. The oscillatory factors $e^{-i(\omega_L t - \mathbf{k}_L\mathbf{R})}$ were eliminated from OBE by transformation in the slow-rotating reference frame. The steady-state solution is obtained by setting all derivatives to zero, which gives:

$$\rho_{gg} = 1 - \rho_{ee} \tag{2.23a}$$

$$\rho_{ee} = \frac{1}{2}\frac{2\left(\frac{\Omega}{\Gamma}\right)^2}{1 + 2\left(\frac{\Omega}{\Gamma}\right)^2 + 4\left(\frac{\Delta}{\Gamma}\right)^2} \tag{2.23b}$$

$$\tilde{\rho}_{ge} = \frac{1}{2}\frac{i2\frac{\Omega}{\Gamma} + 4\frac{\Delta\Omega}{\Gamma^2}}{1 + 2\left(\frac{\Omega}{\Gamma}\right)^2 + 4\left(\frac{\Delta}{\Gamma}\right)^2} \tag{2.23c}$$

Now we can find the steady state total scattering rate by multiplying the excited state population by its decay rate $\Gamma\rho_{ee}(t \to \infty)$ from the formula

$$R_{sc} = \frac{\Gamma}{2}\frac{\frac{I}{I_{sat}}}{1 + \frac{I}{I_{sat}} + 4\left(\frac{\Delta}{\Gamma}\right)^2} \tag{2.24}$$

where the saturation intensity was defined as

$$\frac{I}{I_{sat}} = 2\left(\frac{\Omega}{\Gamma}\right)^2. \tag{2.25}$$

Inserting the density matrix elements (2.23) into equation (2.20) leads to full description of the system. The second term in (2.20), proportional to $\nabla(\mathbf{k}_L\mathbf{R})$, is given by

$$\mathbf{F}_{sc} = \hbar\frac{\tilde{\rho}_{ge} - \tilde{\rho}_{eg}}{2i}\Omega\mathbf{k}_L = \hbar\mathbf{k}_L\frac{\Gamma}{2}\frac{\frac{I}{I_{sat}}}{1 + \frac{I}{I_{sat}} + 4\left(\frac{\Delta}{\Gamma}\right)^2}. \tag{2.26}$$

As one can see from equation (2.26), the scattering force is directly proportional to the scattering rate $\mathbf{F}_{sc} = \hbar \mathbf{k}_L R_{sc}$, which makes it easy to interpret. Since $\hbar \mathbf{k}_L$ represents a momentum per photon, the scattering rate R_{sc} describes the rate of absorption of photons per unit time. The dependence of the scattering rate on the detuning from the atomic transition for rubidium 87 is shown on Figure 2.6. The scattering rate increases with the laser intensity and reaches the limit $R_{sc} \approxeq \frac{\Gamma}{2}$ when the laser intensity is much higher than the saturation intensity $I \gg I_{sat}$.

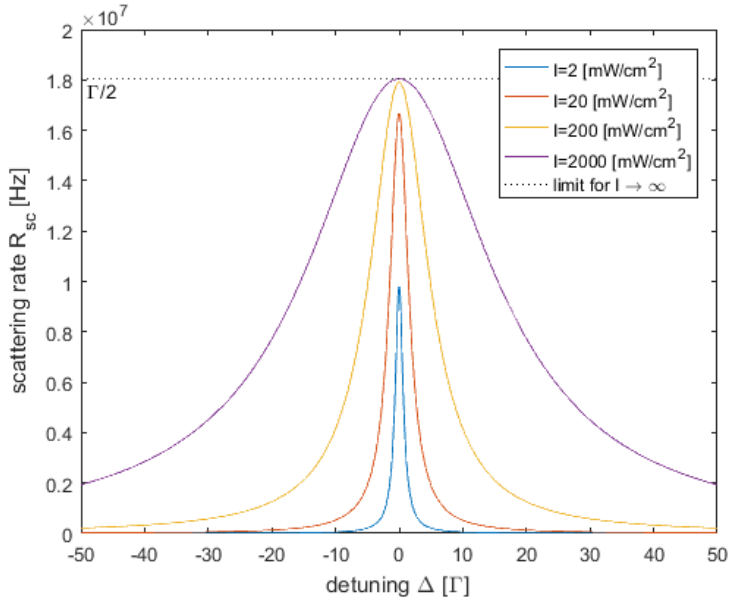

FIGURE 2.6: Theoretical prediction of scattering rate for a Rubidium atom placed in a 780 nm laser beam of various intensities.

2.2.7 Dipole force

The first term in (2.20), which is proportional to $\nabla\left(\Omega_{g_j e_l}(\mathbf{R})\right)$, leads to the so called dipole force. Using the results from the previous section for ρ and $\Omega_{ge} \equiv \Omega$ (section 2.2.6), the explicit expression for this term is

$$\mathbf{F}_{dip} = -\hbar \frac{\tilde{\rho}_{ge} + \tilde{\rho}_{eg}}{2} \nabla\left(\Omega_{g_j e_l}(\bar{\mathbf{R}})\right) = -\hbar \Delta \frac{\frac{I}{I_{sat}}}{1 + \frac{I}{I_{sat}} + 4\left(\frac{\Delta}{\Gamma}\right)^2} \frac{\nabla\left(\Omega(\bar{\mathbf{R}})\right)}{\Omega(\bar{\mathbf{R}})}. \tag{2.27}$$

According to the formula (2.27) the dipole force will vanish for resonant laser light and for plane waves for which $\nabla\left(\Omega(\mathbf{R})\right) = 0$. It shows that the detuning should be significant but still small enough to satisfy the rotating wave approximation, and the laser beams should be focused. The stronger the focusing the bigger the force acting on atoms.

There are two possibilities to create a dipole force that include using blue-detuned or red-detuned laser light. Red-detuned traps attract atoms to the place of the highest beam intensity, whereas blue detuned dipole traps repel atoms from the place of the highest beam intensity, thus blue detuned traps are implemented using hollow laser beams. We use red-detuned dipole trap, where atoms are attracted to the point of the highest intensity of laser beam.

Trapping potential and light shifts

Although the formula (2.27) is useful to understand where the dipole trapping force originates from, it is in fact inappropriate to precisely describe dipole trapping for the far-detuned laser beams. In general, interactions of moving atoms in the non-uniform external electric field are quite complex, but the discussion here is restricted to the assumption that external electric field causes only the so called *AC Stark Effect*[11]. Since the electric field used in typical dipole traps is of the order $1 \times 10^2\,\mathrm{V\,cm^{-1}}$, the energy shift is so small that perturbation theory can be successfully applied [30]. The general equation to find the energy shift is described by

$$\delta E_i = \sum_{j \neq i} \frac{|\langle j| H_{LA} |i\rangle|^2}{E_i - E_j}. \tag{2.28}$$

The wavelength used for dipole trapping, for our experiment in the range from $(830$ to $850)\,\mathrm{nm}$, provides the detuning which is comparable to the fine splitting between D_1 and D_2 lines, as it is shown on Figure 2.7a. Therefore, both lines needs to be taken into account, as the detunings Δ_1 and Δ_2 are of the same order, and thus the laser coupling strength for both lines is comparable. The first order perturbation of all levels of the fine structure, namely $\delta\left(5^2S_{1/2}\right)$, $\delta\left(5^2P_{1/2}\right)$ and $\delta\left(5^2P_{3/2}\right)$ can be calculated from equation (2.2.7), and can be expressed by:

$$\delta\left(5^2S_{1/2}\right) = \frac{\hbar\Gamma^2 I}{8I_{sat}}\left(\frac{1}{3\Delta_1} + \frac{2}{3\Delta_2}\right) \tag{2.29a}$$

$$\delta\left(5^2P_{1/2}\right) = -\frac{\hbar\Gamma^2 I}{8I_{sat}}\left(\frac{1}{3\Delta_1}\right) \tag{2.29b}$$

where Δ_1 and Δ_2 are detunings from D_1 and D_2 lines of rubidium respectively [107]. In the first order perturbation, the shifts of $\left|5^2S_{1/2}\right\rangle$ and $\left|5^2P_{1/2}\right\rangle$ states do not depend on the

[11] The effect is similar to the *dc Stark Shift*, but AC stands here for the time varying fields.

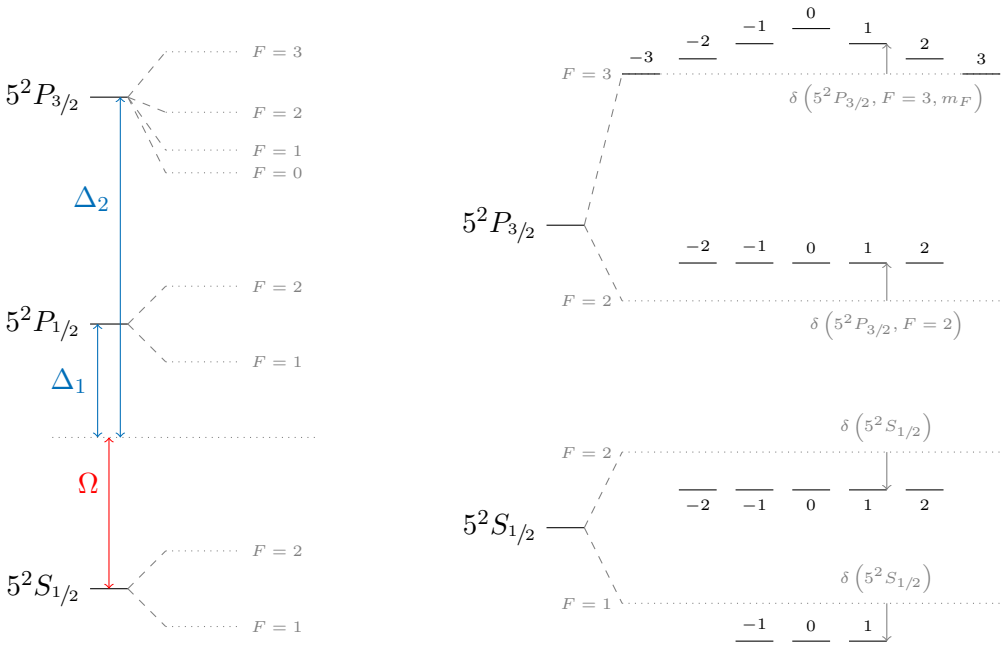

(a) Laser coupling (b) Energy shifts

FIGURE 2.7: Dipole trap laser coupling and corresponding energy shifts for ^{87}Rb. (a) Laser coupling scheme of far red detuned dipole trap laser, where Δ_1 and Δ_2 corresponds to the detunings from D_1 and D_2 lines respectively. (b) Energy shift of selected magnetic sublevels due to AC Stark Effect caused by electric field of dipole trap laser.

quantum number m_J. According to [30], it is possible to write the shift of ground state for different polarisation in the following way:

$$\delta\left(5^2S_{1/2}\right)(\epsilon) = \frac{\hbar\Gamma^2 I}{8I_{sat}}\left(\frac{1-\epsilon g_F m_F}{3\Delta_1} + \frac{2+\epsilon g_F m_F}{3\Delta_2}\right) \tag{2.30}$$

where g_F is Landé coefficient, and $\epsilon = 0, \pm 1$ for π and $\sigma^{\pm}$ polarisation respectively.

Unlike for states $\delta\left(5^2S_{1/2}\right)$ and $\delta\left(5^2P_{1/2}\right)$, the energy shift for state $\delta\left(5^2P_{3/2}\right)$ depends on m_J. Therefore an analysis of the energy shift for D_2 line must take hyperfine structure into account as in [107]. Of interest to us are both $\left|5^2P_{3/2}, F = 2\right\rangle$ and $\left|5^2P_{3/2}, F = 3\right\rangle$ states, which are used in the cooling technique as described in section 3.1.4, therefore only these states will be considered here. The second order perturbation leads to the following expressions [107]:

$$\delta\left(5^2P_{3/2}, F = 2\right) = -\frac{\hbar\Gamma^2 I}{8I_{sat}}\left(\frac{3}{5\Delta_2}\right) \tag{2.31}$$

and

$$\delta\left(5^2P_{3/2}, F=3, m_F=\pm0\right) = -\frac{\hbar\Gamma^2 I}{8I_{sat}}\left(\frac{3}{5\Delta_2}\right) \tag{2.32a}$$

$$\delta\left(5^2P_{3/2}, F=3, m_F=\pm1\right) = -\frac{\hbar\Gamma^2 I}{8I_{sat}}\left(\frac{8}{15\Delta_2}\right) \tag{2.32b}$$

$$\delta\left(5^2P_{3/2}, F=3, m_F=\pm2\right) = -\frac{\hbar\Gamma^2 I}{8I_{sat}}\left(\frac{1}{3\Delta_2}\right) \tag{2.32c}$$

$$\delta\left(5^2P_{3/2}, F=3, m_F=\pm3\right) = 0. \tag{2.32d}$$

All shifts, including fine and hyperfine structure, are depicted on Figure 2.7b. A typically used term, the trapping potential U_{dip}, is associated with the energy shift of the ground state $U_{\text{dip}} \equiv \delta\left(5^2S_{1/2}\right)$.

A trap depth $\frac{U_{dip}}{k_B} = 1\,\text{mK}$ is usually sufficient to trap atoms from a cold reservoir, where the temperature of atoms is about $(100 \text{ to } 500)\,\mu\text{K}$. A desirable $1\,\text{mK}$ depth implies that the intensity I of the beam at the focus plane needs to be $168\,\frac{\text{W}}{\text{mm}^2}$ and $248\,\frac{\text{W}}{\text{mm}^2}$ for 830nm and 852nm respectively. Figure 2.8a presents a rough estimation of required laser power to achieve $1\,\text{mK}$ trap depth assuming top hat beam focused onto $1\,\mu\text{m}$ diameter spot. The graph shows that the further the beam is detuned, the grater the power required for the same trap depth and trap size.

Scattering and heating rate

Even though the laser is detuned far from the resonance frequency, light-atoms interactions still lead to some exchange of energy between photons and trapped atoms, and might destroy the quality of trap. The scattering mechanism in the dipole trap [30] is described by:

$$\Gamma_{sc} = \frac{\Gamma^3 I}{8I_{sat}}\left(\frac{1}{3\Delta_1^2} + \frac{2}{3\Delta_2^2}\right). \tag{2.33}$$

Because of the energy exchange, atoms also experience heating inside the trap [30], which is proportional to the trapping potential

$$\dot{T} = \frac{2/3}{1+\kappa} T_{rec} \frac{\Gamma}{\hbar|\Delta_{eff}|} |U_{dip}| \tag{2.34}$$

where $\dot{T}$ is a change of the atoms' temperature in time, $\frac{1}{3\Delta_1} + \frac{2}{3\Delta_2} = \Delta_{eff}$ and the typical recoil temperature is $T_{rec} = 0.36\,\mu\text{K}$ for ^{87}Rb (see equation (3.3)). Naturally, both scattering and heating rate decrease with the increase of light detuning, as it is shown in Figure 2.8b.

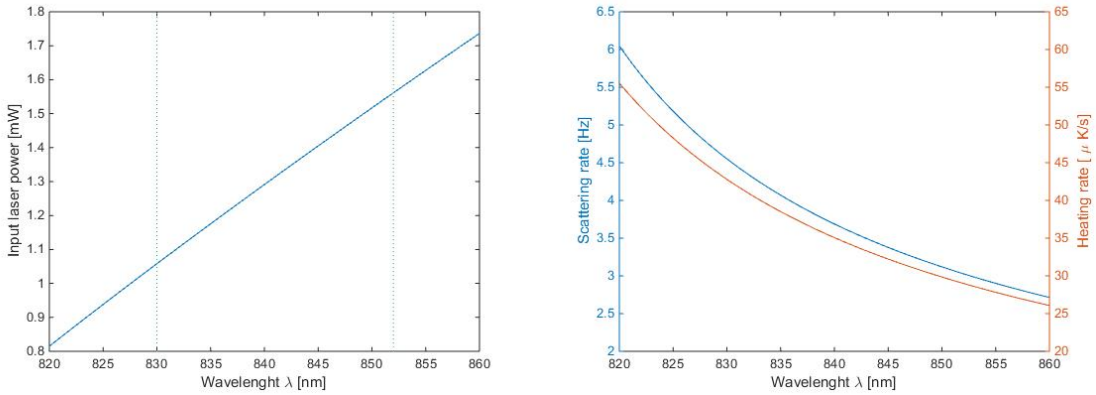

(a) Laser power

(b) Scattering and heating rates

FIGURE 2.8: Theoretically estimated properties of $1\,\mathrm{mK}$ dipole trap in terms of wavelength used for dipole trapping. (a) An estimated laser power required to maintain $1\,\mathrm{mK}$ trap. It is based on equation (2.29) assuming top hat laser beam with a spot diameter $1\,\mu\mathrm{m}$. (b) Dependence of scattering and heating rate in terms on used wavelength assuming a constant trap depth $1\,\mathrm{mK}$.

Although bigger power is need to provide the same dipole trap depth for higher wavelengths, further detuned traps are more beneficial since both scattering and heating rate are diminished.

2.2.8 Electromagnetically Induced Transparency

As it will be shown later in section 2.3, the scheme to implement controlled unitary operation to perform DQC1 (see section 2.1.3) is based upon so called Electromagnetically Induced Transparency (EIT). Although the concept will be used later to discuss the overall proposal of DQC1 with cold atoms, the theoretical principles of the EIT phenomenon are discussed below, based on the approach presented in [108].

Three level system

Let us now consider a generic three level system, $|1\rangle$, $|2\rangle$ and $|3\rangle$, exposed to two different laser beams. The so-called probe beam couples state $|1\rangle$ to $|2\rangle$, states $|2\rangle$ and $|3\rangle$ are coupled by the 'coupling beam', while the transition among states $|1\rangle$ and $|3\rangle$ is forbidden. The probe beam with Rabi frequency Ω_p and coupling beam Ω_c oscillate with driving frequencies ω_p and ω_c respectively. There are three possible energy level systems corresponding to such laser coupling (Figure 2.9) however all of them follow this description and are represented by the same Hamiltonian.

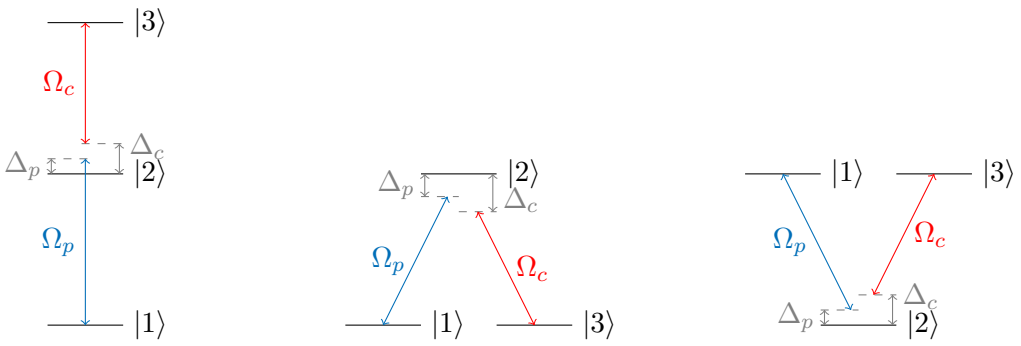

(a) Ladder (b) Lambda (c) Vee

FIGURE 2.9: Three level system interacting with light. Probe beam couples states $|1\rangle$ and $|2\rangle$, states $|2\rangle$ and $|3\rangle$ are coupled by Ω_c and transition $|1\rangle \rightarrow |3\rangle$ is forbidden.

The laser beams interact with the atom simultaneously, so the Hamiltonian consists of terms related to the interactions between individual beams and an atom. The interaction Hamiltonian of an atom in the presence of a monochromatic electromagnetic field (2.17) in a slow-rotating reference frame (RWA), can be expressed as

$$H_{int} = \frac{\hbar}{2} \begin{pmatrix} 0 & \Omega_p & 0 \\ \Omega_p & -2\Delta_p & \Omega_c \\ 0 & \Omega_c & -2\left(\Delta_p + \Delta_c\right) \end{pmatrix} \tag{2.35}$$

where Δ_p and Δ_c are the detunings of laser light from the resonance frequencies [108]. Having the explicit form of the Hamiltonian, it is possible to use the approach presented in section 2.2.6 to describe the system properties.

Electromagnetically Induced Transparency

In the case of resonant light, when $\Delta_p \approx \Delta_c \approx 0$, cancellation of absorption of one of the laser beams may be observed. Such effect was predicted independently by Kocharovskaya and Khanin [109] and Harris [110]. Under the condition $\Delta_p \approx \Delta_c$, the interaction Hamiltonian takes the form

$$H_{int} = \frac{\hbar}{2} \begin{pmatrix} 0 & \Omega_p & 0 \\ \Omega_p & -2\Delta_p & \Omega_c \\ 0 & \Omega_c & 0 \end{pmatrix} \tag{2.36}$$

The solution is given by the following eigenvalues

$$\omega_0 = 0 \tag{2.37a}$$

$$\omega_\pm = \frac{1}{2}\left(\Delta_p \pm \sqrt{\Delta_p^2 + \Omega_p^2 + \Omega_c^2}\right) \tag{2.37b}$$

with corresponding eigenvectors

$$|a_+\rangle = \sin\Theta \sin\Phi\,|1\rangle + \cos\Phi\,|2\rangle + \cos\Theta \sin\Phi\,|3\rangle \tag{2.38a}$$

$$|a_0\rangle = \cos\Theta\,|1\rangle - \sin\Theta\,|3\rangle \tag{2.38b}$$

$$|a_-\rangle = \sin\Theta\cos\Phi\,|1\rangle - \sin\Phi\,|2\rangle + \cos\Theta\cos\Phi\,|3\rangle \tag{2.38c}$$

where $\Theta = \frac{\Omega_p}{\Omega_c}$ and $\tan 2\Phi = \frac{\sqrt{\Omega_p^2+\Omega_c^2}}{\Delta_p}$. State $|a_0\rangle$ is the so-called dark state, as it does not have contribution from the intermediate state $|2\rangle$. This means that the atomic population in this state is trapped in states $|1\rangle$ and $|3\rangle$ and there is no absorption of the probe beam. Moreover, when the coupling beam is much stronger than the probe beam, precisely when $\frac{\Omega_p}{\Omega_c} \approx 0$, the expression for the dark state becomes

$$|a_0\rangle = \cos\frac{\Omega_p}{\Omega_c}\,|1\rangle + \sin\frac{\Omega_p}{\Omega_c}\,|3\rangle \approx |1\rangle\,.$$

According to the equation, atoms will always remain in the ground state $|1\rangle$ and the probe beam is never absorbed. Precisely this phenomenon is called the EIT, and is exploited in various proposals for quantum gates with neutral atoms.

2.3 Implementation of DQC1

The dipole-dipole interactions described in section 2.2.4 between Rydberg atoms underlay the phenomena called Rydberg blockade, which is crucial for the implementation of DQC1 with cold atoms [70]. According to this proposal, based on a $cNOT$ gate, the implementation of the DQC1 requires a full Rydberg blockade. Therefore the concept of Rydberg blockade is first introduced in this section, followed by the description of its application to fast quantum gates [54, 55]. Finally, the detailed proposal of DQC1 with cold ^{87}Rb atoms is described.

2.3.1 Rydberg blockade

A Rydberg blockade occurs when one atom in Rydberg state suppresses the simultaneous excitation of another atom to the Rydberg state. Let us for a moment neglect the complicated energy structure and assume just two level structure, where each atom can be either in the ground state $|g\rangle$ or in the Rydberg excited state $|r\rangle$. Both of the atoms are addressed by the same laser Ω coupling ground state with the Rydberg state $|g\rangle \rightarrow |r\rangle$. The energy structure of atoms pair is presented in Figure 2.10, where the energy levels starting from the lowest one are: both of atoms are in a ground state $|g,g\rangle$, one atom is in an excited state $|g,r\rangle$ or $|r,g\rangle$, both of atoms are in Rydberg states $|r,r\rangle$.

According to section 2.2.4, if both of atoms are excited to the Rydberg states, the energy of double excited level $|r,r\rangle$ depends on the distance between atoms. If the distance between atoms is smaller than the so-called blockade radius R_b (Figure 2.10), the energy shift $\delta E(R)$ (defined by equation (2.14)) becomes bigger than the linewidth of the coupling laser. For distances bigger than the blockade radius $R > R_b$ both of the atoms can be successfully excited to the Rydberg states $|r,r\rangle$. For $R < R_b$, the shift becomes so significant that if one of the atoms is already in the excited state $|r\rangle$, then the coupling of the other atom from the ground state to the Rydberg state is diminished.

The model of Rydberg blockade presented here is very simplistic, but shows the governing principle well. In reality it is for instance possible to address each atom with a laser of slightly different frequency addressing different Rydberg states and aiming for stronger dipole-dipole interactions V_{dd} due to Foster resonance. A careful selection of the Rydberg states helps to achieve a desired strength of Rydberg interactions boosting the fidelity of quantum gates based on the Rydberg blockade. According to section 2.2.4, the energy shift level is equal $\delta = 10\,\mathrm{MHz}$ for a pair of Rubidium atoms with principal quantum number $n = 43$, when the distance between them is about $5\,\mu\mathrm{m}$. Taking into account a typical bandwidth of the excitation laser[12], this shift is high enough to diminish coupling to the Rydberg state, therefore $5\,\mu\mathrm{m}$ distance will be used from now on as a typical Rydberg blockade radius as a reference when describing dipole trapping (see chapter 4 and chapter 5).

2.3.2 Controlled rotation Rydberg gate

The first proposal of a fast controlled gate, based on the Rydberg blockade phenomenon, was presented in 2001 [112], where the Rydberg blockade was recognised as a mechanism

[12] See as an example the stabilization of $480\,\mathrm{nm}$ laser in [111].

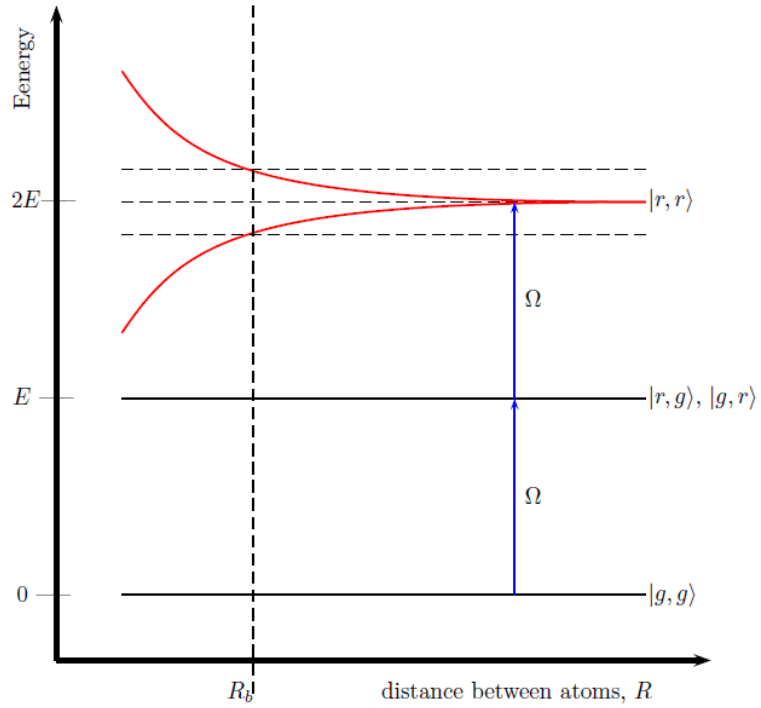

FIGURE 2.10: Rydberg blockade scheme. The energy of the double excited state $|r,r\rangle$ is a function of the distance between atoms R. If R is greater than blockade radius R_b energy states (slightly shifted) are coupled by narrow-band laser Ω. In the case of atoms closer than R_b, the energy shift becomes greater than the laser linewidth and the state $|r,r\rangle$ cannot be populated.

allowing switching on and off the interactions between atoms (see appendix B). Based on this idea, the proposal for the controlled gate which is suitable for implementation of the DQC1 algorithm was presented in [55]. Here, the Rydberg blockade phenomenon is combined with EIT and become a way to perform a controlled rotation operation on an ensemble of qubits. It is worthwhile to point out that the gate requires one control atom, which is individually addressed, and can simultaneously operate on many atoms in ensemble. The Rydberg blockade is used here to block coupling to Rydberg state. Rydberg-Rydberg interactions play here a role of switching on/off the interaction of atoms with the strong beam performing EIT, which allows for a precise control of the atom in its ground state.

For simplicity, the gate can be discussed using a two atom system: one control qubit and one ensemble qubit. Information is encoded in the hyperfine structure of the ground state, as presented in Figure 2.11: for the control atom the qubit is encoded in $|0\rangle$ and $|1\rangle$, while for the target in $|A\rangle$ and $|B\rangle$. The ground states $|A\rangle$ and $|B\rangle$ of the target atom are coupled using Ω_p through the excited state $|P\rangle$ (Figure 2.11a). The purpose of the coupling is to be

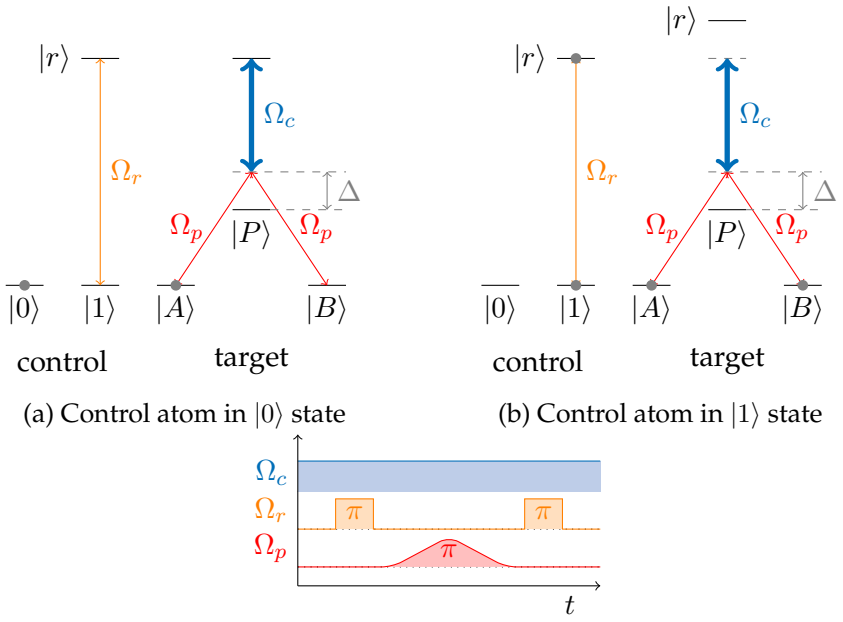

(a) Control atom in $|0\rangle$ state

(b) Control atom in $|1\rangle$ state

(c) Laser sequence

FIGURE 2.11: Scheme of controlled rotation gate based on Rydberg blockade and EIT. (a) Electronic level structure of the control and ensemble atoms. The ground state $|1\rangle$ is resonantly coupled to the Rydberg state $|r\rangle$. The states $|A\rangle$ and $|B\rangle$ are off-resonantly coupled (detuning Δ, Rabi frequency Ω_p) to $|P\rangle$. A strong laser with Rabi frequency $\Omega_c \gg \Omega_p$ couples the Rydberg level $|R\rangle$ to $|P\rangle$ such that $|R\rangle$ is in two-photon resonance with $|A\rangle$ and $|B\rangle$. In this situation (known as EIT) Raman transfer from $|A\rangle$ to $|B\rangle$ is inhibited. (b) With the control atom excited to $|r\rangle$ the two-photon resonance condition is lifted as the level $|R\rangle$ is shifted due to the interaction energy V between the Rydberg states, thereby enabling off-resonant Raman transfer from $|A\rangle$ to $|B\rangle$.

able to drive the target atom between its two ground states. However, the target atom is also constantly exposed to a strong laser light coupling excited state $|P\rangle$ with a Rydberg level $|r\rangle$ by a strong laser beam Ω_c, which is much stronger than the Ω_p. The strong laser induces the EIT phenomenon effectively preventing any possible excitation of the ensemble atom to the intermediate excited state $|P\rangle$. This means that in the presence of Ω_c the Ω_p remains unnoticed to the ensemble atom, as long as EIT 'blockade' works. A sequence of laser pulses is shown on Figure 2.11c, where it is shown that the EIT coupling laser is constantly on throughout the entire experiment.

Meanwhile, the ground state $|1\rangle$ of the control atom is coupled to the Rydberg state by Ω_r Rabi frequency. According to Figure 2.11c, first the π pulse of Ω_r is applied to the control atom, and after that a π pulse is applied to the target atom. If the control atom was initialized in the state $|0\rangle$ (gray dot on Figure 2.11a) the EIT blockade on the target atom is active and it remains so after the pulse of Ω_p beams. However, if the control is initialized in a state $|1\rangle$

(gray dot on Figure 2.11b), it is excited to the Rydberg level, so that now it interacts with the target atom via the Rydberg-Rydberg interactions. Because of the interaction, the energy of doubly excited Rydberg state is shifted and the strong EIT laser becomes off-resonant. As soon as the intermediate excited state $|P\rangle$ and Rydberg state stop being coupled, Ω_p beams can affect the state of the target atom changing the state of ensemble qubit.

As it is shown, the state of the target atom changes only if the control atom is initially put into state $|1\rangle$. If the target atom was initially $|A\rangle$, then after applying a π pulse by Ω_p, it ends in state $|B\rangle$ and vice versa. Depending on the duration of the Ω_p pulse, this protocol implements in general a *controlled rotations gate*, including a special case (π pulse) resulting in $cNOT$ gate. The principles of the gate applies also when there is an ensemble of many target atoms, meaning that the gate performs effectively the unitary operation required for DQC1.

2.3.3 Final protocol

There are two main stages in the experimental implementation of the DQC1 protocol: atoms trapping and then performing the algorithm on the trapped atoms. Atoms trapping and ensuring the appropriate experimental conditions, is the subject of further consideration in chapters 3, 4, 5. In this section we explain the full laser sequence to accomplish a single run of the DQC1 protocol. Let us recall briefly the DQC1 protocol (see section 2.1.3) before delving into the details of the experimental implementation. First, the qubits need to be initialized: the control qubit in a superposition of $|0\rangle$ and $|1\rangle$ while the target qubits in the highly mixed state. Then, a controlled unitary operation is applied, involving the control and the target qubits simultaneously. Finally, the state of the control has to be measured. Only the case with two atoms will be described here for simplicity, one control atom and one target atom, but the same principle applies to many atoms in the target ensemble.

The laser system required for performing the DQC1 protocol is presented in Figure 2.12a. It consists of a pair of Raman beams Ω_p at $\approx 780\,\mathrm{nm}$ (see appendix C), a blue laser Ω_c and Ω_{rc} at $\approx 480\,\mathrm{nm}$, and the beam Ω_{op}. Qubit states are encoded in the hyperfine structure of the ground state of Rubidium 87 atoms and are denoted as $|0\rangle = \left|5S_{\frac{1}{2}}, F=1\right\rangle$ and $|1\rangle = \left|5S_{\frac{1}{2}}, F=2\right\rangle$. A pair of Raman beams Ω_p couples states $|0\rangle$ and $|1\rangle$ to the first excited state $\left|5P_{3/2}\right\rangle$ with a detuning about $1\,\mathrm{GHz}$. Due to the hyperfine split of the ground state, the Raman beams are composed by two laser beams which differ $6.8\,\mathrm{MHz}$ in frequency to ensure an equivalent coupling strength of both hyperfine levels to the excited state. The blue laser

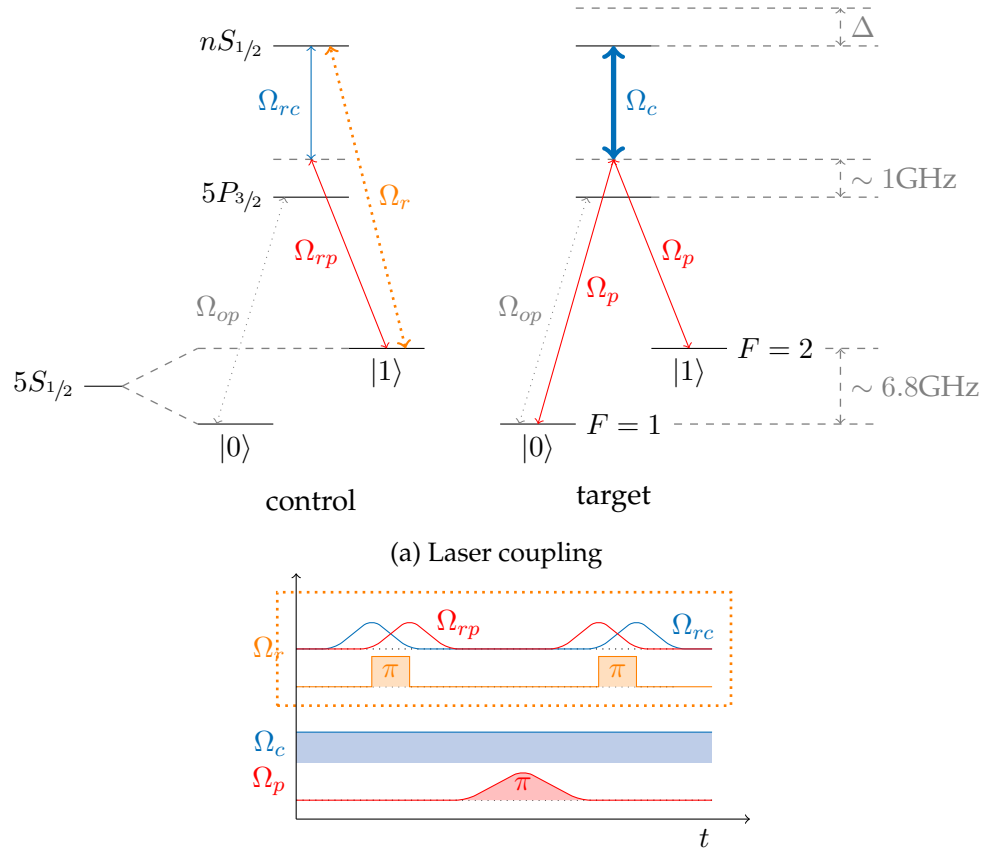

FIGURE 2.12: Implementation of DQC1 with ^{87}Rb. The discussion is provided in the text.

Ω_c and Ω_{rc} couples the first excited state $\left|5P_{3/2}\right\rangle$ with a Rydberg state $|nS\rangle$, while the role of Ω_{op} is to excite atoms from the ground state to $\left|5P_{3/2}\right\rangle$ from which atoms can spontaneously decay back to the ground state.

The initialization of the control atom starts with the atom being optically pumped to the $|1\rangle$ by Ω_{op}, as shown and explained in Figure 2.13. Then the Hadamard gate (see section 2.1.2) is applied using the π pulse of Raman beams Ω_p on the control atom resulting in its superposition of $|0\rangle$ and $|1\rangle$. Regarding target atoms, they can be prepared in a highly mixed state following method presented in [113]. First atoms are prepared in the superposition of $|1\rangle$ using Ω_{op} using optical pumping and the Hadamard gate, the same way as the control qubit is prepared. At this stage the ensemble of atoms is still in a pure state, but the purity can be reduced because of decoherence mechanism, such as spontaneous emission. Hence, one of states ($|0\rangle$ in our case) is pumped to the excited state $\left|5P_{3/2}\right\rangle$ and then allowed to spontaneously decay to a ground state. As a result the information describing the system is

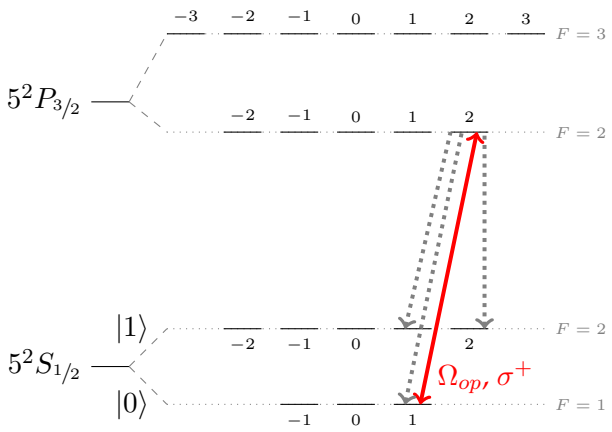

FIGURE 2.13: Optical pumping of ^{87}Rb atoms. Circularly polarized σ^+ laser beam Ω_{op} excites atoms from the $|0\rangle$ state to the excited state $|5P_{3/2}, F = 2\rangle$. From the excited state atom can decay back (dotted gray arrows) to $|0\rangle$ or to $|1\rangle$. After many cycles only state $|1\rangle$ is populated.

partially lost, resulting in the mixed states.

The next step is to perform $cNOT$ gate according to the proposal discussed in section 2.3.2, following the scheme of laser pulses presented on Figure 2.12b. First the control atom is excited using two-photon transition from the ground state $|1\rangle$ to the Rydberg state using Ω_{rp} and Ω_{rc}. A combination of these two pulses results in the direct π pulse driving a transition from $|1\rangle$ to $|nS_{1/2}\rangle$, which is shown as Ω_r on the Figure 2.12a. It is worth mentioning here that not only the sequence of the applied laser pulses is important, but also their shapes (intensities of laser light). The transition Ω_r is applied using a technique called Stimulated Raman adiabatic passage (STIRAP) [114] which allows atoms to change states from $|1\rangle$ to Rydberg state avoiding populating the intermediate excited state. As depicted in Figure 2.12b, to obtain STIRAP a pulse Ω_{rc} is followed by Ω_{rp}. As it was shown in [114], the duration and shape of pulses leads to the deterministic single-atom excitation from a ground state to the Rydberg state, which is important to maintain purity[13]. When the control atom is already excited to the Rydberg state (partially, since it is in superposition), it starts interacting with the ensemble (see section 2.3.2). Now the pulse of the Raman beams Ω_p is applied and interacts (partially) with the ensemble, as the laser Ω_c becomes out of resonance and the EIT does not apply any longer.

The performance of the *controlled rotations gate* results in a build up of correlations across the control and the target. The final step is a readout and requires applying a Hadamard

[13]The same applies to the Hadamard gate which is realised here by coupling $|0\rangle$ and $|1\rangle$ states via *Raman beams*, and thus is also applied using STIRAP.

gate on the control qubit one more time. It is because the normalized trace of unitary operation is stored in the off-diagonal elements of the density matrix. After the rotation, readout is performed by applying a pulse coupling one of $|0\rangle$ or $|1\rangle$ state of the control atom to the excited state. The fluorescence signal from the atom will contain the information about the state of the atom. Naturally, from the experimental point of view, the protocol must be repeated many times to collect a sufficient statistics of events to obtain an accurate result. The expected results of the protocol for different number of atoms in the ensemble are predicted in [70]. According to this work, by varying the rotation angle one should observe the characteristic oscillations (2.9), as in Figure 2.14.

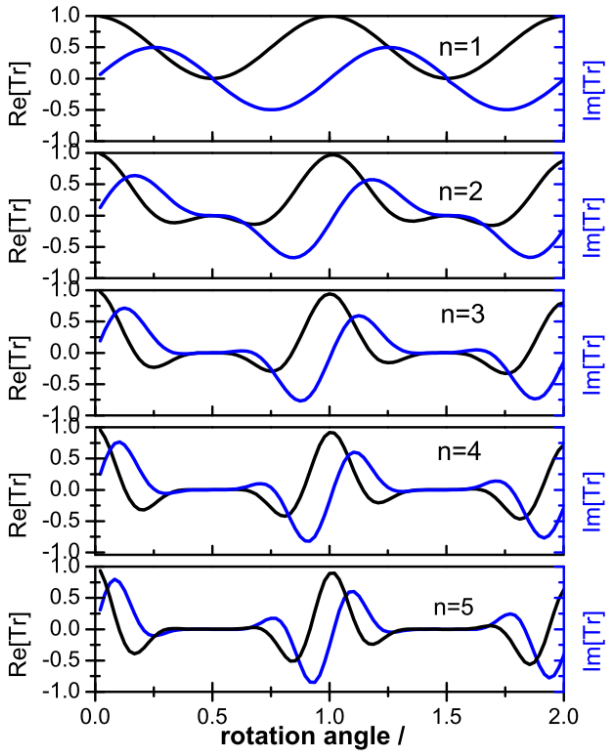

FIGURE 2.14: Theoretical predictions of the outcome of the DQC1 protocol applied on 1 to 5 atoms in the ensemble. Source: [70]

Chapter 3

Cold atoms: principles and experimental setup for a magneto optical trap

This chapter consists of both the theoretical and technical description of the apparatus required for a cold atoms experiment, covering both the Magneto Optical Trap (MOT) as well as the vacuum system. The first section of the chapter relates to the MOT which was already operational the beginning of the course of this thesis, as described in my colleague's work [111], but required partial improvements and an occasional maintenance. Therefore, a brief description of the laser system for MOT is included in this chapter highlighting the parts which were significantly changed and excluding details regarding lasers construction, locking system and electronics. Finally, the vacuum system which is required for operating both MOT and dipole trap is described in the last section of the chapter.

3.1 Cooling atomic sample with radiation pressure

The laser manipulation of neutral atoms uses techniques that exploit the forces arising from atom-light interactions (see sections 2.2.5 and 2.2.6) and have been strongly developed during the last two decades. The idea to use radiation pressure to create a three dimensional ensemble of slow atoms was first proposed in 1975 [115] and remained a theoretical concept for almost a decade. The breakthrough took place in 1986, when the first experimental demonstration of *optical molasses* was presented by the group at Bell Laboratories [116]. In that work, sodium atoms in *optical molasses*[1] were cooled to approximately $240\,\mu K$ before

[1] *Optical molasses* is the name of the atoms cooling technique exploiting only Doppler cooling in the absence of magnetic field. The concept of *optical molasses* is introduced in section 3.1.1.

loading them into another type of trap, namely a dipole trap[2]. After this demonstration, enormous progress was made almost instantly. Only a year later, the technique was improved by adding a weak quadrupole magnetic field developing the technique called Magneto Optical Trapping [117, 118]. In this demonstration, the temperature of the sodium atomic sample was in the range $(300 \text{ to } 1000)\,\mu\text{K}$, just above the theoretically predicted lowest temperature achievable for atoms cooling, the so called *Doppler limit*[3]. The MOT became popular very quickly and was reproduced and studied in different configurations with good agreement to previous experiments [119]. When laser cooling already seemed to be well understood and described, a surprisingly lower temperature of only $40\,\mu\text{K}$ was achieved for an *optical molasses* consisting of six linearly polarized cooling beams [120]. This result obviously invalidated the *Doppler limit*, but very soon [121] and [122] independently proposed an explanation of the phenomenon as *sub-Doppler cooling*[4], which is, as we will see, a polarization-dependent effect.

Since then, multiple experiments on radiation pressure traps for neutral atoms were made [123–128]. Although the technique is well known and has been thoroughly investigated, there is still a great interest in fully understanding the mechanisms responsible for the MOT behaviour. It is enough to mention recent studies: the measurement of MOT escape velocity in [129](2012); an experiment in which the *Doppler limit* is experimentally verified[5] [130](2014); photon reabsorption in MOT [131](2014) and studies of spatial instabilities of cold atoms clouds [132](2016) to understand how useful and complex the cooling technique is.

3.1.1 Doppler cooling

The scattering force (see section 2.2.6) can be exploited to achieve cooling via the Doppler Cooling technique as proposed in [115, 116]. When an atom is placed in a stream of photons, it can absorb a fraction of them while simultaneously emitting all absorbed photons, at a rate R_{sc} (2.24). For each absorbed photon, that carries momentum $\hbar\mathbf{k}_L$, an exchange of momentum results in an acceleration of the atom along the direction of photon propagation.

[2] By this time dipole trap was already known method of trapping neutral atoms. The origin of dipole force is explained in section 2.2.7 while the experimental implementation of dipole trap is discussed in chapter 5.

[3] The lowest possible temperature to be obtain in the *optical molasses* due to the spontaneous emission of absorbed photons. Doppler limit for sodium atoms is about 225 µK, which is estimated from equation (3.2). The concept of *Doppler limit* is introduced in section 3.1.1.

[4] The concept of *sub-Doppler cooling* is introduced in section 3.1.2.

[5] In the configuration of MOT for helium-4 atoms, properties of helium-4 prevents from an effective sub-Doppler cooling.

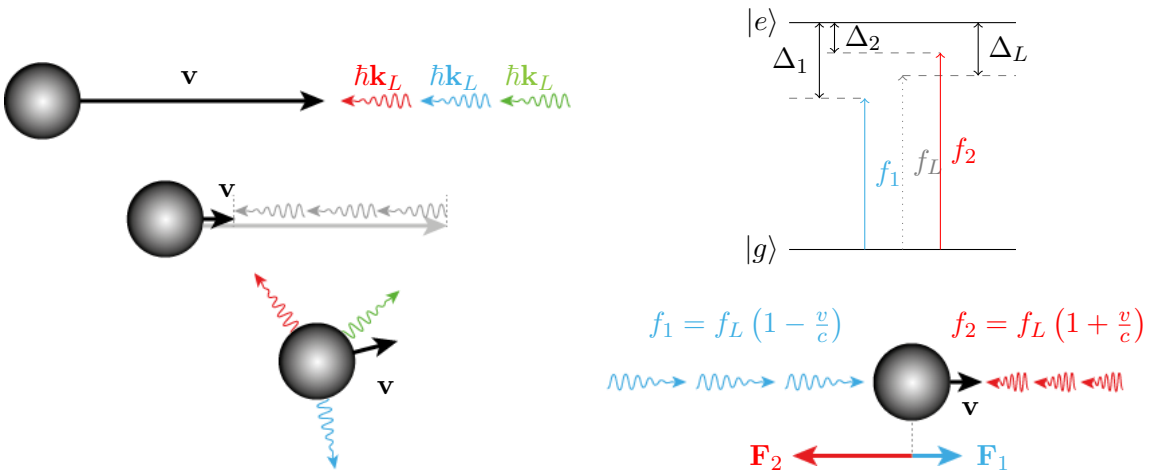

(a) Momentum exchange

(b) Light shift due to atom's movement

FIGURE 3.1: Principles of Doppler Cooling. (a) Two firsts steps show how the initial velocity of an atom $\mathbf{v}$ decreases after the absorption of three counter-propagating photons. At the last stage, all absorbed photons are remitted, resulting in small insignificant acceleration of the atom. (b) The upper scheme shows a simplistic two-level atomic structure, with one ground state $|g\rangle$ and one excited state $|e\rangle$, where f_L is the laser frequency with the detuning Δ_L from the atomic transition. Frequencies f_1 and f_2 corresponds to the shifted laser light frequencies from the scheme below.

If an atom moves toward the coherent stream of photons, it results in a decrease of an initial atom's velocity $\mathbf{v}$ proportionally to the number of absorbed photons $\mathbf{v} - N_{\text{photons}} \cdot \hbar\mathbf{k}_L$, as shown on Figure 3.1a. Each photon absorption process is followed by the spontaneous emission in a random direction (Figure 3.1a) which also creates a momentum exchange, but on average for many photons the acceleration is almost equal zero with a little impact on the atom. Therefore, after many cycles the momentum of the atom changes and the atom effectively slows down, as it is depicted on Figure 3.1a. Assuming very high power of laser light, it takes about $\sim 1\,\text{ms}$ and 5×10^4 photons to bring an atom in a room temperature from a typical velocity $300\,\frac{\text{m}}{\text{s}}$ close to $1\,\frac{\text{m}}{\text{s}}$ (which corresponds to approximately $10\,\text{mK}$ of a mean temperature).

By overlapping two counter-propagating beams, atoms moving in both directions can be significantly slowed down, if an additional detuning is introduced. For the laser intensities typically used in laser cooling, absorption of photons varies with the laser detuning and is much less efficient for non-resonant light. In order to increase the scattering rate of photons counter-propagating to the atom, laser light f_L is set to be red-detuned from the atomic transition, so that the Doppler shift tunes light f_2 closer to the resonance, as depicted in

Figure 3.1b. The atom simultaneously interacts with the second beam f_1, but because its detuning Δ_1 increases, photons from this beam are less likely to be absorbed. The effective force acting on atom is given by the result of two counteracting scattering forces $\mathbf{F_{1,2}}$, as described by (2.26). The maximum acceleration is experienced by atoms with $v_{max} \approx \pm\frac{\Gamma}{2k_L}$. For small enough velocities, lower than v_{max}, the force is proportional to velocity resulting in viscous damping, from which the name *optical molasses* comes, and follows the equation:

$$\mathbf{F_{OM}} = \mathbf{F_1} + \mathbf{F_2} \cong \frac{8\hbar k_L^2 \delta \frac{I}{I_{sat}} \mathbf{v}}{\Gamma\left(1 + \frac{I}{I_{sat}} + 4\frac{\delta}{\Gamma}\right)^2} \equiv -\beta\mathbf{v} \tag{3.1}$$

If there was no other effect apart from the damping force, atoms would soon reach an unphysical steady state with velocity and temperature equal zero $v = 0$, $T = 0$. This is clearly not the case and there is a cooling limit which arises from the discrete momentum exchange between photons and atoms leading to Brownian motion. Due to photon scattering, each atom emits a fixed quantity of energy in a random direction. Equating cooling rate and the heating rate gives the cooling limit T_D

$$T_D = \frac{\hbar\Gamma}{2k_B} \approx 140\,\mu\mathrm{K}, \tag{3.2}$$

which remarkably depends on fundamental physical constants, but neither on the used optical wavelength nor on the atomic mass. The value in equation (3.2) was estimated for rubidium D_2 line for which natural line width is equal approximately $2\pi \times 6\,\mathrm{MHz}$.

A full three dimensional optical molasses is achieved by combining three crossed perpendicular pairs of counter-propagating beams. It results in cooling of atoms moving in all directions in the region of intersection.

3.1.2 Sub-Doppler cooling

A surprisingly low temperature $(43 \pm 20)\,\mu\mathrm{K}$ in *optical molasses* was achieved in [120]. This result clearly invalidates the Doppler cooling limit $T_D \approx 140\,\mu\mathrm{K}$ so further investigation of the mechanics involved in the cooling process was needed. A new cooling mechanism was identified as polarization-gradient cooling. Sub-Doppler cooling originates because the atom experiences different strengths of laser coupling depending on the local light polarization, if this varies in space. There are two main sub-Doppler cooling mechanisms: one for

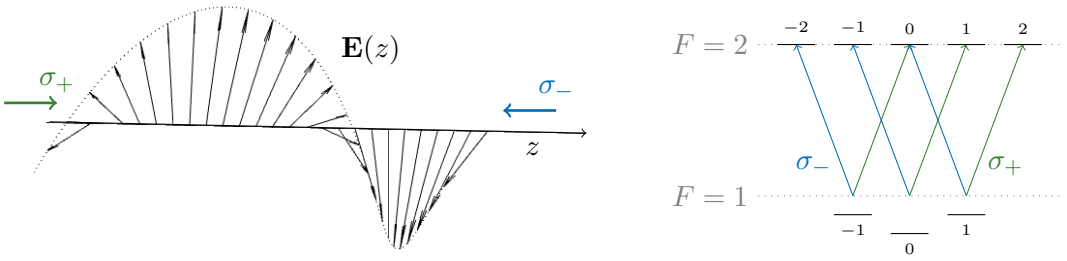

(a) Linearly polarized standing wave

(b) Atomic structure

FIGURE 3.2: Principles of sub-Doppler cooling for configuration $\sigma^+ - \sigma^-$. (a) Two counter propagating $\sigma^+ - \sigma^-$ beams of the same frequency results in the standing wave $\mathbf{E}(z)$. The polarization of the standing wave is linear, but the orientation changes along z. (b) A diagram shows atomic structure of an atom moving along z in the presence of the standing wave. The ground level experiences energy levels shifts, and hence the laser coupling $\sigma^{\pm}$ becomes detuned from the atomic transition.

the configuration with linearly polarized beams[6], and one where the counter-propagating beams are circularly polarized. Although the temperature below Doppler limit was obtained for the first time for the configuration consisting of six linearly polarized beams, the configuration with circularly polarized beams results in much more efficient cooling. Since the MOT requires circularly polarized beams, only the $\sigma^+ - \sigma^-$ configuration is explained briefly in this section following the approach from [121].

The internal atomic energy structure is in general quite complex, but for simplicity only a two level system with $|F = 1, m_F\rangle$ and $|F = 2, m_F\rangle$ is considered here. In the case of two counter-propagating and circularly polarized beams, σ^+ and σ^-, a linearly polarized standing wave is created, with polarization direction changing along the propagation axis z, as in Figure 3.2a. For an atom at rest, the energy shift due to AC Stark Shift described by equation (2.30) is constant along the propagation axis. The situation changes for an atom in motion. To simplify the problem, a rotating reference frame is introduced in a way that it keeps the polarization in a fixed direction. In this frame, the moving atom 'spins' while moving along the propagation axis, as if there was present an additional magnetic field proportional to the atom's velocity and parallel to the rotation axis. The problem can be therefore considered in the rotating frame reference.It was shown that the additional term looks like a fictitious magnetic field proportional to the atom's velocity and parallel to the rotation axis. For small velocities it can be treated as a perturbation leading to the shift of energy levels of the ground state of the atom as shown on Figure 3.2b. Finding the exact

[6]The polarization of the counter-propagating beams must be orthogonal to each other.

values for the couplings leads to the conclusion that there is a bigger probability to absorb a counter-propagating photon σ^- by $|F = 1, m_F = -1\rangle$ than to absorb σ^+, and vice versa for $|F = 1, m_F = 1\rangle$. This imbalance of radiation pressure results in additional damping force, which depends on the laser intensity and laser detuning. The ultimate cooling limit for rubidium is given by the recoil temperature [133] equal

$$T_{rec} = \frac{\hbar^2 k_L^2}{k_B m} \approx 360\,\mathrm{nK}. \tag{3.3}$$

3.1.3 Magneto Optical Trap

Although optical molasses is an efficient technique to slow down atoms, this technique is not able to efficiently accumulate atoms in one place. This means that atoms experiencing a random walk due to the heating mechanism (3.2) eventually leave the cooling region. Optical molasses's forces and atomic density are strongly dependent on the beams alignment, as any misalignment of counter-propagating beams leads to an imbalance of cooling forces and to a less efficient cooling.

The solution for these problems was the first Magneto Optical Trap based on the influence of the external magnetic field on scattering forces. The MOT is composed of three pairs of laser beams, red-detuned from resonance and intersecting in the region where a weak quadrupole magnetic field is created by a pair of coils in anti-Helmholtz configuration, Figure 3.3a. The field is odd and approximately linear in the vicinity of the center of the trap as shown on Figure 3.3b. Therefore, the interaction of atoms with the magnetic field gradient creates an inhomogeneous Zeeman Effect, which is zero at the centre of the trap and increases moving away from it. Each pair of two overlapping and counter-propagating laser beams have a circular polarization $\sigma+$ and $\sigma-$, as described in section 3.1.2. Red-detuned laser light with specific polarization puts predominantly pressure on atoms which are closer to resonance because of Zeeman Effect, as shown on Figure 3.3b. This results in space-dependent imbalance of radiation pressure between counter propagating beams, which pushes atoms always toward the point where magnetic field is zero. As a result, atoms accumulate at the centre of the trap, creating much denser trap than just optical molasses.

The main advantage of MOT is that it is very robust and neither depends on precise balancing of laser beams nor on highly precise adjustment of beams polarization. However, any improvement of these parameters helps to achieve a lower temperature and denser trap.

3.1.4 Implementation of MOT with Rubidium atoms

In order to perform laser cooling an appropriate transition needs to be selected, which is suitable for absorption and re-emission of photons in many 'closed' cycles. For a circularly polarized beams $\sigma^{\pm}$, the allowed electric dipole transitions follow the selection rule: $\Delta F = 0, \pm 1$, $\Delta m_F = \pm 1$. On the other hand, the decay of an atom from an excited state to the ground state might have any polarization and hence the general selection rules applies as follows: $\Delta F = 0, \pm 1$, $\Delta m_F = 0, \pm 1$. In the case of Rubidium 87, the cooling laser is red-detuned to the $\left|5S_{\frac{1}{2}}, F = 2\right\rangle \rightarrow \left|5P_{\frac{3}{2}}, F = 3\right\rangle$ transition, as shown on Figure 3.4. Since the atoms in state $\left|5P_{\frac{3}{2}}, F = 3\right\rangle$ can only decay back to the ground state $F = 2$, the condition of a 'closed' transition seems to be satisfied.

However, even though the cooling laser is tuned to the given transition, an excited state $\left|5P_{3/2}, F = 2\right\rangle$ might be also populated but with a small probability. From this energy level the atom can decay to both hyperfine levels in the ground state, including state $\left|5S_{1/2}, F = 1\right\rangle$ which does not interact with cooling lasers. Even though a leakage of atoms from the cooling cycle is very small, after many cycles all the atoms end up in the state $\left|5S_{1/2}, F = 1\right\rangle$, preventing cooling mechanism. By adding a repumper laser coupling atoms in state $\left|5S_{1/2}, F = 1\right\rangle$ to

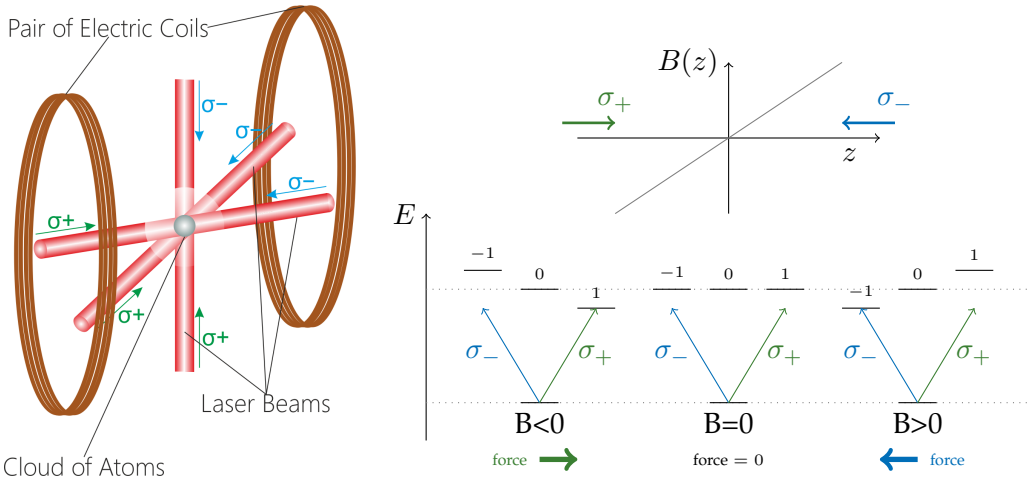

(a) Magneto Optical Trap

(b) Principles of MOT cooling.

FIGURE 3.3: Magneto Optical Trap technique. (a) In our setup, horizontal beams cross with an acute angle, while vertical beam is perpendicular to them. (b) A laser $\sigma^{\pm}$ with the fixed red-detuned frequency interacts with and atom placed in the magnetic field. Zeeman splitting of magnetic sub-levels depends on the strength and the sign on magnetic field. For atoms in $z < 0$ the coupling of σ^{+} polarization is stronger that for σ^{-}. The opposite happens for $z > 0$, which results in the force imbalance always pushing an atom toward center of the trap $z = 0$.

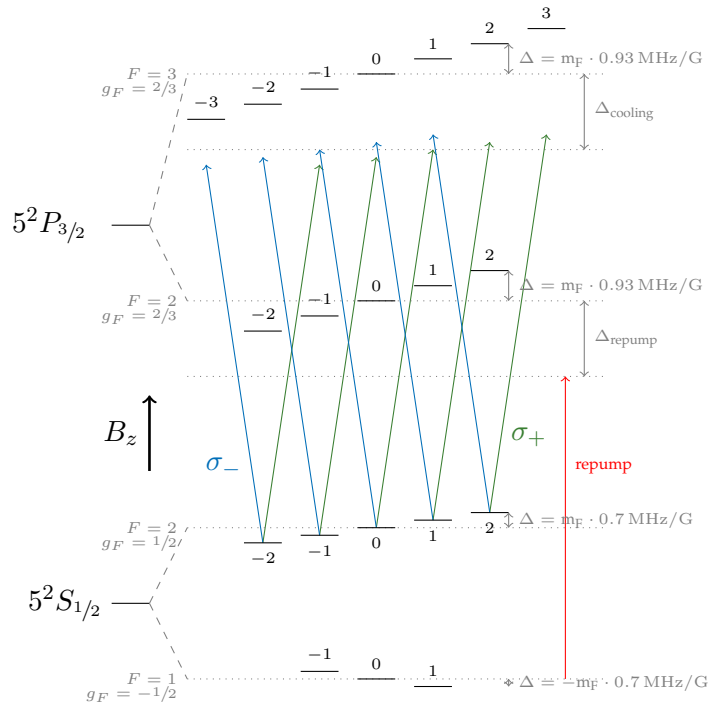

FIGURE 3.4: Cooling and repumping transitions for ^{87}Rb atom placed in the external magnetic field B_z. The atomic energy levels are split due to the Zeeman effect, with the appropriate shifts Δ. States $\left|5S_{\frac{1}{2}}, F = 2\right\rangle$ and $\left|5P_{\frac{3}{2}}, F = 3\right\rangle$ are coupled via circularly polarized cooling laser beams $\sigma^{\pm}$ (green and blue arrows). States $\left|5S_{\frac{1}{2}}, F = 1\right\rangle$ and $\left|5P_{\frac{3}{2}}, F = 2\right\rangle$ are coupled via repumper laser (red arrow).

$\left|5P_{3/2}, F = 2\right\rangle$, the atoms are restored to the main cooling loop. If the intensity of repumper laser is big enough, the optical pumping of atoms back to $\left|5S_{\frac{1}{2}}, F = 2\right\rangle$ is faster than the leakage of atoms from cooling cycle, thus maintaining an efficient cooling cycle.

In conclusion, two lasers of a different frequency are required for atoms cooling: a laser for coupling to the main cooling transition marked at the Figure 3.4 as $\sigma^{\pm}$, and a repumper laser which is shown as 'repump'. Since photons from the repumper laser are required only to maintain cooling mechanism, the only feature that matters for the process is a laser detuning Δ_{repump}, but not other features like beam's polarization or direction of propagation. Therefore for simplicity, the repumper laser is marked on Figure 3.4 without specifying its properties, even though in our setup the repumper overlaps with the optical path of cooling lasers. In Figure 3.4 the cooling lasers $\sigma^{\pm}$ are red-detuned, by $\Delta_{\mathrm{cooling}}$ from the atomic transition to provide Doppler cooling. Detuning is usually set between 0 and few Γ, depending on the expected cloud density and temperature one needs to achieve. Simultaneously an

external magnetic field is applied, that splits the energy levels into magnetic sub-levels (Figure 3.4), to provide a restoring force for a MOT. Our experiment produces a magnetic field gradient of about $(10 \text{ to } 15)\,\mathrm{G/cm}$ close to the trap centre depending on the current applied to the magnetic coils.

3.2 Laser system for MOT

The sub-doppler cooling of atoms requires a cooling laser source that has a linewidth much narrower that the natural linewidth Γ of the atomic transition. Moreover, the cooling laser must be powerful, phase stable and tunable in a scope of few Γ. Laser tunability and stability are crucial for both MOT optimization as well as for running experimental sequences. The requirements of narrow linewidth for the cooling transition can be satisfied using a *master-slave* laser configuration, presented in section 3.2.1. In this configuration, the frequency of the so called *master* laser is fine-controlled and stabilized, while the *slave* laser is forced to operate at the same frequency and benefits from fine stabilisation while retaining high power.

Regarding frequency stabilization, there are several methods to stabilize the laser frequency, for instance polarization modulation [134] or frequency modulation [135–137]. The method used in our setup, namely Doppler-free saturated absorption, is based on frequency modulation [138, 139] and phase sensitive lock-in amplifier. Doppler-free saturated absorption spectroscopy is a commonly used method to accurately stabilize the laser frequency. Its convenience is based on the fact that it exploits the hyperfine structure of atoms using a vapour cell that contains the same species as in the actual experiment. Two different configurations for saturated absorption spectroscopy are applied in the experiment, one for stabilization of the master laser, and one for repumper. These approaches are described in sections 3.2.2 and 3.2.3.

3.2.1 System overview

All lasers exploited in our setup for atoms cooling, namely master, slave and repumper, are semiconductor lasers operating in configuration of extended cavity [140]. Typically, a free running diode consists spectrum of multiple modes that are responsible for the frequency broadening. Since the typical line width of a laser diode is of order $(40 \text{ to } 100)\,\mathrm{MHz}$, which is more than the natural linewidth of the atomic transition, an additional element needs to

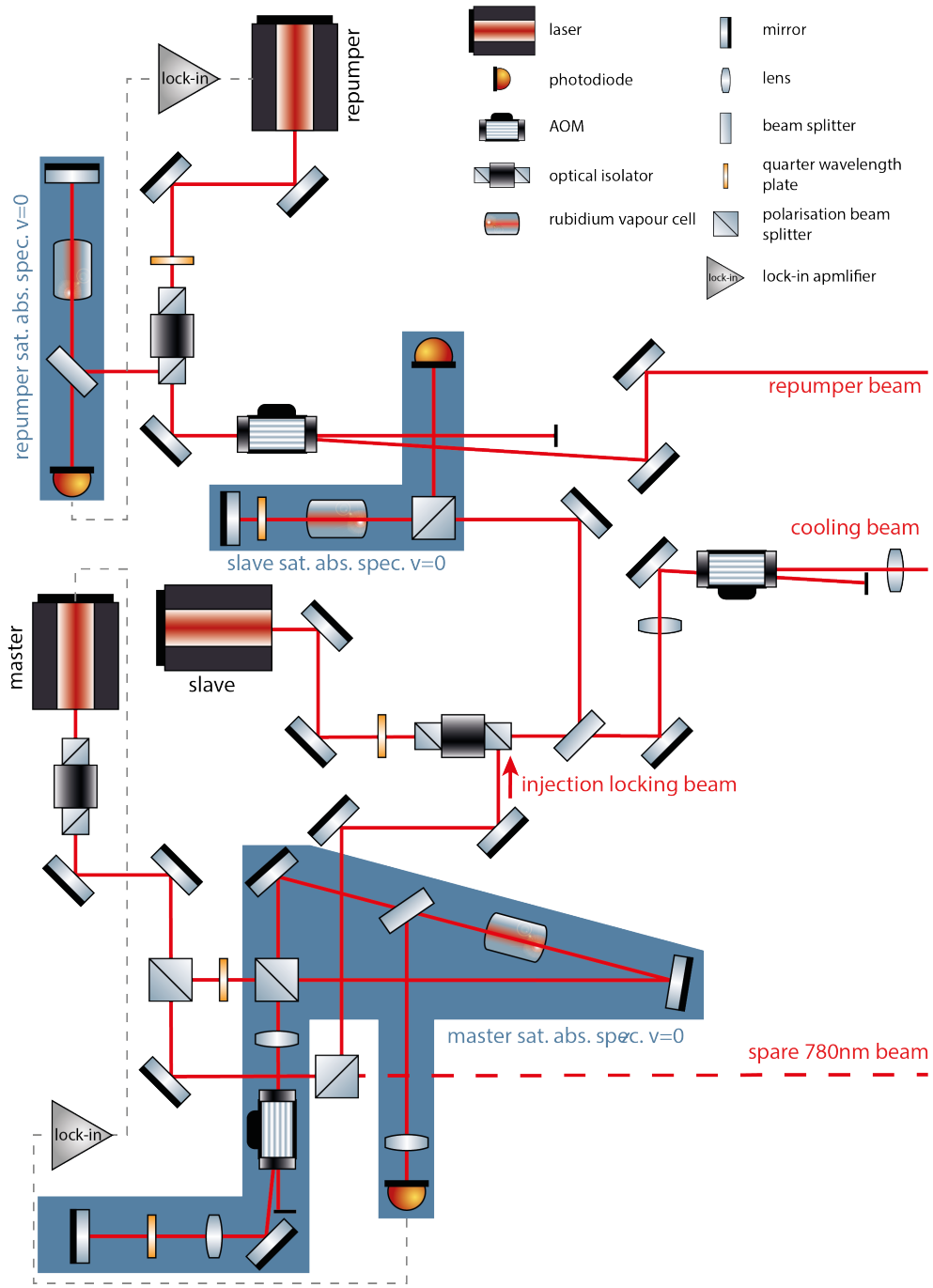

FIGURE 3.5: Laser system for Magneto Optical Trap. Parts of the scheme highlighted with the navy background represents setups for saturated absorption spectroscopy. 'sat. abs. spec. $v = 0$' is used for both repumper and slave monitor, while 'sat. abs. spec. $v \neq 0$' is responsible for master laser stabilization.

be used to narrow down the linewidth. The cavity design applied in our setup is based on the work presented in [141]: a semiconductor diode is placed in the cavity consisting of a diffraction grating set in a configuration to provide feedback from the grating back to the diode. If the cavity is well aligned, only one mode is enhanced and triggers a desirable single mode lasing. The diffraction grating is mounted on the piezoelectric component (PZT)[7], which is used for the fine adjustment of the extended cavity length. The laser frequency can be thus controlled by both the current applied to the diode, as well as by the voltage applied to the PZT.

In a *master-slave* configuration the master laser is narrowband tunable, but not a very powerful light source ($15\,\mathrm{mW}$). It is locked to the $\left|5S_{\frac{1}{2}}, F=2\right\rangle \rightarrow \left|5P_{\frac{3}{2}}, F=1,3\right\rangle$ transition, by the adjustment of the extended cavity, using a *saturated absorption spectroscopy* signal as reference (see section 3.2.3). Stabilised, low power light from master is now injected into the resonant cavity of a free-running slave laser (see Figure 3.5 'injection locking beam') operating at full power ($40\,\mathrm{mW}$). If the frequency of both lasers are similar, the injected light forces slave's diode to operate at exactly the same frequency as the master. *Doppler-free saturation spectroscopy*, shown on the Figure 3.5 as 'slave sat. abs. spec. v=0', is simultaneously used to monitor slave's frequency and ensure that the injection is aligned properly. Such prepared slave laser beam, is then shifted by an AOM[8] in single pass configuration, before it is guided to the vacuum chamber.

Unlike for the cooling transition, the parameters of the repump laser, specifically lower power and the alignment, are not as crucial as for the cooling lasers and hence the *master-slave* configuration is not required in this case. Therefore, the repumper laser is locked to the $\left|5S_{\frac{1}{2}}, F=1\right\rangle \rightarrow \left|5P_{\frac{3}{2}}, F=1,2\right\rangle$ transition, and is shifted afterwards by a single AOM pass by $\Delta_{repump} \approx 75\,\mathrm{MHz}$ (see Figure 3.4). The locking scheme for the repumper is described in the following section.

[7] The term 'piezo' describes all materials, which implement piezoelectric effect. When a piezo material is under external mechanical stress, it generates an additional voltages across the axis of stress, and vice versa: in response of applied voltage piezo material expands its volume. Piezo actuator is usually a cristal which allows fine adjusting by controling its volume.

[8] Acousto-Optic Modulator is a device which modulates the frequency of the laser beam. It consists of a crystal and a piezo-electric transducer, which induces an acoustic wave propagating through the crystal. The propagation of the acoustic wave leads to the local changes of the refractive index in the crystal resulting in modulation of the laser light propagating perpendicularly to the acoustic wave.

3.2.2 Stabilization of the repumper laser

The basic configuration for *Doppler-free saturated absorption spectroscopy* is shown in Figure 3.5 as a 'sat.abs. spec. $v = 0$'. It consists of a laser beam whose wavelength is tuned using PZT, a Rubidium vapour cell and a photodiode to monitor laser intensity. The modulated laser beam travels through a rubidium vapour cell twice, thus interacting with atoms, and eventually its transferred power is detected by a photo detector (Figure 3.5).

Atoms in the vapour cell absorb mainly the photons whose frequency is in resonance to the one of the possible atomic transitions. However, as shown on Figure 3.1b, the atom's movement and corresponding Doppler effect result in atoms absorbing also photons largely detuned from resonance. Because the cell is at room temperature and atoms move in all directions relatively fast with Maxwell velocity distribution, the effective broadening of each transition line is about $500\,\mathrm{MHz}$. Since the separation between atomic transition lines is less than that, it is impossible to resolve individual transitions for a weak probe light propagating through the vapour cell. A signal detected on the photo detector shows a broad dip in the laser spectrum intensity, as shown in Figure 3.6a.

To remove this broadening and resolve particular transitions, another laser beam is sent counter-wise to the probe through the vapour cell. This beam, referred to as the pump, has the same frequency as the probe and is much stronger in intensity so that it saturates transitions and hence promotes the majority of atoms into the excited state. If both beams are aligned to overlap, atoms whose velocity along the beams' propagation is close to zero interact with both of pump and probe beams simultaneously since

$$f_{\text{transition}} = f_{\text{pump}} = f_L - f_v = f_L + f_v = f_{\text{probe}},$$

where Doppler shift $f_v = 0$. These atoms, which are mostly in the excited state because of the pump's strength, do not absorb photons from the probe anymore so that a decrease in absorption is seen as a small peaks in the broad Doppler dip in Figure 3.6a.

The peaks can now be exploited for further laser stabilization via phase-sensitive lock-in amplifier [139] [138] marked on Figure 3.5 as 'lock-in' on Figure 3.5. For laser stabilization, the current of the diode is modulated in a radio-frequency, so that the signal received by the photodiode is also modulated. This signal is further demodulated and serves as an error signal for the stabilization electronics which provides a feedback to the laser current and PZT, thus controlling its output frequency.

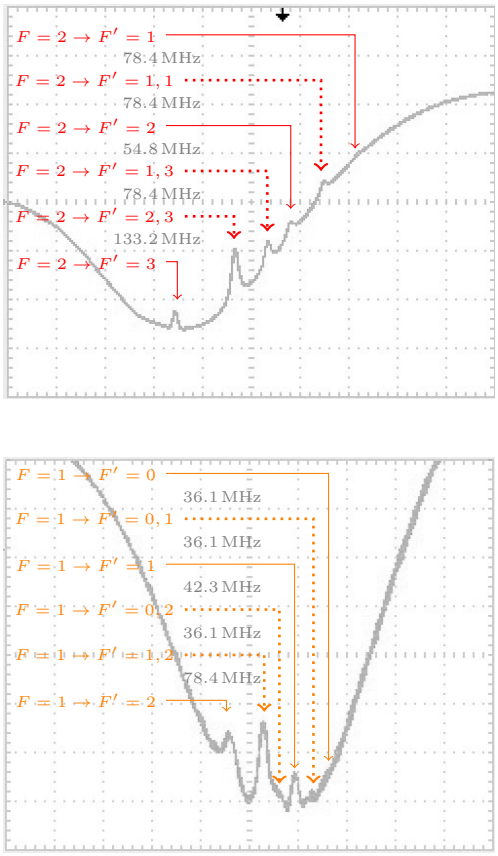

(a) An oscilloscope scan.

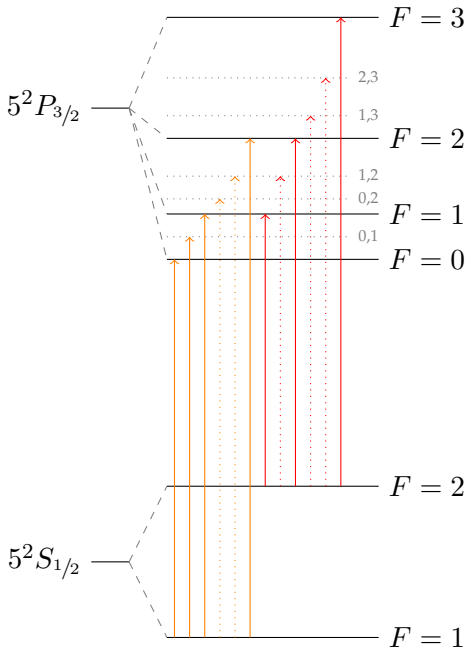

(b) ^{87}Rb hyperfine structure and corresponding transitions

FIGURE 3.6: Doppler free saturated absorption spectra for ^{87}Rb. (a) On the oscilloscope scans, where y axis correspond to different laser frequencies, a broad dip of the D_2 spectra for $|F = 2 \rightarrow F'\rangle$ and $|F = 1 \rightarrow F'\rangle$ is visible, as well as small peaks of subsequent atomic transitions. So called cross-over peaks are marked with dotted lines. (b) Cross-over peaks occurs due to the Doppler shift, when the laser has frequency between two different possible transitions.

3.2.3 Stabilization of the master laser

The master laser is also stabilized using saturated absorption spectroscopy, but with a modification which allows the tuning of the laser frequency externally while keeping the stabilization electronics active. Unlike in the scheme for repumper's stabilization, where both the pump and probe beams have the same frequency, the master lock is implemented with an additional shift in pump frequency in respect to the probe beam. In this case only the pump beam is modulated but not the probe, since the AOM introduces an additional noise on the laser beam which is strong enough to deform the signal and destabilize the locking electronics.

As shown on Figure 3.5 'sat.abs. spec. $v \neq 0$', the master's laser beam with frequency

f_L is initially split on polarization beam splitter (PBS)[9] into two separate pump and probe beams. The frequency of the pump beam is then modulated via an AOM in *double pass*[10] configuration [142], resulting in a frequency shift equal $-2\delta_f$. Both the probe and pump beams are guided then to the rubidium cell, so that they propagate counter wise through the vapour. The probe beam is eventually detected by a photodiode and the absorption signal is shown on Figure 3.7a as a yellow curve.

The general principles of saturated absorption spectroscopy remain as discussed for the repumper laser, however an introduction of pump's frequency shift changes the a target atoms for which the probe is less efficiently absorbed. For atoms moving against pump beam with velocity v the Doppler shift f_v and AOM's shift $-2\delta_f$ results in tuning both pump and probe beams to the atomic transition following the formula:

$$f_{\text{transition}} = f_{\text{pump}} = f_L + f_v - 2\delta_f = f_L - f_v = f_{\text{probe}}. \tag{3.4}$$

For $\delta_f = 0$ the absorption spectra for slave monitor and master look identical, as shown on Figure 3.7a. However, solving the equation (3.4) under assumption of $v \neq 0$ leads to the solution $f_{\text{transition}} = f_{\text{pump}} = f_{\text{probe}} = f_L - \delta_f$, for atoms with velocity $v = c\frac{\delta_f}{f_L} \approx 1 \times 10^{-4}\,\mathrm{m\,s^{-1}}$. This means, that the small peaks in absorption spectrum move by $+\delta_f$, while the Doppler broadening of the probe beam remains unaffected as shown on Figure 3.7b.

This spectra is used to stabilize laser frequency to one of the selected peaks using the same lock-in system which is also used for the repumper stabilization. When the frequency on the AOM changes, peaks also move and a feedback signal from the lock-in is fed into the laser (both current and PZT) to change master frequency. The range in which the AOM in the double pass can be safely operated without distorting the signal used for laser stabilization is from $(67$ to $115)\,\mathrm{MHz}$. The slave frequency is subsequently shifted by an AOM in single pass configuration (see Figure 3.5) by the fixed value of $110\,\mathrm{MHz}$, therefore, the ultimate range of laser detuning varies from -4Γ to $+0.5\Gamma$.

[9] An optical device which splits the beam into two beams, whose polarization is perpendicular to each other. It usually consists of a pair of triangular glass prisms, attached in a way that they create a glass cube. A ratio of the output powers depend on the initial beam's polarization.

[10] AOM in double pass configuration is typical used to minimize spatial movement of the beam while applying different modulation δ_f. When a laser beam passes through an AOM, zero order is blocked while ± 1th order is reflected back to follow its initial path. The beam passes once again the AOM and its frequency is shifted once again. As a result the total shift of the beam is $\pm 2\delta f$.

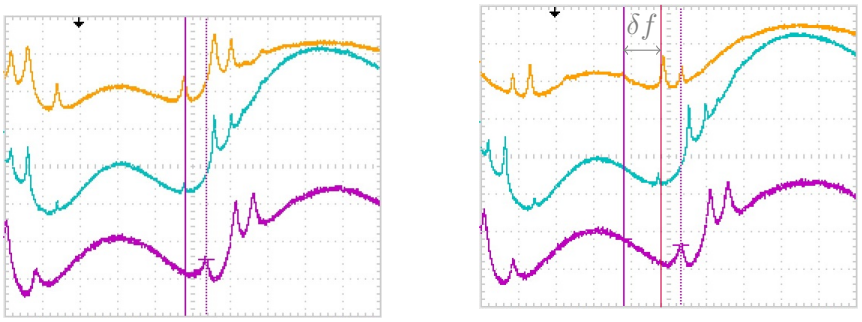

(a) $\delta f = 0\,\mathrm{MHz}$ (b) $\delta f \approx 101\,\mathrm{MHz}$

FIGURE 3.7: Doppler free saturated absorption spectra for ^{87}Rb in double pass configuration. The yellow line represents signal from master lock photodiode, blue corresponds to the slave laser monitor, purple is the slave beam spectra after the single AOM pass just before vacuum chamber.

3.3 MOT optimization and diagnostics

Since the MOT is a rather complicated system, its quality depends on many factors: the laser beam alignment, detunings of the cooling and repumper lasers, strength and gradient of the magnetic field or even pressure and temperature of rubidium vapour and residual gases within the chamber. It is necessary to optimize the loading and lifetime of the MOT in order to control dipole trap loading (see chapter 5). Therefore complete MOT diagnostics, including measurement of the trap density and temperature of the atomic ensemble, is required. This section first introduces the fluorescence imaging technique, principles and apparatus, which is used in our setup to detect atoms. The key features for MOT optimization are discussed, including MOT alignment, density and temperature measurements.

3.3.1 Atoms detection: fluorescence imaging

There are well established methods to image atoms in a cold atoms platform: absorption, phase contrast and fluorescence imaging. The first one is based on the absorption measurement of a weak probe beam propagating through the cloud. The transmitted probe beam is detected by a CCD[11] camera which records a 2D distribution of the laser intensity. In the case of phase contrast imaging, both the absorption image and fluorescence light from atoms are acquired by the CCD, and the interference between them carries an information about the cloud distribution. Fluorescence imaging is based on the collection of photons scattered by the atoms from the laser beam. While the first two methods require setting up a

[11] (Charge-Coupled Device) is a device of digital imaging. CCD matrices are made of p-doped MOS capacitors.

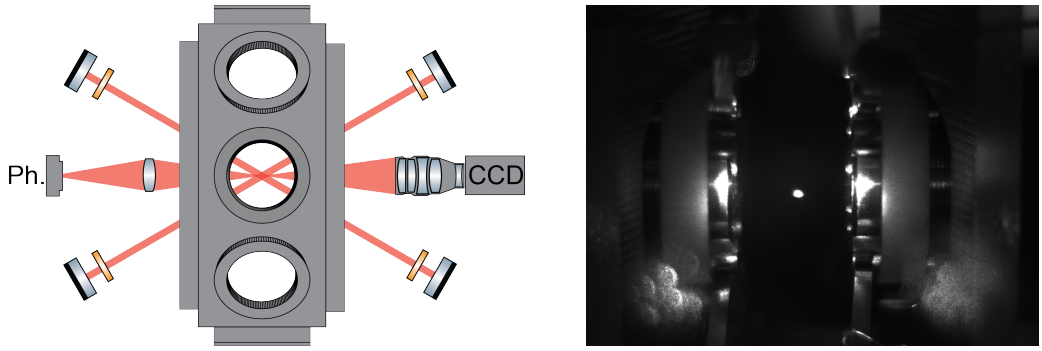

(a) Experimental setup (b) CCD image of MOT

FIGURE 3.8: Fluorescence image of MOT. (a) A scheme of placing photodiode (Ph.) and a CCD camera. (b) Cloud of atoms is visible between two lenses for dipole trapping.

separate probe beam, the fluorescence signal might be obtained from atoms interacting with molasses beams. Therefore this method is more convenient from an experimental point of view as it allows to monitor MOT's behaviour in real time without disturbing it. Moreover, absorption and phase contrast methods become less accurate for low atomic cloud density, while the fluorescence detection is less affected by this.

When near-to-resonance light propagates through an atomic gas, photons are absorbed and re-emitted homogeneously in all directions. This light is detected by a photodiode or CCD camera as shown on Figure 3.8a. The CCD is mainly used for monitoring the position and spatial distribution of atomic cloud. A photodiode acquires the signal from the cloud and is used for monitoring the dynamic changes of number of atoms in the trap.

3.3.2 Alignment optimization

Fluorescence imaging is used to determine and optimize the MOT positioning with respect to the dipole trap position. As will be shown in chapter 4, the position of the dipole trap can be reproduced by a '*mimic beam*', which is a $780\,\mathrm{nm}$ laser beam used for adjustment of dipole trap imaging system (see Figure 4.2b). When both the mimic beam for the dipole trap and the cooling beams are set up with high intensity and are tuned to the resonance transition to maximize fluorescence signal of background atoms, they scatter enough light to be visible on the CCD, as it is shown on Figure 3.9. Since the focal point of the *mimic beam* overlaps with the place where the dipole trap is created, it becomes a reference point for the MOT position optimization. Having a reference point for MOT optimization, fluorescence signal is used to asses whether center of the MOT cloud overlaps with dipole trap (Figure 3.8b).

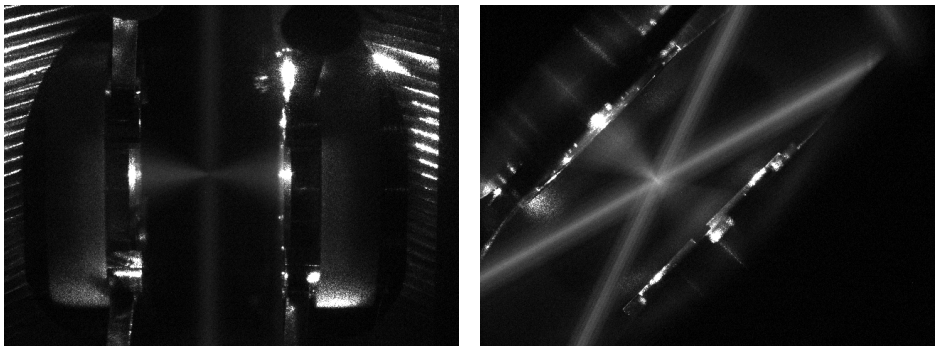

(a) View from the side (b) View from the top

FIGURE 3.9: Fluorescence traces of mimic beam for dipole trap and cooling beams.

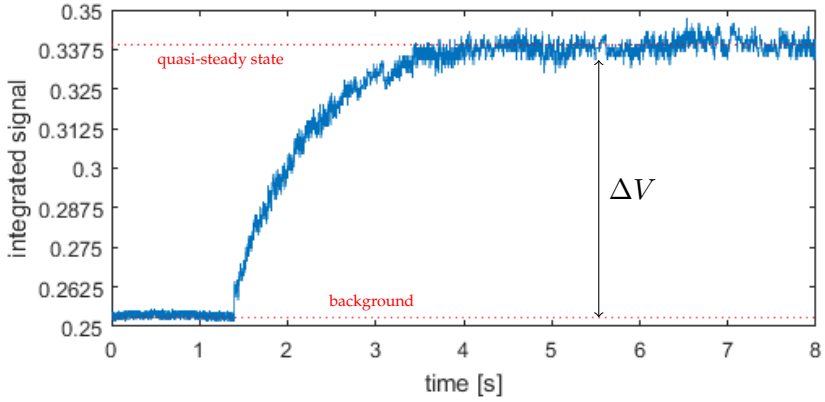

FIGURE 3.10: Fluorescence signal from atomic cloud detected by the photodiode. The first part of the trace is a background due to the refraction of cooling beams on miscellaneous optics in the absence of atomic cloud (absence of magnetic field).

3.3.3 MOT density

A fluorescence signal acquired by the photodiode or the CCD can be converted into the number of atoms. In principle it is easy to calculate the number of atoms in three-dimensional optical molasses knowing the scattering rate in the absence of magnetic field. For a working MOT though, it is more complicated due to the magnetic field gradient. In this work the number of atoms is retrieved by monitoring the entire loading curve of MOT[12] until it reaches a quasi-stable state, as shown on Figure 3.10. The plateau of the loading curve is taken as a signal for further processing.

[12]Loading curve can be described by two characteristic parameters: number of atoms in equilibrium N_{atoms} and characteristic loading time τ. The dynamic process of MOT loading is described in section 3.4.2.

The power of the light emitted by the MOT is proportional to the number of trapped atoms N_{atoms} , the scattering rate R_{sc} (2.24) and the energy carried by an emitted photon E_{photon}. Since only a small portion of fluorescence light reaches out to the imaging devices, the collection efficiency can be estimated taking into account a solid angle κ of the light collecting lens. In the case of a photodiode, where ϵ is the conversion ratio between output volts V and the power of the measured signal[13] from atoms, the number of atoms can be calculated from the formula

$$N_{\text{atoms}} = \frac{\Delta V}{\epsilon P \kappa}.$$

where $P = R_{sc} h\nu$ is the power of light emitted by one atom during one second.

Depending on the trap alignment, the typical number of atoms in MOT measured for our setup varies between 0.2×10^6 and 0.8×10^6 atoms, for a magnetic field gradient equal $15\ \frac{\text{G}}{\text{cm}}$, 1.5Γ detuning and $15\ \frac{\text{mW}}{\text{cm}^2}$ intensity of cooling beams. The size of the atomic cloud, typically σ_{MOT}=(200 to 500) µm could be estimated by fitting a two dimensional Gaussian to the image of the atomic cloud obtained by the CCD camera (Figure 3.8b), returning a typical peak atoms density is in range $(2 \times 10^8$ to $50 \times 10^8)\,\text{atoms/cm}^3$.

The density of the atomic could presented in this thesis is relatively low compared to standard MOT experiments where the peak density can reach $10^{10}\,\text{atoms/cm}^3$ [118, 143], $10^{12}\,\text{atoms/cm}^3$ [116] (sodium), or possibly even $10^{13}\,\text{atoms/cm}^3$ [124] (theory). Undoubtedly, the factor which limits the MOT density in the first place is the unusual geometry of the trap, more precisely the acute intersection angle between the horizontal cooling beams (see Figure 3.9). The majority of experiments based on a similar geometry successfully employ additional cooling methods in order to enhance the MOT density, namely Zeeman slower [144] or 2D MOT. In addition, our experimental system could not be fully optimised due to the design of the chamber and MOT magnetic coils. It was possible to achieve a denser atomic cloud in the system, but such a cloud would never overlap with the dipole trap. The optimization of the MOT to overlap it with the dipole trap (section 3.3.2) resulted in a lower density each time the procedure was taken, even though the zero point of the magnetic field for MOT could be additionally corrected by the set of the Helmholtz coils. Therefore, the results presented relate to the density of MOT which was optimized as much as the apparatus allowed, without significant changes.

[13] ϵ depends on the conversion factor $\tilde{\epsilon}$ of photodiode (PDA50B from Thorlabs) and a resistance R of the circuit used to readout the signal: $\epsilon = R\tilde{\epsilon} = R[\text{Ohm}]0.56[\text{A/W}]$.

3.3.4 MOT temperature: release recapture method

In order to measure the temperature of the trap, a release recapture method is applied as described in [145]. The experimental sequence is shown in Figure 3.11. Initially, the MOT needs to be loaded until the number of atoms reaches a quasi-steady state. Then, the cooling beams and the magnetic field are switched off for a time dt and, as it is shown in Figure 3.11, the fluorescence signal drops since atoms do not scatter any light. During this time atoms freely expand and after time dt both beams are switched on again and the atoms remaining within the capture region instantly load the trap. The «recapture» stage can not last too long

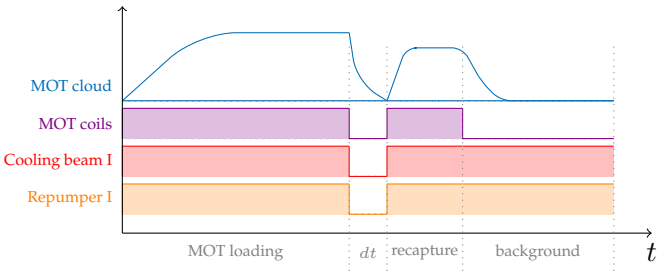

FIGURE 3.11: Scheme of experimental sequence for MOT temperature measurement using release-recapture method.The subsequent stages are: **MOT loading**= 10 s, **dt**= variable time, **recapture** = 50 ms, **background** = 1 s. Names of the events/settings and corresponding values marked on the vertical axes: **MOT cloud** - fluorescence signal acquired by the photodiode, **MOT coils** - current applied to the anti-Helmholtz coils (0 to 3.5) A, **Cooling beam I** - the total intensity of the cooling beams (0 to 15.3) $\mathrm{mW/cm^2}$, **Repumper I** - intensity of the repumper beam (0 to 2) mW.

in order to avoid additional MOT loading. At the last stage («background») the magnetic field is switched off so that the atoms escape the trap but all beams are still present in the chamber. This allows to find a reference signal for zero atoms while including any stray light.

A signal received by the detector for a typical sequence is presented in Figure 3.12a. The recapture fraction $\frac{V_2}{V_1}$ is derived from each sequence which is repeated several times in order to obtain a statistical error. If the atoms expand homogeneously during the time dt, the recaptured fraction [146] will be given by

$$\text{recapture} = \frac{V_2}{V_1} = \left(\frac{r^2+d^2}{r^2+d^2+v_T^2t^2}\right)^{\frac{3}{2}} \exp\left(-\frac{a^2t^4+8b^2}{8\left(r^2+d^2+v_T^2t^2\right)}\right) \tag{3.5}$$

where $v_T = \sqrt{\frac{2k_BT}{m}}$ and v_T stands for thermal velocity of the atoms in MOT. The model used

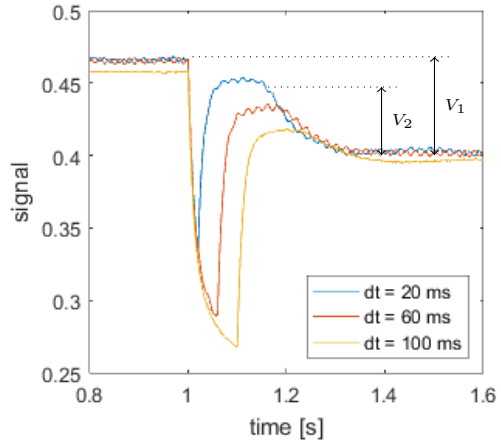

(a) Photodiode signal for a single run of the sequence

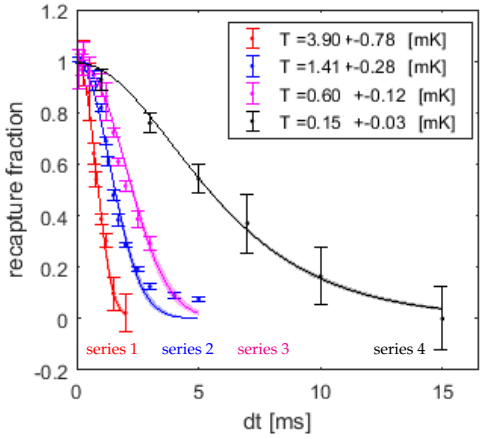

(b) Four independent temperature measurements

FIGURE 3.12: Release-recapture method to determine MOT temperature. (a) Signal acquired by the photodiode for different dt values and for a significant detuning equal 3.5Γ. High detuning results in a low temperature and a slow expansion of the cloud, therefore each stage of the sequence is very clear. (b) Data points represent measured recapture fraction, solid lines represent a theoretical fit with equation (3.5), while the shaded areas represent an error of model prediction. Purple curve: -1.8Γ, number of atoms 8.5×10^5 atoms, loading time $\tau = 1.37\,\mathrm{s}$. Similarly for black curve: -2.3Γ, 3.3×10^5 atoms, $\tau = 8.5\,\mathrm{s}$.

for the data fitting is based on the assumption that the cloud of atoms has initially a Gaussian spatial distribution with the standard deviation r where the atoms velocities follows Maxwell distribution. In the model an imbalance of force, namely an effective acceleration of atoms in one direction a, is taken into account. This takes the minimum value of the Earth's gravitational acceleration, as the atoms falls freely while released from the trap, but can be also the result of the other forces (for instance an imbalanced beams). The recapture region is determined by the size d of the MOT beams, where $2d$ is beams' waist, and a possible cloud displacement b is measured in respect to the center of the intersecting beams.

The data showing a recapture fraction versus the expansion time dt are summarized in Figure 3.12b. All four experimental series in Figure 3.12b differ mainly in the MOT alignment and the relative position between the zero of quadruple magnetic field[14] for the MOT and the position where the cooling beams intersect. The first temperature measurement (red points on Figure 3.12b) is taken just after assembling MOT, and hence its alignment is not optimized yet. Series 2,3 and 4 shows the subsequent attempts toward MOT alignment

[14]The adjustment of the zero field is realised by a three pairs of the offset magnetic coils in the Helmholtz configuration.

optimization.

The results of fitting the model (3.5) to the data to are presented in the Table 3.1. It was checked that in our setup the displacement does not play a significant role as typically b is found to be less that few microns when left as a free fitting parameter, therefore this parameter was ignored in the analysis. The size of the cloud agrees with values measured using the camera (see section 3.3.1). Interestingly, the acceleration is very high of order of

	r [μm]	a [g]	T [μK]
series 1	407 ± 61	250 ± 50	3900 ± 780
series 2	381 ± 57	72 ± 14	1400 ± 280
series 3	429 ± 64	35 ± 7	600 ± 120
series 4	479 ± 72	3.34 ± 0.67	150 ± 30

TABLE 3.1: Detailed results of fitting procedure of the data shown in Figure 3.12b with the equation (3.5). Here the displacement is assumed to be zero $b = 0$ while the size of the cooling beams is $d = 1.2\,\mathrm{mm}$. Acceleration is given in units of Earth's gravitational acceleration $g = 9.81\,\mathrm{m\,s^{-2}}$.

few hundreds of Earth's gravitational acceleration g for the unoptimized, hot MOT. Measurements shows also the trend, that the lower acceleration the lower temperature. It might imply that the acceleration can be related to the beams and magnetic field imbalance which pushes atoms in the given direction just after releasing atoms from the trap. A careful alignment helps to bring the temperature down, and eventually a cold $150\,\mu\mathrm{K}$ MOT experience an effective acceleration close to the Earth gravity.

Since the apparatus for MOT is unstable and drifts over the timescale of days, the MOT requires systematic work to maintain its optimization. Therefore, the temperature in which the MOT is operated remains typically in range $(100$ to $500)\,\mu\mathrm{K}$. These results relate to the MOT optimization without carrying a sub-Doppler cooling as a separate stage. Typically, the temperature of the atomic cloud can be additionally decreased by performing optimized optical molasses. The efficiency of the sub-Doppler cooling strongly depends on the trapped species, initial experimental conditions (MOT temperature) and intensity and frequency of cooling lasers [130]. The procedure is usually performed by ramping down the magnetic field to zero while decreasing the cooling beam intensity and tuning cooling laser frequency closer to the resonance transition. Then, the experimental conditions must be maintained for a certain amount of time until the temperature stabilizes but before atoms escape the trap, typically couple of milliseconds. Much lower temperatures of the atomic can be obtained if the procedure is well-optimized, down to tens of microkelvin.

3.3.5 MOT temperature: peak density decay

The imaging system of the dipole trap, designed in section 4 and applied in chapter 5, can be also exploited for an alternative method for the MOT temperature measurement. Unlike in the release-recapture method, the dipole trap imaging system does not allow to capture the signal from the entire MOT cloud, but only from a small fraction. When the MOT is fully loaded the intensity of light emitted by the atoms is sufficient to be acquired by the ICCD camera as a uniform background signal. If the MOT is centered on the dipole trap, usually the case as it is required for a good dipole trap loading, the background signal can be associated with the peak MOT density n_{MOT}.

Once the MOT is released from the trap, the cloud starts ballistic expansion (see section 5.2.2), and the density of atoms within the scope of the imaging system decreases in time. The peak density of the MOT is a ratio of the total number of atoms N_{atoms} to the volume $n_{\text{MOT}}(t) = \frac{N_{\text{atoms}}}{(2\pi)^{3/2}\sigma(t)^3}$, where the size $\sigma(t)$ changes with time. The evolution of the initial trap size σ_0 depends on the atoms temperature T_{MOT} like $\sigma(t) = \sqrt{\sigma_0 + \frac{k_B T_{MOT}}{m}}$, and hence the observed peak density can be described by equation

$$n_{\text{MOT}}(t) = \frac{n_0}{\left(1 + \frac{k_B T_{MOT}}{m\sigma_0^2} t^2\right)^{3/2}}. \tag{3.6}$$

Since the decay happens on the scale of few milliseconds, and the exposure time is of the same magnitude in order to obtain a good signal on the ICCD, the decay of atoms density while signal acquisition needs to be taken into account. A signal acquired by the ICCD consists of the accumulated light from atoms over the exposure time Δt, which is given by the integral over time $\tilde{n} = \int_{t_0}^{t_0+\Delta t} n_{\text{MOT}}(t)dt$. Thus the normalized accumulated signal $\langle n \rangle$ is described by

$$\langle n \rangle = \frac{\tilde{n}}{n_0 \Delta t} = \frac{1}{\Delta t}\left(\frac{t_0 + \Delta t}{\sqrt{1 + \frac{k_B T_{MOT}}{m\sigma_0^2}(t_0 + \Delta t)^2}} + \frac{t_0}{\sqrt{1 + \frac{k_B T_{MOT}}{m\sigma_0^2} t_0^2}}\right). \tag{3.7}$$

The experimental sequence for temperature measurement is shown on Figure 3.13. It starts with «MOT loading», after which the initial MOT background is taken during «init.» stage. It takes a fixed amount of time for the ICCD to be ready for the next data acquisition, therefore an additional stage «cam. ref.» (which stands for 'camera refreshment') is applied before switching off the MOT. Next, the MOT is switched off for and the peak MOT density decreases with time in the absence of any cooling beams. After a time t_0, the probe beams

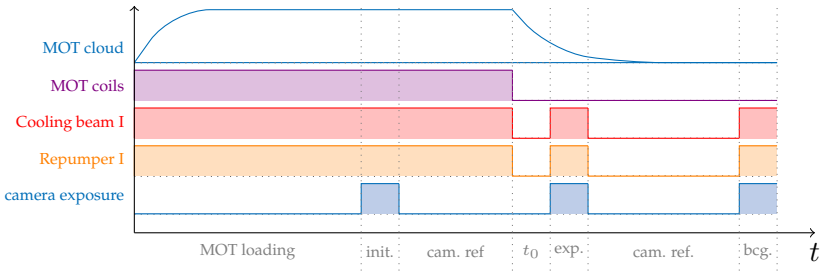

FIGURE 3.13: Scheme of experimental sequence for MOT temperature measurement using peak decay method. The subsequent stages are: **MOT loading** = $10\,\mathrm{s}$, **cam. ref.** = depends on ICCD settings, **init.** = **exp.** =**bcg.** = Δt, **MOT loading**= $10\,\mathrm{s}$, $\mathbf{t_0}$= variable time. Names of the events/settings and corresponding values marked on the vertical axes: **MOT cloud** - fluorescence signal acquired by the photodiode, **MOT coils** - current applied to the anti-Helmholtz coils $(0$ to $3.5)\,\mathrm{A}$, **Cooling beam I** - the total intensity of the cooling beams $(0$ to $15.3)\,\mathrm{mW/cm^2}$, **Repumper I** - intensity of the repumper beam $(0$ to $2)\,\mathrm{mW}$, **camera exposure** - the exposure time when the ICCD acquires the signal.

are switched on thus providing a fluorescence signal which is measured by the ICCD during «exp.». Eventually, a background image «bcg.» is taken after the full MOT decay. The entire sequence is repeated many times to average over possible MOT density fluctuations and to decrease the noise.

Results of temperature measurement are shown on Figure 3.14. For the same MOT configuration three data sets were taken for different exposure times. The detuning of cooling beams from the atomic transition is -1.7Γ while the magnetic field is about $15\,\frac{\mathrm{G}}{\mathrm{cm}}$. The normalized accumulated signal for $(1$ and $2)\,\mathrm{ms}$ integration time is shown in Figure 3.14a. The error bars are based on noise present after images averaging, and naturally for the same number of sequence repetition decreases with longer exposure time. Data are fitted with equation (3.7), where the temperature is a fitting parameter and the initial size of the cloud σ_0 is measured separately using CCD (see section 3.3.1). The results for $\Delta t = (1,\ 5$ and $6)\,\mathrm{ms}$ are $(151 \pm 6)\,\mu\mathrm{K}$ $(242 \pm 9)\,\mu\mathrm{K}$ $(260 \pm 8)\,\mu\mathrm{K}$ respectively, which shows that the probe beams significantly affects atoms and hence the shorter exposure time the more accurate the measurement is. A corresponding decay in time of the normalized peak density $\frac{n_{\mathrm{MOT}(t)}}{n_0}$ is presented on Figure 3.14b and was obtained applying the fitting parameters in the equation (3.6).

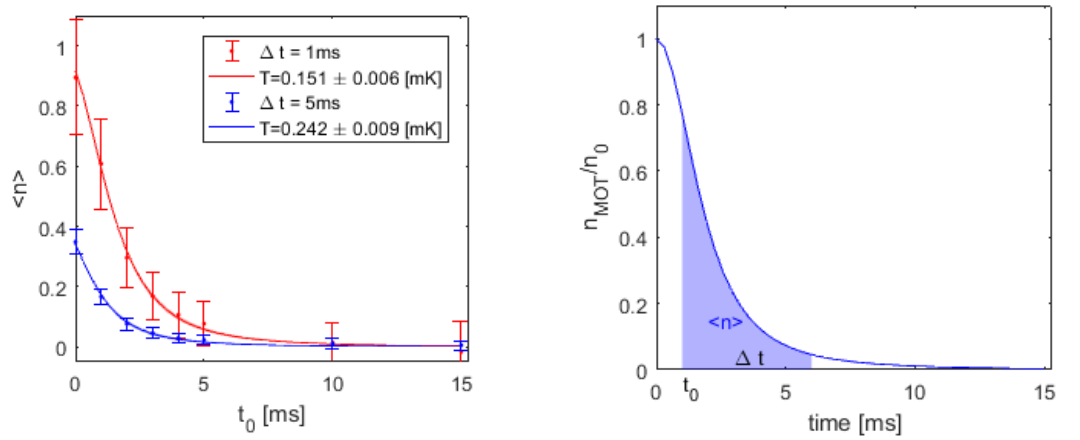

(a) Temperature measurements for different exposure times

(b) Decay of the normalized MOT background

FIGURE 3.14: MOT density decay method to determine MOT temperature. (a) Both red and bue series were taken for the same MOT settings. Solid curves represents fit of the data to equation (3.7). (b) A solid curve presents a normalized MOT background decay versus time $\frac{n_{\mathrm{MOT}(t)}}{n_0}$ for parameters resulting from the fit of the blue curve in (a). The shaded blue area $< n >$ corresponds to the signal acquired by the detector during exposure time $\Delta t = 5\,\mathrm{ms}$ starting at $t_0 = 11\,\mathrm{ms}$.

3.4 Vacuum system

The vacuum system is one of the most crucial elements of the experimental setup, and its performance determines the lifetimes of both the MOT and dipole trap, as the losses of the atoms from traps depend on the presence of residual gases in the vacuum chamber. The cross section for collisions among trapped atoms and background gases was analytically estimated in [147]. Although the model is overly simplified and does not distinguish between atoms in excited and ground states, it generally predicts the observed trap lifetimes and fairly agrees with experimental data obtained in different types of traps: in [148] and [124] traps were obtained in a vacuum of order $10^{-8}\,\mathrm{mbar}$ with a lifetime of about $1\,\mathrm{s}$; in [116] a pressure about $5 \times 10^{-9}\,\mathrm{mbar}$ results in a lifetime close to $2.2\,\mathrm{s}$; and in [126] a vacuum of order $10^{-10}\,\mathrm{mbar}$ gave an average lifetime of about $100\,\mathrm{s}$. Even though a pressure of order of $10^{-9}\,\mathrm{mbar}$ is sufficient for us to obtain and work with a MOT, a long lifetime for dipole trap requires even better conditions. In deep, dense dipole traps two-body collisions are dominant over the collisions with background gases and are the main limiting factor to the atoms loading and traps' lifetime. For a single atom trap, losses due to inelastic two-body collision do not occur. The background collisions dominate and a good vacuum is required

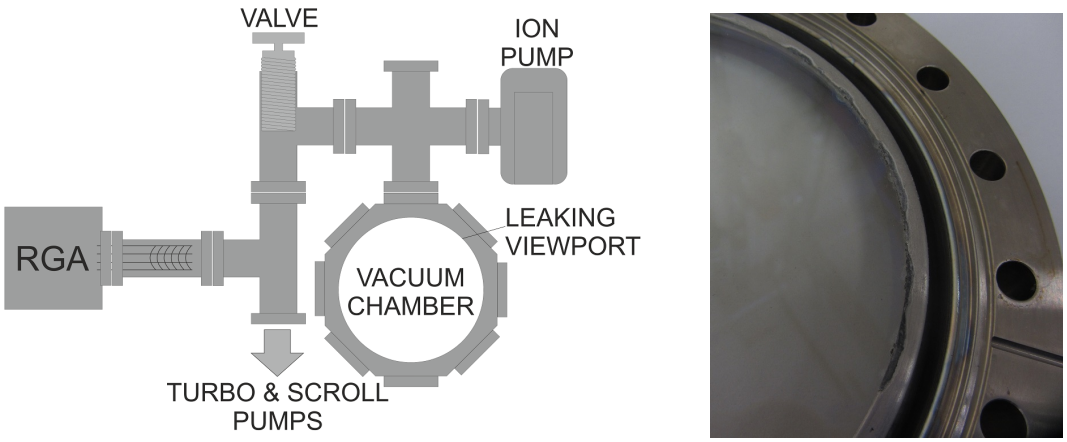

(a) Use of RGA (b) Damaged viewport

FIGURE 3.15: Leak detection of vacuum system. (a) Scheme of the vacuum system with RGA. Vacuum system is normally operated with the valve closed and only the ion pump is responsible for maintenance of UHV. Backing pumping system, consisting of turbo and scroll pumps, provided sufficient vacuum 10^{-8} mbar to open the valve and perform leak examination using an RGA attached just after the valve. (b) Damaged 8″ viewport (NW150CF6). The image shows a part of the viewport which is covered with an unknown black composite close to the place were leak was detected.

to ensure a sufficiently long lifetime of a single atom trap. Hence it is important for us to obtain as low vacuum as possible, $\sim 10^{-10}$ mbar.

The dependence of a trap behaviour on the pressure of residual gases might also become an indication of possible vacuum problems, such as a leak or contamination of the system. During the course of this PhD, issues with the vacuum chamber arose and were diagnosed by monitoring the behaviour of the MOT. The number of atoms in the trap drastically decreased under typical operating conditions, while the trap lifetime increased for an increase of Rubidium pressure in vacuum chamber. These symptoms clearly meant that the system was not Rubidium dominated even when aggressively injecting rubidium atoms into the vacuum chamber. The details of the MOT behaviour are presented in section section 3.4.3. Using a Residual Gas Analyzer (RGA) Figure 3.15a and helium gas helped us to localize a small leak in one of the viewports at the seal between the glass and the metal flange. The damaged part of the viewport is visible on Figure 3.15b, which shows a black deposit. The leak was indeed very small but noticeable. Even though the RGA head was attached to the system very far away from the main chamber and leaking viewport (see Figure 3.15a), an increase of helium gas pressure from 1×10^{-10} to 4×10^{-10} Torr could be detected. A possible reason behind the deterioration of viewport's sealant is Rubidium itself, which is very

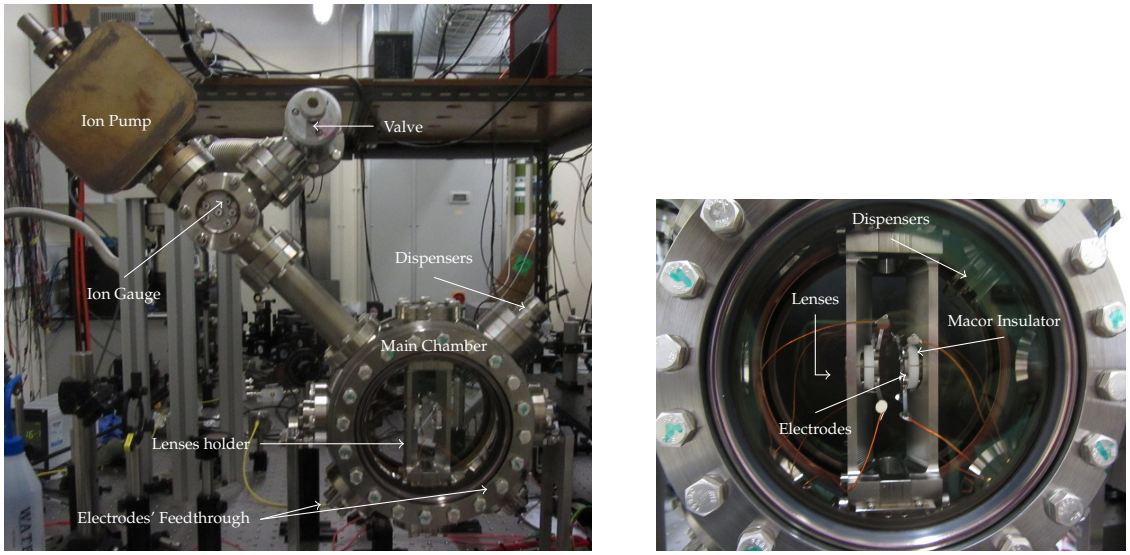

(a) An overview

(b) Main vacuum chamber

FIGURE 3.16: The experimental setup of vacuum system.

reactive and can chemically interact with it.

3.4.1 System description

Current vacuum technology allows to obtain and maintain Ultra High Vacuum (UHV) which is characterised by pressure below $10^{-9}\,\mathrm{mbar}$ and at best up to $10^{-12}\,\mathrm{mbar}$. It is obviously preferable to conduct trapping experiments in the conditions of vacuum as low a possible, but vacuum of the order $10^{-10}\,\mathrm{mbar}$ is considered sufficient [116, 126]. To obtain such a low pressure, special care of the vacuum system needs to be taken, ensuring that all mechanical components are UHV compatible, well cleaned before assembling and eventually the system is baked out to thoroughly remove residuals from all surfaces. Figure 3.16a presents a general view of the experimental setup.

The main vacuum chamber is a commercially available spherical octagon chamber (8" Multi-CF Spherical Octagon: MCF800- SphOct-G2C8) with $1.75\,\mathrm{l}$ volume. Inside the chamber, the holders for dipole trap lenses (see chapter 4) are attached to the body of the chamber by special grooves and grooves grabbers[15] as shown on Figure 3.16b. Electrodes, also visible in the picture, are fit into a ceramic ring, made out of UHV compatible macor, to insulate

[15]Lens holder is placed on four groove grabbers which are clipped on two grooves. Grooves were machined by the OU workshop in the internal surface of the vacuum chamber. Four groove grabbers are also designed and manufactured by the workshop, they are place on top of grooves and fixed in a place by few screws working as a cramp.

them from the grounded chamber and then clipped on top of the lenses' holders [16]. All of the mentioned elements: lenses holder, groove grabbers and electrodes are designed and machined by OU ST Workshop and are made out of stainless steel 316L, which is non-magnetic and has very low out-gassing rate. Two standard $2^3/_4''$ CF[17] sealing surfaces in the body chamber are used to mount electric feedthroughs to power the electrodes through capton wires (marked at Figure 3.16b). We used two feedthroughs symmetrically placed on the sides of the holder to keep the symmetry of electric field created by electrodes as much as possible.

Another electric feedthrough is attached to the main chamber. The commercially available alkali metal dispensers (AMD) from SAES Getters company are mounted directly at the end of feedthrough's pins. The dispensers are a source of rubidium vapour required for the laser cooling experiment, and are designed in a to reduce any contamination with gases other than rubidium. AMD contain a mixture of an alkali-metal chromate (RbCrO4) with the special reducing composition whose role is to suppress the release of gasses other than Rubidium (getter material consisting of 84% Zr and 16% Al). With a typical current of about $4\,\mathrm{A}$ running through the dispensers, the heating starts the reduction reaction which releases rubidium vapour while other gases are being partially absorbed by the reducing composition. Although there exist other methods of rubidium vapour generation, such as light induced atomic desorption [149], alkali dispensers are a controllable source of Rb vapor density in the range of 10^8 to $10^{10}\,\mathrm{cm}^{-3}$ and are sufficiently clean to be considered as a long term solution [150].

Optical access for lasers to the vacuum chamber is provided by viewports. Two $2^3/_4''$ windows of the chamber, situated above and below the lenses mounts, are closed with viewports NW35CF providing an access for the vertical beam of MOT. Access for the dipole trap beam is provided by two small $1^1/_3''$ viewports (NW16CF), which are mounted to the chamber body through an adapter. To enhance the performance of dipole trapping and atoms imaging, viewports are covered with anti-reflection coating which is optimized for 780 to $830\,\mathrm{nm}$. These vieports gives $1''$ of total optical access, however only a part of the coating in the middle is uniform (about 50% of the total glass surface) and hence it is preferable to always assure that the dipole trap beam is centered on the viewport. Eventually, sides of the

[16] The detailed discussion over lenses holders and electrodes design can be found section 4.4.

[17] CF flanges are designed for UHV and consist of two symmetrical flanges with cutting edges and a metal flat gasket which is placed between them. Oxygen-free copper is generally used as a sealing material which much softer than the surface of the flanges. During assembly the cutting edges of the flanges are pushed into the enclosed sealing disc.

chamber are sealed with two big $8''$ viewports (NW150CF6) from Torr Scientific, which are covered with anti reflection coating for 480 to $780\,\mathrm{nm}$ (both sides of glass).

The remaining window of the chamber is used to attach a pumping system. The Varian Plus Star Cell ion pump is employed with a nominal pumping speed for nitrogen of $20\,\mathrm{l/s}$. As shown in Figure 3.16a, the pump is mounted at the five-cross which is moved away from main vacuum chamber to minimise the effects of the magnetic field from the pump inside the chamber. An ion gauge with tungsten filament is mounted close the the pump, so that the pressure of the system can be monitored by both the ion pump current and the gauge. One of the ends of the five cross remains blank, while the last one is closed by an all-metal angle valve, MAV-150-v, which can seal the chamber from the atmospheric pressure down to $10^{-11}\,\mathrm{mbar}$.

Vacuum baking

As a rule, experiments are performed in a system with a closed valve, when only the ion pump passively maintains the pressure. Taking into account the volume of the system and provided there are no leaks in the system, the ion pump is sufficient to maintain the pressure. However, baking procedure must first be applied before the desirable UHV is achieved from an atmospheric pressure, that requires an additional pumps to efficiently remove air and a substantial amount of water and other gasses contaminating the inner surface of the chamber.

A turbo pump of pumping speed $60\,\mathrm{l/s}$ is mounted on a stable support which is fixed to the table to reduce the harmful vibrations while operating the pump. The pump's inlet is attached to the system via a 'Tee' component, whose one end is closed by a combi gauge and the other one is connected to the open valve through a welded bellow flange. Initially, the turbo pump is backed up by the dry pump (Edwards nXDS10i) with peak pumping speed $11\,\mathrm{m^3/h}$ to the initial pressure $10^{-3}\,\mathrm{mbar}$. Then the turbo pump might be switched on and within a day reaches the pressure of order $10^{-8}\,\mathrm{mbar}$. This is a limit reached by the system that can not be pumped further down due to the outgassing of chamber's surfaces. Next step requires rising up the temperature of the chamber taking some precautions. Special care needs to be taken for the big viewports (NW150CF6) to avoid any damage during the procedure. The maximum temperature the viewport can reach is $220\,^{\circ}\mathrm{C}$ increasing at a maximum rate of $2\,^{\circ}\mathrm{C/min}$. It should be assured that the whole viewport is getting warmed up evenly, not to create any mechanical tensions.

Baking was done during a week keeping the temperature below $150\,^{\circ}\mathrm{C}$ for both the chamber and the ion pump, with regular outgassing of combi gauge and dispensers until the pressure eventually stabilized. The pressure at this stage was measured by the combi gauge situated next to the turbo pump and was about $1.15 \times 10^{-7}\,\mathrm{mbar}$. After cooling down the system to room temperature and sealing the chamber by closing the valve attached to the bellow leading to the turbo pump, the pressure was measured by monitoring the ion pump's current, which was fluctuating in range $1.7\,\mu\mathrm{A}$ to $1.8\,\mu\mathrm{A}$. Taking into account a background current of value $1.6\,\mu\mathrm{A}$, which was read out from ion pump when the magnets were taken off, the pressure was found to be in range $1 \times 10^{-9}\,\mathrm{mbar}$ to $8 \times 10^{-10}\,\mathrm{mbar}$.

3.4.2 Vacuum diagnostics using MOT loading curves

The formation of the cloud is a dynamic process, and can be described by the phenomenological equation:

$$\frac{dN(t)}{dt} = \alpha P_{Rb} - \beta P_{Rb} N(t) - \gamma P N(t) - \zeta \tilde{n} N(t) \tag{3.8}$$

where the trapped population $N(t)$ is the result of the balance between loading and loss processes. The rate at which atoms are captured is described by the first term and consists of a constant coefficient α describing the MOT trapping cross-section and is proportional to the partial pressure of Rubidium vapour P_{Rb}. Simultaneously some of the captured atom are lost from the trap due to collisions with remaining Rubidium atoms and other background gases P, with constant loss rates β and γ respectively. In practice, both the rubidium and background pressure may vary over time, but if the timescale of changes is much slower than the time required for the MOT to reach an equilibrium state, it does not have an impact on the solution of equation (3.8) and both parameters might be treated as constant values for a single loading process.

The last term $\zeta \tilde{n} N(t)$ describes loses due to inelastic two-body collisions within the trap, where ζ is the loss rate and $\tilde{n}$ is the mean density of the trap [143]. The time-dependence of the trap density $\tilde{n} \approx \frac{N(t)}{V(t)}$ needs to be determined in order to solve the equation. Two typical regimes can be distinguished, one when the number of atoms is small and the volume of the trap remains constant regardless of number of trapped atoms: $V = const.$ and hence $\tilde{n} \propto N(t)$; and one when the volume of the trap increases proportionally with the number of atoms $V \propto N(t)$ and hence $\tilde{n} = const.$ For a small or not dense MOT cloud, typically

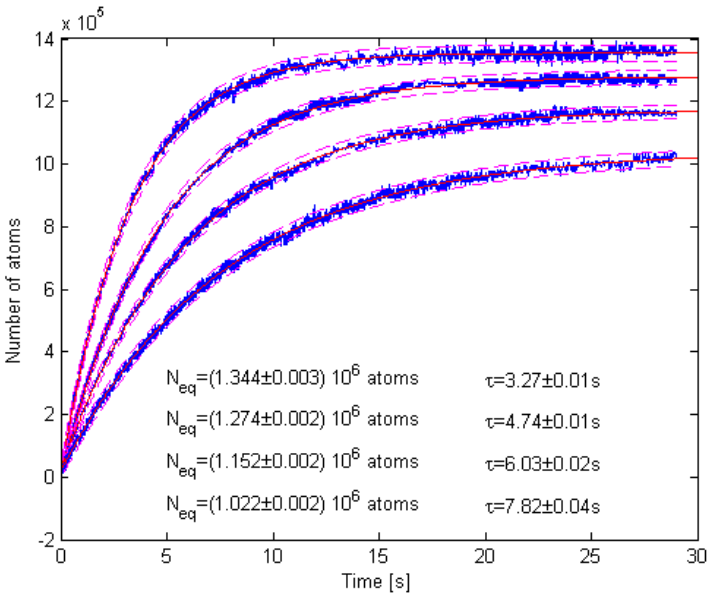

FIGURE 3.17: Loading curves acquired for different pressure of rubidium gas inside the vacuum chamber.

when the number of atoms does not exceed 1×10^7 atoms, the latter applies with a constant density. This allows to solve the equation and results in an exponential loading curve:

$$N(t) = N_{eq}\left(1 - e^{-t/\tau}\right) \tag{3.9}$$

where

$$\tau = \frac{1}{\beta P_{Rb} + \gamma P + \zeta \tilde{n}} \tag{3.10a}$$

$$N_{eq} = \alpha P_{Rb} \tau. \tag{3.10b}$$

The parameters N_{eq} and τ can be obtained from fitting the loading curve with the equation (3.9), as it is shown in Figure 3.17. Introducing a relatively slow change of partial rubidium pressure over the time $P_{Rb}(\tilde{t})$, allows measurements of multiple loading curves with different characteristic values of $N_{eq}(\tilde{t})_i$ and $\tau(\tilde{t})_i$, where i stands for subsequent loading curve as shown in Figure 3.17. This can be achieved by drastically increasing the density of rubidium vapour in the chamber, and then taking measurements when the rubidium source is off and a slow, typically exponential decay of rubidium pressure over time is observed.

It was shown in [143], that the dynamics of MOT loading can be used for vacuum system diagnostics, especially to measure the pressure of background gasses. The method presented in the paper starts with the characterization of the vacuum system. Pumps were switched off for a given time, and simultaneously both loading curves were acquired while the value of the pressure in the vacuum was measured by an ion gauge. From the measured data set for rising background pressure, authors could find the linear dependence between the pressure and the loading time. Extrapolation of the data set gave a hypothetical loading time for the zero background pressure. Then, the rubidium source was activated and while its pressure was increasing, more loading curves were acquired. A new data set allowed to relate the loading time directly with rubidium pressure. Again, the loading time was extracted from the extrapolation of the fit to the data sets for a hypothetical zero rubidium and background pressure. This value is nothing else but just a term responsible for two body losses and has a finite value. The paper concludes that the method sensitivity is limited by the two-body loss term which is in general difficult to measure. The sensitivity of the method for this particular setup was found to be $3.33 \times 10^{-10}\,\mathrm{mbar}$ - is better than the read out from the ion-pump current, but less sensitive than an ionization gauge.

Another attempt to measure the pressure via the MOT loading curve was made in [151], where the effect of two body collision $\zeta\tilde{n}$ was neglected, as the dominant loss process was due to collisions with background gases. By eliminating two-body collisions, N_{eq} and τ were related to each other by a single equation [151]:

$$N_{eq} = \frac{\alpha}{\beta}\left(1 - \gamma P \tau\right). \tag{3.11}$$

The benefit of representing the data in this way is the fact that the rubidium pressure is not directly present in equation (3.11). Crossections for scattering β and γ can be estimated using the Salter-Kirkwood formula [143, 152] taking into account different scattering by different species. If additionally, the background pressure $P\left(\tilde{t}\right)$ is time-independent, N_{eq} is a linear function of τ, which provides information about the loading rate α[18] and the background pressure P. In [151] the group used the method of loading curves to characterise the system and obtain α and the typical operational P. Then, by switching off the pump, they introduced a change in rubidium and background pressure over time that could be monitored.

[18] Both α and β are non-negative values.

The problem becomes more complex if the assumption of a constant value of background pressure is violated. The plot N_{eq} versus τ is not anymore a straight line, as in Figure 3.18b or Figure 3.21a. If the background pressure changes much slower than the rubidium pressure and the results are close but clearly do not follow the linear model, one can approximate the pressure at a given moment $\tilde{t}_i$ by finding the tangent line to the plot at $\tau\left(\tilde{t}_i\right)$ as on Figure 3.21b. It can be assumed that the tangent line represents the data as if the background pressure was constant and both α and P can be estimated. Eventually knowing P, the rubidium pressure can be derived from relation for loading time (3.11) with the assumption that two-body collisions are negligible.

However, when the change of background pressure is significant in comparison to rate of change in Rubidium vapour pressure, equation (3.11) is not sufficient to estimate the background pressure anymore. If it is known that both rubidium and background pressures change is monotonic over the time, it is possible to use a simplified model

$$P_{Rb}\left(\tilde{t}\right) = a_1 e^{-a_2 \tilde{t}} + a_3 \tag{3.12a}$$

$$P\left(\tilde{t}\right) = a_4 e^{-a_5 \tilde{t}} + a_6 \tag{3.12b}$$

where parameters a_3 and a_4 stands respectively for a Rubidium and background gases pressure when the system is in the equilibrium for $t \to \infty$. The model with all seven coefficients a_k can be fitted to the measureble values $N_{eq}\left(\tilde{t}\right)$ and $\tau\left(\tilde{t}\right)$ as follows:

$$N_{eq}\left(\tilde{t}\right) = \frac{\alpha}{\beta + \gamma \frac{P(\tilde{t})}{P_{Rb}(\tilde{t})}}$$

$$\tau\left(\tilde{t}\right) = \frac{1}{\beta P_{Rb}\left(\tilde{t}\right) + \gamma P\left(\tilde{t}\right)}$$

Both methods are discussed and presented in detail in the following sections with experimental data and discussion of results.

3.4.3 Using the MOT diagnostics to detect a defect in vacuum system.

At the early stage of this PhD, the MOT presented unexpected behaviour. The trap became visibly weaker, even after long activation of the rubidium source. The quality of the trap was progressively deteriorating requiring each time more rubidium atoms, until the cloud could be barley seen with the camera and reached the stage when the number of atoms was

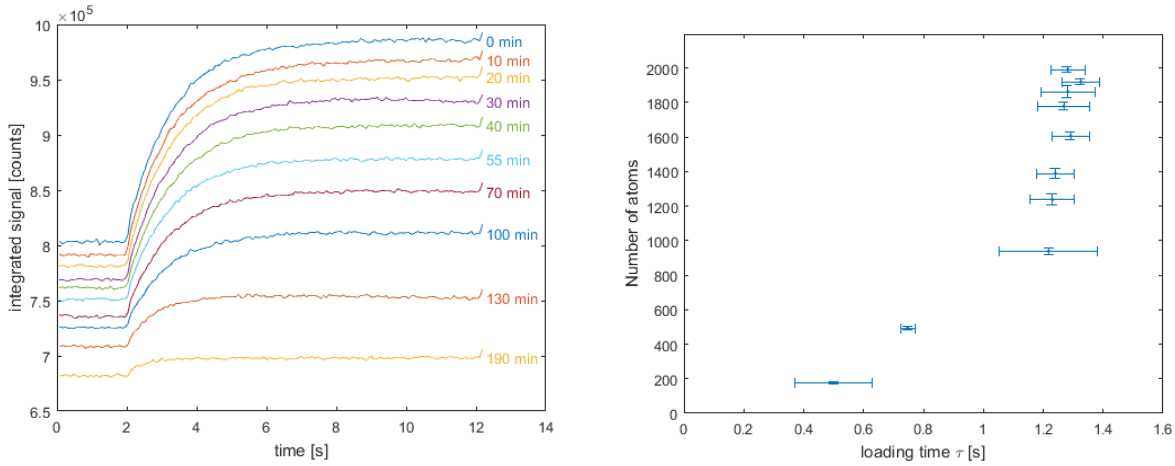

(a) Loading curves $N(\tilde{t})$

(b) Correlation $N_{eq}(\tilde{t}, \tau(\tilde{t}))$

FIGURE 3.18: Pressure diagnostics using MOT. Subsequent measurements corresponds to $\tilde{t}$ which is in range $(0 \text{ to } 190)\,\mathrm{min}$. (a) Loading curves for different levels of rubidium pressure. An integrated signal is simply a sum over an area consisting of the MOT. For each curve an offset comes from the background fluorescence of atoms which are not in the trap but contribute to the signal. The bigger density of rubidium gas the bigger stray signal. (b) The correlation between $N_{eq}(\tilde{t})$ and $\tau(\tilde{t})$ from fitted loading curves.

estimated to be only about few thousands. Since the laser system and the trap alignment had been thoroughly examined, the next element to test was vacuum system. Reading a pressure out of the ion pump was very inaccurate, due to the pump contamination and a high leak current, as it had been operating for a long time without baking. In order to determine the background pressure, we used the method discussed in the previous sections and measured the MOT loading curves to diagnose the vacuum conditions.

A significant amount of rubidium atoms was injected into the vacuum chamber, so that the atomic cloud was bright enough to capture the signal on the CCD. Then the rubidium source was closed and a series of loading curves were recorded, whilst the rubidium pressure was decreasing. The measurements were conducted for about three hours, obtaining curves for different decay times in range $(0 \text{ to } 190)\,\mathrm{min}$ until the cloud was almost invisible. Each of the loading curves visible in Figure 3.18a is in fact an average over six loading curves acquired during about 1 minute, where we assume that during this time the rubidium pressure can be considered constant. In order to quantify the influence of the pressure inside the chamber on the MOT, we used equation (3.9) to fit all loading curves. The dependence of the MOT size in equilibrium N_{eq} versus loading time τ is shown in Figure 3.18b.

The result presented in Figure 3.18b shows a departure from the linear model (3.11)

that assumes a constant background pressure. According to [151], this behaviour is a clear indication that $P\left(\tilde{t}\right)$ rises over time and it is obviously meaningless to fit data with linear function. Moreover, the background pressure changes too fast with respect to rubidium pressure to even try an approximation with the tangents method[19], hence the more general method based on fitting the number of atoms and loading time as a function of the time needs to be employed.

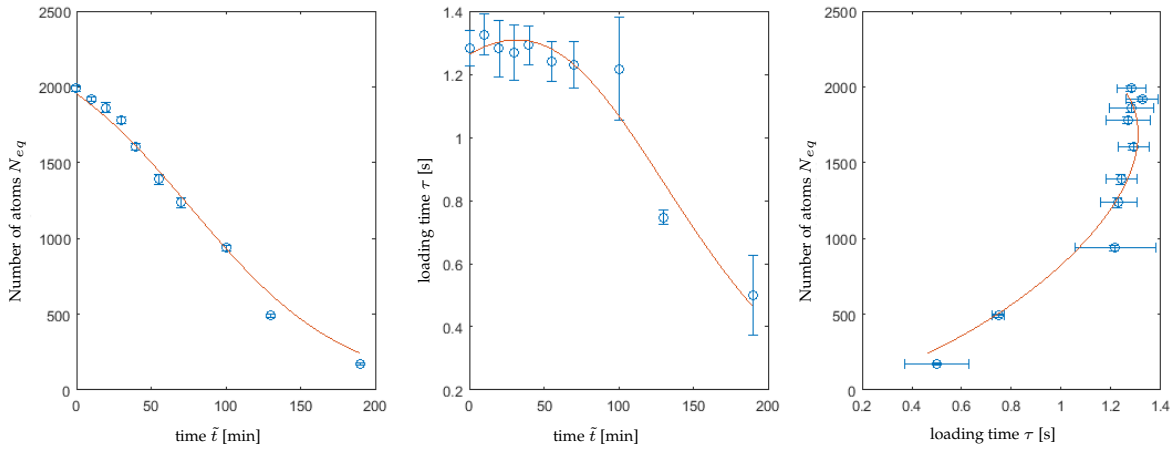

FIGURE 3.19: The fit of a general pressure model to the MOT behaviour. The three plots represent the number of atoms in equlibrium $N_{eq}\left(\tilde{t}\right)$ over time $\tilde{t}$, loading time of MOT over time $\tau\left(\tilde{t}\right)$ over time $\tilde{t}$, and the correlation between $N_{eq}\left(\tilde{t}\right)$ and $\tau\left(\tilde{t}\right)$. Blue points with error bars represents experimental data while the red solid curve is a model based on equation (3.12).

Figure 3.19 shows the experimental results for $N_{eq}\left(\tilde{t}\right)$, $\tau\left(\tilde{t}\right)$ and $N_{eq}\left(\tau\right)$. These three sets of data are used to find the fitting parameters a_k from the general model in equation (3.12). It is found that the pressure of the rubidium and residual gases was $a_1 = (1.4 \pm 0.3) \times 10^{-10}$ Torr and $a_4 = (4.0 \pm 0.8) \times 10^{-9}$ Torr respectively at the beginning of the measurement. The change of rubidium and background pressure at time $\tilde{t}$ accordingly to the general model is shown as a blue solid line on Figure 3.20. The data analysis shows that the background pressure was indeed increasing and was also very high of order 10^{-8} Torr. The speed at which the background pressure rises up is surprisingly high. The Rubidium vapour behaves as it is expected, the initial pressure of rubidium is very high and decreases at reasonable pace, less then an order of magnitude in over two hours. These results are reasonable and indicate a clear presence of a leak or malfunctioning pump.

[19]This method would still give reasonable results for the background pressure, but it would not not make sense because it would result in a negative value of rubidium pressure. For each tangent line rubidium pressure is obtained from: $P_{Rb} = N_{eq}/\alpha\tau$, hence for a negative α it takes negative values.

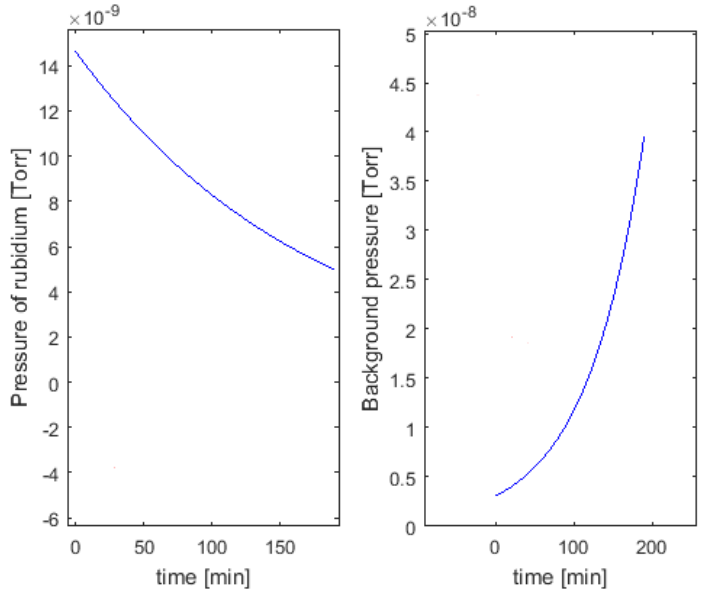

FIGURE 3.20: Analysis of pressure measurements using MOT while having vacuum problems. Graphs represent the background pressure $P(\tilde{t})$ and $P_{Rb}(\tilde{t})$ in respect of time. The blue solid lines represent the equation (3.12) where parameters a_k comes from the fitting of the data with the general model.

Based on this measurement, we decided to attach the RGA to the system and check the true cause of the vacuum problems. We localised the leak at one of the large viewports. The vacuum parts were reassembled and the faulty viewport was replaced. The chamber was then baked and prepared to operate under UHV according to the procedure discussed in section 3.4.1.

3.4.4 Using MOT diagnostics to verify the performance of vacuum system

To ensure that new vacuum worked sufficiently well, a series of similar experiments were conducted as soon as the MOT become operational. The measurement was launched in the early morning when the rubidium pressure was quite low after the weekend, as could be observed in the small number of atoms in the MOT. After the dispensers were switched on the first loading curves were recorded. After some time the source of rubidium was switched off, and now a decrease of rubidium pressure could be observed. The rate of changes in rubidium pressure was high while running the dispensers up until $20\,\mathrm{min}$ after switching them off, therefore a single loading curve was taken once per every minute to monitor these changes. After that the change was not so significant and the MOT behaviour was being monitored once per few hours until the next morning.

All loading curves were fitted with MOT loading equation (3.11) to obtain a correlation between N_{eq} and τ as it was explained before. The results are shown in Figure 3.21a, where the black dots are the experimental data points. The first clear remark in Figure 3.21a is that

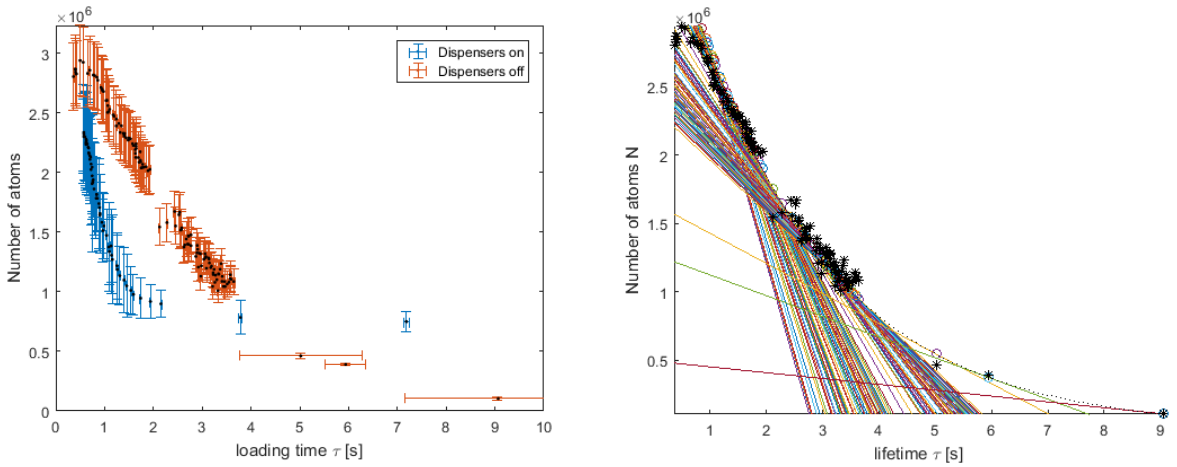

(a) Measurement (b) Tangents method

FIGURE 3.21: Pressure diagnostics using MOT. (a) Data points representing relation $N_{eq}(\tilde{t}, \tau(\tilde{t}))$ for different $\tau(\tilde{t})$. (b) In order to find a tangent line for each τ_i an arbitrary exponential function was first fit to the data.

when the pressure of rubidium raises the correlation between $N_{eq}(\tilde{t})$ and $\tau(\tilde{t}))$ is different than when the dispensers are switched off. For simplicity these two cases are distinguished in Figure 3.21a using two different colors for errorbars, although it is clear from the plot that the process is continuous and the first few points from the brown plot visibly belong also to the blue series.

The difference between plots is truly puzzling and indicates a change of the experimental conditions during the experiment and only two factors might change, namely the rubidium and background pressure. Regarding the rubidium pressure, it is expected that the rate at which the rubidium vapour pressure increases, thanks to the hot dispensers, is quicker than the free decay of rubidium pressure when rubidium source is off. However, it still does not explain the difference between plots since $N_{eq} = \frac{\alpha}{\beta}(1 - \gamma P\tau)$ for a constant background pressure, and in principle the relationship between N_{eq} versus τ does not depend on rubidium pressure at all. Hence the conclusion that, the background pressure changes over time differently when the dispensers are on and when they are off. The blue curve for τ in range $(0.7 \text{ to } 1.1)\,\mathrm{s}$ and the brown one for τ in range $(0.7 \text{ to } 4.0)\,\mathrm{s}$ are approximately linear. According to the model, the background pressure is higher with working dispensers than when they are switched off, which implies that the dispensers might be responsible for outgassing

additional residual gasses.

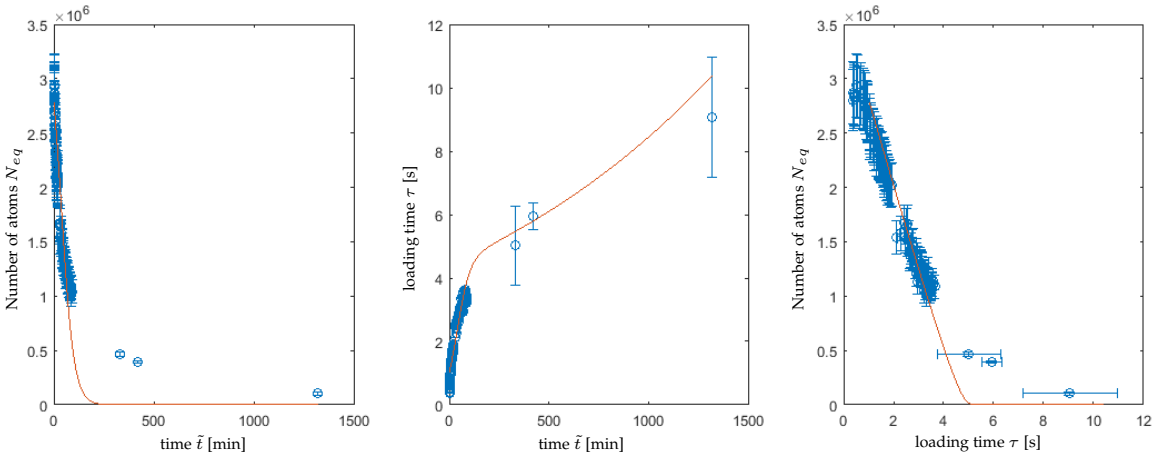

FIGURE 3.22: The fit of a general pressure model to the MOT behaviour. The three plots represent the number of atoms in equlibrium $N_{eq}\left(\tilde{t}\right)$ over time $\tilde{t}$, loading time of MOT over time $\tau\left(\tilde{t}\right)$ over time $\tilde{t}$, and the correlation between $N_{eq}\left(\tilde{t}\right)$ and $\tau\left(\tilde{t}\right)$. Blue points with error bars represents experimental data while the red solid curve is a model based on equation (3.12).

Since it might be difficult to analyze the pressure change while the conditions are affected by the working dispensers, further analysis was made only for the situation when dispensers were switched off. As it was already mentioned, the data for free rubidium decay (dispensers off) lie mostly on a straight line and only the last three points (taken five, seven and twenty two hours later) show a clear evidence of a slope change, which implies that the background pressure is not constant. This means that the use of the method based on tangents is justified. Figure 3.21b presents the first method base on tangents applied to analyze the data, while the corresponding pressure values are presented on Figure 3.23. For comparison the more general model (3.12) was also applied to the same set of data. Figure 3.22 contains three plots $N_{eq}\left(\tilde{t}\right)$, $\tau\left(\tilde{t}\right)$ and $N_{eq}\left(\tau\right)$, and the fit to the model where parameters a_k are optimized.

As shown in Figure 3.23, both methods agree on the order of magnitude of background gasses pressure $3.5 \times 10^{-9}\,\mathrm{mbar}$. Both methods also imply that the background pressure decreases less than an order of magnitude during 24 hours. Interestingly, according to the tangents method, the rubidium pressure seems to rise until it reaches an equilibrium state, whereas it is known that the rubidium vapour should decrease. This can be simply because the initial change of background pressure is quite rapid and the assumption that it should be almost constant for a given measurement does not apply in this case. The model does

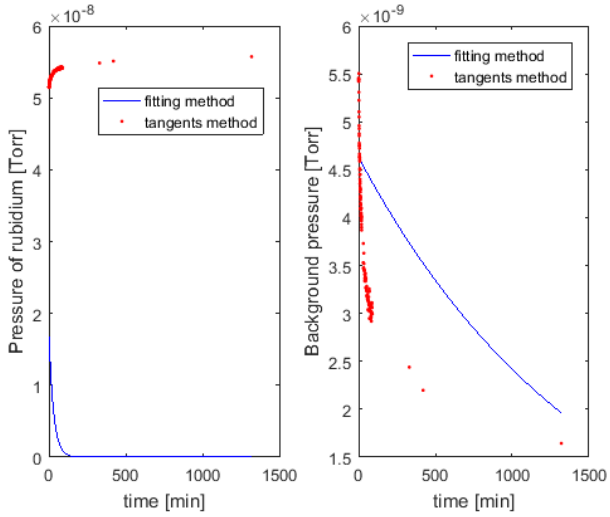

FIGURE 3.23: Analysis of pressure measurements using MOT after vacuum chamber redesign. Graphs represent the background pressure $P(\tilde{t})$ and $P_{Rb}(\tilde{t})$ versus time. The blue solid lines represent the equation (3.12) where parameters a_k comes from the fitting of the data with the general model.

not fit the data in Figure 3.22, as the experimentally measured number of atoms N_{eq} differ from the theoretical prediction at long times $\tilde{t}$. Most likely, the decay of rubidium and background gases is not purely exponential just after switching off the dispensers, since a kind of hysteresis was observed (see Figure 3.21a).

The conclusion is that, after boosting the dispensers and subsequently switching them off, the background pressure indeed changes over time but the change is not significant. At this stage dispensers were still slightly contaminated with residual gases, even though special care was taken while baking procedure to outgas dispensers. Readings out of the ion pump's current also indicated a rise of overall pressure in the chamber. The background pressure, which is usually measured at the level of $0.6\,\mu\mathrm{A}$ of the pump's leak current, used to rise an order of magnitude up to $5\,\mu\mathrm{A}$ while running on the dispensers with $3.7\,\mathrm{A}$ current. After gaining enough rubidium vapour inside the chamber we would then decrease the current on the dispensers to a safe level $3.4\,\mathrm{A}$, which would maintain a slow continuous release of rubidium atoms whilst avoiding outgassing of other species. As a result the leak current used to decrease back to $0.7\,\mu\mathrm{A}$. The phenomenon vanished after few weeks of operating dispensers and now the leak current on the ion pump remains stable and the typical current on dispensers is $4.3\,\mathrm{A}$.

3.5 Conclusions

A properly functioning vacuum system is crucial for MOT and dipole trap based experiments. During the course of this work the vacuum system broke down leading to problems with efficient MOT loading. Thorough diagnostics of the system were conducted using the basic principles of the MOT loading dynamics. It was shown that the background pressure was indeed unstable and too high. This results clearly implied some malfunction of the vacuum system, and thanks to that more detailed investigation with RGA uncovered a small leak in one of the windows. After redesigning the chamber and replacing the damaged window, once again the same diagnostics was performed. This time the result was satisfactory and confirmed low and stable pressure. It also revealed that at the early stage of using new dispensers some portion of residual gasses coming from the dispensers' surface still polluted the chamber, but the effect vanished after a few months.

The experimental apparatus for Magneto Optical Trap has been improved and can provide a reservoir of atoms for dipole trapping. It consists of a laser system in *slave-master configuration* and uses saturated absorption spectroscopy to stabilize lasers frequency to the atomic transition in rubidium. The typical peak atoms density in MOT is in range $(2 \times 10^8$ to $50 \times 10^8) \, \mathrm{atoms/cm^3}$, while its typical optimized temperature is in the range $(100$ to $500)$ µK.

Chapter 4

Dipole trap system design

This chapter will describe the design and implementation of an optical system for dipole trapping and imaging. Dipole trapping was previously implemented in the laboratory (Figure 4.1), but the system had limited functionality. In this chapter we discuss a new setup which was conceived to overcome the shortcoming of the previous system, so a comparison between the two will also be made to demonstrate the improvement. The general layout of both systems consists of a red-detuned dipole trap and an imaging system coupling the fluorescence light to an ICCD camera, used to observe the trapped atoms. A red-detuned trap was chosen, because of its significant advantage over blue detuned: only a single focused beam is sufficient to create a dipole trap (see section 2.2.7).

Regarding the previous setup, the key element of the design was a high numerical aperture lens (352240 from Geltech) which simultaneously was used to focus $830\,\mathrm{nm}$ dipole trapping beam and to collect $780\,\mathrm{nm}$ fluorescence light. For this lens, the dipole trap beam needed to enter the objective lens with a convergence of 4^o to achieve optimal trapping. This was inconvenient for both the system alignment and maintenance. The lenses were held in stainless steel mounts, attached to the chamber's flange, as shown in Figure 4.1b. This led to difficulties in aligning the axis of the lens holders when attaching the flange to the chamber through a copper gasket. The mounting procedure often resulted in a tilt of the lenses' axes that also had an impact on the alignment of the imaging system. Moreover, the system did not take into account another potential issue related to stray charges building up at the lenses surface. As shown in [153], during a Rydberg experiment a DC electric field can build up, which results from charge induction on the lens's surface close to atoms. The system had no mechanism preventing or compensating the impact of a stray electric field, and thus we could expect problems with Rydberg excitations in future experiments.

Although the previous setup allowed us to trap atoms, as shown in Figure 4.1c, a number of improvements could be made. Therefore I designed a new optical system for trapping

(a) Vacuum chamber (b) Lens holder (c) Dipole trap image

FIGURE 4.1: Previous experimental setup for dipole trapping.

and imaging atoms, with the goal of overcoming these challenges. Recently a new commercial lens (355561 Geltech) was developed for dipole trapping, which is designed especially for this kind of experiments [153] and benefits from a higher numerical aperture (NA) and hence a larger solid angle for fluorescence light collection. We decided to take advantage of that and upgrade our system with this new lens and by redesigning the rest of trapping and imaging system. The new lenses required a custom built lens holder which was designed and manufactured by the OU workshop (see section 4.4). The lens and the holder facilitated an alignment of the trapping and imaging system in comparison to the previous setup. Moreover, stray electric charges issue was addressed by coating the lenses with a conductive ITO layer ($100\,\mathrm{nm}$ thick) to provide a stable electrostatic environment. Furthermore, a set of electrodes was placed around lenses so that any residual stray electric field could be balanced. In the following chapter, the analysis of the optical performance of the new system and the new lens is presented.

4.1 Remarks on design

A scheme of the optical system is presented on Figure 4.2. $852\,\mathrm{nm}$ laser beam (see 'dipole trap beam' in Figure 4.2a) acts on a high NA lens which focuses it inside the vacuum chamber, resulting in a trapping potential for atoms. A fraction of the fluorescence light emitted by the atoms at $780\,\mathrm{nm}$ is collected by the lens and its path overlaps with trapping beam.

Although only one lens is used for both atoms trapping and imaging, a second identical lens which will be used in the aligning procedure of the dipole trapping system, is placed at a distance of double focal length. The alignment of the imaging system is guided by a $780\,\mathrm{nm}$ laser beam mimicking a trapped atom, which is counter-propagating to the dipole trap beam as shown in Figure 4.2b. The distance between lenses restricts the angle α for the

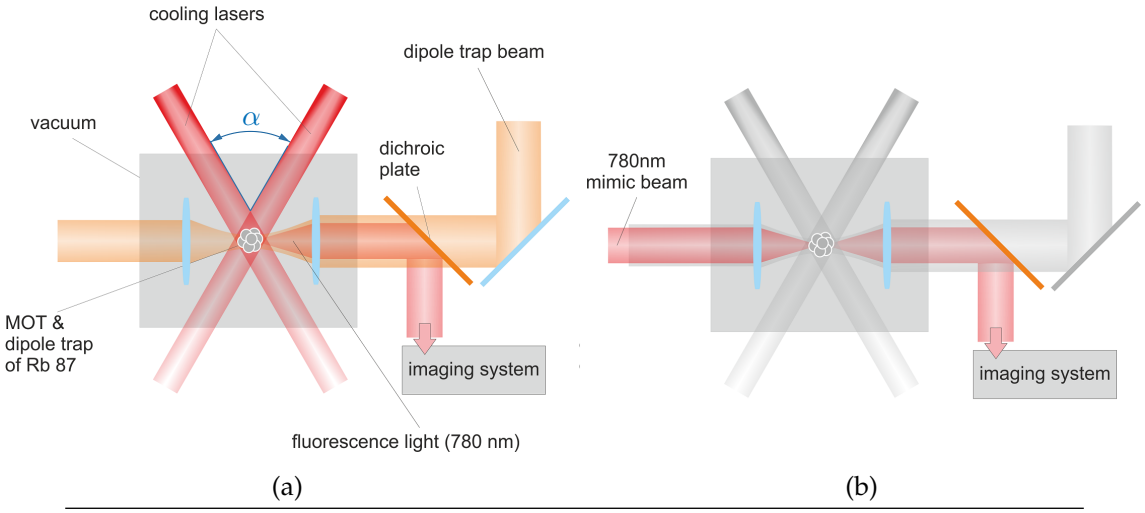

FIGURE 4.2: A general scheme of experimental dipole trap setup. (a) Optical system for trapping and imaging of atoms. (b) Alignment of imaging system using the auxiliary $780\,\mathrm{nm}$ mimic beam.

cooling lasers, and hence typically $\alpha \leq 90°$. This angle depends on the size of the cooling beams, the lenses diameter and the distance between lenses according to:

$$\Phi_{beam} = 2(\mathrm{BFL}) \cos\frac{\alpha}{2} - \Phi_{lens} \sin\frac{\alpha}{2} \tag{4.1}$$

where Φ_{beam} is the cooling beam diameter, Φ_{lens} is the total lens diameter and $2(\mathrm{BFL})$ is the distance between lenses.

4.1.1 Design aims and constrains

Dipole trapping is a well established technique, which can confine an ensemble of atoms to few micrometers [30]. Constrains onto the dipole traps designs are usually imposed by the prospective use of these traps. In the course of this work, a full Rydberg blockade needs to be obtained in order to implement DQC1 (see section 2.3). Since the typical Rydberg blockade range is of the order of few micrometers, we aim to achieve a Rayleigh length and a waist of the focused trapping beam of the order of a few micrometre, while providing a beam with minimal spherical aberration to maintain the Gaussian profile.

In addition, from the experimental point of view, ease in aligning the apparatus is also desirable. The first challenge is to create enough optical access for the MOT beams between the two lenses, in other words to maximise the angle α in Figure 4.2a. Therefore, we will be looking for a lens with sufficiently long back focal length (BFL[1]). To facilitate the alignment,

[1]Back Focal Length (BFL) is a distance from last surface to focal plane.

it is desirable to have the incident beam acting on the lens fully collimated. This will also help us in modifying easily the optical path of dipole trap laser in the future, for instance splitting the beam into two to have multiple dipole traps or adding an SLM[2] which requires certain operating conditions.

Another important aspect of the design is the imaging system, which is our main measurement tool. The trapped atoms emit fluorescence light isotropically and only a fraction of this light reaches the camera or the avalanche photodiode (APD). The power of the fluorescence light is relatively weak in comparison to the readout noise of the detector. In order to optimise the signal to noise ratio, we want to maximise the solid angle from which fluorescence light is collected. Additionally the imaging of atoms should have enough spatial resolution to distinguish two dipole traps separated by a few microns. We are also considering creating a two dimensional array of many traps in the future, with few microns distance between traps. Hence, we are particularly interested in a good performance of the trapping and imaging system for both ($850\,\mathrm{nm}$ and $780\,\mathrm{nm}$) wavelengths on and out of the optical axis up to tens of $\mu\mathrm{m}$.

The single aspheric lens used previously in our experiment (352240) was designed for diode laser collimation at $780\,\mathrm{nm}$. The working distance was $5.92\,\mathrm{mm}$, with the assumption that every laser diode has a thin glass in front of the window. The new lens (355561) has a bigger working distance ($7.03\,\mathrm{mm}$), and its performance was optimised for the two wavelengths, to achieve a good compromise between dipole trap quality and the capturing of fluorescence light from atoms.

4.1.2 Method used for design evaluation

The design of the optical system and its analysis were performed with Zemax studio [154], a dedicated software for optical system design, which has the ability of analyzing real systems suffering from a variety of distortions, aberrations and more. There are two general methods exploited by Zemax studio: ray tracing (or ray-based diffraction computations) where rays are treated separately and propagate in space as plane wavefronts, and Physical Optics Propagation (POP) where the image at a given plane is computed using wavefront propagation (Fresnel diffraction). The ray tracing method is accurate enough to describe the vast majority of traditional optical design, and is really much faster comparing to the POP method which requires much more computational power, but is suitable for analysis

[2]Spatial light modulator (SLM) is discussed briefly in section 1.1.

of laser beam propagation. All of the parameters mentioned in this section are based on the ray tracing method. (For detailed methods description see Appending D.1).

Due to the simplicity of our system and the required size of the focus spot, spherical aberration is the main factor limiting the system's performance. For a perfect system not suffering from spherical aberrations, the waist ω_f of the beam after the lens in the focal plane can be estimated[3] by equation:

$$2\omega_f = \frac{4\lambda}{\pi}\frac{f}{D} \tag{4.2}$$

and the depth of field (DOF):

$$\mathrm{DOF} = \frac{8\lambda}{\pi}\left(\frac{f}{D}\right)^2 \tag{4.3}$$

where λ is the wavelength, f is the focal length and D is the diameter[4] of the input beam. It is worth noticing that, in the absence of aberrations, the bigger the diameter the sharper the trap/image is. However, for an imperfect system with spherical aberrations, different annular zones of the lens focus at different points along optical axis. This causes the plane with the highest axial intensity not to overlap with the natural waist of focused beam (see Figure 4.3). This also means that increasing the input beam diameter might increase the spot size due to the aberrations, instead of decreasing it. The reason why the point of the minimum blur[5] is different than the diffraction focus[6] is because the energy of the beam is spread beyond the main spot in additional rings. The profile of the spot is shown in Figure 4.3 as the Point Spread Function (PSF)[7] graph. Since the place of highest intensity and natural waist do not overlap, we should consider which parameter is the most reliable to designate the position of the trap. Atoms will be effectively trapped in the place of the highest laser beam intensity, hence in my analysis, the BFL is defined by the diffraction focus (Figure 4.3 red line).

The analysis of a real imperfect system requires a quantitative method for evaluation of

[3] The estimation is based on the Gaussian beam propagation using ABCD matrices. If a thin lens is placed in the waist of a Gaussian beam, the beam after the lens focuses at the distance d: $d = f\left[1 + \left({}^{\lambda f}/_{\pi\omega_{in}^2}\right)^2\right]^{-1}$ where λ is the wavelength, f is the focal length and ω_{in} is the beam's waist before the lens. The waist of the focused beam at the distance d is $\omega_f = {}^{f\lambda}/_{\pi\omega_{in}}\left[1 + \left({}^{\lambda f}/_{\pi\omega_{in}^2}\right)^2\right]^{-1/2}$. Since typically ${}^{\lambda f}/_{\pi\omega_{in}^2} \ll 1$, these expressions take approximately forms: $d \approx f$ and $\omega_f \approx {}^{f\lambda}/_{\pi\omega_{in}^2}$. Introducing the diameter $D = 2\omega_{in}$ the equation for a waist ω_f follows the expression (4.2) in the main text.

[4] Diameter of the beam is a double of the beam waist ω_{in} before the lens $D = 2\omega_{in}$. Diameter is an intuitive parameter to be used when discussing properties of lenses and their impact on the beam's propagation.

[5] Plane characterised by the smallest spot.

[6] Diffraction focus, is the point of the highest beam irradiance. If the aberrations are small enough, the diffraction focus is unique, otherwise there can be more than one.

[7] Point Spread Function describes the response of an optical system to a point source of light.

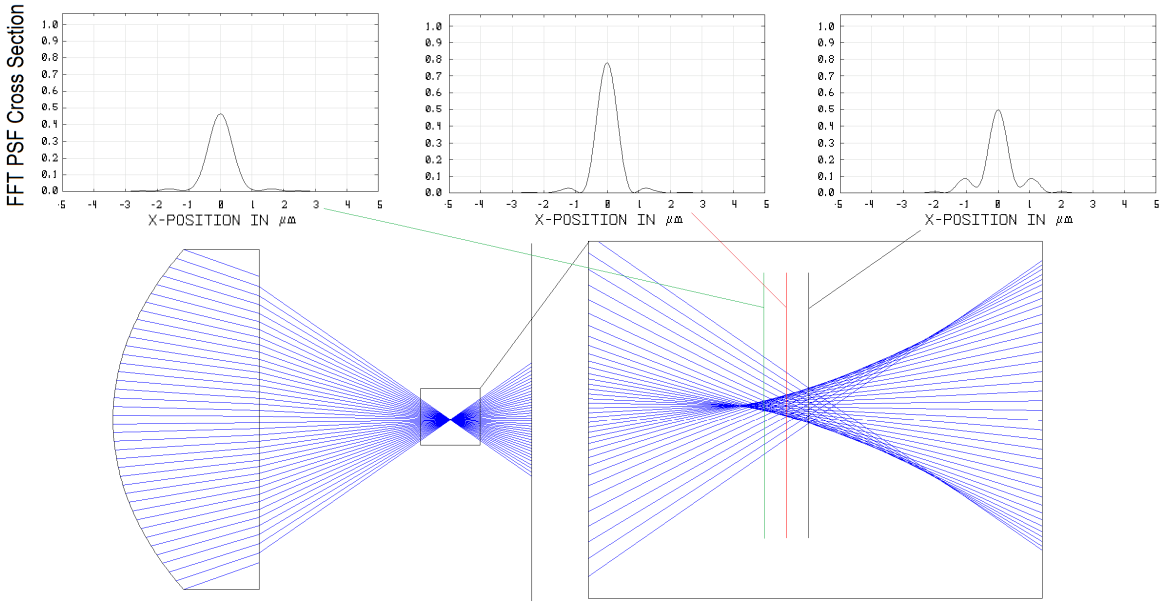

FIGURE 4.3: The ray plot of focused beam. The plane of the highest beam intensity (diffraction focus) is marked by the red vertical line; black line marks the plane intersecting natural waist of beam (minimum blur); green line denotes an arbitrary chosen plane. The distance between each pair of planes is $1.7\,\mu\mathrm{m}$. Corresponding values of Point Spread Function (FFT PSF Cross Section) are presented above the ray plot. Data was obtained with Zemax for 355561 lens illuminated by fully collimated $852\,\mathrm{nm}$ beam.

the optical performance. The quality of the optical system might be described by the Strehl ratio, which is defined as the ratio of the peak intensity of a measured point spread function in the presence of aberrations I_{aberr} to the peak intensity of a perfect diffraction-limited PSF I_{ideal} for the same optical system:

$$S = \frac{I_{aberr}}{I_{ideal}} \tag{4.4}$$

In near diffraction limited systems the Strehl ratio is also a good indication of the axial intensity, therefore the majority of the analysis is based on this parameter.

Eventually, the size of the spot and depth of field need to be defined, as both of these parameters matter while determining the imaging system resolution, design tolerances and the actual size of dipole trap. The spot size at a given distance is described either by RMS spot radius[8] or the Airy radius[9], which is the theoretical limit of spot size caused by diffraction

[8]The RMS spot radius is the root-mean-square radial size. The distance between each ray and the reference point is squared, and averaged over all the rays, and then the square root is taken. The RMS spot radius gives a rough idea of the spread of the rays, since it depends upon every ray [154].

[9]Airy radius is calculated by Zemax from formula $r = 1.22\lambda F/\#$, where image space $F/\#$, due to the used settings, is defined as the ratio of the paraxial effective focal length calculated at infinite conjugates over the paraxial entrance pupil diameter [154].

of light. If the RMS spot size is smaller than the Airy radius, the system may be considered as diffraction limited, otherwise the system is limited by spherical aberrations.

4.1.3 Matching the imaging system to camera resolution

The signal from a single atom is very weak and should be detected ideally by a single pixel on the camera in order to reduce the signal to noise ratio. At the same time, we should be able to distinguish between two atoms situated close to each other. In other words, we want to keep the image spot size diameter equal or close to equal to the pixel size, and maximise the image resolution. Two objects are distinguishable by the CCD if they can be imaged on different pixels without significant overlapping. This puts constrains on the magnification and spot size of imaging system.

The ICCD [10] has two different resolutions specified in manual: the resolution of the CCD pixels ($13\,\mu\mathrm{m}$) and the resolution of the intensifier ($19\,\mu\mathrm{m}$). Even if the trap size image was matching the pixel's size, light from the trap would still be spread over more than one pixel because of the intensifier. Fortunately there is a possibility of binning pixels on the CCD into one without increasing noise. For 2×2 binning we adjust the magnification and PSF of the imaging system so that the light from atoms is captured by a 'single' $26\,\mu\mathrm{m} \times 26\,\mu\mathrm{m}$ pixel. In this way we obtain a desirable resolution which is not limited by the intensifier.

4.2 Meeting the design constrains: quality of aspherical lens

Before delving into the detailed design of the whole imaging and trapping system, we will pay attention to the most crucial of the optical component - the lens closest to the atoms. The lens had been originally designed in [153] so that the curvature of the aspheric surface is optimised[11] for collimated incident $850\,\mathrm{nm}$ light, and at the same time allowing the same working distance for $780\,\mathrm{nm}$ light. So we can expect a good compromise between the dipole trap efficiency and the resolution of the imaging system.

Fluorescence light is unpolarised, as the fluorescence from a cloud of atoms can be seen as a collection of many independent point sources. Therefore the imaging system can be successfully analysed using the ray tracing method. In the case of a dipole trap, where the trapping potential is created by a tightly focused linearly polarised Gaussian laser beam,

[10] ICCD (Intensified CCD) has the analogue intensifier of light before CCD matrix. The intensifier consists of photocathode, transport channel and fluorescence screen. See section 5.1.3 and appendix E for more details.

[11] Optimised means that the shape of lens was profiled to obtain Strehl ratio close to one. It means that the spherical aberrations are minimised for the given wavelength.

		new setup	old setup
dipole trap beam	wavelength	@850nm	@830nm
	collimation [rad]	collimated	diverging 0.007
	Airy radius [µm]	aberr.lim. (0.868)	1.071
	RMS [µm]	1.383	diff.lim. (0.179)
	Strehl ratio	0.808	0.989
@780nm	collimation [rad]	converging 0.002	diverging 0.016
	Airy radius [µm]	0.794	1.005
	RMS [µm]	diff.lim. (0.063)	diff.lim. (0.157)
	Strehl ratio	0.997	0.991
	BFL [mm]	7.03	5.72
	N.A.	0.53	0.43

TABLE 4.1: Table presents the fundamental features of dipole trap and imaging quality for lens 355561 from Lightpath Technologies. For comparison with previous setup lens 352240 is also included in the last column. All of the parameter are calculated by Zemax software and for the object lying on the optical axis and the entrance pupil equal $12\,\mathrm{mm}$, while the maximum lens aperture is $12.5\,\mathrm{mm}$. Diffraction limited system is designated as (diff. lim.) and the given value is not considered in determining spot size, and vice versa for system limited by spherical aberration (aberr. lim.). Table is divided horizontally into three sections: trapping beam, where quality of optics is considered for given beam wavelength; 780nm, with the quality of optics for fluorescence image; last three rows with BFL and N.A. values for both of trapping and fluorescence light. To avoid confusion while using terms related to the alignment of the trapping beam ($850\,\mathrm{nm}$ or $830\,\mathrm{nm}$) as well as fluorescence light, the axis of light propagation remains the same for both wavelengths and is indicated by fluorescence light.

the properties of the trap depend on the exact irradiance profile of the beam near the focus. Although a detailed analysis of the dipole trap profile is later obtained using a different method (POP), using the ray tracing method helps to asses the quality of the lens.

Table 4.1 contains the brief performance analysis of the two aspherical lenses for comparison. The first column consist of the new optical setup with lens 355561 from Lightpath technologies, while the last column presents the previous optical setup with the 352240 lens. The new lens provides higher numerical aperture (> 0.5) than the old setup and a working distance above 7mm. This means that, according to (4.1), the angle between the MOT beams (see α on Figure 4.2a) is equal to approximately $40°$ for new lens, while it was $35°$ for the previous setup, for the same chosen diameter of $8\,\mathrm{mm}$ for the cooling beam. Analysis of the Strehl ratio, RMS spot size and Airy radius leads to the conclusion that the new setup will

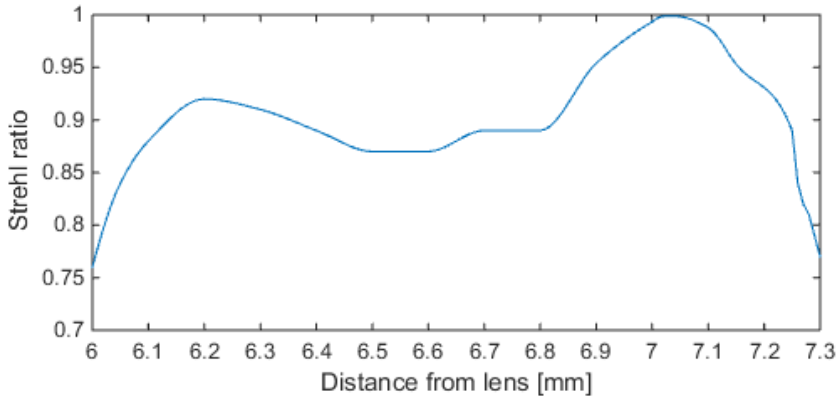

FIGURE 4.4: Simulation of Strehl ratio as a function of the cloud position in respect to the lens (for the lens 355561 from Geltech). The horizontal axis describes the distance between atoms and the flat surface of lens. The assumption is that the light emitted by the atoms is collected through the whole aperture of the lens and then focused at the image plane, the position of which is adjusted accordingly to compensate change of focal plane. Fluorescence light is diverging for distance below 6.8 mm. Data set was obtained with Zemax OpticStudio.

give us of an excellent image of atoms with Strehl Ratio above 99.7%. On the other hand, regarding the trapping light at $852\,\mathrm{nm}$ the same configurations gives a Strehl ratio about 0.8, which means that there is a contribution of spherical aberration to the trap profile. However, this is not significant and results in a spot size of the order of a micrometer ($\approx 1.4\,\mu\mathrm{m}$). Although the profile of the trap is distorted, it still benefits from a reduced depth of field because of the bigger aperture.

The conclusion is that the configuration with the new lens 355561 allows for a collimated dipole trap input beam at $852\,\mathrm{nm}$ and improves the previous experimental setup. It is convenient to adjust the dipole trap beam and also it will be easier to rebuild and change its path in the future, as the beam acting on aspherical lens is fully collimated. The alignment of the MOT will be easier because of the longer focal distance (BFL=$7.03\,\mathrm{mm}$), the dipole trap will be of a size $1.4\,\mu\mathrm{m}$, and the imaging system will collect more fluorescence light.

Moreover, a detailed analysis of this configuration states (Appendix D.2), that the position of the trap is also robust in terms of trapping beam wavelength fluctuation, as $1\,\mathrm{nm}$ difference results only in $1\,\mu\mathrm{m}$ of shift of the trap position along the optical axis. This means that normal thermal stabilization of the laser diode will be enough for stability of dipole trap position. The tolerance of the trapping beam's collimation is $\pm 56\,\mu\mathrm{rad}$, which corresponds to a shift of the trap position by $\pm 1\,\mu\mathrm{m}$. Even if the trap is misplaced, the quality of the fluorescence imaging remains very good, as the Strehl ratio is above 0.8 up to 1mm along

optical axis, as shown on Figure 4.4.

4.3 Final design of imaging system

After having studied the lens behaviour for both the trapping and imaging light, the rest of the imaging system was designed. This required routing of the fluorescence light through optical elements so that they will not introduce any additional optical aberrations and an adjustment of the optical magnification to match the camera resolution. This section describes the final set of optical components and the performance of the trapping and imaging of atoms.

4.3.1 Optical setup

In Figure 4.5 the complete optical setup for trapping and imaging is presented. The orange beam represents the dipole trapping laser, while the fluorescence light is marked in pink. The dipole trap laser is coupled to the system through a single mode optical fibre to ensure that the profile of the beam is Gaussian at the output. Then a telescope, which consist of the fibre coupler and a single lens on a XYZ translation stage, allows for a very precise alignment of the beam size and collimation before entering the vacuum chamber. Two mirrors direct the beam into the vacuum chamber through a dichroic plate and the beam enters the chamber via a viewport covered by broadband anti-reflection coating for both $780\,\mathrm{nm}$ and $850\,\mathrm{nm}$ wavelengths. The beam is tightly focused by the high numerical aperture (N.A. = 0.52) aspheric lens (Geltech 355561) which is also covered with anti-reflection coating from both sides.

The fluorescence light from the atoms is collected by the same aspheric lens (Geltech 355561), hence the optical path for fluorescence imaging and dipole trap beam overlap. The collimated fluorescence light travels through the viewport of the vacuum chamber and is reflected by the dichroic plate, which now separates the paths of the fluorescence light and dipole trap beam. Finally, the fluorescence light is focused by a large aspheric lens_1 (Asphericon 75-150LPX) with a pinhole placed in the focal plane. The role of the pinhole is to reduce stray light. Eventually the fluorescence light is focused onto the ICCD (Andor iStar 334T) camera by an aspheric lens_2 (Asphericon 50-40HPX). A 780 nm interference filter (Thorlabs FB780-10) is attached to the front of camera in order to block any undesirable light, especially residual stray light.

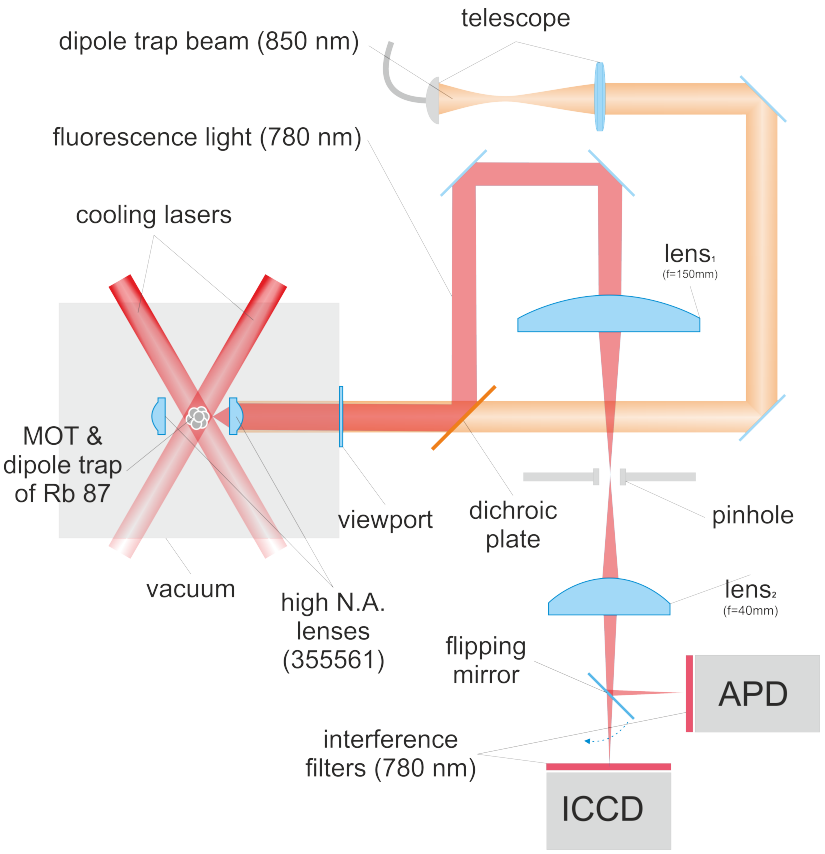

FIGURE 4.5: The optical setup for the dipole trapping with an incorporated system for atoms detection. The detailed description of the scheme is provided in the text.

The last element of the imaging system, not presented on the scheme, is a flipping mirror and the photodiode detector. The mirror allows one to easily change the final path of the fluorescence light and should be placed after the iris and before the last lens and the imaging sensor. When the flipping mirror is in place, the fluorescence light is directed onto an APD (Perkin Elmer SPCM-AQRH-12), which allows the performance of fast-timescale experiments by monitoring the photon numbers emitted by the atoms.

4.3.2 Dipole trap irradiance profile

The analysis in the previous section (see, sec. 4.2) was based on ray tracing and ray based diffraction computations, which is useful for determining parameters such as the position of the focal plane or whether the system is diffraction of aberration limited. However in the case of the dipole trap, where the trap volume depends on the irradiance profile of the laser beam near focus, it is more suitable to use diffraction-based methods to model the exact

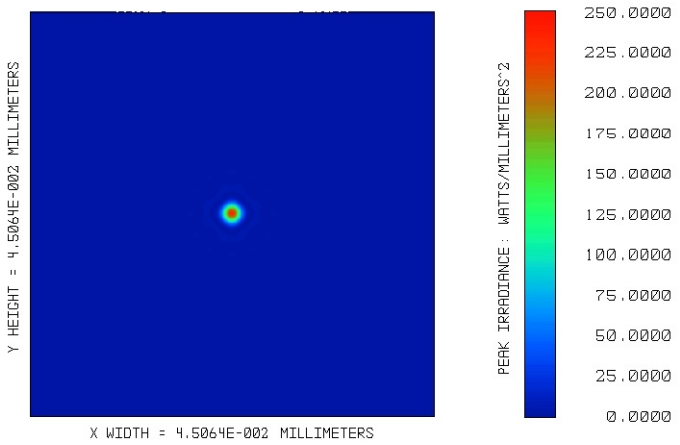

FIGURE 4.6: Physical Optics Propagation at focus surface for a collimated incident light at $852\,\mathrm{nm}$ of $1\,\mathrm{mW}$ power. Data set was obtained with Zemax OpticStudio.

beam intensity near the focus. The Zemax package provides the Physical Optics Propagation[12] tool which allows to specify the properties of a laser beam, such as its mode[13], profile, phase, waist or power, and then propagate it through the optical system. This method allows prediction of a 3D dipole trap profile by conducting a series of simulations of the Gaussian beam in the vicinity of focal plane.

Figure 4.6 presents the POP analysis of the dipole trap profile at the focus. In the simulations the initial beam is Gaussian and it is propagating along optical axis with $3.6\,\mathrm{mm}$ waist, while the maximum lens aperture is $12.5\,\mathrm{mm}$. The fundamental properties of the trap might be read out from a pilot beam description provided by POP, which corresponds to an ideal Gaussian beam based on the actual wavefront parameters. The pilot beam, which does not overlap perfectly with the real beam profile due to aberrations, is rather a guidance for the user[14] to choose the correct settings and assess the result. Table 4.2 presents the parameters for the beam propagation through the lens at the focal plane.

The beam intensity at the focal plane needs to be $248\,\mathrm{W/mm^2}$ for $852\,\mathrm{nm}$ to obtain $1\,\mathrm{mK}$ trap depth (see section 2.2.7). Table 4.2 shows that laser power of about $1\,\mathrm{mW}$ is enough to achieve this. The focal plane position was obtained by identifying the point of highest intensity, and BFL agrees up to micrometre precision for both ray tracing (see BFL in Table 4.1) and POP methods. The last three parameters relate to the pilot beam, whose waist

[12] POP uses wavefront propagation, Fresnel diffraction, to obtain the irradiance at the given point. For more details see Appendix D.1.

[13] $\mathrm{TEM_{00}}$

[14] The pilot beam is also used internally by the software to determine an appropriate algorithm for the given task.

	@852nm
input power [mW]	1
transmission [%]	99.7
peak irradiance [W/mm^2]	240
BFL [mm]	7.031
beam size [µm]	1.34
pilot beam waist [µm]	0.738
pilot beam Rayleigh length [µm]	2

TABLE 4.2: Laser intensity profile of dipole trap obtained using Physical Optics Propagation method. Input power is the total power of Gaussian beam before the lens, transmission tells us what portion of beam was transmitted through the lens, peak irradiance relates to the highest value of intensity.

was found to be about $1.5\,\mu m$ away focal plane. Here, the beam size corresponds to the size of the pilot beam at the designated focal plane, and also agrees with RMS according to Table 4.1.

Although BFL, beam size and Rayleigh length agree with the values previously predicted by ray tracing, the waist of the pilot beam deserves attention as it becomes smaller than the wavelength. Systems with a very high numerical aperture can indeed focus laser beams to sub-wavelength spot[15]. In this case POP algorithms provided by Zemax, which are based on scalar diffraction theory and which neglect the vector nature of an electric field, might give inaccurate results. The loss of POP accuracy cannot be precisely quantified and hence there is no distinct limit when POP cannot be applied. An alternative method to obtain accurate results is based on full vectorial beam propagation schemes [155–158] and takes into account the wave-like nature of light, but is unfortunately not included in the package as it is not very common problem in optics design. Fortunately, ray tracing is very accurate while simulation of beam propagation except near the focus and can handle propagation of fast beams[16] very well. Hence, in order to enhance the accuracy of the simulations, a mixed method of ray tracing and POP was used, allowing for a detailed simulation of the beam's profile near the focus.

Figure 4.7 presents detailed irradiance profile for an input beam of waist $3.8\,mm$. Gaussian fitting of the beam's profile across the optical axis at the focal plane (Figure 4.7d) gives a waist equal $\omega_f = 0.810\,\mu m$, while the expected value for the perfect thin lens would be $0.714\,\mu m$ according to (4.2). Moreover, Figure 4.7c shows that the beam's propagation along

[15]Following equation (4.2), for our system with $f = 10.03\,mm$ according to the lens's specification the estimated waist is $\omega_f = 0.714\,\mu m$.

[16]Fast beam stands here for the beam converging very quickly at the short distance.

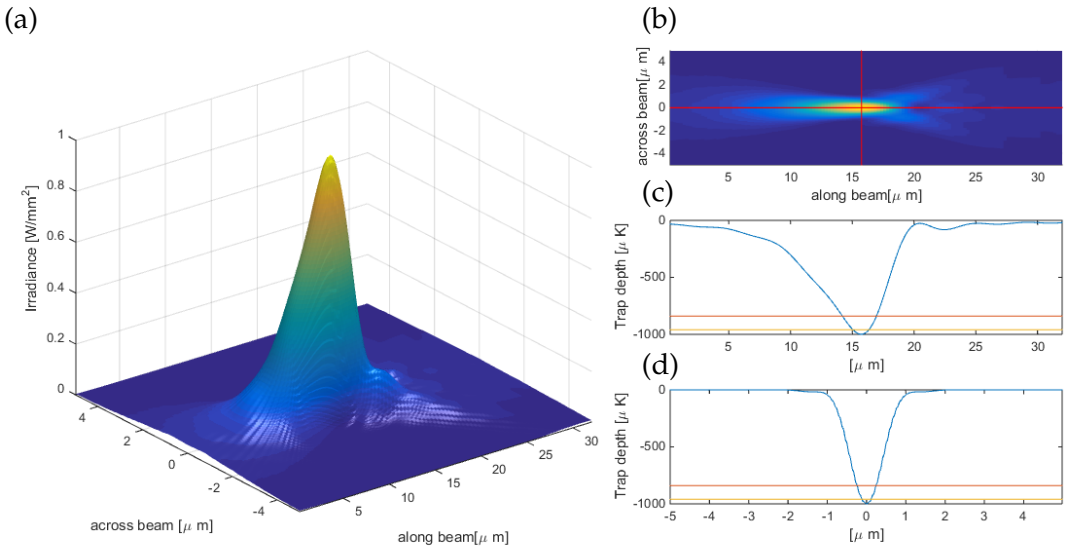

FIGURE 4.7: Simulation of dipole trap irradiance profile. (a) 3D graph presents irradiance profile along and across optical axis. (b) False color graph is the projection of 3D graph on the plane. Red horizontal line denote the optical axis of beam propagation, whereas red vertical beam corresponds to the diffraction focus. Two following graphs below display a cross section (c) along optical axis and (d) in focal plane. Additional orange and yellow horizontal lines indicate the temperature of trapped atoms at level $160\,\mu\mathrm{m}$ - orange line, and $40\,\mu\mathrm{K}$ - yellow line. Data set was obtained with Zemax OpticStudio.

the optical axis is not symmetrically Gaussian. These results suggest that the beam is distorted due to spherical aberrations, which is not unlikely to happen since the lens was not directly optimised for the dipole trapping wavelength. Therefore, the discussed profile is just an example of a possible trapping potential as it depends on the size of the input beam and the contribution of spherical aberrations. Thus, for a smaller waist of the input beam, the profile will be closer to the ideal Gaussian beam propagation, while bigger beams will show more significant distortions. Dipole trapping potential is not the only parameter which determines the volume of the trap, as it also depends on the energy of the captured atoms. The size of dipole trap was estimated for typical atoms' temperatures in the Doppler and sub-Doppler limit, assuming that atoms are localized at the centre of the trap below a given temperature, as shown on Figure 4.7c and 4.7d where yellow and orange lines denote atoms temperature. According to the simulation, the size of dipole trap is about $0.23\,\mu\mathrm{m}$ wide and $1\,\mu\mathrm{m}$ long for an ensemble with average temperature $40\,\mu\mathrm{K}$ or $0.47\,\mu\mathrm{m}$ wide and $2.5\,\mu\mathrm{m}$ long for $160\,\mu\mathrm{K}$. Although the results are very promising, the simulation might suffer out of numerical errors which are hard to estimate, so it is just an indication of what to expect and requires cross-checking with experimental methods. The volume of the trap can be tuned

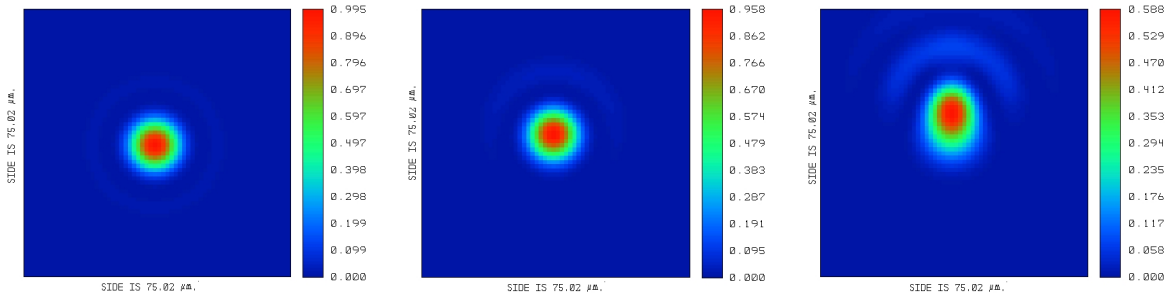

(a) On axis (b) 20 µm away (c) 60 µm away

FIGURE 4.8: Simulation of Point Spread Function for imaging system for different fields. The values on the colour bar scale correspond to the Strehl Ratio. Data set was obtained with Zemax OpticStudio.

by either changing the beam diameter or by optimizing atoms reservoir if necessary.

4.3.3 Performance of the optical imaging setup

The main challenge of the optical imaging setup is to ensure that the quality of the image is good enough to detect a single atom. In real experiments many factors might cause the misplacement of atoms in space or the deterioration of the imaging system performance. What is truly interesting for us is the knowledge of how robust the system is against these uncertainties. The analysis must take into account the influence of magnification so that it suits the camera resolution, as well as the impact of the position of optical elements and their tolerances.

By comparing the RMS radius and Airy radius it is clear that the whole imaging system is diffraction limited (diagram D.3 in the Appendix D). This means that when all of the components are perfectly aligned, the imaging system optics do not add up on aberrations. However, even the perfect imaging system experiences a blur of image at the focal plane, which is described by Point Spread Function (PSF) [17] and which needs to be taken into account while designing any optical system. Therefore, the actual spread of fluorescence light on the detector depends on the object size (trap irradiance profile and atoms temperature), PSF and obviously on the optical system magnification. Figure 4.8 presents the PSF for different fields, where fields are defined as points lying in the same plane perpendicular to the optical axis.

The system is setup to obtain a magnification ≈ 14.5 times, so that the Airy radius in the image plane becomes about $\approx 11.5\,\mu m$ as shown on Figure 4.8a. This means that light

[17] Point spread function is the response of the system for the point source.

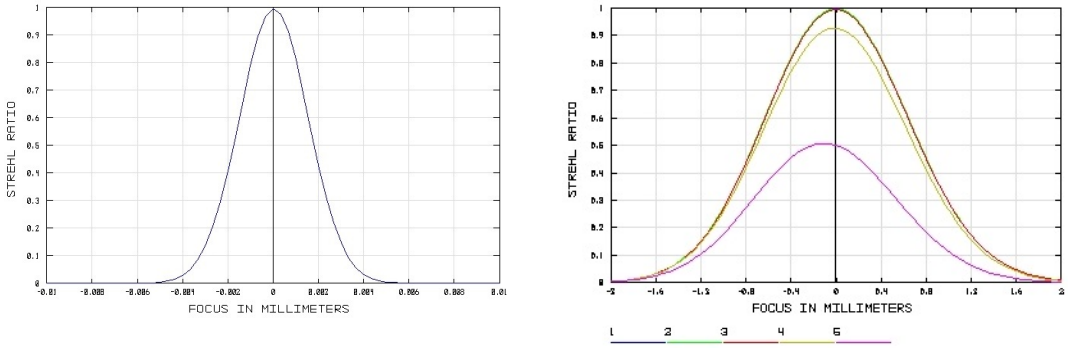

(a) Defocus in object plane (b) Defocus in image plane

FIGURE 4.9: Simulation of Strehl ratio versus defocus. Different colours denote different fields. Field 1 - on axis; 2 - 1 µm; 3 - 5 µm; 4 - 20 µm; 5 - 60 µm away from optical axis. Data set was obtained with Zemax OpticStudio.

emitted by atoms at $160\,\mu\mathrm{K}$ is imaged on a disk of diameter $\approx 29.5\,\mu\mathrm{m}$. Taking into account the size of a 2×2 binned pixel ($26\,\mu\mathrm{m} \times 26\,\mu\mathrm{m}$), and assuming that both the image disk and the binned pixel are concentric, about 91 % of the its surface receives fluorescence light. Moreover about 90 % of fluorescence light is being captured by a single pixel, while the remaining 10 % is distributed among adjacent pixels. Similarly, a magnification of 12 times results in an image disk just smaller than the pixel, and hence all the fluorescence light is captured, but more than 30 % of the pixel surface is illuminated by background stray light. For 18 times the image disk diameter is equal to pixel diagonal, which means that there is no stray light detected but about 35 % of fluorescence light is spread on adjacent pixels. Therefore, a magnification ≈ 14.5 times seems to be a good choice in terms of signal to noise ratio received by one pixel, while its two extreme values 12 and 18 times might be considered as boundaries.

The PSF results are quite promising as even $60\,\mu\mathrm{m}$ away from optical axis the Strehl Ratio remains above 0.58, as shown in Figure 4.8c. The magnification of the system mostly depends on distance between lenses 1 and 2 (see. Figure 4.5). The rough adjustment of the magnification is fairly easy, as fluorescence light is nearly collimated outside the vacuum chamber and placing the second lens in at a distance $22\,\mathrm{cm} \pm 1\,\mathrm{cm}$ results in magnification between 12 and 18 times. Moreover, mounting the lens on the micrometre translation stage, with total adjustment $2\,\mathrm{cm}$ can easily optimize the magnification in order to obtain the best contrast of the trap on the ICCD.

What deteriorates the quality of obtained image the most is the shift of the object out of focus along optical axis (so called *defocus*) if the position of the sensor is not readjusted

to compensate for this change. The Strehl ratio vs *defocus* in object and image plane are presented on Figure 4.9a and 4.9b respectively. The optical performance is considered good when the Strehl ratio is above 0.8 , which corresponds to DOF $\approx 2\,\mu\mathrm{m}$ (Figure 4.9a). It is also possible to increase the depth of field by simply reducing the aperture of the system with an iris, but this unfortunately implies losing a precious fraction of an already weak signal. Figure 4.9b shows the Strehl ratio with respect to the image plane *defocus*. It shows that the adjustment of the image plane does not require high precision, as the depth of field is approximately equal to $1\,\mathrm{mm}$.

Figure 4.10 shows the normalized Modulation Transfer Function (MTF) for the optical system, which describes the relative contrast of a periodic pattern[18] for a given resolution. It is very convenient to use MTF for experimental characterization of the imaging system, as it allows to use MTF targets, objects with well characterised spatial resolution such as ronchi grating. The spatial resolution of the target (spatial frequency) is usually given in number cycles per $1\,\mathrm{mm}$ while the contrast is a number between 0 and 1. The graph represents MTF in the image plane ($\mathrm{MTF}_{\mathrm{imag}}$), whereas to obtain the actual resolution in the object space, the magnification M needs to be taken into account. According to the graph, the highest resolvable frequency is approximately 75 cycles/mm, which corresponds to about 1000 ($75 \times 14.5 = 1087$) cycles per millimetre in the object space. This means that at best the system is able to resolve objects which are placed within $0.5\,\mu\mathrm{m}$ distance. However, this is only an upper limit of the system performance, while typically contrast is considered to be good for frequencies for which MTF values is around 0.5. Such a contrast is obtained for frequency about $34\,\mathrm{cycles/mm}$, which gives about $500\,\mathrm{cycles/mm}$ in object space. Therefore, it is safe to say that the system is capable of distinguishing two objects if the distance between them (from edge to edge) is of the order of $1\,\mu\mathrm{m}$.

Finally, the last part of the analysis, so called tolerancing, consists of the response of the imaging system to the system's imperfections. In reality, the response of the system depends on both a correct placement of the optical component, as well as on the manufacturing accuracy. In this analysis the manufacturing is omitted as it is a factor which is beyond our control. There are many components in the system, but not all of them needs to be taken into account while performing tolerance analysis. Figure 4.11 presents a simulation of the imaging system in Zemax, where surfaces are marked with numbers. A pair of surfaces,

[18] MTF is an absolute value of optical transfer function (OTF), which is a Fourier transform of the point-spread function. The diffraction MTF computation in Zemax is based upon a Fast Fourier Transform of the pupil data. The resulting MTF presents the contrast for a sine, not square, wave object of a given spatial frequency.

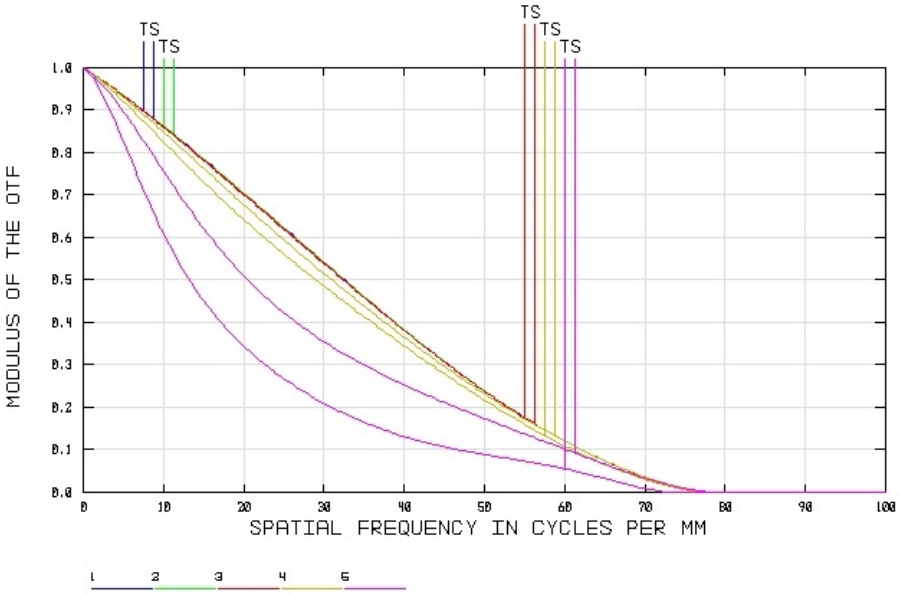

FIGURE 4.10: Simulation of Modulation Transfer Function of imaging system for objects in different fields. Field 1 - on axis; 2 - 1 µm; 3 - 5 µm; 4 - 20 µm; 5 - 60 µm away from optical axis. away from optical axis. Two lines of the same colour denotes the system response for tangential (T) and sagittal(S) directions. Data set was obtained with Zemax OpticStudio.

namely (1,2), (14, 15) and (16, 17) denote lenses, surfaces (3,4) are a viewport, while 6, 9 and 12 are mirrors. The medium in which rays propagate before the viewport is set to be vacuum, while it becomes air afterwards.

Since the performance of the system strongly depends on the magnification, it needs to be checked how it changes in terms of elements placement. What is important regarding the magnification is the distance between surfaces 15 and 16, as well the total distance between surfaces 2 and 14 since 780 nm light is slightly converging. Table 4.3 shows the tolerance on these two values and their influence on the magnification. The imaging plane is a *compensator*[19] in this case and is adjusted to obtain the minimum RMS wavefront error[20]. Looking at the table the conclusion is that it will be relatively easy to place lenses (14, 15) and (16, 17) in a good position to obtain a magnification between 12 and 18 times. The required precision is about ± 40 cm between the objective lens (1,2) and the set of lenses (14,15) and (16,17), and ± 1 cm between the lenses (14,15) and (16,17).

Another important aspect of the imaging system alignment is the system's response for

[19]The term compensator in the tolerancing analysis is used for the element of the system which is used to obtain a target performance, while other parameters of interest are changed during the analysis.

[20]RMS wavefront error is related to Strehl ratio by the formula $S = 1-\left(2\pi\frac{\delta}{\lambda}\right)$ where $\frac{\delta}{\lambda}$ denotes RMS wavefront error.

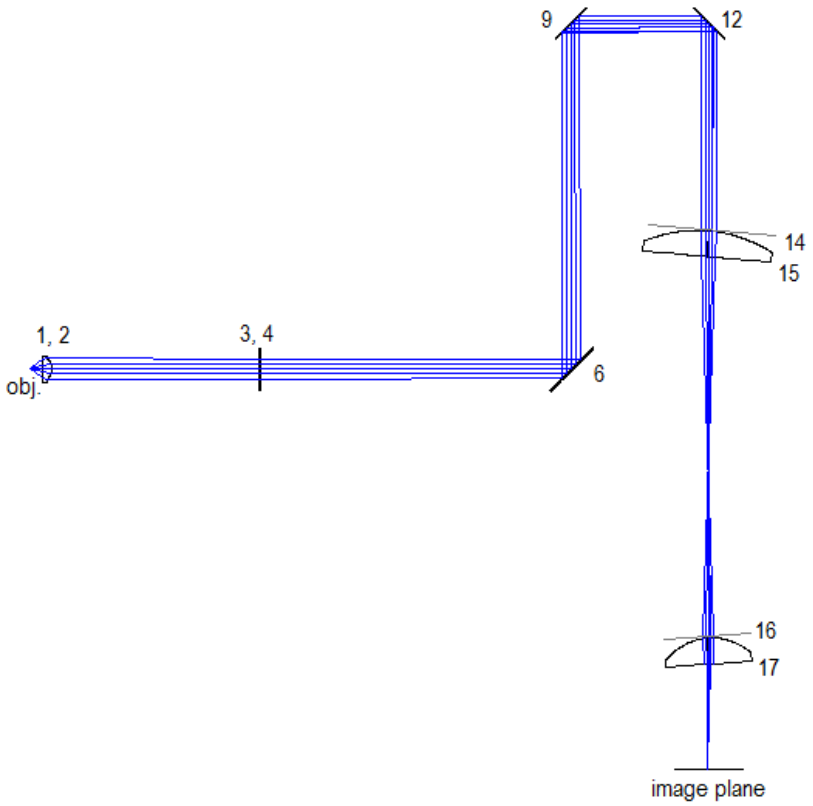

FIGURE 4.11: A scheme of imaging system with tilts and decenter for which the tolerancing procedure was performed. The tangents of the front curved surfaces of lenses (14, 15) and (16, 17) are marked as straight lines, and determinate lenses' tilts. The scheme is an output of Zemax OpticStudio.

elements' *tilts* and *decentre*. The role of mirrors 6,9 and 12 is to ensure that light acts perpendicular on the centre of the lens (14, 15) so they are irrelevant in this analysis. Moreover the viewport can be also neglected in the analysis as its tilt introduces only a shift of the fluorescence light, which in practice is being corrected by the following mirrors. A tilt of all three lenses is presented in Figure 4.11. Lenses are tilted with respect to the axis, which passes through the center of the first surface of each lens, namely surfaces 1, 14 and 16. Table 4.4 gives the tolerance analysis for lenses' tilts and decentering. A decentring of the lens (1, 2) is omitted in the analysis, because it is equivalent to the analysis of the system performance for different fields of view presented in Figure 4.8. Here the criterion was to find such values for tilt and decentre for which the Strehl ratio does not drop below 0.8. The position of the image plane is again a *compensator*.

According to the Table 4.4, even a small tilt of the first lens (1, 2) in respect to the rest of the imaging system, can decrease the system's performance. This tilt should be smaller

			criterion	min(RMS wavefront err.)
			compensator	imagine plane position
			nominal value	60.629 mm
distance	nominal value	tolerance value	MAG	compesator value [mm]
2-14	701 mm	+380 mm	17.58	58.66
		-430 mm	12.25	62.15
15-16	221 mm	+10 mm	12.33	56.09
		-10 mm	17.91	67.19

TABLE 4.3: Imaging system tolerance on elements placement and its influence on magnification.

		criterion	strehl ratio=0.8
		compensator	imagine plane position
		nominal value	$60.629\,\mathrm{mm}$
surface	tolerance type	tolerance values	compesator change [mm]
1	tilt	$\pm 0.168°$	negligible
14	tilt	$\pm 3.97°$	+0.248
14	decenter	$\pm 1.71\,\mathrm{mm}$	+0.248
16	tilt	$\pm 2.65°$	+0.176
16	decenter	$\pm 3.36\,\mathrm{mm}$	+0.280

TABLE 4.4: Influence of elements' tilts and decenter on imaging system performance.

than $0.2°$, therefore it is recognized that the mounting of this lens has to be very precise. Regarding lenses (14, 15) and (16, 17), only a significant changes decrease a Strehl ratio to 0.8. For both lenses the range of the acceptable tilt remains within $5°$, what should be easy to be controlled just using standard mounts. The system is also very robust in terms of a decenter of both lenses from the optical axis, and is of order of a few millimeters. Additionally two mirrors (surfaces 9 and 12) should also help to optimize the decenter of lens (14, 15). All imperfections listed in Table 4.4 change the position of the image plane less than $250\,\mu\mathrm{m}$ in respect to the original position ($\approx 60\,\mathrm{mm}$). It affects the quality of the image on the detector very little, since as it was shown in Figure 4.9b the Strehl ratio remains above 0.9 for $\pm 250\,\mu\mathrm{m}$ defocus.

4.4 Build-up of experimental setup. Verification of the design predictions

The design discussed in the previous section is based upon certain considerations of tolerances for the position of optical elements as well as for the degree of beam collimation. After

(a) Stand alone holders (b) Lens holders inside the chamber

FIGURE 4.12: New mounts for lenses inside vacuum chamber. (a) The holders, a detailed description can be found in the main text. (b) The holders are placed inside the vacuum chamber as described in section 3.4.1. The visible red cloud between the lenses is the MOT and the red traces are the cooling beams.

combining the designed components with the rest of the equipment, the dipole trap setup was tested to ensure that the system serves its purpose and that the optical components are correctly placed and aligned. Results of the optical performance check, especially the trapping potential and resolution of imaging system, are presented in the following section.

A key element of the new experimental setup is a new holder for the lenses inside vacuum chamber (Figure 4.12). The new holder was designed and manufactured in a way that it satisfies constrains given by both tolerance of lenses position and vacuum requirements. The material used for manufacture is stainless steel 316L, which makes the holder's construction UHV compatible while the shape of holder's body ensures stability under baking procedure. Additionally, this material has a very low magnetic permeability and hence it will not create additional stray magnetic fields inside the chamber.

The lenses are placed inside a tube (lens holder Figure 4.12a) which is threaded from inside and outside. The inside thread allows to place and fix the lenses, while the role of the outside thread is to mount and adjust the whole tube inside the holder's body. Because both the lens holder and the body are made out of the same stainless steel there is a clearance of $0.255\,\mathrm{mm}$ between two threads to avoid seizing. Eventually the position of each tube is fixed by a locking ring, which ensures stability during the baking process. Regarding the optical performance, it is important to ensure that the lenses are on the same optical axis, which was achieved by first assembling the body of the holder and then precisely drilling a slot for both of the lens holders in one go. The advantage of our holders is that it is possible to adjust the relative position of lenses simply by rotating a lens holder inside the threaded

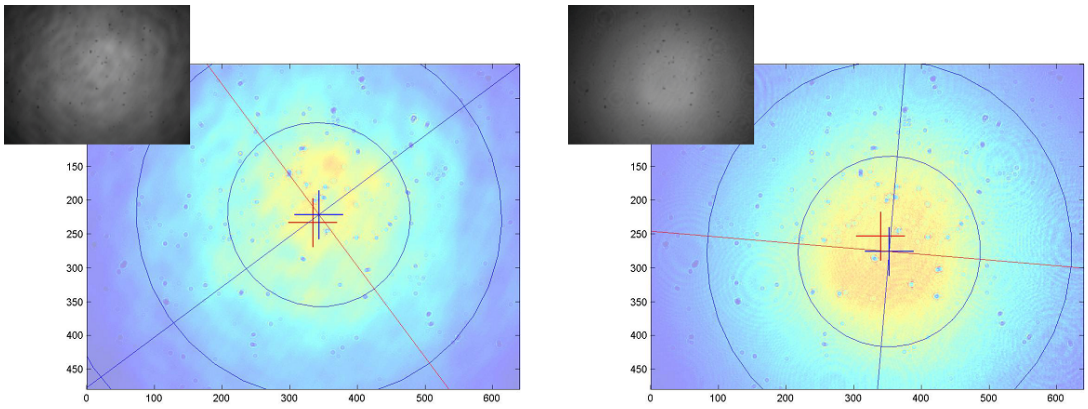

(a) Beam profile right after the telescope (b) Beam profile at the distance $1.7\,\mathrm{m}$

FIGURE 4.13: Measurement of the dipole trap beam collimation with CCD camera. Axes of the images are given in pixels, where size of each pixel is $9.9\,\mu\mathrm{m}$. The fitting is represented by ellipses where the straight red and blue lines denotes the axes of rotation. Crosses in the middle shows centre of the mass for the picture (red cross) and centre of the Gaussian fit (blue cross). Goodness of fit: $R^2 = 0.95$

slot, as a one turn results in $1\,\mathrm{mm}$ of translation along optical axis. This means that we can adjust lens position up to $\approx 30\,\mu\mathrm{m}$ per $10°$ of rotation.

4.4.1 Experiment preparation (aligning procedure)

The preparation of the system starts with the alignment and shaping of the dipole trap beam before entering vacuum chamber. The desired collimation and the size of the laser beam are achieved by adjusting the telescope (consisting of fiber coupler and the first collimation lens after the coupler). The maximum tolerance for the beam's collimation is $\pm 56\,\mu\mathrm{rad}$ to ensure that the trap position does not move along optical axis more than $\pm 1\,\mu\mathrm{m}$ according to the design. The two pictures below (Figure 4.13) present the measurement of the beam profile with CCD camera right after the telescope and $1.7\,\mathrm{m}$ further. The images were fitted with a two dimensional Gaussian. The waist of the beam is $3.8\,\mathrm{mm}$ with a collimation degree equal $-1 \pm 12\,\mu\mathrm{rad}$ taking into account the uncertainty of camera position $\pm 10\,\mathrm{cm}$ and 95% confidence bound of fitting parameters to estimate measurement error.

4.4.2 Measurement of dipole trap profile

The profile of the dipole trap beam near the focus can be measured using the trapping beam, which is sent through the windows of the vacuum chamber and both aspheric lenses. At this point of work the relative position of lenses was bigger than double of working distance,

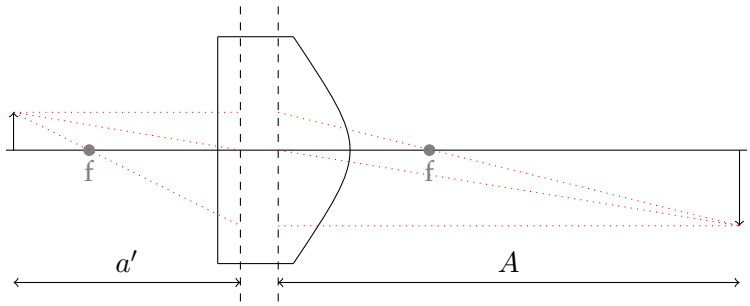

FIGURE 4.14: Dashed lines represents principal planes of a thick lens.

and hence the beam was converging after the chamber. This method allows for a quick and fairly accurate verification of the dipole trap profile based on simple geometrical optics principles. Although thick lenses behave differently than a perfect thin lenses, they might be considered as thin lenses under certain assumptions. For a thick lens, one can define the so called principal planes and a focal length f, as it is shown on Figure 4.14. Principal planes are the theoretical equivalent to the plane of an ideal thin lens. By neglecting the distance between them, the behaviour of rays might be considered with respect to principal planes in the same way, as if it was a thin lens. The focal length and the magnification M of the image can be described by the formulas:

$$\frac{1}{f} = \frac{1}{A} + \frac{1}{a'} \tag{4.5a}$$

$$M = \frac{A}{a'} \tag{4.5b}$$

where the distances of an object and its image are a' and A respectively from the principal planes.

The experiment was conducted by taking the magnified images of the beam near the focus between points P_1 and P_m at the distance $A_m = a_{off} + a_m$ after the lens P_0, where the newly introduced index m stands for the single measurement as shown in Figure 4.15a. The irradiance profiles captured by the CCD camera, which was moved along optical axis in a range of $\approx 20\,\mathrm{cm}$ are presented at Figure 4.15b. For each position of the camera, the magnification was measured using a ronchi grating illuminated by incoherent $850\,\mathrm{nm}$ light, which was placed and adjusted with micrometre precision between lenses until a sharp interference pattern was obtained.

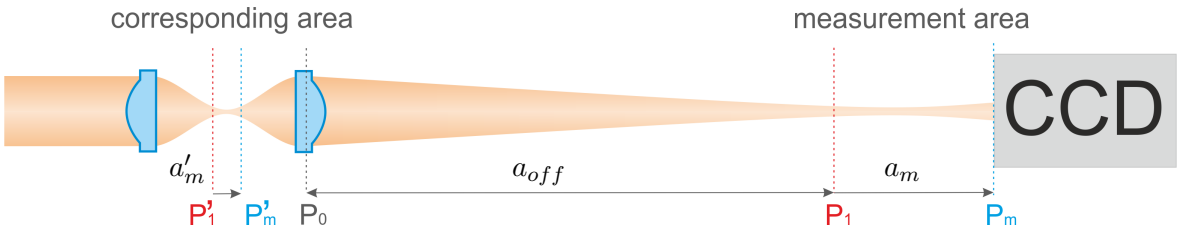

(a) A scheme of the experiment

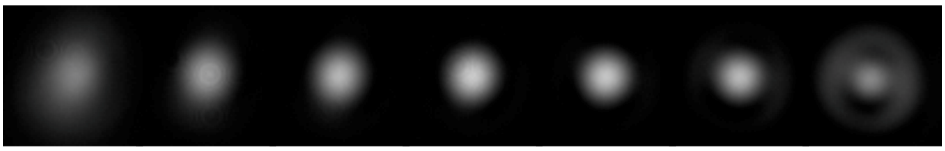

(b) Subsequent images of the beam near the focus

FIGURE 4.15: Measurements of dipole trapping beam's irradiance profile. Geometric optics is used here to estimate properties of the laser beam in planes $P'_{1,m}$ using an image of the beam in planes $P_{1,m}$, under the assumption that the system is perfect with no aberrations. (a) A scheme of the experiment. Sharp image of the object placed in plane P'_1 (P'_m) is created in P_1 (P_m) respectively, while the distance a_m in the image space corresponds to the distance a'_m in the object space. The collimated laser beam acts on a pair of high NA lenses which are in the relative distance slightly bigger than two focal lengths. Therefore, the first lens focuses the beam between planes P'_1 and P'_m and then, after P_0, the beam converges. The CCD captures the beam profiles in planes $P_{1,m}$. (b) Subsequent images of the beam between planes P_1 and P_m.

Combining (4.5) gives a relation between the magnification M_m and the total distance of the image from the lens $a_{off} + a_m$:

$$M_m = \frac{1}{f} a_m + \left(\frac{a_{off}}{f} - 1 \right) \tag{4.6}$$

Here the total distance A_m of an image from a lens was decomposed into a fixed offset value a_{off} and a variable a_m. It is wiser from an experimental point of view to measure the offset value only once and consider its uncertainty as a systematic error if the image is formed far away from the lens and the measurement points lay in close vicinity to each other ($a_{off} \gg a_m$). The accuracy of the camera positioning a_m was $\pm 0.1\,\mathrm{mm}$ and is the main contribution to the error in estimation the position in the object space. Despite a precise adjustment of ronchi grating position, the depth of view was $20\,\mu\mathrm{m}$. It leads to a great uncertainty of the single measurement, since the distance between subsequent measurements is of the order of a micrometre in object space. Hence, to minimise the error, all the experimental values of magnification M_m versus camera position a_m were fit with linear function according to (4.6), and replaced with their theoretical values. The relations (4.5b) and (4.6) allow scaling

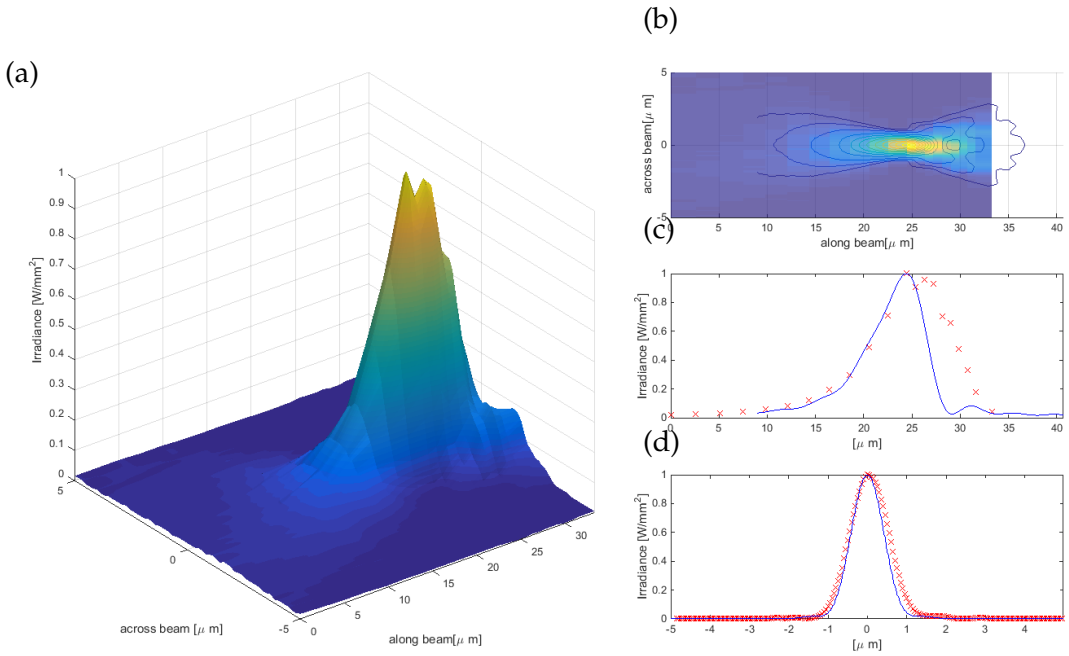

FIGURE 4.16: Experimentally measured three dimensional profile of dipole trap irradiance. (a) represents a 3D reconstruction; (b) shows the simulation data depicted as a contour plot overlapped for the experimental data; red crosses on (c) and (d) show the cross sections at the highest intensity along and perpendicular to the beam's propagation direction. The results are compared to the simulation (for the same beam waist), which is marked as blue solid lines on (c) and (d).

of the captured pictures and to translate the camera's positions a_m into the object space a'_m:

$$a'_m = \frac{a_{off} + a_{m=1}}{M_{m=1}} - \frac{a_{off} + a_m}{M_m} \tag{4.7}$$

Having pictures of beam and corresponding distances a'_m, the three dimensional irradiance profile in vicinity of beam's waist is eventually reconstructed. The result is presented in Figure 4.16, where the first figure presents the experimental data, and the second shows the contour plot of the numerical simulation produced by ZEMAX overlapped for the experimental data. It is clear that the profile obtained in the experiment is less confined that the simulation's predictions. It is difficult to assess whether the simulation was inaccurate, or whether it is just due to the experimental uncertainties.

Next, each of the images (Figure 4.15b) was fit with two-dimensional standard distribution, where outer rings were neglected as non-Gaussian profiles, especially far away from the beam focus where aberrations become significant. Results are presented inFigure 4.17, which shows the amplitude and the size of the beam's profile. It is worth noting that

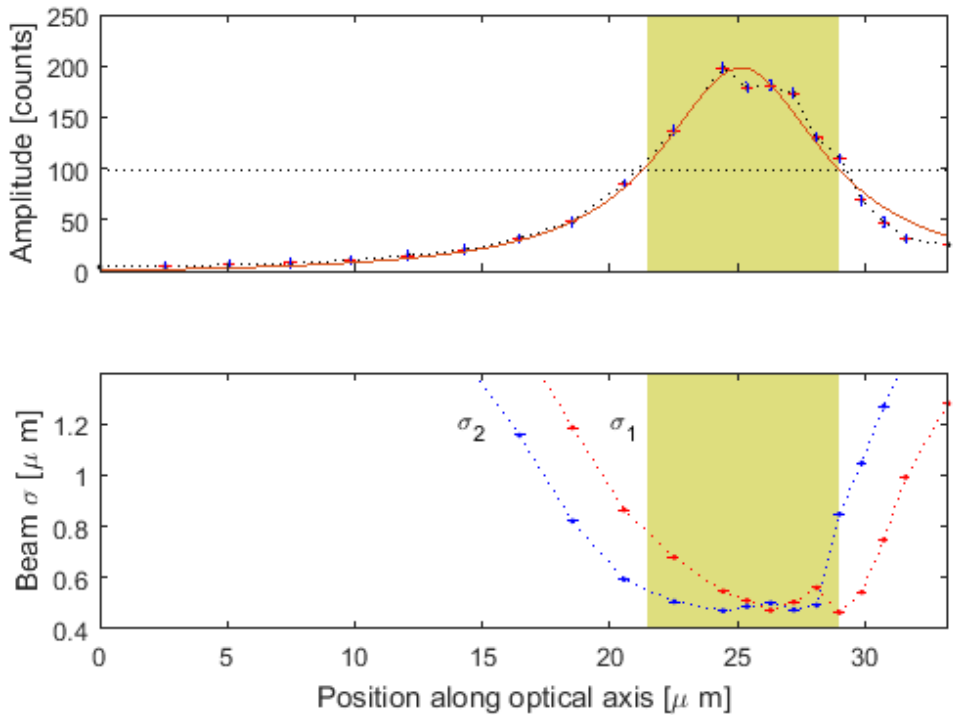

FIGURE 4.17: Dipole trap irradiance profile postprocessing data. Figure presents fitting of experimental data to standard distribution with an amplitude measured in counts and a standard deviation σ_1 and σ_2. The graph shows that the shape of the beam profile is not perfectly circular beyond the focal plane, and hence fitting results with elliptic shape described by different σ_1 and σ_2 what suggests an occurrence of coma in the optical system.

the vertical error bars are also marked on the graphs, but their values are truly negligible (they depend only on the fitting accuracy). The highest measured intensity and the corresponding beam size are marked by a dark green line. It is safe to assume that the peak of maximum intensity is somewhere in the shaded light green area which corresponds to the double of Rayleigh length as the intensity drops there by a factor of two. Hence, the beam size is $w_1 = 1.093\,\mu\text{m}$ (between $1.359\,\mu\text{m}$ to $0.945\,\mu\text{m}$) and $w_2 = 0.99\,\mu\text{m}$ (between $1.013\,\mu\text{m}$ to $0.941\,\mu\text{m}$). For such values of the waist the theoretical Raleigh length should be about $3.5\,\mu\text{m}$, but in fact according to the graph and fitting values with Lorentzian function Rayleigh length is $z_r \approx (3.91 \pm 0.25)\,\mu\text{m}$.

A number of uncertainties arise while using this method as it is obviously not a direct measurement, but the most important question is whether measurements of the beam profile in the image space are reliable to assess the beam profile in the object space. The main assumption requires the second lens to introduce very small or no aberrations. Even though

we are aware of possible beam's distortion (as the Strehl ratio for $850\,\mathrm{nm}$ is about 0.8), we still use this method as a rough estimation of dipole trap irradiance profile. There are other methods that could be employed for the dipole trap measurement, such as cutting edge knife[21] [159] or its different variations[160], which are a direct measurement of the beam size in a given plane. However both of the measurement methods, especially pinhole variation, requires a very precise equipment which we did not have. What is nice about our method is that the results show a full two dimensional beam profile, which together with a measured magnification can easily give the size of the beam with a good accuracy.

4.4.3 Performance of the imaging system

Having prepared the dipole trap beam, the next step was preparation of the imaging system. The first step was to obtain a rough alignment of the imaging optics using a *mimic* beam (see section 4.1, Figure 4.2b). Therefore, the relative lenses position was first adjusted so that the dipole trapping beam is collimated from both sides, before and after passing through the aspheric lenses. After the vacuum chamber, the dipole trap beam is guided and coupled into the optical fibre, which is used later as an output for the $780\,\mathrm{nm}$ mimic beam. This ensures, that the mimic beam (counter-propagating to the $850\,\mathrm{nm}$ beam) follows a similar path to the trapping beam, and thus can be used to mimic the trap position and to align roughly the imaging system.

When the initial alignment is done, a ronchi grating characterised by 200 lines pair per millimetre is placed between the lenses, illuminated with incoherent $780\,\mathrm{nm}$ light and adjusted to obtain a sharp image. An interference pattern (Figure 4.18a) is imaged on the CCD camera (Marlin from Allied Vision) and helps us to adjust the magnification of imaging system. The *vignetting*[22] on the image is due to the iris after the vacuum chamber, which was placed to reduce a stray light from outside the area of interest. Fitting the image using a cosine function gives us the value of magnification as 14.32. This magnification was carefully adjusted by moving the last lens before CCD ad the CCD position on translation stages.

[21] As a necessity the cutting edge knife method requires to assume a circular symmetry (e.g. Gaussian, Airy spot, Gaussian with rings) to reconstruct beam's profile.

[22] Vignetting has two meanings: it is an effect in the photography, but it is also a parameter commonly used in optical design. In optics vignetting factors describe the beam which passes through the system unobscured.

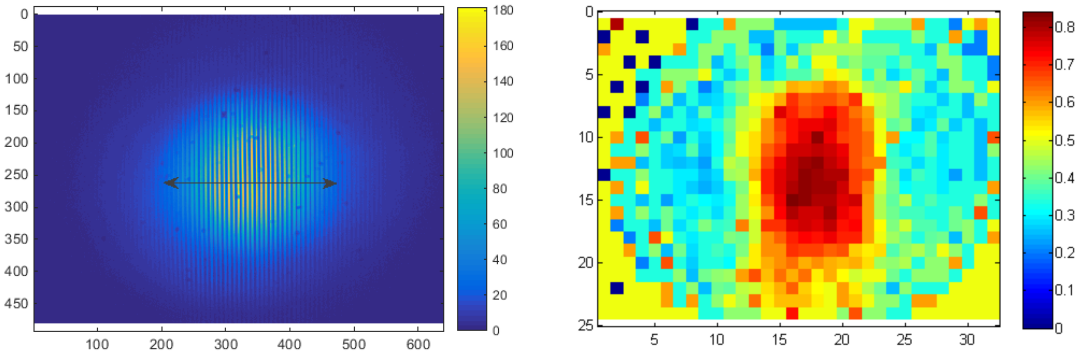

(a) Image of ronchi grating

(b) 2D MTF applied to grating

FIGURE 4.18: Experimental measurement of atoms imaging system quality. The arrow on (a) presents an approximate diameter of the image which is not influenced much by vignetting. (b) The image from (a) is divided into small 20 by 20 pixels divisions and for each of them the contrast is calculated using equation (4.8).

Having obtained a sharp image with the desired magnification, the contrast can be calculated as it is presented in Figure 4.18b. Here the contrast C is given by formula:

$$C = \frac{I_{max} - I_{min}}{I_{max} + I_{min}} \tag{4.8}$$

where I_{max} and I_{min} are respectively the signal for a bright line and signal for a dark line. Because the contrast is equivalent to the Modulation Transfer Function, the result might be compared to the simulation predictions. As we can see in the centre of the image the contrast is close to 0.8, which is in a good agreement with the model where $MTF(\frac{200}{14.32}) \approx 0.81$ (see sec: 4.3.3). Further analysis compares the quality of the image for objects lying away from optical axis. Figure 4.19 shows the measured contrast for different fields of views, and compares it to MTF predicted by the simulation. The experimental data was obtained from Figure 4.18b and the simulation points are given by averaged values of *tangential* and *sagittal*[23] MTF for the grating used in the measurement (see. Figure 4.10 for $\approx 14\,\mathrm{cycles/mm}$). Experimental results agrees with predictions very well, although close to vignetting edge they start to differ. Beyond the area marked on Figure 4.18a, the image intensity decreases and naturally the data do not describe the quality of the image accurately. The radius of the image (radius of a vignetting) is about 150 pixels, which gives about $100\,\mu\mathrm{m}$ with magnification 14.32 times and a pixel size $9.9\,\mu\mathrm{m}$.

[23]For a different field of views, two different types of MTF can be calculated. Assuming the the stripe pattern is placed in some distance from the optical axis, sagittal MTF is defined for the orientation of a stripe pattern toward the center. Tangential MTF is for the case when the pattern orientation is perpendicular to the radius connecting the optical axis and the field of view. On the optical axis sagittal and tangential MTF are equivalent.

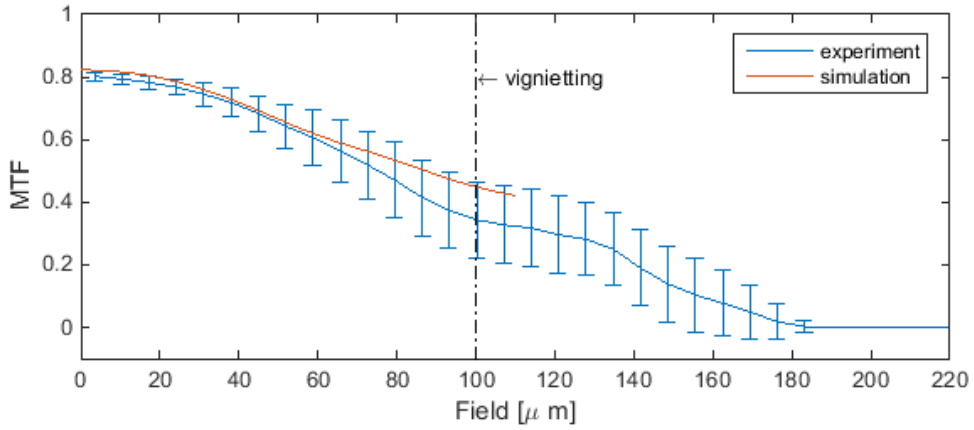

FIGURE 4.19: MTF of the adjusted imaging system for different fields of view. First a 2D MTF is applied to the grating image, and then the image is divided into a finite size concentric rings. Each point of MTF is an average of the contrast values for a subsequent ring characterised by a given distance from the centre of the image. Error bars results from the standard deviation.

4.5 The dipole trap laser system

The laser beam used for a dipole trapping is generated by a high power (up to $150\,\mathrm{mW}$), near infrared 852nm laser. The laser diode is operated in free running mode with controlled temperature to avoid significant changes in wavelength. The laser beam travels through an AOM which controls the injection of the laser beam into an optical fiber. The optical fiber guides the laser further to the chamber and the optical setup, as discussed earlier in this chapter. The optical path of the dipole trap laser beam before the fiber is presented in Figure 4.20.

An essential feature of the setup is the ability to efficiently couple and decouple the leaser beam into the optical fibre while preserving a good stability of the laser beam power. This allows a fast switch on/off of the dipole trap potential. Any unwanted fluctuations of laser power may affect the trap depth and thus impose a different Stark Shift or change in the number of trapped atoms. A crucial point in laser stability is the AOM response to an applied control signal. In order to monitor the behaviour of the dipole trap beam, a photodiode was placed at the output of optical fiber. As shown in Figure 4.21 the response of the AOM to the applied signal is not stable and consistent, and results in fluctuation of the beam intensity.

Fortunately, our experiments do not require the dipole trap beam to be switched off for a long time, just for tens of microseconds. Thus, we can keep the beam constantly on and switch it off only when needed, not to affect the stability of dipole trap. However, if we

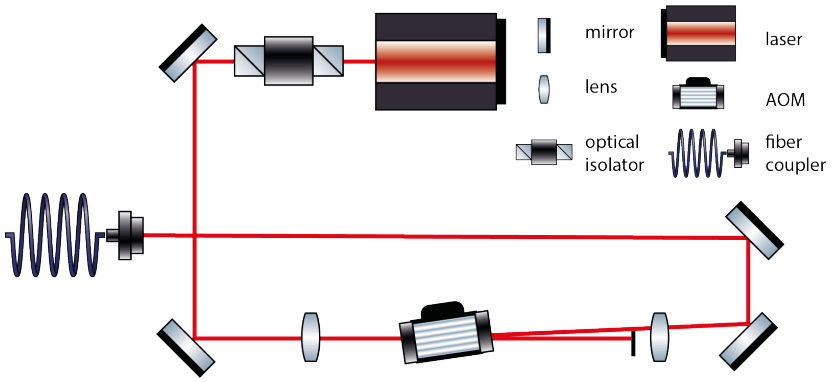

FIGURE 4.20: The dipole trap laser system. A near infrared laser (852 nm) is passing through an AOM and the first order beam is sent to the experiment. After the AOM, the beam is coupled via an optical fibre to a second part of the setup, where laser beam is directed into the vacuum chamber to form a dipole trap. The AOM, which controls the beam's coupling into the optical fibre, is controlled indirectly by LabVIEW software via a voltage control oscillator (VCO) and a voltage control attenuator (VCA).

would like to implement in the future the experimental sequence where dipole trap beam is off for longer time (hundreds of ms) an appropriate intensity stabilization should be used.

4.6 Conclusions

The analysis of the optical design shows that the requirements for dipole trapping system (see section 4.1) are satisfied, and that the new system outperforms the old setup. The distance between the lenses increased and also improved the light collection efficiency (N.A. =0.53). Thanks to the shape of the lens which was optimized for both trapping and fluorescence light, the trapping intensity profile is submicron size ($\omega_f = 0.810\,\mu\text{m}$) for a collimated input dipole trap beam, while providing very high performance of the imaging system (Strehl ratio close to unity). The imaging system magnification should be between 12 and 18 times to ensure that the majority of fluorescence light is captured by a binned pixel (2 by 2 pixels) taking into account the expected trap size and PSF of the system. The resolution should also allow the ability to distinguish two sub-micron traps in a distance of $1\,\mu\text{m}$ between them. According to the tolerancing analysis, the design is easy to be implemented. A desired magnification and adjusting the detector's position can be done if the appropriate elements, ICCD and the last lens before it (lens_2 from the Figure 4.5), are placed on translation stages.

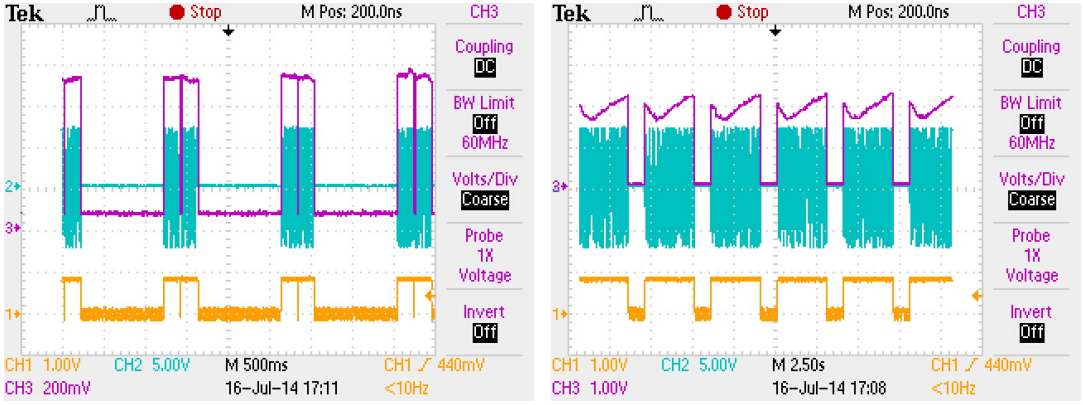

(a) AOM response for $\approx 3\,\mathrm{ms}$ change (b) AOM response for $\approx 200\,\mathrm{ms}$ change

FIGURE 4.21: Oscilloscope scan of dipole trap beam intensity while performing the experimental sequence. Yellow signal from LabVIEW controls VCA, green line is the signal directly sent to AOM, purple line is the signal recorded by photodiode.

The design was implemented following the tolerancing analysis and then experimental tests were performed. The profile of the trapping potential was verified to be close to the expected submicron size with the waist $\omega_f \approx 1\,\mu\mathrm{m}$ and the Raleigh length $z_r \approx 4\,\mu\mathrm{m}$. Regarding the optical system, the comparison between the measured and predicted MTF allowed us to confirm that the imaging system was well aligned.

Chapter 5

Dipole trap characterisation

The concept of dipole force was first proposed in 1962 [161]. Soon after that the dipole force was proposed to be used as a trapping method in [162], even before the concept of laser cooling. An experimental attempt to exploit dipole force for trapping was reported in [163], where microscopic size particles in a liquid medium were accumulated in the region of laser focus. Dipole trapping was improved later on by combining it with Doppler cooling methods resulting in trapping of neutral atoms from an atomic beam [164, 165]. But a real breakthrough came in 1986, when eventually neutral atoms from a MOT were trapped into a dipole trap for the first time [116]. Since then, the understanding of dipole trapping techniques significantly improved and many experimental methods were developed to provide traps of tens of micrometres and trap depth a of few millikelvins [166, 167]. Nowadays it is possible to achieve micrometre size of traps capable of manipulating single atoms [77–79, 168].

In this work, dipole trapping will be used as a method to create very confined, small ensemble of atoms for a DQC1 algorithm. DQC1 requires a fully operational Rydberg blockade between two traps, one providing control and one target ensemble. This means that all atoms within the traps should be localised within a blockade radius, approximately $5\,\mu\mathrm{m}$ (depending on the chosen Rydberg states, see section 2.2.4). Moreover, it is desirable to control the number of atoms loaded into the *target* dipole trap to perform and investigate the DQC1 protocol thoroughly. There is particular interest in checking its performance for just a few atoms to verify the model's prediction from [70], and to vary the number of atoms in ensemble up to 100 to proove the scaling of the model. To achieve this we also need the ability to operate the *control* trap in the collisional blockade regime [79], when only one atom at the time populates the trap. Another important issue is the timescale of the experimental sequence for the DQC1 protocol, which will last about few milliseconds. For the protocol to run successfully, atoms must not be lost during the experiment, as this would result in

loosing the information encoded in the atomic system. We therefore need to implement a trap with long lifetime: we expect a lifetime of at least $1\,\mathrm{s}$ to ensure $99\,\%$ probability of atoms survival in the trap for $10\,\mathrm{ms}$. This condition is feasible as it was shown in early studies [116, 169] where a typical dipole trap lifetime varies from $(1$ to $10)\,\mathrm{s}$.

Both the MOT's temperature and density influence the dipole trap loading [169, 170], hence an appropriate preparation of the atomic reservoir (MOT) is essential. The combination of the atoms' temperature in the dipole trap, the trap depth, and the intensity profile, are responsible for the overall atom's confinement. Regarding the intensity profile, the design of the dipole trap optical system was made with the aim of minimising the waist of the trapping beam, which is in range from $0.7\,\mu\mathrm{m}$ to a few micrometers (depending of the input beam size, section 4). Our aim is to have a trap of about $1\,\mathrm{mK}$ trap depth, which would provide efficient loading for a typical MOT temperature of 40 to $200\,\mu\mathrm{K}$. Therefore, minimising the MOT temperature before dipole trapping will in general increase the efficiency of loading and improve atoms confinement.

In fact all these three parameters are related, and the operation of the dipole trap depends on the accurate tuning of them all. This chapter discusses the implementation and characterization of the dipole trap. The first part of the chapter describes how the experiment and the imaging system were set up. The following sections provide a characterization of the dipole trap, namely its temperature, confinement, density, lifetime and collisional dynamics within the trap. Finally, data analysis and the characterization of the dipole trap quality are discussed.

5.1 Preparation of the experimental set-up

This section describes the first implementation of the dipole trap with the new optical system (section 4) and improved vacuum system (section 3.4). As discussed in section 4.4, the imaging system was set up and tested before closing the chamber. We ensured that the intensity profile of the focused dipole trap beam was purely Gaussian with the waist about $1\,\mu\mathrm{m}$ and the Rayleigh length about $4\,\mu\mathrm{m}$. The Magneto-optical trap was implemented and optimized, as it was shown in section 3.3, to provide an atomic reservoir for dipole trapping. The diagnostics of our setup showed that the typical MOT temperatures varies in range $(140$ to $500)\,\mu\mathrm{K}$ and the peak density from $(2 \times 10^8$ to $50 \times 10^8)\,\mathrm{atoms/cm^3}$. Initially we tried to

use a dipole trap beam with micrometre size, however the detection proved very challenging. Two explanations exist for this observation: either the imaging system was out of focus due to the baking procedure (some thermal expansion, chamber moved), or the fluorescence light from the trapped atoms was too low. The imaging system is robust in terms of elements displacement (see section 4.3.3) and we could verify the correct camera position using the mimic beam at $780\,\mathrm{nm}$ (Figure 4.2b). Regarding the fluorescence signal from atoms, in theory we should be able to trap and detect a single atom. However, imaging a single atom for the first time is very difficult due to the signal to noise ratio, stray light from MOT, and simply because the system had not been optimized with a real signal from atoms at this point. It could be that a very low number of atoms (limited for instance by the collisional blockade) combined with a decreased scattering rate[1] resulted with insufficient fluorescence to distinguish dipole trap from the atoms reservoir. Therefore it is reasonable to first aim to trap tens of atoms, to ensure the capabilities of the imaging system and optimize it for atoms detection. The average number of atoms in the trap is dependent on the balance between loading rate R and a mechanisms limiting the trap population. The steady state number of atoms increase with the loading rate for two distinct regimes (see section 5.4): $N_{st} \propto R$ for weak loading where collisions with the background gases plays a dominant role, and $N_{st} \propto \sqrt{R}$ when the trap population is limited by two-body collisions withing the trap. In any case, improving loading rate should clearly help.

The loading rate can be estimated through the model introduced in [169]. In this model, the loading rate is proportional to the flux of atoms through the surface which defines the trapping region, where the dipole force combined with cooling mechanism is efficient enough to capture an incident atom. Therefore, the loading rate can be described as follows:

$$R = \frac{1}{4} n_{MOT} \langle v \rangle A P_{\text{trap}} \tag{5.1}$$

where n_{MOT} is the peak density of the reservoir, $\langle v \rangle = \sqrt{\frac{k_B T_{\text{MOT}}}{m}}$ is the average velocity of atoms in the MOT, A is the effective surface area of the dipole trap and P_{trap} is the probability of atoms trapping. Since the MOT capture efficiency is limited because of experimental constrains, the value of $n_{MOT} \langle v \rangle$ could not be significantly increased (see section 3.3). The probability of trapping atoms in a dipole trap, P_{trap}, depends on the reservoir temperature,

[1] The decreased scattering rate is due to the energy shifts in the atomic structure of an atom placed in a dipole trap, see section 2.2.7. The Stark shift and the corresponding decrease of the scattering rate is measured in section 5.3.

the trapping potential and the MOT viscosity as defined in [171]. By increasing the trap depth, one can trap atoms of the higher temperature. However, the bigger the trap depth the bigger the energy shift resulting in weaker cooling and hence lower viscosity. Although varying the trap's depth might help to balance these two mechanisms, in our case when the available range of the trap depth was $(1 \text{ to } 6)\,\mathrm{mK}$, it was perhaps too small to significantly improve loading.

Hence, atom loading was improved through the adjustment of the effective size of the dipole trap A. Since the dipole trap is much smaller than the MOT, the effective surface area can be estimated by the ellipsoid surrounding the space, $A = \frac{4}{3}\pi r_{eff}^2 z_{eff}$, where the the dipole trap potential U_{pot} becomes significant compared to the reservoir's temperature $k_B T_{\mathrm{MOT}} = U_c$. Setting up the condition $U_c = U_{pot}\frac{\omega_0^2}{w(z)^2}\exp(-\frac{2r^2}{\omega(z)^2})$ for a Gaussian dipole trap beam, one can find that

$$r_{eff} = \omega_0\sqrt{\frac{1}{2}\ln\left(\frac{U_{pot}}{U_c}\right)} \quad z = 0 \tag{5.2a}$$

$$z_{eff} = z_R\sqrt{\frac{U_{pot}}{U_c} - 1} \qquad r = 0. \tag{5.2b}$$

As the equations shows, the semi-principal axes of the ellipsoid are directly proportional to the waist and Raleigh length of the trapping beam. Therefore, to overcome the difficulty with the loading and capture sufficient number of atoms a larger volume dipole trap, defined by bigger ω_0 and z_R, had been setup as described in following section.

5.1.1 Adjustment of the dipole trap profile

By adjusting the size of the laser beam acting on the objective lens and providing the necessary power, a wider trap of $1\,\mathrm{mK}$ trap depth could be achieved. The need for higher power obliged us to bypass the optical fiber, thus compromising the spacial profile of the beam. The beam was clearly not Gaussian before the vacuum chamber, as it was converging along one axis while slightly diverging along the other, resulting in non-circular beam profile with the averaged waist was about $1.8\,\mathrm{mm}$ just before the chamber.

The intensity profile of the new trap has been characterised using a method similar to the one presented in section 4.4.2. A thin lens was placed after the chamber to focus the dipole trap beam on the CCD. Then, a series of images was acquired, which were used to reconstruct the 3D irradiance profile using principles of geometrical optics. Results are presented

in Figure 5.1a. According to these measurement the beam's «waists»[2] are (6.14 ± 0.54) µm

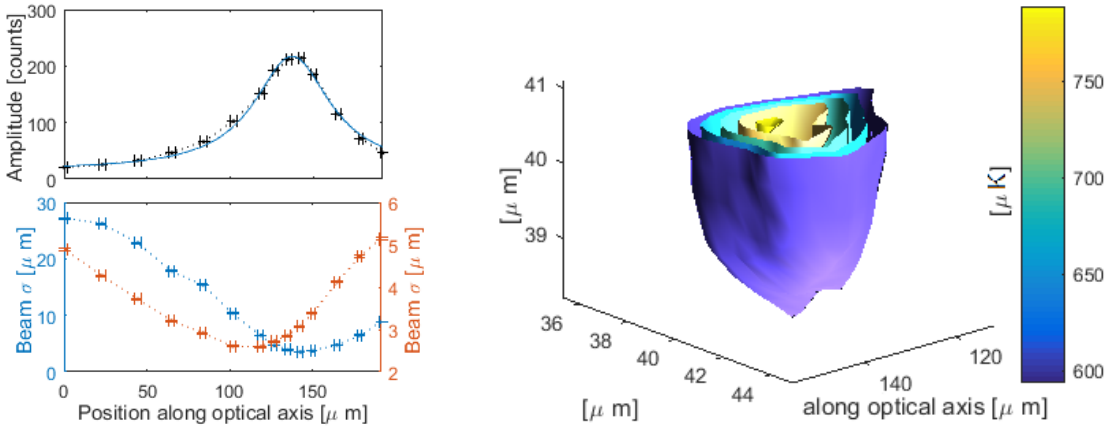

(a) The irradiance profile

(b) 3D irradiance potential

FIGURE 5.1: The representation of the results of measurement irradiance profile of dipole trap beam near focus. (a) Each of images was fitted with a 2D Gaussian function. The upper plot represents the amplitude along the optical axis, with the fit to the Lorentzian function where half-width at half-maximum defines *Rayleigh length*. The bottom plot shows the parameters of Gaussian fitting, where $2\sigma = \omega$. (b) 3D equipotential surfaces corresponding to the estimated trap depth.

and (7.01 ± 0.54) µm with (27.9 ± 1.5) µm «Rayleigh length»[3].

The trap depth can be estimated from equation (2.29) having the irradiance profile of the beam and knowing the power of the laser (130 mW) as:

$$\frac{U_{dip}}{k_B} = (662 \pm 109)\,\mu\text{K}$$

and the corresponding energy shift (see section 2.2.7):

$$\delta\left(5^2S_{1/2}\right) = 2\pi(13.8 \pm 2.3)\,\text{MHz} \tag{5.3}$$

A reconstructed 3-D profile of the trap potential is shown in section 5.1b. Assuming a temperature of 250 µK for the atoms, as measured later in section 5.2.3, the atoms' cloud size is estimated to be $\sigma_1 = (3.42 \pm 0.25)\,\mu\text{m}$ and $\sigma_2 = (2.99 \pm 0.25)\,\mu\text{m}$ and along the optical axis $\sigma_3 = (21.7 \pm 2.2)\,\mu\text{m}$. These values will be compared later on with atoms' imaging measurements.

[2]Here $\omega = 2\sigma$, where σ is a standard deviation of the fitted Gaussian function. The term «waist» It is not strictly a waist in a sense of the Gaussian beam propagation.

[3]Even though the beam is not Gaussian, since a corresponding Rayleigh length to 6 µm waist should be approximately 133 µm, a term «Rayleigh length» is used here as distance at which beams intensity drops twice. Therefore, the half-width at half-maximum from Figure 5.1b designates «Rayleigh length»

The last important set of parameters which will be highlighted in the next sections is the energy shift of the hyperfine structure $\left|5^2P_{3/2}, F = 3, m_F\right\rangle$ due to the ac Stark shift. Because of the π polarization of the dipole trapping beam, magnetic sublevels undergo energy shifts according to equation (2.32) as follows:

$$\delta\left(5^2P_{3/2}, F = 3, m_F = \pm 0\right) = 2\pi(-7.6 \pm 1.2)\,\mathrm{MHz} \tag{5.4a}$$

$$\delta\left(5^2P_{3/2}, F = 3, m_F = \pm 1\right) = 2\pi(-6.7 \pm 1.1)\,\mathrm{MHz} \tag{5.4b}$$

$$\delta\left(5^2P_{3/2}, F = 3, m_F = \pm 2\right) = 2\pi(-4.2 \pm 0.7)\,\mathrm{MHz} \tag{5.4c}$$

5.1.2 Dipole trap detection

Assuming a $250\,\mu\mathrm{K}$ MOT temperature and $1\,\mathrm{mK}$ trap depth, the effective surface of the first trapping attempt was approximately $A_{\omega\approx 1} \approx 55\,\mu\mathrm{m}^2$, while it is approximately $1700\,\mu\mathrm{m}^2$ for the bigger trap. This increased the loading rate approximately by a factor 30, and the first signal from dipole trapped atoms could be obtained Figure 5.2. The fluorescence signal from both dipole trap and MOT atoms, which are in the scope of the imaging system, is captured by the CCD. The first detection of the dipole trap was obtained in continuous mode, with the trap continuously loading from the MOT, for a long exposure time $0.3\,\mathrm{s}$. Visible vignetting is due to the aperture of the objective lens, with the radius of about $190\,\mu\mathrm{m}$.Although the dipole trap seems to be well detected in Figure 5.2, the imaging system still needs to be better adjusted to enhance the signal to noise ratio. Image acquisition and camera operating modes will be discussed in the following section.

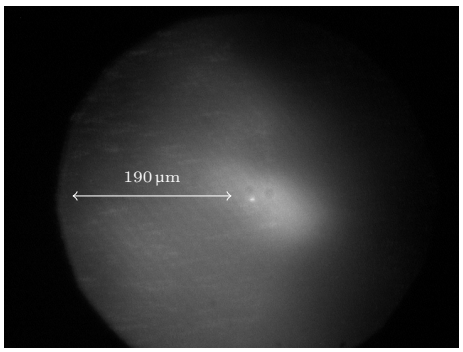

FIGURE 5.2: Fluorescence signal of MOT and dipole trap detected by dipole trapping imaging system. The bright spot in the middle is the dipole trap, while the haze comes from the stray light emitted by atoms in MOT.

5.1.3 Atoms detection

A detection of the atoms in the dipole trap requires to understand in detail how the imaging system works, especially the capabilities and settings of the detector. This section covers two main topics: how to estimate the number of trapped atoms from the detected signal, and how to optimise the signal to noise ratio so that the atoms can be detected efficiently.

Conversion of the fluorescence signal into number of atoms

Atoms from the dipole trap can be detected using the fluorescence imaging technique explained in section 3.3.1. However, due to the presence of the ac Stark shift caused by the dipole trap beam, the scattering rate per atom is reduced inside the dipole trap. The imaging system described in section 4.3 allows the collection of the fluorescence light and guides it to the detector (ICCD). The amount of photons reaching the ICCD is equal

$$N_{\text{photons}} = N_{\text{atoms}} R_{sc} \kappa \tag{5.5}$$

where and R_{sc} is a scattering rate (see equation (2.24)), N_{atoms} is the number of atoms in the trap, and κ is represents the loss of the signal through the optics. The loss rate κ depends on the collection efficiency of the objective lens (14%), the transmissivity through the objective lens coated (90%), losses on the imaging system lenses and mirrors (10%), and eventually losses on the $780\,\text{nm}$ interference filter 50%.

The next step is the conversion of the digital signal from the ICCD to the number of photons which reached the camera. The intensified CCD camera consists of a standard CCD and an analogue intensifier placed before it Figure 5.3a. When light is coming through the input window, photons hit the photocathode, which converts light into photoelectrons. Single photoelectrons are converted into a cloud of electrons by a microchannel plate (MCP) as shown on Figure 5.3b. The cloud of electrons acts on the fluorescence screen, which emits far more light than initially, and the intensified light is finally collected by the CCD. In order to correctly interpret the image given by the ICCD camera the number of photons may be estimated by formula:

$$N_{\text{photons}} = \frac{N_{counts}\text{PAG}}{\gamma_0 \gamma_1 \eta} \tag{5.6}$$

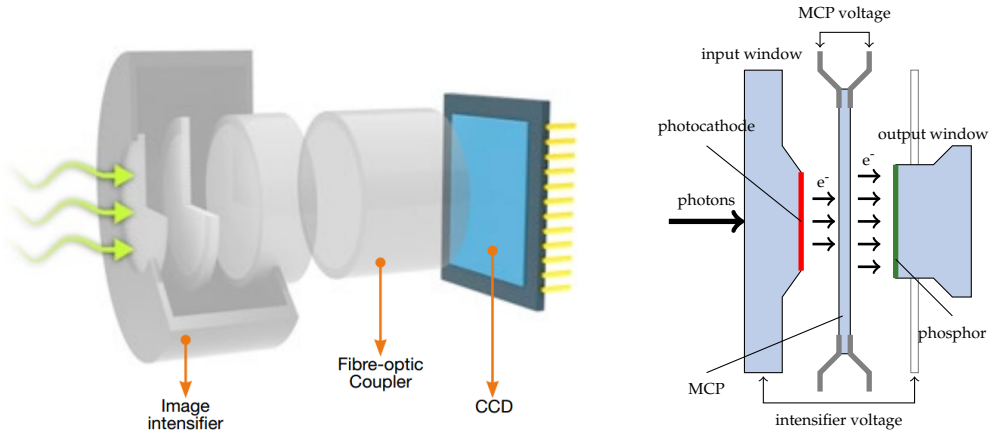

(a) General scheme of ICCD (b) Intensifier

FIGURE 5.3: Diagram of ICCD camera components. (a) Source: Andor Manual. (b) MCP voltage activates the avalanche of electrons and enhances the initial signal. The intensifier voltage allows for a flow of electrons from a photocathode toward the phosphor screen. This voltage can be used as an optical shutter: no signal is transferred through the intensifier when it is set to 0.

where N_{counts} denotes number of counts recorded by camera, η is the quantum efficiency of the photocathode, γ_0 is the Minimum System Gain, γ_1 is the relative gain of the system and PAG determines the sensitivity of the analogue to digital converter which depends on the readout settings. Since these values differ for different operating settings, the values used for the conversion from digital counts into the number of photons and corresponding ICCD specs are in appendix E.1 .

Image acquisition

The detection of a weak signal is challenging, therefore optimization of the ICCD settings is necessary. The signal obtained from the dipole trap atoms is first optimised via the optical system alignment, to increase the fraction of light reaching the detector. This is done by adjusting the position of the ICCD using the translation stage on which the camera is mounted. Movement of the camera by $50\,\mu\text{m}$ in the image space results, on average, in the change of the focus position of $0.5\,\mu\text{m}$ micrometre in the object space, as shown in Figure 5.4. Taking into account the feasible placement of the ICCD, which is restricted by mounts, the maximum range at which the camera can be focused is $(6.9 \text{ to } 7.4)\,\text{mm}$ in the object space and corresponds to $(22.9 \text{ to } 4.1)\,\text{cm}$ in image space.

The next step is the optimisation of the image acquisition, achieved by reducing the contribution to noise of the detector itself. Typical sources of noise and their values for the ICCD

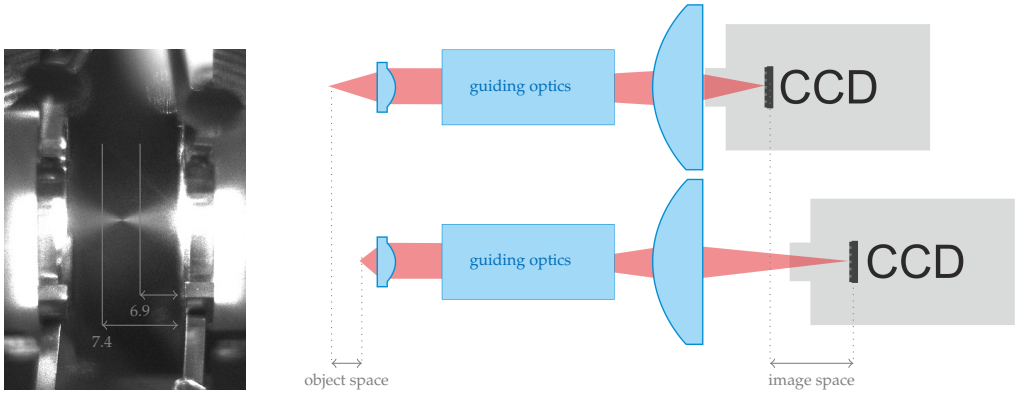

FIGURE 5.4: Optimization of ICCD position using dipole trap light. Left image represents the scope of imaging system focus shown in respect to the feasible placement of the CCD.

are listed and explained in appendix E.2. According to the appendix, the CCD needs to be kept at sub-ambient temperatures (usually $-20\,°C$), and with the slowest available readout rate $50\,kHz$. The gating mode, controlled by applying the intensifier voltage marked in Figure 5.3, also impacts the total noise significantly. If the intensifier is constantly switched on regardless of when the acquisition occurs, the CCD chip is continously exposed to light. To ensure that only the desired signal is captured by CCD (and hence decrease any stray light), it is good to exploit the intensifier as an optical shutter[4]. The following sections describe the measurements for the dipole trap characterization, and the specific settings of acquisition for the ICCD camera are listed in details in appendix E.3 for each measurement.

Some techniques used to determine the trap properties require very short pulses of microsecond scale, therefore it is important to take into account any delays in the apparatus response while acquiring the signal. When the ICCD is triggered from the computer controlling the experiment, it starts the acquisition with a certain delay which depends on the readout rate settings. Most importantly, while repeating the experiment many times, the delay is not always the same and varies in time, due to a mismatch between the internal ICCD clock and the experimental sequence. The response of other components, such as AOMs, switching on/off the dipole trap, also need to be taken into account. Typical values of the ICCD delay and the apparatus response are listed in appendix E.4. It is important to ensure that these delays are taken into account while designing the experimental sequence.

[4]Using an intensifier as an optical shutter means, that for for no voltage applied on the intensifier no signal is detected on the CCD (see Figure 5.3b). The most commonly used setting in our experiment is so called *fire only* mode. This means that the intensifier is switched on only when acquiring the signal by the CCD chip.

5.2 Temperature measurement

The very first important trap parameter to be verified is the temperature of the atomic ensemble. The confinement volume depends both on the shape of the trapping potential and the atoms distribution within the trap, which is dependent on the temperature. The *Time of Flight* method had been used in this section to measure the temperature.

5.2.1 Atoms thermalisation

The distribution of atoms in a dipole trap has been thoroughly studied in [172]. For high temperatures, classical kinetic motion of diluted gas is suitable for the description of the dynamics, and the initial energy distribution can be described by a Boltzmann distribution. For a finite trap potential U_{dip}, atoms whose initial energy exceeds the trapping potential are instantly lost from the trap. This implies that the phase-space distribution is a truncated Boltzmann distribution, where $\theta(U_{dip} - E)$ is the Heaviside step function:

$$f(E) = \exp(-\frac{E}{k_B T})\theta(U_{dip} - E).$$

On the other hand, the density of states can be expressed using eigenenergies of the harmonic potential, which gives the simple expression

$$D_s(E) = \frac{(E - U_{dip})^2}{2\hbar^3 \omega_x \omega_y \omega_z}$$

where the density of states $D_s(E)$ denotes here all possible values in phase-space for which the energy E can be obtained. The total number of atoms within the trap

$$N = \int D_s(E) f(E) dE,$$

can be calculated as the integral over all energies of the the phase-space distribution and the density states. For temperatures higher than the trap depth a significant part of the distribution has higher energy than the dipole potential and thus some atoms are lost from the trap instantly. The remaining atoms within the trap exchange their energy during elastic collisions, aiming to an even redistribution of energies. As a result, the temperature decreases until it reaches an equilibrium state, providing that there is no additional loading of new hot atoms into the trap. It has been found that the process usually thermalizes when

$k_B T \approx 0.1 U_0$ [166]. In this case the truncated tail of the Boltzmann distribution is negligible, which means that the trapping potential can be treated as if it was infinite. Therefore, the integration of phase-space distribution over momentum states leads to the density distribution

$$n = n_0 \exp\left(-\frac{U_{dip}(\mathbf{r})}{K_B T}\right)$$

where n_0 is the particle density at the minimum of the trap and T can be interpreted as the thermodynamic temperature of the system. Since the dipole trapping potential U_{dip} is approximately harmonic at the center of the trap, the density distribution takes a form of a Gaussian

$$n = n_0 \exp\left(-\frac{m(\omega_x^2 x^2 + \omega_y^2 y^2 + \omega_z^2 z^2)}{k_B T}\right).$$

5.2.2 Temperature of atoms in the dipole trap

Similarly to the MOT diagnostics section 3.3, the temperature of the dipole traps can be measured using release-recapture and time of flight (TOF) [120] [173]. These methods are well documented and understood when it comes to the temperature measurement of a large ensemble of atoms, where the spatial distribution of the atomic cloud is Gaussian,

$$n(\mathbf{r}) = \frac{1}{(2\pi)^{3/2}\sigma_x\sigma_y\sigma_z} \exp\left(-\frac{x^2}{2\sigma_x^2} - \frac{y^2}{2\sigma_y^2} - \frac{z^2}{2\sigma_z^2}\right)$$

and the velocity distribution is described by Maxwell distribution

$$f(v_i) = \sqrt{\frac{m}{2\pi k_B T_i}} \exp\left(-\frac{m v_i^2}{2 k_B T_i}\right).$$

Here σ_i is the width of the cloud and i stands for different coordinates. The cloud which is released from the trap starts a homogeneous expansion, and its size increases following the equation:

$$\sigma_i(t) = \sqrt{\sigma_{0,i}^2 + \frac{k_B T_i}{m} t^2} \tag{5.7}$$

where $\sigma_{0,i}$ is the initial size of the cloud before the expansion. For TOF experiments, the atoms are released from the trap for a variable time t during which they are expanding. After this time an image is taken, from which the spatial distribution of the cloud can be resolved and hence providing a value for T_i.

However, in the case of dipole traps it might be conceptually inaccurate to talk about a temperature of a single or just a few atoms in the trap. As it was shown in section 5.2.1, the spatial distribution of the atomic cloud is indeed Gaussian, but the velocity distribution is clearly not Maxwellian. Nonetheless, as it was shown in [174] by repeating the temperature measurement many times for a trap filled with small number of atoms, and by collecting sufficiently large statistics, the acquired results represent a velocity distribution similar to the one discussed above. Following this principle, the temperature of very small ensembles was measured in [174] (both methods), and in [144] (TOF).

5.2.3 Experiment and results

The experiment presented in this section is based on the TOF method, assuming that by taking many measurement and averaging the results the outcome will agree with the concepts described in section 5.2.2.

Sequence

The experimental sequence for a TOF measurement is presented in Figure 5.5. There are two variants of the experiment presented here. The option shown in Figure 5.5a represents the sequence for measurements of atomic cloud expansion for variable time dt. The second variant shown in Figure 5.5b consists of the similar sequence apart from switching off dipole trap, thus not allowing for the free expansion of atoms. This sequence provides the initial size of the cloud before expansion, and gives additional valuable information about the trap depth which is discussed further in section 5.3.1.

In our measurement the dipole trap is loaded from the MOT, therefore the first stage of the sequence consists the loading of a sufficient reservoir of atoms. The «MOT loading» (see Figure 5.5) stage needs to be long enough to allow the MOT to fully load, until it reaches its equilibrium state. For the MOT characteristic loading time (see τ section 3.4.2) about $4\,\mathrm{s}$, the loading stage was set up to last $8\,\mathrm{s}$ to ensure that both MOT and the dipole trap could be efficiently loaded. The detuning of the cooling beams from the atomic transition is 2Γ and the beams intensity is $I \approx 15.3\,\mathrm{mW/cm^2}$. The MOT is switched off for $10\,\mathrm{ms}$ during the «off» stage, while keeping the dipole trap on, to ensure that all atoms that are not trapped in the dipole trap have the time to escape the region and do not contribute to the measured signal. The $10\,\mathrm{ms}$ timing was chosen by measuring the fluorescence decay for the MOT, which is presented in section 5.4.2. After the removal of the MOT atoms, the

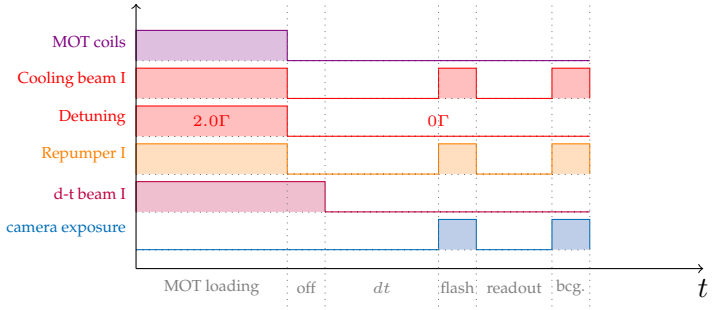

(a) Sequence variant for measurement of the cloud expansion

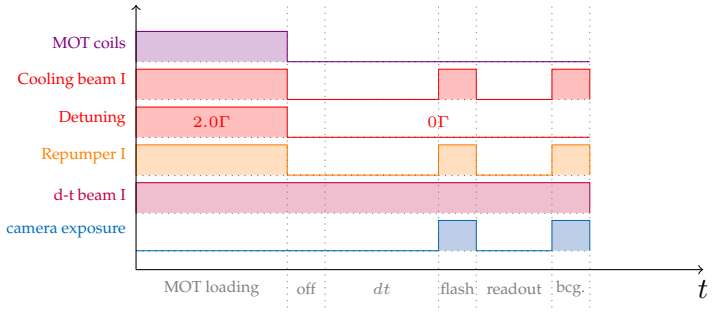

(b) Sequence variant for measurement of the atoms in the dipole trap

FIGURE 5.5: The experimental sequence for the Time-of-Flight measurement. The different stages marked under the time axis are: **MOT loading**= $8\,\mathrm{s}$, **off**= $10\,\mathrm{ms}$, **dt**= variable time, **flash**= $50\,\mu\mathrm{s}$, **cam. ref.** = $1.4\,\mathrm{s}$, **bcg.** = $1\,\mathrm{ms}$. Events/settings and corresponding values in the figure are: **MOT coils** - current applied to the anti-Helmholtz coils $(0$ to $3.5)\,\mathrm{A}$, **Cooling beam I** - the total intensity of the cooling beams $(0$ to $15.3)\,\mathrm{mW/cm^2}$, **Detuning** - the detuning of the cooling beam from the cooling transition 0 to 2Γ, **Repumper I** - intensity of the repumper beam $(0$ to $2)\,\mathrm{mW}$, **d-t beam I** - intensity of the dipole trap beam $(0$ to $130)\,\mathrm{mW}$, **camera exposure** - the exposure time when the ICCD acquires the signal.

dipole trap beam is switched off and the atoms start an expansion. Then, after a time dt, the probe beams are switched on to enable an acquisition of the fluorescence signal («flash» stage). The probe beams (cooling and repumper lasers) provide a resonant quick flash with intensity of cooling beams equal $I \approx 15.3\,\mathrm{mW/cm^2}$.

The last two stages are needed to acquire a background signal, which is used to remove the contribution of stray light in data processing. The «readout» stage stands for the read-out and preparation time for the ICCD (for the setting used in the experiment time $1.4\,\mathrm{s}$ is enough). The background image is taken with the probe beams on, but with no atoms during «bcg.» stage. The sequence discussed here is simplified, while the detailed sequence considering camera triggering and equipment delays is discussed in appendix F.

Noise analysis

The acquisition settings, which are specified in appendix E.3, were chosen to minimise the noise generated by the camera (described in more detail in appendix E.2.1). Even then, the signal to noise ratio (SNR) is poor for a single cycle of the experiment, shown in Figure 5.6a and 5.6b. The comparison between these images shows that the noise originating from stray light (see appendix E.2.2) is almost as strong as the original signal from atoms. Therefore, for a single acquisition it is impossible to distinguish the signal originating from the atoms from the noise due to the scattered MOT beams. However, taking many cycles and averaging them shows a Gaussian distribution of atoms on Figure 5.6c.

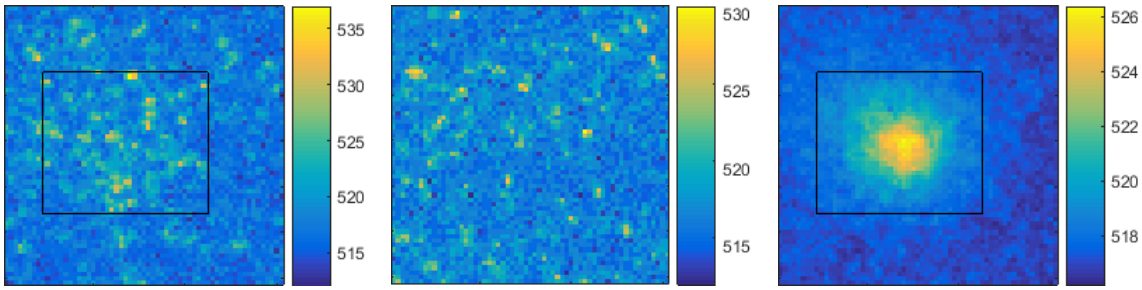

(a) Image of «flash» stage (b) Image of «bcg.» stage (c) Averaged «flash» images

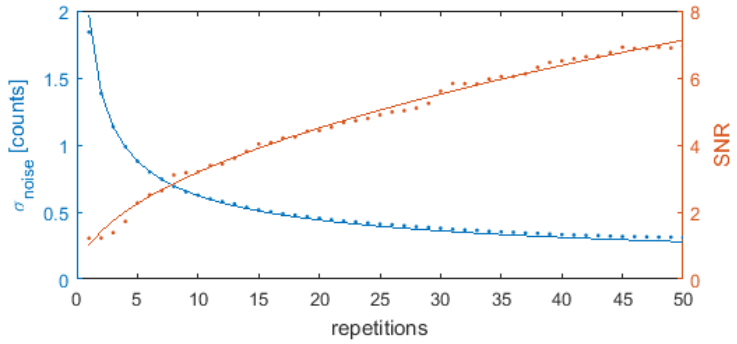

(d) Noise σ_{noise} and signal to noise ratio SNR for data represented in (a-c)

FIGURE 5.6: The analysis of noise and signal to noise ratio for the Time of Flight experiment for $dt = 10\,\mu\text{s}$. (a) An image of a single acquisition of atoms. (b) The corresponding background image taken in the same cycle as (a). Bright spots are the noise generated by stray light. (c) The image of atoms averaged over 50 cycles. (d) The graph showing the dependence of the noise and signal to noise ratio on the number of repetitions. Dots represent values of noise and SNR for the accumulation of frames. Solid lines are theoretical fits to $\frac{\langle\sigma_{\text{noise}}\rangle}{\sqrt{\text{repetitions}}}$ and $\langle\text{SNR}\rangle\sqrt{\text{repetitions}}$, where $\langle\sigma_{\text{noise}}\rangle$ and $\langle\text{SNR}\rangle$ are fitting parameters.

For a single repetition of the sequence, the signal[5] to noise[6] ratio is close to unity as shown on Figure 5.6d. Increasing the number of repetitions decreases the noise and thus enhances signal to noise ratio proportionally to the square root of the number of repetitions. For 50 cycles, SNR is about seven times higher than initially, which is sufficient to provide a clear signal for data analysis.

Data analysis

The background corrected images of the cloud expansion for dt in range $(25 \text{ to } 95)\,\mu\text{s}$ are presented in Figure 5.7a. As shown, each image was fit with a two dimensional Gaussian to monitor the evolution of the trap size in time. Due to the slightly elliptical shape of the atoms' ensemble, the expansion along both axes was tracked separately, as the data in Figure 5.7c show. An expansion of the cloud was fit with the equation (5.7), and the data show that the temperature is $T_{\text{red}} = (230 \pm 22)\,\mu\text{K}$ and $T_{\text{blue}} = (257 \pm 8)\,\mu\text{K}$ with the initial trap size $\sigma_{0,\text{red}} = (3.43 \pm 0.79)\,\mu\text{m}$ and $\sigma_{0,\text{blue}} = (2.61 \pm 0.33)\,\mu\text{m}$. It seems reasonable to assume that the temperature of the ensemble should not vary for different axes and hence the measured value of temperature is $(244 \pm 30)\,\mu\text{K}$. A Gaussian fit for each image allows also to calculate the corresponding integrated signal as shown in Figure 5.8. Since the probe beam was resonant to the cooling transition, the integrated signal could be easily converted into the number of atoms in dipole trap using the calibration described in appendix E.1. On average a dipole trap was populated with $(48 \pm 6)\,\text{atoms}$.

Discussion and conclusion

We use an integration time of $50\,\mu\text{s}$, which is very large in comparison with the timescale of the experiment (dt is in range $(0 \text{ to } 70)\,\mu\text{s}$). During the $50\,\mu\text{s}$ of integration, the atoms rapidly expand, as shown in the Figure 5.7c for $dt > 10\,\mu\text{s}$. The resulting signal, shown in Figure 5.7a, is therefore the time averaged signal of the expanding cloud, where we define an effective expansion time as $dt + \frac{1}{2}(\text{flash time})$.

The size of the trap before expansion is measured in the TOF experiment and agrees well with the predicted trap sizes based just on geometrical optics measurement (see section 5.1), where the temperature of $250\,\mu\text{K}$ was used to calculate the size of the trapped

[5]Signal is calculated as an average value of pixels for the area marked as marked on Figure 5.6a by the rectangle. The signal for each frame and fluctuates around constant value and on average is equal to the signal calculated from Figure 5.6c.

[6]Noise σ_{noise} is defined as a standard deviation of counts per pixel.

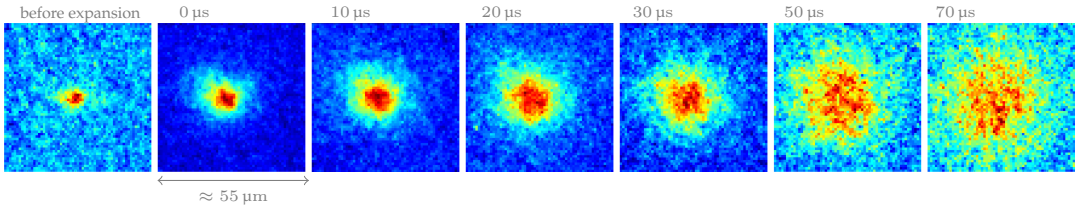

(a) Background corrected images of cloud expansion

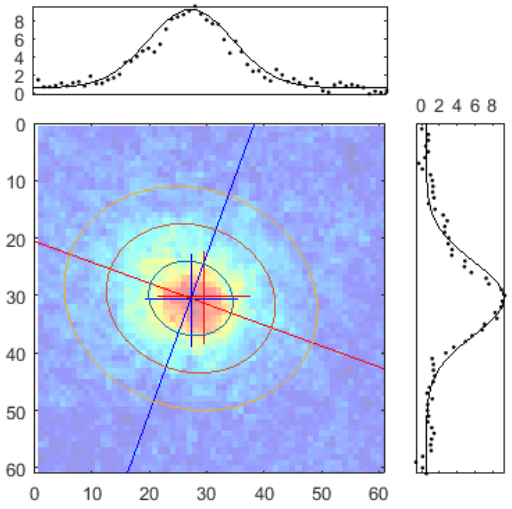

(b) Gaussian fit of the background corrected image

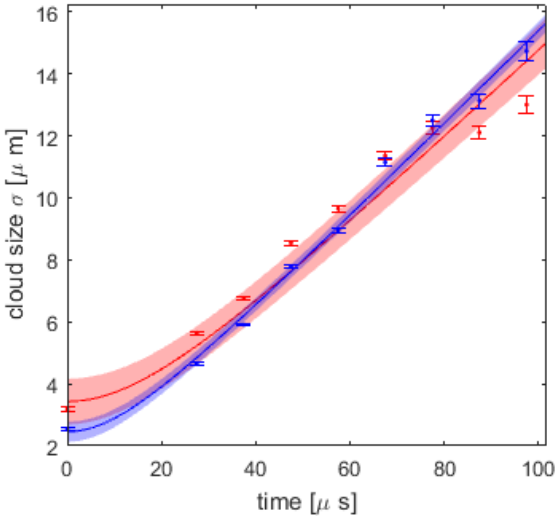

(c) Size of the cloud versus expansion time

FIGURE 5.7: Results of time-of-flight experiment for atomic cloud in the dipole trap. (a) Each image shows region of 61x61 pixels that gives a size of about $55\,\mu\mathrm{m}$ of the acquired image, taking into account the magnification of the system 14.36 times measured in section 4.4.3. Time above the images corresponds to expansion time dt. (b) Two dimensional Gaussian fit of dipole trap for $dt = 10\,\mu\mathrm{s}$. (c) Results of the fitting Gaussian model to the acquired signal. Red and blue data points corresponds to the parameters along the red and blue axis on figure (b). The effective expansion time on the x axis is given by $dt + \frac{1}{2}$(flash time). Solid lines corresponds to the fit of equation (5.7), while the red and blue bands represents the error of the fitting.

atoms. This also validates the previous prediction for the trap size along the optical axis $\sigma_3 = (18.3 \pm 1.0)\,\mu\mathrm{m}$.

This value, together with $\sigma_{0,\mathrm{red}}$ and $\sigma_{0,\mathrm{blue}}$ might be used to calculate the total volume of the trapped ensemble using formula: $V = (2\pi)^{\frac{3}{2}}\sigma_{0,red}\sigma_{0,blue}\sigma_3 \approx 2500\,\mu\mathrm{m}^3$. Combining the volume with the known number of atoms in dipole trap $(48 \pm 6)\,\mathrm{atoms}$, the peak density for the dipole trap appears to be $(190 \pm 100) \times 10^8\,\mathrm{atoms/cm}^3$. The experimental conditions for the reservoir during the experiment are known from a complementary measurement of MOT (see section 3.3.1). The MOT is small, consisting of only about 200000 atoms in a cloud of radius of $140\,\mu\mathrm{m}$, which gives a reservoir of peak density $(45 \pm 7) \times 10^8\,\mathrm{atoms/cm}^3$. It

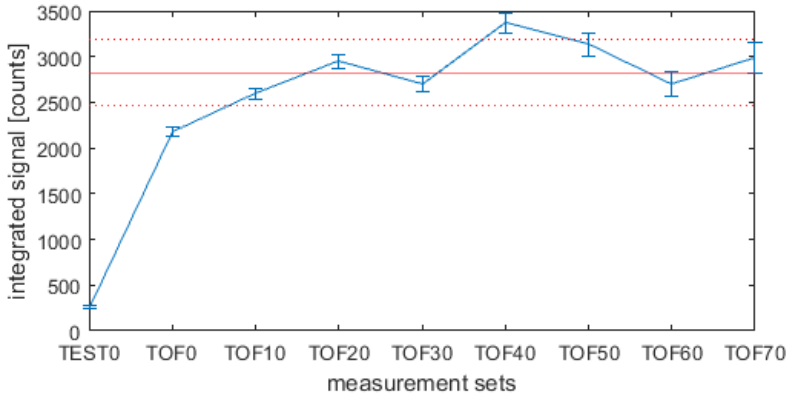

FIGURE 5.8: An integrated signal of dipole trap. The first data TEST0 corresponds to the version of the sequence when dipole trap is constantly on, while the rest corresponds to TOF with dt =(0, 10, 20, 30, 40, 50, 60 and 70) µs. Red solid line is an averaged value for all dt and the dotted line represents standard deviation.

means, that the peak density in the dipole trap is about five times higher than the reservoir density.

5.3 Measurement of the effective Stark shift

The Stark shift (see section 2.2.7, equation (2.29)) is an interesting phenomenon to observe since it is directly linked to the trap depth. In this section, the Stark shift is measured by comparison of the scattering rate of atoms within the trap with the scattering rate of the atoms which are released from the trap. Since the trapping potential is proportional to the intensity of the used laser, it is relatively easy to characterise trap depth in terms of laser power, and predict the waist of the trapping laser beam. Simultaneously, the number of atoms loaded into the trap is measured. Having the dependence of the trap population on the trap depth, it is possible to understand the loading mechanism under given conditions. The aim of the experiment is to measure the Stark shift, trap depth and number of trapped atoms versus the power of the dipole laser.

5.3.1 Methodology

In the TOF measurement the trap was illuminated by a cooling beam in order to obtain a fluorescence signal. As shown in Figure 5.8 the integrated signal for the measurement with the dipole trap beam on is much lower than for the other images taken with the beam off. This is because the intense dipole trap beam generates Stark shift, that increases the

detuning from the probe light, thus reducing the atoms scattering rate. We assume, that the number of atoms immediately after release is the same as the number stored in the trap, and its value varies only from run to run due to the statistical fluctuations of the initial number of atoms loaded into the trap.

According to equations (5.5) and (5.6), the strength of the signal received by the camera is

$$N_{\text{counts}} = N_{\text{atoms}} R_{sc} \frac{\kappa \gamma_0 \gamma_1 \eta}{\text{PAG}}.$$

where the term $\frac{\kappa \gamma_0 \gamma_1 \eta}{\text{PAG}} = const.$ since all the acquisition settings were the same during the entire experiment. Thus the ratio between the signal without and with dipole trap beam on is

$$\frac{N_{\text{counts, off}}}{N_{\text{counts, on}}} = \frac{R_{sc,\text{ off}}}{R_{sc,\text{ on}}}$$

where $N_{\text{counts, off}}$ and $N_{\text{counts, on}}$ denotes the integrated signal when the dipole trap beam is off and on respectively. The scattering rate follows the equation (2.24)

$$R_{sc} = \frac{\Gamma}{2} \frac{\frac{I}{I_{sat}}}{1 + \frac{I}{I_{sat}} + 4\left(\frac{\Delta+\delta}{\Gamma}\right)^2}$$

where Δ denotes the detuning of the cooling laser and δ is the detuning arising from the ac Stark shift. The scattering rates $R_{sc,\text{ on}}$ and $R_{sc,\text{ off}}$ differ because of the trapping laser, since $\delta = 0$ in the absence of the dipole trap beam. Rearranging the equations, the Stark shift can be obtained:

$$\delta = \frac{\Gamma}{2} \sqrt{\frac{N_{\text{counts, off}}}{N_{\text{counts, on}}} \left[1 + \frac{I}{I_{sat}} + 4\left(\frac{\Delta}{\Gamma}\right)^2\right] - 1 - \frac{I}{I_{sat}}} - \Delta. \tag{5.8}$$

In the case of TOF measurement the probe beam was resonant ($\Delta = 0$), with its maximum intensity $\frac{I}{I_{sat}} \gg 1$ and circularly polarised, returning an *averaged Stark shift* equal to $2\pi(29 \pm 2)\,\text{MHz}$.

What is worth noticing is that, due to the fact that the probe beams were circularly polarised $\sigma^{\pm}$ and the atoms within the trap could be in any $|m_F\rangle$ state, the contribution of different energy shifts is rather complicated and hence it is difficult to resolve from the result the exact Stark shift for the ground state $\delta\left(5^2S_{1/2}\right)$. Therefore, the results presented here will evaluate an *averaged Stark shift*. Taking into account the predicted values for the energy levels in section 5.1.1, results (5.3) and (5.4), the measured averaged Stark shift can be

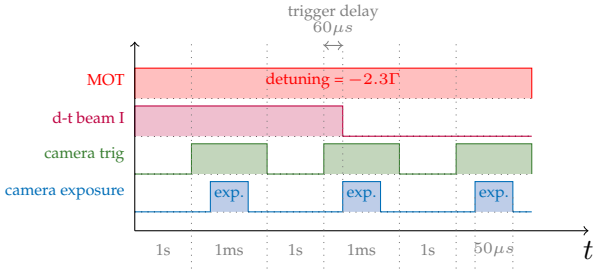

FIGURE 5.9: Scheme of experimental sequence for an averaged Stark shift measurement. Trigger delay represents how much in advance the camera is triggered before a start of the camera exposure. Events/settings and corresponding values in the figure are: **MOT** - constant MOT running with $3.5\,\mathrm{A}$ on anti-Helmholtz coils, cooling beams on $15.3\,\mathrm{mW/cm^2}$ repumper $2\,\mathrm{mW}$ and 2.3Γ detuning, **d-t beam I** - intensity of the dipole trap beam $(0$ to $150)\,\mathrm{mW}$, **camera trig** - TTL signal, **exp.** - the exposure time when the ICCD acquires the signal.

expected to have a higher value.

5.3.2 Experiment and results

Sequence

The experiment is conducted in continuous MOT operation in order to to speed up the measurement process since the MOT loading stage usually takes $(8$ to $10)\,\mathrm{s}$. In continuous MOT operation the sequence is only about $3\,\mathrm{s}$ long and the number of repetitions could be increased to 300 times. This is needed as it is expected that for low laser power the reduced number of atoms in the trap will result in a low signal to noise ratio. The experimental sequence is presented on Figure 5.9. Three snapshots are taken during the run of a sequence and all images are taken with the same camera settings, which are listed in appendix E.3. The time required for the camera to refresh and be ready for the next acquisition was taken into account as a $1\,\mathrm{s}$ break between snapshots. The first image acquires a signal from atoms within dipole trap while the trap beam is on and atoms experience Stark shift. For the second image, the camera is triggered $60\,\mu\mathrm{s}$ in advance before switching off the dipole trap beam in order to ensure that the acquisition starts after the dipole trap beam is switched off (see appendix E.4). The exposure time of the camera is $50\,\mu\mathrm{s}$, enough for atoms to start expanding once being released from the trap, but not enough to escape the imaging region. Finally the last snapshot is a background image, containing the MOT signal and stray light, taken in order to remove background.

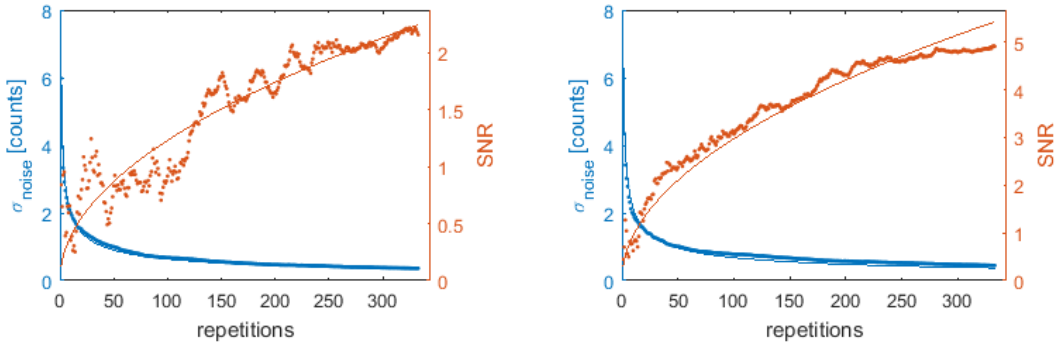

(a) With dipole trap beam

(b) Without dipole trap beam

FIGURE 5.10: The analysis of the noise σ_{noise} and signal to noise ratio SNR versus sequence repetitions for Stark shift measurement and $150\,\text{mW}$ dipole trap laser power. Dots represents values of noise and SNR for the accumulation of subsequent frames. Solid lines are theoretical fits to $\frac{\langle\sigma_{\text{noise}}\rangle}{\sqrt{\text{repetitions}}}$ and $\langle\text{SNR}\rangle\sqrt{\text{repetitions}}$, where $\langle\sigma_{\text{noise}}\rangle$ and $\langle\text{SNR}\rangle$ are fitting parameters.

Noise analysis

For this experiment, the noise generated by the ICCD camera (see noise analysis in appendix E.2) is relatively small in comparison to the light pollution coming from the surrounding MOT. The signal from atoms withing the trap is indistinguishable from the noise and background for a single run of the experiment, and therefore SNR is less than one. Increasing the number of repetitions decreases the noise and therefore increases SNR, as shown in Figure 5.10. Because of the low signal to noise ratio especially for images of atoms in the presence of AC Stark shift, the sequence has been repeated about 300 times. By removing the accumulated background image from the averaged image of the trap, the contrast was improved 20 times and a SNR ≈ 2.25 was eventually obtained as shown on Figure 5.10a and Figure 5.11a. Meanwhile, the signal from atoms released from the dipole trap is much stronger, due to the increased scattering rate. Figure 5.10b shows that it requires only 50 repetitions to achieve a comparable contrast, and after 300 repetitions $SNR \approx 5$.

The averaged and background corrected signal is shown in Figure 5.11. The spatial distribution of the cloud, depicted in Figure 5.11, is Gaussian, so that it can be easily fitted with two dimensional model. Atoms in the dipole trap experience a Stark shift, therefore the signal is weaker than the signal from the released cloud, but for a SNR ≈ 2 it is still possible to resolve the signal distribution using two a dimensional Gaussian fit.

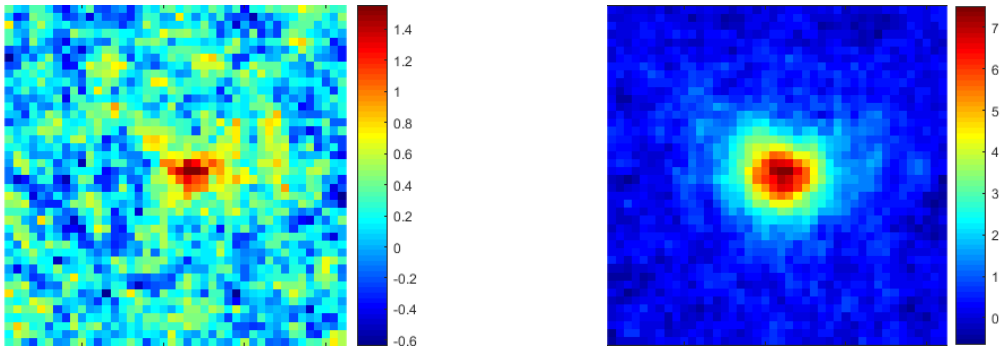

(a) Dipole trap beam on (b) Dipole trap beam off

FIGURE 5.11: Fluorescence image of atoms for the Stark shift measurement for 150 mW laser power. The images are averaged over 300 cycles and background corrected.

Data analysis

The sequence was repeated for different dipole trap laser powers in range $(50 \text{ to } 145)\,\mathrm{mW}$. Each pair of images with and without dipole trap beam Figure 5.11, was fit with a Gaussian. This allows to calculate the total signal $N_{\text{counts, on}}$ and $N_{\text{counts, off}}$ acquired from atoms. Then, Stark shift is calculated from equation (5.8) using the known ratio between these two signals $\frac{N_{\text{counts, off}}}{N_{\text{counts, on}}}$ and experimental conditions, namely the detuning 1.7Γ and probe beam intensity $15.3\,\mathrm{mW/cm^2}$.

Results are presented in Figure 5.12a, where the Stark shift obtained from the TOF measurement (see section 5.2.3) is also shown for comparison. According to equations (2.29 to 2.32) the trap depth and the associated Stark shift are supposed to be linear in terms of laser power. The data of Stark shift versus laser power can be fit with a linear equation (solid red line in Figure 5.12a), which results in increment equal to $2\pi(174 \pm 14)\,\mathrm{kHz/mW}$. Having measured the dependence of the Stark shift on the laser power, the beam waist is predicted to be $(5.0 \pm 0.6)\,\mu\mathrm{m}$ based on (2.29). The Stark shift $\delta(5^2S_{1/2})$ derived in section 5.1.1, where the dipole trap profile was measured optically, is also shown on the Figure 5.12a for comparison. The discrepancy between the Stark shift measurement with atoms and the predicted trap depth in Figure 5.12a is puzzling, but it can be explained. As discussed in 5.3.1, the measurement with atoms represents an *averaged Stark shift* which includes a contribution of all atomic transitions between the ground state and the magnetic sublevels of the state $\left|5^2P_{3/2}, F = 3, m_F\right\rangle$. The maximum possible shift corresponds to the level $\left|5^2P_{3/2}, F = 3, m_F = 0\right\rangle$ and its value is almost a half of the trap depth $\delta\left(5^2S_{1/2}\right)$, as shown by formulas (5.3) and (5.4). It is difficult to predict the exact contribution of each

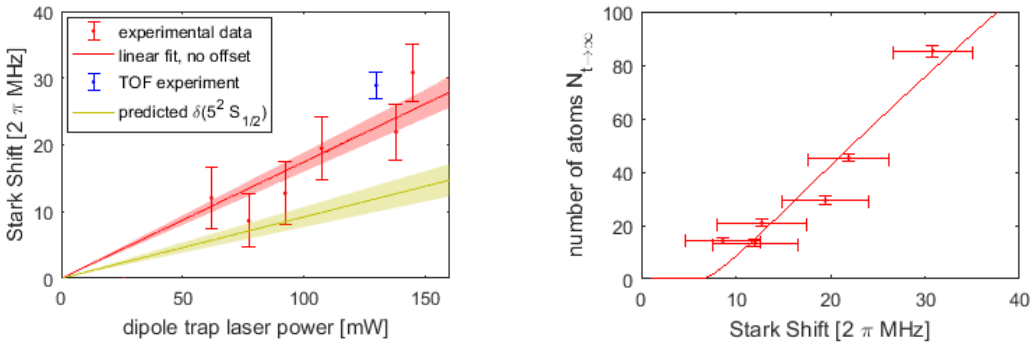

(a) (b)

FIGURE 5.12: Results of the Stark shift measurement for atomic cloud in the dipole trap. (a) Effective Stark shift versus dipole trap laser power. For comparison, the result of the Stark shift from the TOF experiment is depicted with the red color. Uncertainties are based on the goodness of Gaussian fit to the images. (b) Number of atoms in the dipole trap versus corresponding averaged Stark shift.

transition, but undoubtedly the measured *averaged Stark shift* is expected to be higher than the trap depth, but no more than 50%. Additionally, the optical measurement (see section 5.1.1) was a coarse estimation used only to facilitate the first alignment of the dipole trapping system and thus may suffer from a systematic error. According to optical measurement, the beam's waists are $(6.1 \pm 0.5)\,\mu\mathrm{m}$ and $(7.0 \pm 0.5)\,\mu\mathrm{m}$, while the measurement with atoms estimates the waist to be about $5\,\mu\mathrm{m}$. Although these values do not lay withing their uncertainties, both results are reasonably close to each other.

The number of atoms within the dipole trap is obtained from the signal acquired during the cloud release, when SNR is higher and provides lower uncertainties. The number of atoms versus the corresponding Stark shift is presented on Figure 5.12b, and, as expected, the bigger trapping potential (Stark shift) the more atoms in the trap. As will be discussed in depth in sections 5.4.1 and 5.5.1, the trap population is stable when continuously loading from the reservoir and, in the case of low density in the trap, the number of atoms loaded is proportional to the loading rate $N_{t\to\infty} \sim \frac{R}{\gamma}$ ($N \to \infty$ stands for a quasi-steady state). Following the theory from section 5.1, the loading rate R can be estimated based upon the features of the reservoir and dipole trap, namely MOT density (n_{MOT}), MOT temperature (T_{MOT}), dipole trapping depth (U_{pot}), shape of the potential (ω_0, z_R) and the trapping probability (P_{trap}). Thus, the relationship between these parameters and the number of atoms is

$$N_{t\to\infty} \sim \frac{R}{\gamma} = \frac{1}{4} n_{\text{MOT}} \langle v \rangle A P_{\text{trap}} \frac{1}{\gamma} = \\ = \frac{1}{4} n_{\text{MOT}} \langle v \rangle \frac{4}{3} \pi \omega_0^2 z_R \frac{1}{2} \ln\left(\frac{U_{pot}}{k_B T_{\text{MOT}}}\right) \sqrt{\frac{U_{pot}}{k_B T_{\text{MOT}}} - 1} P_{\text{trap}} \frac{1}{\gamma} \tag{5.9}$$

which is obtained by combination of equations (5.1) and (5.2). A coarse estimation of the loss rate γ[7] and MOT temperature can be obtained by a fit of the data to the equation (5.9) with the assumption that every atom which finds itself within the trapping area A is effectively trapped, thus $P_{\text{trap}} = 1$. The fit (red solid plot on Figure 5.12b) of atoms loading into the dipole trap is compared to the data in the Figure 5.12b. The loss rate $\gamma = (0.015 \pm 0.004)\,\text{s}^{-1}$ and MOT temperature $T_{\text{MOT}} = (307 \pm 76)\,\mu\text{K}$ are derived here from the fit, while values for other parameters are estimated based on results from previous experiments[8]

5.4 Trap lifetime

There are many mechanisms responsible for trap depopulation including collisions within trapped atoms or collisions between atoms in the trap and residual gasses. As it was discussed (see section 3.4), a vacuum level of order $10^{-10}\,\text{mbar}$ is required since the collisions with background gases limit the trap's lifetime. However, there are also other possible mechanisms resulting in depopulation of a trap which can occur due to the presence of light. This section discuss the mechanism of loading and presents the experimental approach to measure some of these values. Specifically, the lifetime of the trap is monitored here for three different experimental conditions: for two different temperatures of the reservoir and in presence of the laser light close to resonance. These results should give an insight how to operate the trap properly to obtain a long lifetime.

5.4.1 Loading and losses processes of dipole trap

The traps' loading dynamics are rather complex. In general, the phenomenological rate equation expressing the dipole trap loading might be expressed as follows

$$\frac{dN}{dt} = R - \gamma N - \beta N(N-1) \tag{5.10}$$

[7] One body collision loss rate of atoms from a dipole trap.
[8] $n_{MOT} = (45 \pm 7) \times 10^8\,\text{atoms/cm}^3$, $\omega_0^2 z_R = (7.01 \pm 0.54)\,\mu\text{m} \cdot (6.14 \pm 0.54)\,\mu\text{m} \cdot (21.7 \pm 2.2)\,\mu\text{m}$.

where N stands for number of trapped atoms, R represents loading rate, γ and β describe one-body and two-body losses.

The dipole potential is conservative, therefore in order to keep the atom into the trap, an additional cooling mechanism must be present. Combining the dipole trap loading with a MOT stage, any atom within dipole trap undergoes an additional cooling process that lowers the initial energy of an atom. As a result, the atom gets effectively trapped, provided that the trap depth exceeds the atom's energy. The loading rate R at which atoms enter and populate the trap depends on the density and temperature of atoms reservoir, the efficiency of laser cooling within the trap, and the trap parameters.

However, even if the energy of trapped atoms is insufficient to escape the trap, atoms in the trap may get heated from external sources. As it was mentioned in section 3.4 the lifetime of a trap might be limited due to inelastic one-body collisions with residual gasses. This process does not depend on the number of trapped atoms. Other losses, $\beta N(N-1)$, linked to two-body collisions arising in the regime of very high density in the trap strongly depend on the population of the trap, unlike one-body loss. Collisions between two atoms in different hyperfine states $\left|5^2S_{1/2}, F=1\right\rangle$ and $\left|5^2S_{1/2}, F=2\right\rangle$ might cause a spin-flip and release energy equal to the hyperfine splitting of the ground state[9] [175]. Other causes of losses are not relevant for this work since they matter starting from densities $10^{15}\,\mathrm{atoms/cm^2}$, which is clearly not the case of our trap. Regarding losses in the presence of light, it will be shown in this section that losses from the trap can be enhanced when atoms are exposed to the near-resonance laser light, but a thorough examination of the phenomenon will be discussed in section 5.5.

5.4.2 Experiment and results

The slow decay of the number of atoms within the trap can be observed and characterised. In order to achieve it, survival probability of atoms within the trap is measured with respect to the holding time. Since the mechanisms governing atoms losses are rather complex, the experiment consists of three variants all discussed in the following section, whose aim is to resolve which experimental parameters have the biggest influence on the trap lifetime.

Sequence

The experimental sequences are presented in Figure 5.13. Each run of the sequence starts

[9] 6.8 MHz of ground state energy split is more than 100 times greater than typical 1 mK trap depth

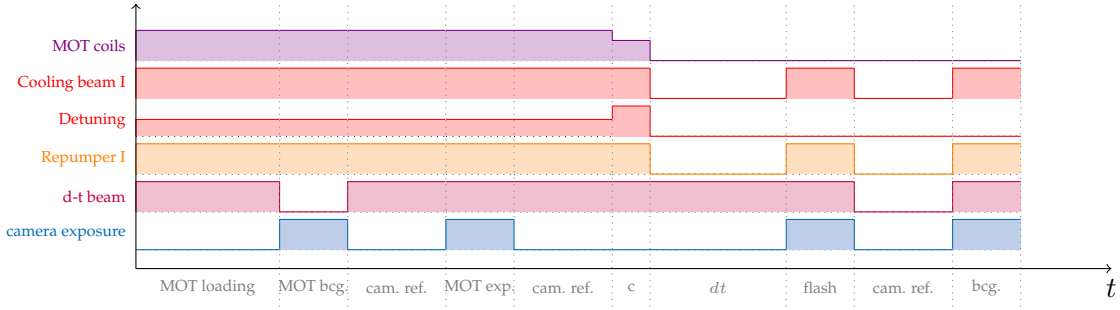

(a) Variants 1 and 2: no repumper during holding time

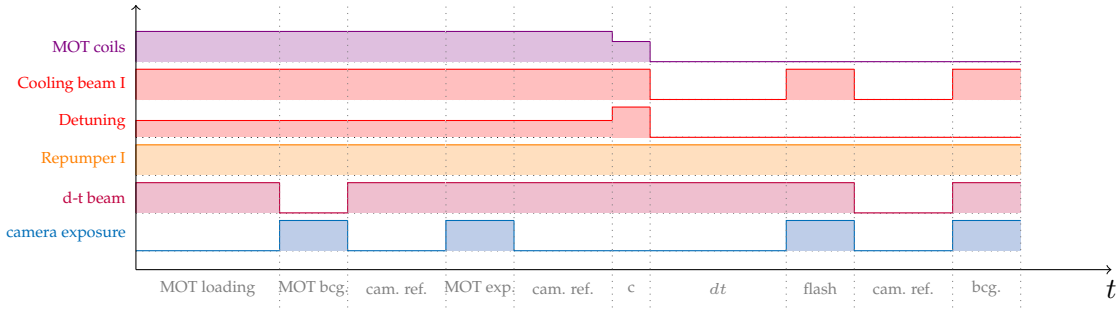

(b) Variant 3: repumper constantly on

FIGURE 5.13: The experimental sequence for the lifetime measurement. The different stages marked under the time axis are: **MOT loading**= 8 s, **c**= 10 ms, **dt**= variable time, **MOT bcg.** = **MOT exp.** = **flash** = **bcg.** = 5 ms, **cam. ref.** = 1 s. Events/settings and corresponding values in the figure are: **MOT coils** - current applied to the anti-Helmholtz coils (3.5, 3.4 and 0) A, **Cooling beam I** - the total intensity of the cooling beams (0 to 15.3) $\mathrm{mW/cm^2}$, **Detuning** - the detuning of the cooling beam from the cooling transition 1.7, 2.3 and 0Γ, **Repumper I** - intensity of the repumper beam (0 to 2) mW, **d-t beam I** - intensity of the dipole trap beam (0 to 130) mW, **camera exposure** - TTL camera trigger and the the exposure time of ICCD.

with «MOT loading» stage for about 8 sec, which (as discussed earlier in section 5.2.3) is sufficient taking into account a typical MOT loading time of about 4 s. While the MOT is fully loaded two images are taken, with «MOT exp.» and without «MOT bcg.» dipole trap, to determine the initial number of atoms in the dipole trap before starting an actual lifetime experiment (similarly as in section 5.3.2). Additionally an optional stage «c»= 10 ms is applied for further cooling of the sample by increasing the detuning of the cooling beams and slightly decreasing the magnetic field. Finally, the MOT is switched off for a varying time dt while the atomic ensemble is being held by the dipole trap. After the «dt» stage, a 5 ms flash of probe light illuminates te atoms and the camera acquires a fluorescence signal during «flash». Eventually, the background image «bcg.» is taken to correct the signal from any stray light. Detailed setting of laboratory equipment used during each stage are listed in the caption of Figure 5.13.

There are three versions of this experiment, which differ only in applying optional stage «c» and the way that repumper is being operated. The first variant simply follows the sequence presented on Figure 5.13a, when the optional «c» stage is applied and no beams are present inside the vacuum chamber during the holding time «dt». The second option also follows Figure 5.13a, but sets «c» to 0, skipping completely this stage. The last version of the experiment is shown on Figure 5.13b, where the «c» is applied but the repumper is kept on during the entire experiment. Results for all three options are processed in the same way and eventually compared in the following sections revealing the impact that the cooling stage and repumper have on the trap lifetime.

Noise analysis

The relatively long exposure time ($5\,\mathrm{ms}$) benefits of an increased signal to noise ratio, even though the scattering of photons by atoms is decreased because of the dipole trap beam presence. For such a long exposure time, the noise related to the CCD readout (see appendix E.2.1) is irrelevant, since the signal from atoms within dipole trap and from the MOT are much above the CCD's noise level. Moreover, the noise caused by the intensifier (see appendix E.2.2) is also reduced due to the increased statistics of single photon events. A single frame from the experiment is presented in Figure 5.14a and where a clear signal from atoms is visible. In comparison, the typical background Figure 5.14b is much lower than the signal from atoms. The analysis of the signal to noise ratio during the loading of the dipole trap from the MOT shows that the SNR is reduced because of the surrounding MOT atoms, but still even for a single acquisition the signal to noise ratio is above 1 (see Figure 5.14d). The SNR is higher for the data acquired during «dt» stage, due to the decreased MOT background, and for a single run of the experiment SNR ≈ 2. For each dt the sequence was repeated 25 times, which was enough to get good signal for both cases within and out of the MOT, as it is shown at Figure 5.14d.

Data analysis

Each of the averaged background corrected images of the dipole trap was fit with a two dimensional Gaussian function giving information about the atoms distribution and the background offset. The MOT residual background is also a useful parameter to roughly quantify the temperature of the atoms reservoir. Initially, after switching the MOT off during the «dt» stage, the MOT's background is still visible and decreases almost to zero for

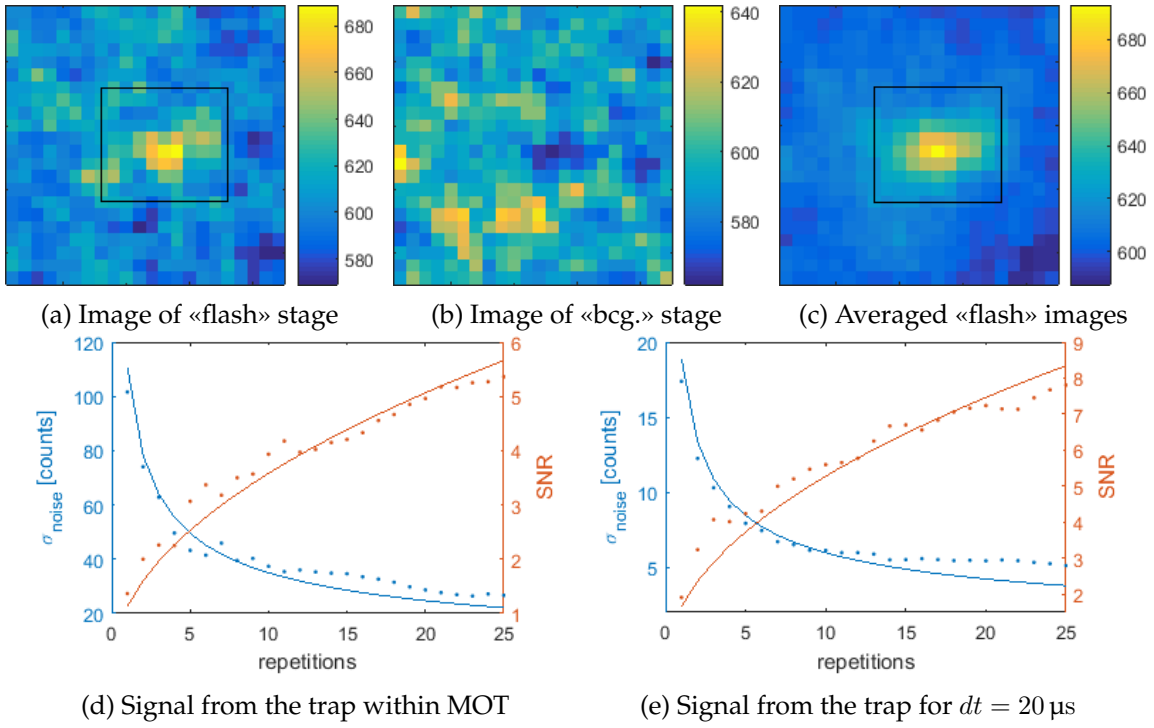

(a) Image of «flash» stage (b) Image of «bcg.» stage (c) Averaged «flash» images

(d) Signal from the trap within MOT (e) Signal from the trap for $dt = 20\,\mu s$

FIGURE 5.14: The analysis of noise and signal to noise ratio for the Lifetime experiment for $dt = 20\,\mu s$. (a) The image of a single acquisition of atoms held by dipole trap beam. (b) The corresponding background image taken in the same cycle as (a). (c) The image of atoms averaged over 25 cycles. (d-e) The analysis noise σ_{noise} and signal to noise ratio SNR versus sequence repetitions for $130\,mW$ dipole trap laser power. Dots represents values of noise and SNR for the accumulation of subsequent frames. Solid lines are theoretical fits to $\frac{\langle \sigma_{noise} \rangle}{\sqrt{repetitions}}$ and $\langle SNR \rangle \sqrt{repetitions}$, where $\langle \sigma_{noise} \rangle$ and $\langle SNR \rangle$ are fitting parameters.

$dt \approx 5\,ms$. Based on this decay, the known initial value for MOT background measured during «MOT bcg.», and the known measured MOT cloud size, it is possible to retrieve the temperature of atoms reservoir as described in section 3.3.5. According to the model, the temperature varies significantly depending on the presence of the cooling stage «c». For the first and third experiment, when the cooling stage was present, the estimated temperature is $(100 \pm 20)\,\mu K$ and $(115 \pm 20)\,\mu K$ respectively, and it raises up to $(334 \pm 100)\,\mu K$ without cooling stage «c».

The integrated signal from the trapped atoms was obtained from the Gaussian fit and converted into the total photons number, using the previously measured Stark shift value. The ratio between the initial atoms number and the atoms remaining after dt gives the survival probability, which is presented in Figure 5.15. Atoms decay is characterised by a double exponential decay with two lifetimes, where an initial fast decay with characteristic time

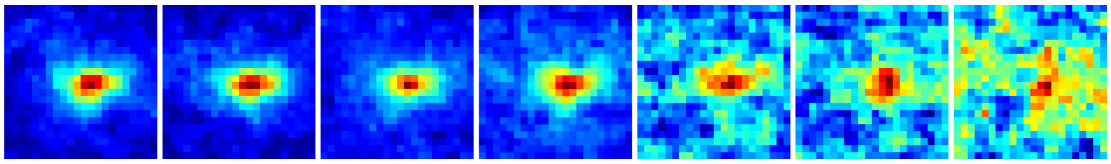

(a) Subsequent results for $dt = (5, 20, 50, 200, 1000, 2000 \text{ and } 3000)\,\text{ms}$.

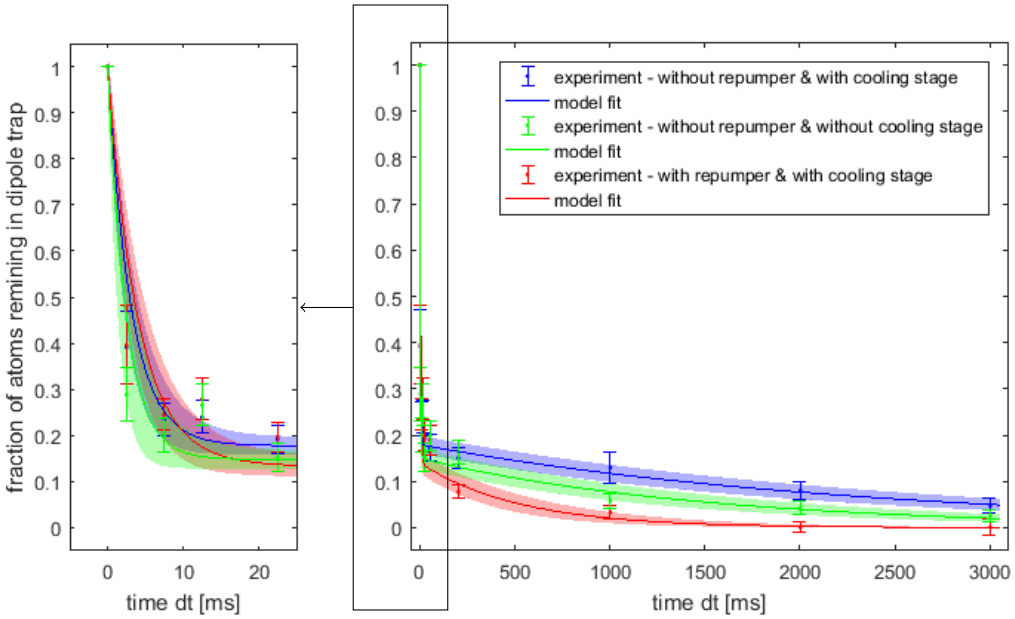

(b) Survival probability of atom in the trap in terms of holding time dt.

FIGURE 5.15: Measurement of dipole trap lifetime for atomic cloud in the dipole trap.

τ_1 is followed by a slower rate with characteristic time τ_2. The fast decay time τ_1 is similar for all three variants of the experiment and the characteristic time lie within uncertainties as follows $(3.1 \pm 0.8)\,\text{ms}$ (blue), $(2.5 \pm 1.0)\,\text{ms}$ (green), $(4.0 \pm 0.9)\,\text{ms}$ (red). The long decay τ_2 is $(2359 \pm 283)\,\text{ms}$, $(1503 \pm 216)\,\text{ms}$ and $(521 \pm 119)\,\text{ms}$ for blue, green and red curves respectively.

Discussion and conclusions

In the results presented in Figure 5.15b the most surprising is the initial fast decay. Interestingly, the feature of the initial fast atoms' depopulation was observed in other works [176, 177]. In [176] the number of atoms was of the order 2×10^6 in the CO2 dipole trap characterised by $1.9\,\text{mK}$ trap depth and $89\,\mu\text{m}$ waist. It gives the density of the trap about $2.5 \times 10^{12}\,\text{atoms/cm}^3$. In [177] the trap depth was $2.7\,\text{mK}$ and the waist was five times smaller than ours ($\approx 1\,\mu\text{m}$) with a comparable number of atoms ≈ 80, resulting in cloud

density $4.59 \times 10^{12}\,\mathrm{atoms/cm^3}$. In both cases it was concluded that the first fast decay is due to the rethermalization of atoms inside the dipole trap soon after suppressing the atoms reservoir. Also in [170] two body collisions were observed but less strong than in two examples discussed above. In [170] a trap of similar waist to ours ($5.6\,\mu\mathrm{m}$) consisted of 1200 atoms, the density of the trap was of the order $1 \times 10^{11}\,\mathrm{atoms/cm^3}$ and the observed decay showed features of both one body and two body collisions.

In our case, the density of the dipole trap was much lower of order $1.7 \times 10^{10}\,\mathrm{atoms/cm^3}$, thus a rethermalization is less likely to be the reason for the fast decay. On the other hand, the fast decay shows a characteristic time comparable to the MOT background decay, which might imply that it can be caused by a locally increased background density due to the atoms in MOT. Since the uncertainties on τ_1 are substantial, it is impossible to distinguish whether difference in the experimental conditions between variants 1, 2 and 3 of the sequence have an impact on the fast decay.

Apart from the quick initial depopulation of the trap, the following long lifetime τ_2 due to the collisions with background gasses is as expected in the order of seconds. The lifetime is indeed strongly reduced if the trap is exposed to any near-resonant light while holding the atoms [170]. Varying the initial temperature of the MOT (through cooling stage «c») also has an impact on the lifetime, reducing the temperature of MOT from $300\,\mu\mathrm{K}$ to $100\,\mu\mathrm{K}$ resulted in increasing the long decay from $1500\,\mathrm{ms}$ to $2300\,\mathrm{ms}$.

5.5 Losses in the presence of light

In section 5.4, losses from the trap due to inelastic collisions in the absence of light are discussed and compared to the losses in the presence of light. As it is shown, in the presence of light, loss mechanisms due to possible light-matter interactions arises and might play a dominant role. Since any measurement of the atoms ensemble occurs in the presence of probe light, it is important to characterise these loses in order to optimise atoms detection. Understanding loss mechanisms will be also essential during optimisation of the dipole trap loading from the MOT.

The very first mechanism responsible for losses, and usually negligible in comparison with others, is heating of an atom due to the light scattering of dipole trap laser. Since the dipole trap is far detuned from the atomic transitions, the scattering rate is diminished.

However, the closer to the resonance, the stronger one-body loss is, and hence using resonance probe beams to obtain fluorescence signal might have more significant impact and heat the atoms in the trap. Moreover, the phenomenon of light assisted collisions (two body losses nature) can also occur and even dominate over heating under some circumstances, such as a very long exposure to the intense probe beams.

The strength of two-body collisions within the trap depends on many factors, namely the trap waist, probe beam intensity and its detuning from the atomic transitions. Two main mechanisms were recognized to be responsible for hyperfine-changing collisions and radiative escape. A semi-classical model for light assisted collisions was derived and tested using Na atoms in [178]. The collisions were extensively studied in many different configurations including experiments with potassium - rubidium mixture [179]; work where only hyperfine-changing collisions were measured [175]; measurement of light assisted collision for rubidium in FORT [180]; studies of collisions in micrometre size dipole traps [181] and [182].

The aim of this section is to study atoms loss rate in the presence of probe beams for our experimental setup under typical operating conditions and determine whether the main loss mechanism is governed by light assisted collisions. This will allow determination of the optimal conditions for atoms detection as well as optimization of dipole trap loading from the reservoir of atoms.

5.5.1 Many body physics

Following the phenomenological equation (5.10)

$$\frac{dN}{dt} = R - \gamma N - \beta N(N-1)$$

for the dipole trap, three different operating regimes can be identified: weak loading, blockade regime and strong loading, as shown in [183]. For weak loading, the main mechanism responsible for atoms loss is one-body loss (γ) for which the steady state number of atoms is $N_{t\to\infty} \sim \frac{R}{\gamma}$, while for a very dense traps the collisional blockade limits the trap population resulting in $N_{t\to\infty} \sim \sqrt{\frac{R}{\beta}}$. Here, the parameter γ includes losses due to the collisions with background gasses as well as heating mechanism in the presence of light, while β is responsible for two-body light-assisted collisions. This means that the number of atoms loaded

into the trap can be effectively limited either by the background gases (measured in section 5.4), or by the light-matter interactions (heating rate or light-assisted collisions).

When atoms are being held in the dipole trap without loading from the reservoir ($R = 0$) and under conditions of an ultrahigh vacuum, it is the light-matter interaction that is mostly responsible for losses. Assuming that only a heating rate is responsible for losses, the equation takes form $\frac{dN}{dt} = -\gamma N$ with a trivial solution $N(t) = N_0 \exp(-\gamma t)$. If the atoms are continuously exposed for a probe beam during time Δt, which results in fluorescence light, then the total signal collected by the detected during this time is:

$$\text{signal} \propto \int_0^{\Delta t} N(t)dt = \frac{N_0}{\gamma}\left(1 - e^{(-\gamma \Delta t)}\right), \tag{5.11}$$

where N_0 is the initial number of atoms.

For traps of a high density it is reasonable to assume that two body collisions dominate and that the dipole trap loading equation reduces to $\frac{dN}{dt} = -\beta N(N-1)$. The solution to the rate equation above becomes:

$$N(t) = \frac{N_0 \exp(\beta t)}{1 - N_0 + N_0 \exp(\beta t)} \tag{5.12}$$

where N_0 is the initial number of atoms. When the atoms in the trap are exposed to the probe light during time Δt, the scattered light is captured by the detector and the measured accumulated signal is proportional to

$$\text{signal} \propto \int_0^{\Delta t} N(t)dt = \frac{\ln\left(1 - N_0 + N_0 \exp(\beta \Delta t)\right)}{\beta}. \tag{5.13}$$

5.5.2 Experiment and results

The experimental sequence is very similar to the one presented in the lifetime experiment (section 5.4.2). However, this time, we measure the accumulated fluorescence signal radiated by atoms in the trap within the exposure time Δt. Depending on the mechanism dominating the loss rate, the trend of the signal accumulation will follow one of the two equations (5.11) or (5.13). However, for many atoms in the trap the measured loss rate will be most likely some combination of both. Ideally, to disentangle light assisted collisions from the heating rate, the heating rate γ should be first established by measurements performed on a single atom as in [181]. Since we do not have a control over the number of atoms in the trap yet, the loss rate will be measured for many atoms.

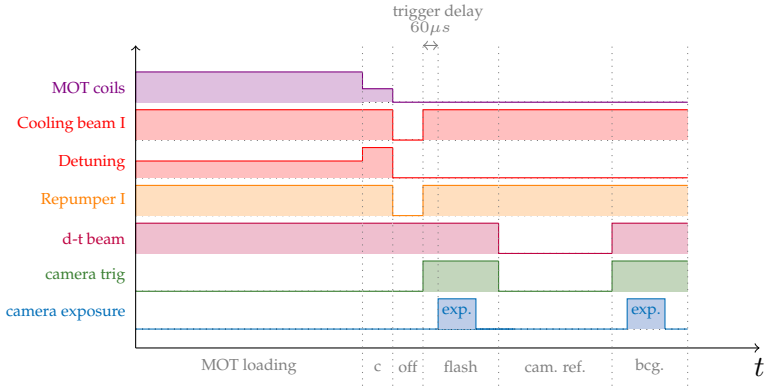

FIGURE 5.16: The experimental sequence for measurements of losses in the presence of light. The different stages marked under the time axis are: **MOT loading**= 8 s, **c**= 10 ms, **off**= 10 ms, **flash**= 6 ms, **cam. ref.** = 1 s, **bcg.** = 6 ms. Events/settings and corresponding values in the figure are: **MOT coils** - current applied to the antihelmholtz coils (0 to 3.5) A, **Cooling beam I** - the total intensity of the cooling beams (0 to 15.3) $\mathrm{mW/cm^2}$, **Detuning** - the detuning of the cooling beam from the cooling transition 1.7, 2.3 and 0Γ, **Repumper I** - intensity of the repumper beam (0 to 2) mW, **d-t beam I** - intensity of the dipole trap beam (0 to 130) mW, **camera trig** - TTL signal, **exp.** - the exposure time when the ICCD acquires the signal.

Sequence

In order to measure the β loss rate due to the probe beam, the experiment is conducted when the atoms reservoir is released and hence $R = 0$. The initial stage of the sequence is hence the same as the one presented in sections 5.2.3 and 5.4. The sequence starts with «MOT loading» and «c» (cooling) stages, then the MOT is released by turning off the cooling beams intensity to zero and by switching off the magnetic field. The actual measurements for each sequence start always 10 µs after the atoms from the MOT are released, to ensure that the MOT background does not contribute to the acquired signal. The camera trigger is fired simultaneously with turning on the probe beams during «flash», which means that atoms are already exposed for about 60 µs to the probe beam before the ICCD starts the acquisition (see appendix E.4). The duration of the signal accumulation Δt in equation (5.13) is controlled by the camera exposure time «exp.». Eventually the background image for stray light correction is taken at the end of the sequence after the readout time. Having in mind that the lifetime of the trap can be up to 2 s, the dipole trap beam is always switched off during «cam. ref.» stage to ensure that the no atoms with the dipole trap are left while taking the background image.

Noise analysis

The main sources of the noise are the ICCD and stray light. However, since the scale of the exposure time varies in the scope of few orders of magnitude, from $(10$ to $5000)$ µs, the noise has a different impact on the data quality. For the exposure time $(500$ to $5000)$ µs the behaviour is similar to Figure 5.14e and even the single run of the sequence results in the SNR is above 1. Therefore, for this set of measurements it was enough to repeat the sequence 25 times. However, for the fast exposure times $(10$ to $100)$ µs, stray light contribution to the noise has an impact as it was described in Figure 5.6d, so the sequence was repeated 50 times.

Data analysis

The signal acquired by the detector was obtained integrating a Gaussian fit to the averaged data images for each Δt. The results are presented in Figure 5.17. Recalling the discussion from section 5.5.1, the data do not follow equation (5.11) which describes losses due to the heating mechanism. On the other hand, the trend represented by the data follows the model describing light assisted collisions. Therefore, the results were fitted with (5.13) leaving both N_0 and β to be a free parameters. According to the fitting, the initial number of atoms at the beginning of the ICCD acquisition was (50 ± 15) atoms, while the losses rate due to the light assisted collisions is $(146 \pm 23)\,\mathrm{atoms\,s^{-1}}$. Taking into account that atoms had been already exposed to the probe light for about $(60$ to $90)$ µs, the initial number of atoms is estimated to be around 100 at the beginning of the «flash» stage.

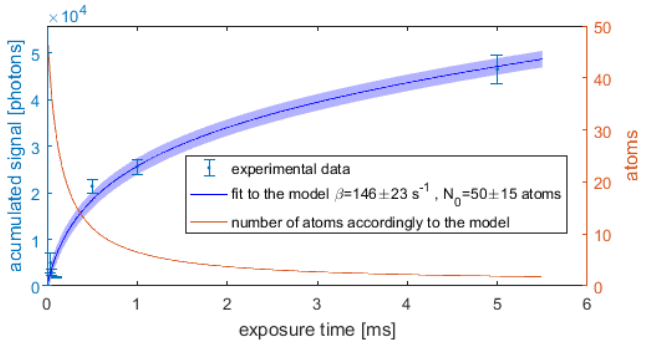

FIGURE 5.17: Results of the light-assisted collisions measurement for atomic cloud in the dipole trap. The orange solid line is the decrease of atoms population within the trap due to the two body collisions and is described by equation (5.12).

The corresponding theoretical prediction of atoms population over exposure time is described by equation (5.12) and can be predicted using N_0 and β parameters obtained from the fit. Therefore, as it is shown in Figure 5.17 by the orange line, atoms number decreases very quickly within the first $1\,\mathrm{ms}$ for our experimental conditions. For short light pulses, of order $10\,\mu\mathrm{s}$, the decay of number of atoms in the trap can be considered approximately linear. However, for a $5\,\mathrm{ms}$ pulse the trap population decreases to 4% of its initial value.

Discussion and conclusions

In order to compare our results to the typical values reported from other groups, a brief summary is presented in Table 5.1 (page 147). The experimental conditions and methods exploited in each work differ, therefore parameters significant for understanding the phenomenon need to be recognized and standardized for a convenient comparison of results. A normalised two-body loss rate $\beta_{\mathrm{norm}} = \beta 2\sqrt{2}V$ is calculated, where V is the volume occupied by the trapped atoms and for this work is estimated based on results from section 5.2. Moreover two parameters of the probe beam, light intensity and detuning from the atomic transition, are recognised to have an impact on the loss rate and hence they are directly listed in the table for comparison. Therefore, to compare the probe beam intensity for all experiments a saturation parameter $s = \frac{I}{I_{\mathrm{sat}}}$ is standardised here. Depending on the experimental method and how the probe beam is implemented (distinctive probe beam or MOT beams), the columns representing the detuning Δ and saturation parameter s consists of values denoted with various indices (e. g. s_{MOT}, s_{R} or s_{probe}) to incorporate substantial experimental details.

Measurement of the light assisted collisions was first reported for a $26\,\mu\mathrm{m}$ waist trap in [169], where the loss rate was measured by comparing the evolution of atoms decay in the absence or presence of molasses light while holding them in FORT. The same method was used later in [170], but on a further detuned trap ($\lambda_{\mathrm{FORT}} = 1064\,\mathrm{nm}$) of smaller waist $5.6\,\mu\mathrm{m}$. Comparing the results from these two papers shows a surprising contradiction: in [169] the higher the repumper light intensity s_{R} is the higher loss rate β, whereas it is the exact opposite as seen in [170]. Comprehensive studies were presented in [181], studying collisions in the submicron trap. In this work the trap was first operated in the collisional blockade regime with single atom in order to determine losses due to the radiative heating and background. Then, the measurement of atoms survival in the presence of a probe beam was conducted in a three atom trap. This allowed to distinguish the light assisted collisions

from other mechanisms. The most recent work on this topic [184] provides a non-destructive way of atoms imaging within the trap and also studies the light assisted collisions. In this work ^{85}Rb is trapped in $1064\,\mathrm{nm}$ FORT while for fluorescence detection it is probed with blue detuned beam from D_1 line. Although the experimental setup is rather different from ours, the experimental method used in the paper is more similar to the one presented in this work: atoms in the dipole trap are exposed to the probe beam for a variable time and fit with the integrated equation (5.13). The table shows also a theoretical work [183] where a collisional blockade radius, which is determined by the relation between two body collision and one body collisions in the trap, was theorized for a traps of a various waists.

In our case, the loss rate due to the light assisted collisions is surprisingly high in comparison to the typical values reported from other groups, see Table 5.1. The reason for that might be the very high beams power used during the exposure of atoms to the probe beam for fluorescence imaging. In our experiment the repumper beam is of a very high intensity in comparison to other similar experiments [169] and [170]. Such a high value of β_{norm} means that either the light-assisted collisions are so strong, or that the measured value includes also the heating rate.

According to [169], losses due to the light assisted collisions should follow the model:

$$\beta = \frac{K I_{\mathrm{MOT}}}{V} \frac{I_{\mathrm{R}}}{I_{\mathrm{R}} + a I_{\mathrm{MOT}}} \tag{5.14}$$

where K is a density dependent loss rate, a reflects relative pumping rate between hyperfine states, I_{MOT} and I_{R} are intensities of cooling and repumping beams respectively. If the repumper intensity is close to zero, the loss rate should be constant regardless of the I_{MOT} value. If both cooling and repumper beams intensities are comparable, β scales with the increase of beams intensity. Moreover, losses could be additionally enhanced by detuning close to zero. Taking into account the Langevin semi-classical limit [185] for light assisted collisions, a small detuning Δ_{MOT} increases the maximum loss coefficient as follows

$$\beta_\infty = 4\pi \left(-\frac{C_3}{\hbar\Delta}\right)^{2/3} \sqrt{\frac{16 k_B T_0}{\pi m}}. \tag{5.15}$$

This tell us that using lower intensities for the flash light for fluorescence imaging would minimise the loss rate, but this is the subject of future investigations.

The final remark in this section concerns an impact of the losses in the presence of light in other measurements. Since the value for light assisted collisions is so high, it highlights

some possible challenges in other measurements (see sections 5.2, 5.3 and 5.4) where the fluorescence signal is used for atoms detection. Regarding TOF (section 5.2) and averaged Stark shift (section 5.3) experiments, the impact of light assisted collisions is negligible because of the short exposure time. The decay of number of atoms during the $50\,\mu s$ is approximately linear, therefore it is justified to take the acquired signal sig at time t_0 and scaled by the exposure time $N(t_0 + \Delta t) = \frac{sig}{\Delta t}$. In lifetime measurement, loss due to fluorescence imaging is significant as the flash pulse ($5\,\mathrm{ms}$) is very long and the majority of atoms is lost withing first $1\,\mathrm{ms}$. However, the impact of the flash pulse had been taken into account in the analysis, and since the interesting information is described by the survival probability of atoms in the absence of any MOT light, this factor does not impact outcome of the analysis.

5.6 Conclusions

As it was shown in this chapter the MOT optimization plays a crucial role for an efficient and controllable dipole trap loading. The optical design from chapter 4 was verified to work properly both for atoms trapping and for atoms detection. A series of measurement for the dipole trap characterization show that the dipole trap in the current configuration has a temperature of about $250\,\mu K$ ($250\,\mu K$ for TOF, $300\,\mu K$ estimated from Stark shift), the atomic ensemble is a Gaussian cloud with dimensions $\approx 3\,\mu m$ by $18\,\mu m$, and typically loads between 20 and 100 atoms with $2.5\,s$ lifetime. All the results are consistent within each other, apart from a very fast decay of trap population during first few milliseconds after switching off the MOT Figure 5.15, and surprisingly high loss of atoms in the presence of probe beams Table 5.1. Regarding the fast decay in lifetime measurement, it can be related to the collisions of atoms in the trap with background rubidium atoms or to the thermalisation processes. On the other hand, the high loss rate of atoms from the dipole trap during exposure to the probe beams (see section 5.5) can be presumably better controlled in the future by adjustment of the MOT parameters (decrease of repumper intensity and increase probe beams detuning).

who	isotope	λ_{FORT}	ω_0 [µm]	$s = \frac{I}{I_{\mathrm{sat}}}$	Δ [2π MHz]	β [s^{-1}]	β_{norm} [$\mathrm{cm}^3\,\mathrm{s}^{-1}$]
this work	^{87}Rb	850 nm	6	$s_{\mathrm{MOT}} = 8$, $s_{\mathrm{R}} \approx 1$	$\Delta_{\mathrm{MOT}} \approx 0$, $\Delta_{\mathrm{R}} \approx 0$	1.46×10^{2}	1×10^{-6}
[169](2000)	^{85}Rb	784 nm	26	$s_{\mathrm{MOT}} = 1.17$, $s_{\mathrm{R}} = 0$	$\Delta_{\mathrm{MOT}} = -3$, $\Delta_{\mathrm{R}} = 0$	1×10^{-5}	3.7×10^{-11}
[169](2000)	^{85}Rb	784 nm	26	$s_{\mathrm{MOT}} = 1.17$, $s_{\mathrm{R}} = 0.003$	$\Delta_{\mathrm{MOT}} = -3$, $\Delta_{\mathrm{R}} = 0$	2×10^{-5}	7.4×10^{-11}
[183](2002) theory	-	-	<1	-	-	1×10^{3}	from [169]
[183](2002) theory	-	-	11	-	-	1.6×10^{-2}	from [169]
[170](2010)	^{85}Rb	1064 nm	5.6	$s_{\mathrm{MOT}} = 14$, $s_{\mathrm{R}} = 0.003$	$\Delta_{\mathrm{MOT}} = -12$, $\Delta_{\mathrm{R}} = 0$	4×10^{-3}	2×10^{-12}
[170](2010)	^{85}Rb	1064 nm	5.6	$s_{\mathrm{MOT}} = 14$, $s_{\mathrm{R}} = 0.06$	$\Delta_{\mathrm{MOT}} = -12$, $\Delta_{\mathrm{R}} = 0$	4×10^{-4}	2×10^{-13}
[181](2012)	^{87}Rb	850 nm	<1	$s_{\mathrm{probe}} = 0.5$	$\Delta_{\mathrm{probe}} = -10$	1.2×10^{3}	2.4×10^{-9}
[181](2012)	^{87}Rb	850 nm	<1	$s_{\mathrm{probe}} = 1.5$	$\Delta_{\mathrm{probe}} = -10$	1.5×10^{4}	3×10^{-8}
[184](2015)	^{85}Rb	828 nm	1.8	$s_{\mathrm{probe}} = 25$	$\Delta_{\mathrm{probe}} = 15$ (D_1 line)	6	1.4×10^{-9}

TABLE 5.1: Comparison of measured light assisted collisions with results published by other groups. Here λ_{FORT} is the wavelength of the dipole trapping beam, ω_0 is the waist of the focused dipole trapping beam, $s = \frac{I}{I_{\mathrm{sat}}}$ is the saturation parameter where saturation intensity I_{sat} is appropriately chosen for each probe beam, Δ is the detuning of the probe beam from the atomic transition. In this work, [169] and [170] the probe beam is realised through MOT beams, therefore the saturation parameter s and the detuning Δ are given here separately for both main cooling beam s_{MOT}, Δ_{MOT} and repumper beam s_{R}, Δ_{R}. For [170] the normalized loss rate (namely the volume V) is estimated from the equilibrium state of atoms in the trap of the known trap depth (4 mK) and atoms temperature (400 µK). For [184] the saturation parameter s_{probe} is be obtained from a given power and waist of the probe beam. The probe beam is blue detuned from D_1 transition of ^{85}Rb.

Chapter 6

Conclusions and outlook

In this thesis, the design and implementation of the dipole trap apparatus are shown as a part of the bigger long-term project to implement the DQC1 algorithm with cold atoms. The project is motivated by the increasing interest in quantum computing and therefore the need for a better understanding of quantum correlations in quantum algorithms. DQC1 is an unusual algorithm in the sense that quantum discord is utilised to perform quantum computations, as opposed to entanglement. The proposal of DQC1 with atoms is based on Rydberg interactions mediated gate $cNOT$ [55], which exploits EIT and Rydberg blockade to obtain non-classical correlations between atoms. Therefore, the recent successful attempt at full Rydberg blockade [76] gives a promising perspective to implement the algorithm using cold atoms platform. The aim of this work is to design and implement the apparatus which would confine atomic ensembles into a cloud satisfying the requirements of the DQC1 algorithm. The constraints were identified based upon the original proposal [55, 70], according to which all atoms should be confined within $5\,\mu\mathrm{m}$ radius, so that the full Rydberg blockade can be achieved for $n \approx 43$ Rydberg states. The main research question is whether the dipole trap in the current stage is sufficient for performing the DQC1 protocol, and how to optimise it if it is not.

Considering the main limitations identified in similar experimental setups [107, 153, 177], the new design features several improvements. Most importantly, the lenses are now ITO-coated to prevent stray charge accumulating on the surface that would otherwise form an electric field, affecting the Rydberg atoms and thus decreasing the fidelity of the protocol. Moreover, the new system benefits from the new specially-designed high numerical aperture lenses (NA=0.53), which increase the collection efficiency of the fluorescence light from trapped atoms, but also leaves enough space inside the chamber for MOT alignment. The analysis shows that the performance of the system is very robust in terms of the optical element adjustment and that obtaining the expected imaging quality is feasible with standard

optics. The optical tests confirm that the performance of the implemented system indeed follows the predictions of the design. When the dipole trap beam is aligned according to the design, the intensity profile of the beam at the focus (where the atoms are trapped) has $1\,\mu\mathrm{m}$ waist and $4\,\mu\mathrm{m}$ Raleigh length. Regarding the imaging system, the quality of atom imaging is very high, as the measured MTF agrees with the simulation and results in the resolution which enables distinguishing two adjacent traps at a distance of $1\,\mu\mathrm{m}$ from each other. The first attempt toward dipole trapping was carried on a bigger trap than initially intended, allowing us to easily load atoms from the MOT reservoir. The dipole trap profile, which was not Gaussian, was characterised to have $6\,\mu\mathrm{m}$ waist and $28\,\mu\mathrm{m}$ of HWHM[1], while the typical number of atoms loaded into the trap varied in the range of 20 to 100 atoms. The trap's lifetime was approximatelly $2.5\,\mathrm{s}$ depending on the experimental settings. The trap typically had a temperature of $250\,\mu\mathrm{K}$, which corresponds to the atoms' ensemble of the size $\approx 3\,\mu\mathrm{m}$ across, and $18\,\mu\mathrm{m}$ along the optical axis of the trapping beam. The measurements (section 5.5) also shows that the current setting of the experiment resulted in an unusually high atoms loss from the dipole trap in the presence of the MOT light. Firstly, the measured trap's lifetime is satisfactory and implies a good vacuum. It is an important observation, since one of the main concerns is to not lose any atom from the atomic ensemble while performing the algorithm. Moreover, the quality of the vacuum was confirmed using an independent method based on the observation of the MOT's behaviour [143, 151] in the vacuum chamber. With this method, which earlier helped to detect a leak in the system and help fix it, it was confirmed that the current vacuum conditions remain below $10^{-9}\,\mathrm{mbar}$. Taking into account both dipole trap lifetime ($2.5\,\mathrm{s}$) and the established UHV conditions, a survival probability of atoms within the trap is sufficient that decoherence will not be added to the protocol.

The key finding of the trap characterisation is that the spatial distribution of the atomic ensemble is currently too big to provide full Rydberg blockade, since the length of the cloud is about $18\,\mu\mathrm{m}$ along the optical axis. Therefore, the size of the trap should be decreased, using the full capacity of the designed system. Simultaneously, the number of trapped atoms should remain in the same range as currently, with the possibility to tune it further. It was theorized in [183] that the balance between loading rate and loss mechanism determines the number of atoms in the ensemble of the given size. As shown using a Monte Carlo simulation [183], a collisional blockade typically occurs for the beams characterised by waists

[1] Since the trap profile is not Gaussian it is meaningless to talk about the Raleigh length. Instead, the value for which the intensity drops to the half of its maximum characterises the size of the trap along the optical axis.

below $4\,\mu m$ assuming the typical value of the light-assisted collisions. In this regime, the loading processes are tuned in such a way that the losses from the trap allow loading either a single atom in the trap or none. Having a dipole trap of $6\,\mu m$ waist is close to the limit, but the collisional blockade was not the dominant phenomenon in this case since we were able to observe tens of atoms in the trap. Recalling the high value of losses in the presence of MOT beams, it might suggest that the number of atoms in the trap is currently limited by losses caused by cooling beams. These results suggest that the atoms' population in the trap will decrease while decreasing the size of the ensemble if the experimental conditions are not optimized. As discussed in the last chapter, the optimization will require decreasing the power of cooling beams used, especially using a repumper.

The other factor that may limit the number of atoms in the trap is the loading rate at which atoms are being captured. The smaller trap, the smaller cross-section for atoms from the reservoir to be attracted by the trapping potential and hence the smaller loading rate. Therefore, the loading rate can be enhanced by increasing the density of atoms in the reservoir. The current MOT density does not satisfy us, as it is comparable to the dipole trap density and means that the loading rate into the trap is low and the cooling inside the dipole trap is not efficient. According to the diagnosis of the MOT, the typical atomic density was about $(2 \times 10^8$ to $50 \times 10^8)\,\mathrm{atoms/cm^3}$ while the temperature was in range $(100$ to $500)\,\mu K$. Decreasing MOT's temperature should help in trapping efficiency while increasing MOT's density will result in a higher loading rate. To conclude, the current dipole trap is not sufficient to serve its purpose in the DQC1 experiment and hence it still requires further improvements. Most importantly, the size of the trap needs to be decreased using the full capacity of the implemented system. In order to do this, the loading processes need to be optimized including a decrease of atoms losses due to the interaction of atoms with MOT light (heating rate and light assisted collisions), as well as optimisation the atoms reservoir (increase atomic density and decrease the temperature. Ideally, parameters of the atoms reservoir could be significantly improved if an additional experimental apparatus for cooling would be used, namely 2D MOT [186] or Zeeman slower [187]. This would allow for loading hundreds of atoms into a submicron trap. However, even with the current approach it is possible to optimise the system for obtaining micrometre traps but with fewer atoms [107, 153, 177]. Following the discussion above, the suggested steps toward sufficient dipole trapping with the current experimental apparatus would be:

- Performing a set of measurements to understand what causes the initial loss of atoms

from the dipole trap after switching off the MOT (Figure 5.15). The main suggestion is to vary the reservoir's parameters. The temperature can be tuned by performing additional sub-Doppler cooling step or MOT alignment optimisation. The density depends on the rubidium vapour pressure in the chamber, which is easily controllable by dispensers.

- Investigating the loss of atoms from the dipole trap due to the presence of imaging light (Figure 5.17). Depending on the results, optimising settings for more efficient fluorescence imaging.

- Systematically decreasing the size of the dipole-trapping potential while carrying the same set of characterisation and optimisation measurements, until the micrometre size trap is achieved.

The long-term goals of the project will eventually lead to the final implementation of the DQC1. It covers first testing the electrodes which are currently placed in the vacuum chamber, but are not in use yet. Then, the EIT and Raman beams will be implemented using the STIRAP method first for a demonstration of the full blockade. The design of the laser system for Raman beams is discussed in appendix C. Finally, two adjacent dipole traps will be created for an implementation of the entire DQC1 protocol, either by simply combining two beams on the cube, or by using the design based on SLM [31]. Even though a large amount of work is required before the DQC1 protocol will be demonstrated with this experimental setup, the results presented in this thesis are a significant step toward implementation of the protocols based on Rydberg blockade with the cold atoms platform.

Appendix A

Light-matter interaction

A.1 Dipole moment operator: definition and properties

The term $H_{LA}(\mathbf{R},t)$ corresponding to the light-atom interaction, deserves more attention, as it eventually results in trapping forces. The dipole moment operator by definition has form

$$\mathbf{D}_{g_j e_l}(t) = \tilde{\mathbf{d}}_{g_j e_l} \left|g_j\right\rangle \left\langle e_l\right| e^{-i\delta\omega_{g_j e_l} t} = \mathbf{d}_{g_j e_l} \left|g_j\right\rangle \left\langle e_l\right| \tag{A.1}$$

where $\delta\omega_{g_j e_l} = \omega_{e_l} - \omega_{g_j}$ is the transition frequency between states $|g_j\rangle$ and $|e_l\rangle$ and the dipole matrix elements are

$$\mathbf{d}_{g_j e_l} = \tilde{\mathbf{d}}_{g_j e_l} e^{-i\delta\omega_{g_j e_l} t} = \left\langle g_j\right| e\mathbf{r} \left|e_l\right\rangle . \tag{A.2}$$

Because the matrix elements $\mathbf{d}_{g_j e_l}$ are real $\mathbf{d}_{g_j e_l} = \mathbf{d}^*{}_{e_l g_j}$, and $\langle\Psi| e\mathbf{r} |\Psi\rangle = 0$ due to the antysymmetry of the operator $\mathbf{r}$, so the dipole matrix elements can be written as

$$\mathbf{D}_{g_j e_l}(t) = \mathbf{d}_{g_j e_l} \left|g_j\right\rangle \left\langle e_l\right| + \mathbf{d}_{e_l g_j} \left|e_l\right\rangle \left\langle g_j\right| \tag{A.3}$$

It this form (A.2) dipole matrix elements is difficult to be calculated, so it is useful to simplify the expression using the Wigner-Eckart theorem and reduce the dipole operator. The angular dependence can be factored out, which leads to expression that is a product of Clebsch-Gordan $C^{j,J',I}_{F,m_F,F',m'_F}$ coefficient and a reduced matrix element as follow:

$$\left\langle F m_F\right| e\mathbf{r} \left|F' m'_F\right\rangle = C^{j,J',I}_{F,m_F,F',m'_F} \left\langle J\right| \left|e\mathbf{r}\right| \left|J'\right\rangle . \tag{A.4}$$

Due to the Wigner-Weisskopf equation, the dipole matrix elements are related to the decay rate Γ by the formula

$$\Gamma_{J,J'} = \frac{\omega_0^3}{3\pi\epsilon_0\hbar c^3}\frac{2J+1}{2J'+1}\left\langle J\right|\left|e\mathbf{r}\right|\left|J'\right\rangle. \tag{A.5}$$

It is also possible to take advantage of some symmetries of the dipole operator and simplify the expressions for the matrix elements $\mathbf{d}_{g_j e_l}$, even though the energy level structure of an atom is usually complicated. But, if the interactions with fine structure J and J' are treated separately, in other words if light is interacting only with one of the fine-structure components at the time, and that coupling is independent of the particular sublevel, then

$$\sum_{F,m_F}\left|\left\langle Fm_F\right|er_q\left|F'm'_F\right\rangle\right|^2 = \frac{2J+1}{2J'+1}\left|\left\langle J\right|\left|e\mathbf{r}\right|\left|J'\right\rangle\right|^2. \tag{A.6}$$

This formula describes an averaged decay among given fine structure of the atom. It means that one does not have to take into consideration all possible decaying rates from each of excited sublevel into ground sublevels.

A.2 Small Atomic wave packet limit

The description of the effective motion of an atom can be considered as a motion of the whole atomic wave packet. Thus, the average force taken over the atomic wave function is

$$\begin{aligned}\left\langle\mathbf{F}(\mathbf{R},t)\right\rangle_{int} &= -\left\langle\nabla H_{LA}(\mathbf{R},\mathbf{t})\right\rangle_{int}\\ &= \sum_{j=1}^{N_g}\sum_{l=1}^{N_e}\frac{1}{2}\left\langle\left|g_j\right\rangle\left\langle e_l\right|\nabla\left(\mathbf{d}_{g_j e_l}\cdot\mathbf{E}_0(\mathbf{R})e^{-i(\omega_L t-\mathbf{k}_L\mathbf{R})}\right)\right\rangle_{int}+h.c.\end{aligned} \tag{A.7}$$

The evaluation of this expression requires assuming that the atomic wave packet is small in comparison to the optical wavelength (Small Atomic Wave Packet Limit). For a heavy system the de Broglie wavelength of atom is in general much smaller than the scale of spatial variations of the electromagnetic field. In this case it is reasonable to replace $\mathbf{R}$ with its mean

value $\bar{\mathbf{R}}$, leading to the following equivalence:

$$\begin{aligned}\left\langle |g_j\rangle \langle e_l| \nabla \left(\mathbf{d}_{g_j e_l} \cdot \mathbf{E}_0(\mathbf{R}) e^{-i(\omega_L t - \mathbf{k}_L \mathbf{R})} \right) \right\rangle_{int} \equiv \\ \langle |g_j\rangle \langle e_l| \rangle_{int} \nabla \left(\mathbf{d}_{g_j e_l} \cdot \mathbf{E}_0(\bar{\mathbf{R}}) e^{-i\left(\omega_L t - \mathbf{k}_L \bar{\mathbf{R}}\right)} \right).\end{aligned} \tag{A.8}$$

By the definition of expectation value of an operator which is an observable of the system, the averaged transition probability between two states may be calculated in term of density matrix ρ in a way:

$$\langle |g_j\rangle \langle e_l| \rangle_{int} = Tr\left[\rho |g_j\rangle \langle e_l|\right] = \rho_{g_j e_l}. \tag{A.9}$$

Appendix B

A phase Rydberg gate

The first proposal of a fast controlled gate, based on the Rydberg blockade phenomenon, was presented in 2001 [112]. The proposed controlled gate can perform a conditional phase gate on a system of qubits, but for the sake of simplicity a two atom system will be considered.

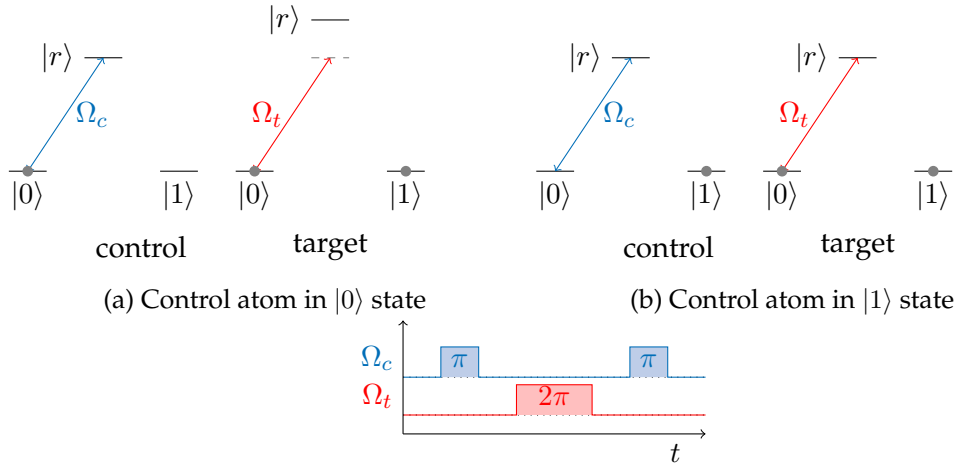

(a) Control atom in $|0\rangle$ state

(b) Control atom in $|1\rangle$ state

(c) Laser sequence

FIGURE B.1: Scheme of controlled phase gate based on Rydberg blockade. Both of atoms are initialized before performing a gate in a superposition of $|0\rangle$ and $|1\rangle$. The order of application optical pulses is as follows: π pulse applied to control atom, 2π pulse responsible for phase shift applied to ensemble atom, and again π pulse applied to control atom to restore it into its initial state.

Figure B.1 presents the concept of Rydberg gate. Both atoms are prepared in pure states and both possess a three level energy structure. The hyperfine structure of ground levels is exploited for encoding information in $|0\rangle$ and $|1\rangle$, and $|r\rangle$ represents the Rydberg state. First, a π pulse[1] of laser light coupling states $|0\rangle$ and $|r\rangle$ is applied to the first, so-called

[1] π pulse (and similarly 2π etc. pulses) is a notation used to indicate an effect of the coupling laser light action on atoms. The ultimate effect depends on laser intensity, frequency and duration of the pulse, because the Rabi frequency is dependent on all these parameters. So for instance for 2π pulse, the atom which was in the given state will return to the same state at the end of the laser pulse.

control, atom. Then, the second atom is exposed to a 2π pulse with the same driving frequency, and again the same π pulse is applied to the first atom (Figure B.1). If the control atom was initially in a state $|0\rangle$, the coupling light excites it to the Rydberg state and that results in shifting the energy of a Rydberg double excited state. Due to the Rydberg blockade phenomenon, the second pulse applied to the ensemble atom becomes off-resonant and the ensemble atom remains in its initial state. In the opposite case when the control atom was prepared in a state $|1\rangle$, a 2π pulse results in a π phase shift. It is visible from this example, that based upon the initial state of the control atom, the target atom experienced or not a phase shift.

Appendix C

Raman beams design

Driving transitions between two hyperfine levels of ground state through an excited state is carried by bichromatic laser beams set in so-called Raman configuration. Various approach can be used to produce bichromatic laser beam, such as diode modulation, phase locking of two separate lasers, or modulation of the single laser beam. The design proposed here consists of a single frequency tuneable NIR laser source locked to a suitable transition from the D_2 line of ^{87}Rb, from which two sidebands are created, corresponding to the hyperfine energy splitting ($\pm \sim 3.4$ GHz) Figure C.1a. Sidebands appear when a single frequency beam propagates through an electro optic modulator (EOM) driven by ~ 3.4 GHz sinusoidal signal. After that the laser spectrum consists of three frequencies, from which the original unmodulated wavelenght must to be filtered out. This situation is presented in Figure C.1b.

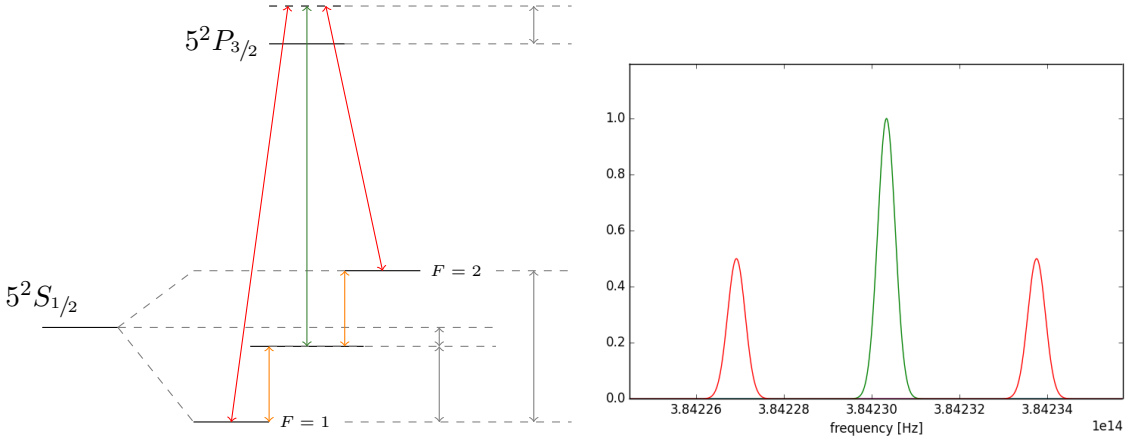

(a) Laser coupling scheme

(b) Beam spectra

FIGURE C.1: Laser coupling scheme and beam spectra for Raman beams. (a) Energy level and laser coupling scheme for Raman beams. The transition to which laser source is locked to is depicted by green colour. Creating a sideband marked as orange arrows results in two resonant beams (red arrows). (b) Simulation of Raman beam spectra. Colours correspond to the specific transitions from scheme (a).

The filtering of an unwanted frequency can be done by an optical resonance cavity, whose resonance frequency overlaps only with the frequency of sidebands. All technicalities regarding to the cavity design are described in section C.1. Next, the intensity of the beam is stabilized by an AOM with feedback loop. Afterwards, an additional AOM is placed for controlling the beam alignment and hence 'switch on and off' signal coming into experiment. Eventually the beam is coupled to the experiment by a single-mode fibre which provides a Gaussian spatial mode for the Raman beams.

C.1 Cavity design

One of the key elements in Raman beams path is the filtering cavity. An optical cavity (or optical interferometer) is a system of two or more mirrors, which are arranged in such a way that light propagates in a closed path. There are two basic types of interferometers: standing wave resonators or traveling wave resonators. Designing a cavity, that can amplify a given frequency, requires considering many significant element such as the geometry of the cavity, the properties of the optics used, the properties of the mechanical elements responsible for a fine adjustment of optics (piezo actuator, optic mounts) and corresponding electronic devices. The standard approach of regulating a cavity length is mounting one of the cavity mirrors on a piezoelectric crystal, which can typically control cavity length up to 0.0001 μm. It is also important to design a system of optics responsible for properly injecting laser light into the cavity. Due to the simple geometry non-confocal Fabry-Perot interferometer was chosen, consisting of two spherical mirrors with the same radius.

C.1.1 Resonance frequencies

A laser beam is coupled into an optical resonator and propagates inside its cavity many times on the same path. Due to the interference, only eigenmodes are sustained by the resonator, while other frequencies are suppressed by destructive interference. Considering two coaxial mirrors separated by distance d, resonance frequencies ν_{res} satisfy equation

$$\frac{\nu_{res}}{FSR} = m \tag{C.1}$$

where m is an integer number and Free Spectral Range (FSR) is the spacing between cavity resonance fringes m and $m+1$ and is described by formula

$$FSR = \frac{c}{2d}. \tag{C.2}$$

The performance of the resonator depends not only on the geometry, but also on the quality of the mirrors. Any given mirror can be characterized by its reflection coefficient r. Then, the finesse of the cavity is given by

$$F = \frac{\pi\sqrt{r}}{1-r}. \tag{C.3}$$

If the cavity losses are low, then finesse can be also described by

$$F = 2\pi b \tag{C.4}$$

where $b = \frac{1}{losses}$ describes all resonator intensity losses. The cavity finesse is a parameter which helps to characterise interference fringes, which have essentially Lorentzian shape for a cavity with low losses. The width of the resonance fringes at half maximum $FWHM$ is given by

$$FWHM = \frac{FSR}{2\pi b}. \tag{C.5}$$

The quality of the resonator, which is a measure of the capability to store the energy, can be calculated from formula

$$Q = \frac{\nu}{FWHM}. \tag{C.6}$$

The elements of the cavity which were taken into account durig the design process are: the reflectivity of mirrors, the distance between mirrors, the piezo accuracy and accuracy of positioning of the optics mounts. The length of the cavity resonator corresponding to a free spectral range matching energy difference of $\left|5S_{1/2}, F=1\right\rangle$ and $F=2$ is $d = 21.93\,\mathrm{mm}$. However, to understand how these parameters, including the cavity length, are related to each other one needs to consider when the resonance frequencies are matching the sidebands and what is the tolerance for the cavity to still perform well.

It was assumed in the simulations that the distance between mirrors reaches the cavity performance limit when the sideband peak decreases to 50% of its initial value. There are two possible scenarios when the cavity is not tuned to the sidebands. The first one occurs

when free spectral range of the cavity differs significantly from the separation between sidebands Figure C.2a. Then, even if one of sideband matches a resonance frequency, the second is too far from resonance frequency and is suppressed. This problem occurs when the cavity length is misaligned significantly, tens of microns, from the best position. The second scenario is associated with the traveling of resonance peaks across frequency scale due to (C.1) formula, even though the cavity FSR is very close distance between sidebands Figure C.2b. A small change in cavity length results in a small difference in FSR value, which is multiplied by a huge integer number so that the resonant frequency could match a sidebands frequencies. This is why even the small misalignment of cavity length leads to mismatching between resonance frequencies and sidebands frequencies. Matching tolerance depends on

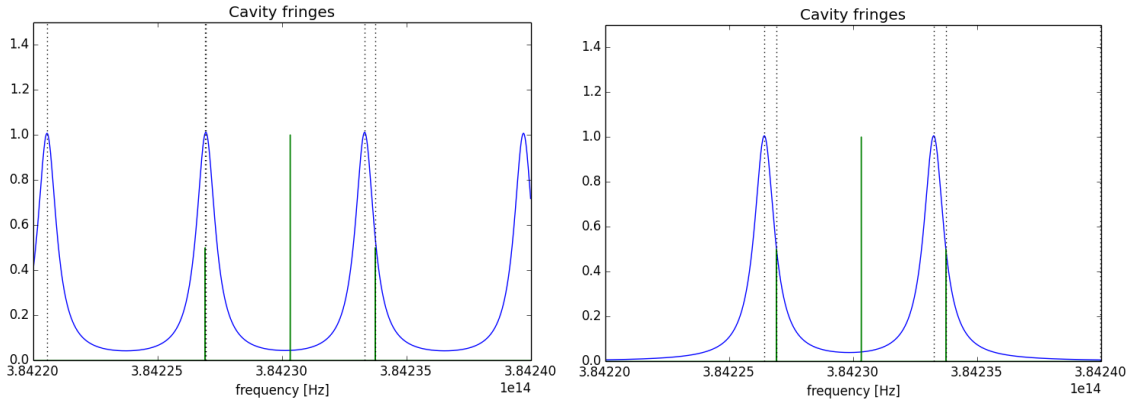

(a) Scenario 1 (b) Scenario 2

FIGURE C.2: Simulation of the cavity performance in terms of mirror separation distance d. Green peaks represent the frequency constituents of laser beam before filtering, while blue peaks are the resonance frequencies of the cavity. (a) One of sidebands is covered by a resonance frequency, whilst the second one is away from the centre of the resonance peak at a distance of $\frac{FSR}{2}$. (b) Both of the sidebands are away from the centre of the resonance peaks at a distance of $\frac{FSR}{2}$.

the reflectivity of mirrors, as it is determined by width of resonance fringes. The results of simulation are presented in Table C.1.

Reflectivity r %	Finesse	FWHM MHz	distance accuracy (scenario 1) μm	distance accuracy (scenario 2) μm
0.90	29.80	229.3	368.0	0.0131
0.95	61.24	111.6	179.1	0.0064
0.98	155.50	43.9	70.5	0.0026
0.99	312.58	21.87	35.1	0.0013

TABLE C.1: Cavity properties and accuracy in terms of mirror reflectivity.

C.1.2 Mode matching

The spatial distribution of the electromagnetic field inside the cavity depends on the curvature of the spherical mirrors. Modes which are supported by a resonator have a well-defined and discrete spatial structure. The most basic and desired mode is a Gaussian mode. Any cavity can be characterised by its natural waist W_{cav} which is the function of the mirrors curvature R_{cav} and a cavity length d

$$W_{cav} = \sqrt{\frac{\lambda}{\pi}\sqrt{\frac{d}{R}\left(R_{cav} - \frac{d}{2}\right)}} \tag{C.7}$$

Mode matching is based on injecting laser beam into cavity in such a way that the size and focal plane of injected beam overlaps with natural waist of the cavity. Mode matching allows the supporting of Gaussian mode and suppressing the generation of higher spatial modes, which in general have different resonance modes.

In order to achieve mode matching, an additional optical components are required before the cavity. The evaluation of the design and the optical path it is based on the ABCD matrices method for Gaussian beam. If z is the propagation axis, the amplitude of the beam can be described by

$$U(\mathbf{r}) = E_0 \frac{W_0}{W(z)} e^{-\frac{\rho^2}{W^2(z)}} e^{ik\left(z + \frac{\rho^2}{2R_c(z)}\right)} \tag{C.8}$$

where $W(z)$ is the transverse beam size and $R_c(z)$ is the wavefront curvature. In order to manipulate a Gaussian beam a complex-valued parameter q, which describes both the spatial size and curvature of the beam, is introduced in a form

$$\frac{1}{q} = \frac{1}{R_c} + i\frac{\lambda}{\pi W^2}. \tag{C.9}$$

In terms of ABCD matrices method, a Gaussian beam can be expressed by a vector $\begin{pmatrix} q_2 \\ 1 \end{pmatrix}$ which follows the equation:

$$\begin{pmatrix} q_2 \\ 1 \end{pmatrix} = k \begin{pmatrix} A & B \\ C & D \end{pmatrix} \begin{pmatrix} q_1 \\ 1 \end{pmatrix}, \tag{C.10}$$

where $\begin{pmatrix} A & B \\ C & D \end{pmatrix}$ represents an optical element. Following this equation an input q_1 parameter is transformed into q_2 in a way

$$q_2 = \frac{Aq_1 + B}{Cq_1 + D} \tag{C.11}$$

In the design the following optical elements were simulated:

- Transmission through a thin lens of focal length f

$$\text{Lens} = \begin{pmatrix} 1 & 0 \\ -\frac{1}{f} & 1 \end{pmatrix} \tag{C.12}$$

- Propagation through a medium, where d is the length of propagation and n is index of refraction:

$$\text{Propagation} = \begin{pmatrix} 1 & \frac{d}{n} \\ 0 & 1 \end{pmatrix} \tag{C.13}$$

- Refraction at a spherical boundary of radius R entering medium characterized by refraction index n_2 from medium characterized by n_1

$$\text{Refraction} = \begin{pmatrix} 1 & 0 \\ -\frac{n_2 - n_1}{n_2 R} & \frac{n_1}{n_2} \end{pmatrix} \tag{C.14}$$

- Reflection from a spherical surface having radius R.

$$\text{Reflection} = \begin{pmatrix} 1 & 0 \\ \frac{2}{R} & 1 \end{pmatrix} \tag{C.15}$$

After considering many options, a simple path including one $f = 100\,\mathrm{mm}$ lens and a given input spot size about 0.39mm was selected as relatively easy for aligning. The distance between the mode matching lens and the cavity must be $80\,\mathrm{mm}$.

C.2 Final setup

The NIR laser source is provided by high intensity Toptica laser (DL 100), which can achieve a power up to 300mW and whose typical linewidth is 100kHz to 1MHz. The laser will be

frequency-locked using Modulation Transfer Spectroscopy (MTS) based on Toptica EOM with 10 MHz bandwidth. The laser beam passes through free-space EOM having 6GHz of bandwidth, and after that will be coupled by optical fibre (Thorlabs P1-780A-FC 1) into the cavity system. The input collimator of optical fibre (Thorlabs PAF-X-7-B) has an input diameter about 2mm, while output collimator (Thorlabs PAF-X-2-B) provides 0.33 mm of output beam diameter. Then the collimated output beam is focused by 100mm, AR coating, matching lens (Thorlabs LA1207-B) mounted on XYZ Translation Mount for Ø1/2" Optics (Thorlabs CXYZ05). A translation stage provides the necessary accuracy in adjusting mode matching. The converging beam is entering now a cavity consisting two -$100\,\mathrm{mm}$ plano-concave lenses (Laseroptik L-07865), where the plane surface is coated with anti-reflection layer ($r < 0.25\%$) and the spherical surface is coated by high reflection coating ($r = 98\% \pm 1\%$). One of the cavity lenses is attached to a piezo ring (piezoststemjena HH1-2515-20), which can adjust a cavity length with 0.0002 μm resolution. An additional lens with piezo ring is mounted on Z-Axis translation mount (Thorlabs SM1Z) which has $1\mu m$ resolution and the maximum range of traveling is $1500\,\mu\mathrm{m}$. After the cavity, a 100mm lens collimates the laser beam which is sent to an intensity beam stabilizer and further to the experiment.

Appendix D

Miscellaneous data for dipole trap and imaging system design

D.1 Discussion over methods used in design process

Zemax uses two different methods for modeling optical systems. The first and the most popular method is ray tracing where lines normal to the surface of the constant phase (wavefront) are called rays. Rays are propagated along straight lines through optical elements according to geometrical optics laws and do not interfere witch each other. Ray propagation allows to obtain such a parameters like effective focal length and hence F number and Airy radius, RMS spot radius, ray aberration and many more. Although the mentioned parameters based on ray tracing represent geometrical optics, Zemax also includes some diffraction computations (e.g. diffraction PSF or MTF) based on ray tracing using so called śingle step approximation. This simple approximation assumes that all of the important diffraction effects come from the exit pupil and that they are directly reflected on the image. First rays are used to propagate through the system, find exit pupil and the ray distribution on this surface. Then the amplitude and phase are computed for the exit pupil for the grid of rays, where subsequently an FFT algorithm is performed to find a complex amplitude wavefront. Next a diffraction computation propagates the complex wavefront to the region near focus where the imagine plane is set. This method is clearly not accurate for a systems with a big exit pupil aberrations, what is typically the case for a systems with the large angle of a chief ray exceeding about $20°$. Fortunately a ray based diffraction analysis is appropriate for the design presented in this work, where both object and image are close to the optical axis.

On the other hand, ray tracing fails for several cases including: when the diffraction effects far from focus are of interest; and when the propagation of the beam needs to take

its Gaussian nature into account. These problems are being dealt with by using a different approach to analyse the optical system which is called Physical Optics Propagation (POP), which uses wavefront propagation. The Huygens-Fresnel principle states, that each points of the wave can be considered as a source of a secondary spherical wavelets, which mutually interferes which each other while propagating through a free space ([188] chapter VIII). In Zemax, wavefront which is represented by a lattice of discreet points, is subsequently propagated through the free space (according to [154] and [189]) between optical surfaces, and then an optical transfer function is computed when the wavefront passes through each of an optical surfaces. Both of the mentioned cases are interesting for us while analysing dipole trap profile. POP allows to compute the irradiance of the beam for each point in free space, and eventually to compute three dimensional model of dipole trap profile.

D.2 Detailed remarks on lens performance

This appendix consist of some detailed ray tracing analysis of the lens performance for the configuration with lens 355561 and collimated light of trap beam. Although the trapping beam is far detuned and hence a maintainance of the beam frequency with a high accuracy is not necessary, a change in laser wavelength might cause the shift of the trap position along optical axis.

As we can see on Figure D.1, the BFL depends on used wavelength, but the difference is not so significant and the fluctuation of beam wavelenegth in range of 5nm results only in about $4\,\mu\mathrm{m}$ shift of diffraction focus. Meanwhile, the same figure shows the significant

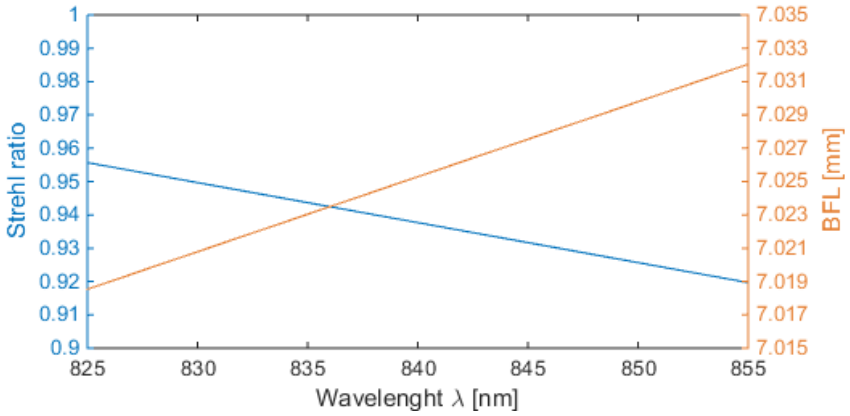

FIGURE D.1: Simulation of the lens's performance and BFL in terms of dipole trap beam wavelength. BFL is calculated for the collimated input beam. Entrance pupil diameter: 11mm. Data set was obtained with Zemax OpticStudio.

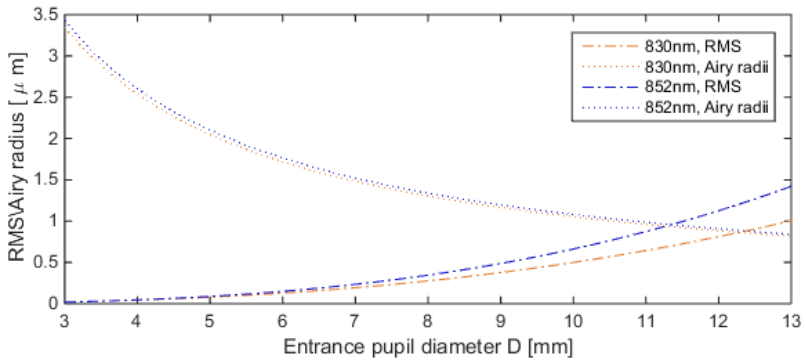

FIGURE D.2: Simulation of the dependence of the spot size (RMS and Airy radius) at the focal plane in terms of the diameter of input aperture. Yellow colour designates $830\,\mathrm{nm}$ wavelength, while blue is related to $852\,\mathrm{nm}$. Data set was obtained with Zemax OpticStudio.

difference in Strehl ratio in respect of used wavelength. The reason why Strehl ratio differs so much is the presence of spherical aberration, which decreases as the wavelength is getting closer to 780nm, what makes perfect sense as the lens curvature was optimised for this wavelength.

Having such a significant aberrations means that the selection of a proper optical aperture of the beam needs to be done carefully. The consequences of changing the beam diameter are presented in Figure D.2. Decreasing of the diameter obviously reduces the impact of aberrations on the lens performance, but also increases the waist of beam due to diffraction limit (4.2). The most confine possible trap for this configuration is obtained when RMS and Airy radius are equal, which means that the diffraction limit is achieved. Further decrease of diameter results in increasing of the spot size by diffraction. For 852nm trapping beam the most optimal configuration is when the aperture of illuminated lens is equal 11.3 mm.

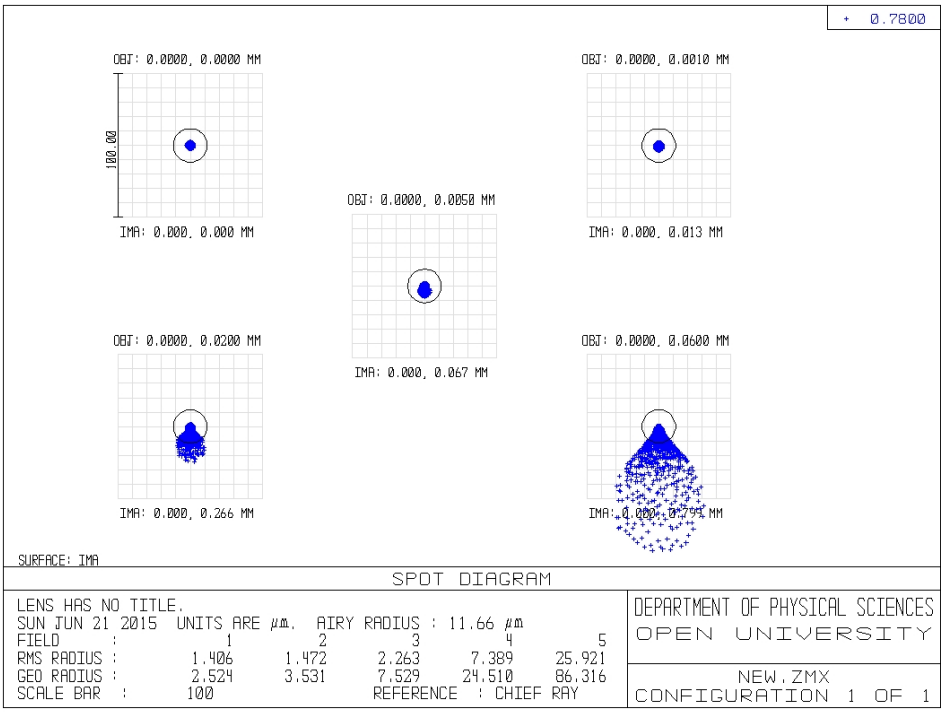

FIGURE D.3: Spot diagrams of 780 nm light for different fields of view. On axis, 1, 5, 20 and 60 µm away from optical axis. Data set was obtained with Zemax OpticStudio.

Appendix E

Technical data for operating ICCD

E.1 Details for conversion of digital signal into photons

The formula used for conversion of digital counts N_{counts} into the number of photons N_{photons} follows equation:

$$N_{\text{photons}} = \frac{N_{counts}\text{PAG}}{\gamma_0 \gamma_1 \eta} \tag{E.1}$$

where:

setting			value	units
η			10 %	photocathode electron per photon
γ_0			2.65	CCD electrons per photocathode electron
γ			Equation E.2	dimensionless
PAG	5 MHz	x1	4.8	CCD electrons per A/D count
		x2	2.4	
		x3	1.1	
	3 MHz	x1	4.7	
		x2	2.3	
		x3	1.0	
	1 MHz	x1	4.7	
		x2	2.3	
		x3	1.0	
	50 kHz	x1	4.8	
		x2	2.3	
		x3	1.0	

TABLE E.1: The detailed values of ICCD performance for various settings. Definitions of settings are explained in the text.

- η - Quantum efficiency of the photocathode. The value presented in the Table E.1 corresponds to the ratio of generated electrons to the number of initial photons for 780 nm wavelength.

- PAG – The averaged value of how many electrons trapped in CCD is required to generate one digital count. This value depends on two settings, the readout rate (5 MHz, 3 MHz, 1 MHz or 50 kHz), and the preamplifier gain (x1, x2, x4). The slower readout rate, the lower noise. And also noise decreases with the higher preamplifier gain.

- γ_0 - Minimum System Gain. A numbers of electrons measured in the CCD for every electron originating in the intensifier for zero MCP voltage (see Figure 5.3).

- γ_1 – Relative gain corresponding to applied MCP voltage (see Figure 5.3). It shows how the gain for a given settings compares to the gain with 0 voltage applied on MCP. The relative gain is shown on Figure E.1.

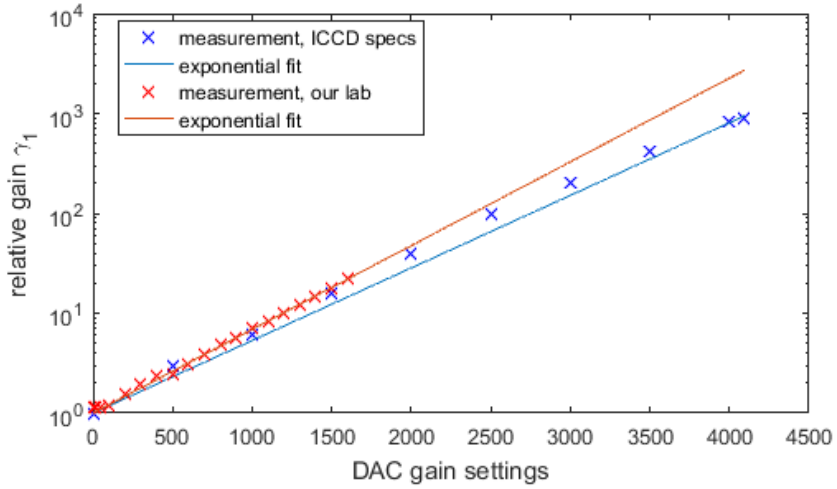

FIGURE E.1: The relative MCP gain of the ICCD camera used for dipole trap detection. Values on horizontal axis represent the software settings, namely DAC gain. Blue and red data represents measurements performed by the producer and in our laboratory respectively. The data (ICCD specs) are fitted with the exponential function, but as it is visible from the plot the response of the intensifier is not purely exponential in the entire range.

Data marked in blue on Figure E.1 were measured by the ICCD producer, and cover the entire range of provided gain. The MCP response is approximately exponential to the applied gain and the maximum relative gain is about 1×10^3 times. However the response of the MCP deteriorates with time when operated at a high voltage, therefore it is good to avoid running the ICCD with high gains if possible. In the scope in which the camera is usually operated, 0 to 1700 DAC gain, the additional calibration was performed in our laboratory for better fit, and the values for the relative gain can be

approximated from the formula

$$\gamma_1 = \exp(0.00193 \cdot \text{gain}) \tag{E.2}$$

where gain denotes DAC gain in software settings.

E.2 Noise and light pollution

E.2.1 Sources of noise generated on ICCD:

- Shot noise caused by statistical nature of detection of photons by CCD.
- Dark current, which is an electronic noise generated by the CCD camera itself even during absence of photons. By additional cooling the CCD chip one can remove much of noise. For instance decreasing temperature from $0\,^{\circ}\mathrm{C}$ to $-20\,^{\circ}\mathrm{C}$ reduces noise by a factor of 10, resulting in dark current at the level 0.4 electrons per pixel per second.
- Readout noise, which is a feature of the on-chip amplifier while converting the collected charge into analogue voltage. This noise depends on both readout rate and the pre-amplifier gain as shown in Table E.2. Slower readout rate benefits from a substantial improvement on noise.

readout rate	PAG	Single pixel noise [electrons]
5 MHz	x1	32.8
	x2	21.1
	x3	16.9
3 MHz	x1	19.2
	x2	14.3
	x3	12.5
1 MHz	x1	11.5
	x2	8.8
	x3	8.3
50 kHz	x1	5.6
	x2	5.3
	x3	5.0

TABLE E.2: Readout noise for different ICCD settings.

A typical noise for our setup is presented on Figure E.2a. To increase signal to noise ratio, it if recommended to take many acquisition for the experiment and average the results.

E.2.2 Light pollution

Other type of problems impacting the quality of image are sources of light pollution:

- Light pollution coming from MOT beams reflected on lenses and the vacuum chamber windows.
- Stray light from atoms in MOT surrounding a dipole trap.

Stray light causes an additional noise, which has a statistical nature and might be much above the typical CCD's noise. Figure E.2a shows the ICCD response in the absence of

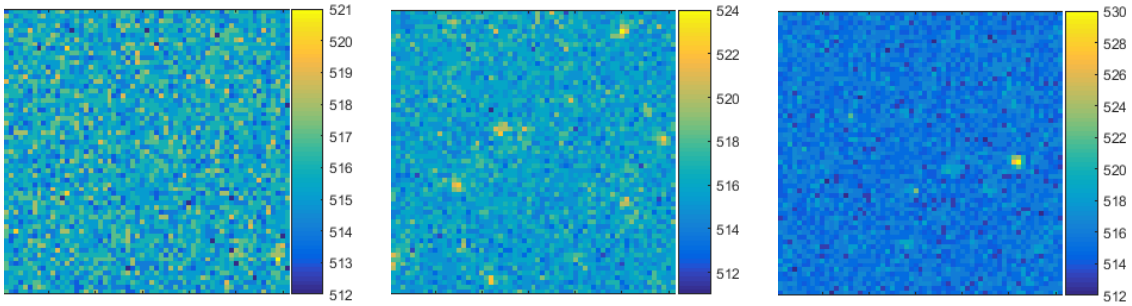

(a) Closed shutter (b) Opened shutter (c) Opened shutter

FIGURE E.2: ICCD noise due to stray light. ICCD settings are: $50\,\mu s$ exposure time, $-20\,^{\circ}C$ CCD cooling, $50\,kHz$ readout rate. (a) Image acquired by ICCD when the shutter is closed. It represents both the dark current and readout noise. (b-c) Images acquired by ICCD when the shutter is opened, and the ICCD gating is in *Fire Only* mode.

light. Our setup was tested under various conditions leading to the conclusion that the noise, mean value $\langle N_{\text{counts}} \rangle$ of all pixels and its standard deviation σ_{noise}, does not change in the presence of laboratory lights when operating in fire only mode with gain up to 20 times. For this setup there are no events encountered above the noise level described as $\langle N_{\text{counts}} \rangle + 6\sigma_{\text{noise}}$.

However, in presence of MOT laser beams the noise due to the light pollutions starts becoming visible. The main source of noise comes from reflection of cooling beams inside the chamber. Stray light from only optical bench results in $(0.4 \pm 0.1)\,\text{events}$ on average per 60x60 pixels image and it raises up to $(2.2 \pm 0.3)\,\text{events}$ when the camera is exposed for the MOT beams reflected from optics inside of the vacuum chamber. The ICCD imaging system is shielded from the optical bench by encapsulating this part of optics in the separate box, therefore this noise is mostly dependent on the beams alignment and theirs intensity inside the chamber.

Figures E.2b and E.2c shows two images acquired by ICCD from a series of 50 images in total. As it is visible on Figure E.2b, some events are clearly above the noise level, but there are also some events which seems to have different structure than typical CCD noise, but they can not be discriminated as they are within the noise level. On Figure E.2c the event which is very strong in comparison to the standard CCD's noise is presented. This kind of events might be very misleading while performing the experiment, as they might be mistakenly interpreted as a signal form an atom.

The mechanism underlying the additional noise related to the stray light is based upon the build of the ICCD, specifically it is due to the intensifier (see Figure 5.3). When a stray photon hits the photocathode its response undergoes the same statistical rules as shot noise. A single photon which acts on the photodiode might cause an event and generate an electron accordingly to the quantum efficiency described in Table E.1. The electron is subsequently amplified by the MCP plate, whose resolution was characterised to be $19\,\mu\mathrm{m}$ [**Technology2012**], and detected by the CCD as a Gaussian signal.

Since the nature of the noise is statistical, it can be successfully suppressed by averaging single acquisitions over many repetitions. Figure E.3 compares the signal for both closed an opened shutter over 50 cycles, which shows that both of the signals do not differ between each other. Figure E.3b is not entirely uniform and the upper part consists of brighter pixels

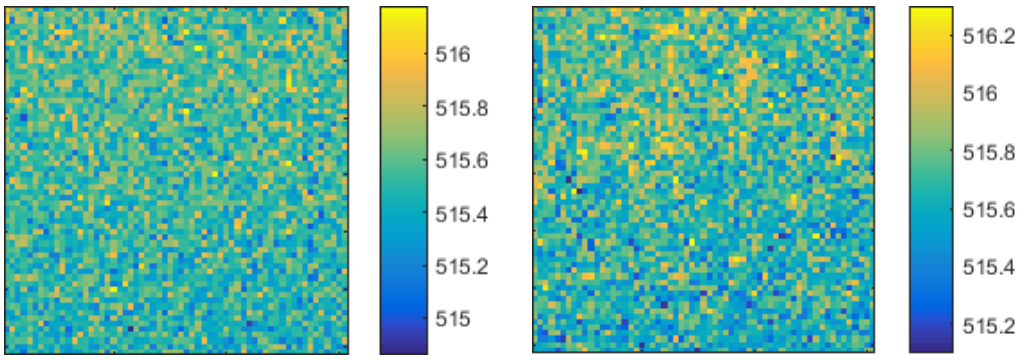

(a) Closed shutter (b) Opened shutter

FIGURE E.3: Comparison of the nature of the noise due to stray light (opened shutter) to the intrinsic dark current noise (closed shutter) of the ICCD. The images represents an average over 50 repetitions. (a) $\langle N_{\text{counts}} \rangle = 115.5$, $\sigma_{\text{noise}} = 0.2$ (b) $\langle N_{\text{counts}} \rangle = 115.7$, $\sigma_{\text{noise}} = 0.2$

than the bottom of the image. It is caused possibly by the light pollution, which reveals some scattering pattern. It is solved by taking background images with the same settings and under the same conditions as the imaging acquisition during the experiment.

E.3 Experimental settings

experiment	ICCD settings					
	PAG	readout rate	DAC gain	temp.	gating	exp. time
TOF subsection 5.2.3	x1	50 kHz	1600	−20 °C	fire only	50 µs
Stark Shift subsection 5.3.2	x1	50 kHz	1500	−20 °C	fire only	50 µs
Lifetime subsection 5.4.2	x1	50 kHz	1500	−20 °C	fire only	5 ms
LAC section 5.5	x1	50 kHz	1500	−20 °C	fire only	(10 to 5000) µs

TABLE E.3: Detailed acquisition settings for dipole trap measurements. temp. denotes the cooling temperature at which the CCD is operated, gating mode corresponds to settings of the intensifier.

E.4 ICCD response to trigger

When waiting for the external trigger, the camera performs continuously *External Keep Clean Cycle*, which ensures that charge build up on the CCD is kept to a minimum. Once the trigger is received the routine needs to be accomplished, and then the acquisition of the CCD starts. The routine consists of a one charge shift in the vertical direction followed by the one horizontal shift in a cycle controlled by the internal ICCD clock. Because just a single charge transfer from pixel to pixel is relatively long and takes 6.5 µs, while the total size of the ICCD is 1024x1025 pixels, the *External Keep Clean Cycle* was designed in a way to minimize the delay before the actual image acquisition. Typical values of the acquisition delay were measured and listed in Table E.4. Since the repetitions of an experimental sequence and the

readout rate	delay
5 MHz	(20 to 30) µs
3 MHz	(20 to 30) µs
1 MHz	(20 to 35) µs
50 kHz	(60 to 90) µs

TABLE E.4: The acquisition delay due to the mismatch of the internal clock of the ICCD and the sequence repetitions.

internal ICCD's clock are most likely not synchronized, the typical acquisition delay varies over time.

E.5 Apparatus response for triggers

apparatus	delay
MOT coils	50 µs
AOM in single pass	1.6 µs
Dipole trap intensity	13 µs

TABLE E.5: The delay in apparatus response for a trigger signal. Definitions of the parameters are explained in the text.

- MOT coils - the delay time shows how much time is required to switch off the curent in the coils from its maximum value 3 A to zero. The crucial part is the optimisation of the coil driver, which might result in the delay as long as $5\,\mathrm{ms}$ when not being optimised, or $50\,\mu\mathrm{s}$ after driver optimisation.

- AOM in single pass - Model of the AOM used in the experiment is ISOMET 1205C-2-804 with PbMoO4 crystal. According to the specs the minimum time required to switch between different frequencies is described by *Access Time* and equals $1.6\,\mu\mathrm{s}$ for this model [190]. The response of AOM for changing the amplitude of frequency of the RF signal, depends on how long does it take for the acoustic wave to travel through the crystal and reach the laser beam affecting its deflection. Since the crystal is $6\,\mathrm{mm}$ long and the acoustic velocity is $3.63\,\mathrm{mm}/\mu\mathrm{s}$, it takes $1.65\,\mu\mathrm{s}$ to travel through the entire crystal. Therefore, the time required to response is less or equal *access time*.

- Dipole trap intensity - In the configuration when the optical fibre was bypassed, the role of switching off the beam intensity was taken by the modulation of the diode current. The delay for a diode intensity was estimated from the decay time of the current supplied by the driver.

Appendix F

Details for experimental sequence for temperature measurements

After the «off» stage the camera trigger is fired in preparation for the ICCD acquisition. Taking into account the typical delay of ICCD's response, which is not constant and varies in the range $(60 \text{ to } 90)\,\mu\text{s}$ as it was explained in section E.4, the next steps must be adjusted in such a way that acquisition takes place when the probe beams are on during the «flash» stage. To achieve that, the dipole trap beam is switched off a time dt' after the camera is triggered (Figure 5.5), and during the next variable time dt the atoms experience a free expansion. In total both stages are equal to the maximum trigger delay $dt' + dt = 90\,\mu\text{s}$. Then, the probe beams are switched to enable the fluorescence signal. The exposure time of the camera acquisition (exp. $= 80\,\mu\text{s}$) is larger than the flash duration (flash $= 50\,\mu\text{s}$), to ensure that the entire fluorescence signal is acquired by the camera.

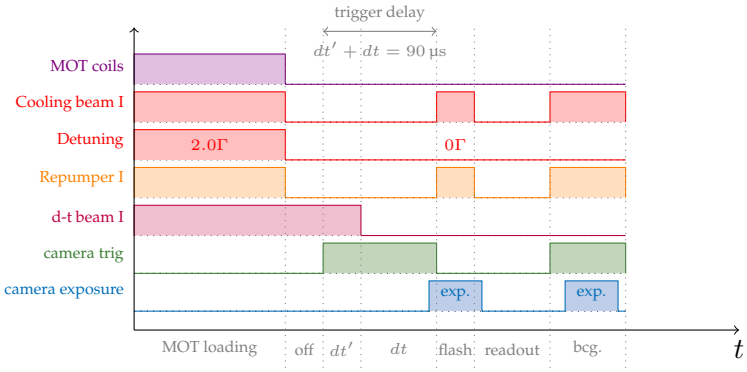

(a) Sequence variant for measurement of the cloud expansion

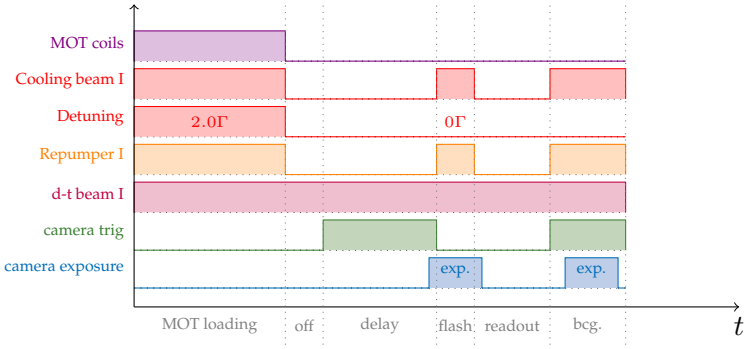

(b) Sequence variant for measurement of the atoms in the dipole trap

FIGURE F.1: Detailed scheme of the experimental sequence for Time of Flight measurement. The subsequent stages are: **MOT loading**= 8 s, **off**= 10 ms, **dt'**= variable time, **dt**= variable time, **exp.** = 80 µs, **flash**= 50 µs, **cam. ref.** = 1.4 s, **bcg.** = 1 ms. Names of the events/settings and corresponding values marked on the vertical axes: **MOT coils** - current applied to the antihelmholtz coils (0 to 2.3) A, **Cooling beam I** - the total intensity of the cooling beams (0 to 15.3) mW/cm^2, **Detuning** - the detuning of the cooling beam from the cooling transition 0 to 2Γ, **Repumper I** - intensity of the repumper beam (0 to 2) mW, **d-t beam I** - intensity of the dipole trap beam (0 to 130) mW, **camera trig** - TTL signal, **exp.** - the exposure time when the ICCD acquires the signal.

Bibliography

[1] H. J. Kimble et al. "Conversion of conventional gravitational-wave interferometers into quantum nondemolition interferometers by modifying their input and/or output optics". In: *Physical Review D* 65 (2001), p. 022002.

[2] B. P. Abbott et al. "Observation of gravitational waves from a binary black hole merger". In: *Physical Review Letters* 116 (2016), p. 061102.

[3] M. Schmidt et al. "A mobile high-precision absolute gravimeter based on atom interferometry". In: *Gyroscopy and Navigation* 2 (2011), pp. 170–177.

[4] Y. Bidel et al. "Compact cold atom gravimeter for field applications". In: *Applied Physics Letters* 102 (2013), p. 144107.

[5] B. J. Bloom et al. "An optical lattice clock with accuracy and stability at the 10(-18) level." In: *Nature* 506 (2014), pp. 71–75.

[6] J. King et al. "Benchmarking a quantum annealing processor with the time-to-target metric". In: *arXiv* 1508.05087 (2015).

[7] A. Douglass, A. D. King, and J. Raymond. "Constructing SAT Filters with a Quantum Annealer". In: *Theory and Applications of Satisfiability Testing – SAT 2015*. Ed. by M. Heule and S. Weaver. Vol. 9340. Springer, Cham, 2015, pp. 104–120.

[8] A.D. Córcoles et al. "Demonstration of a quantum error detection code using a square lattice of four superconducting qubits". In: *Nature Communications* 6 (2015), p. 6979.

[9] S. Bravyi et al. "Tapering off qubits to simulate fermionic Hamiltonians". In: *arXiv* 1701.08213 (2017).

[10] S. Debnath et al. "Demonstration of a programmable quantum computer module". In: *Nature* 536 (2016), pp. 63–66.

[11] E. Knill et al. "A scheme for efficient quantum computation with linear optics". In: *Nature* 409 (2001), pp. 46–52.

[12] S. Gasparoni et al. "Realization of a photonic controlled-NOT gate sufficient for quantum computation". In: *Physical Review Letters* 93 (2004), p. 020504.

[13] J. Carolan et al. “Universal linear optics”. In: *Science* 349 (2015), pp. 711–716.

[14] P. Wolfgang. “Electromagnetic traps for charged and neutral particles”. In: *Reviews of Modern Physics* 62 (1990), pp. 531–540.

[15] M. G. Raizen et al. “Ionic crystals in a linear Paul trap”. In: *Physical Review A* 45 (1992), p. 6493.

[16] J. I. Cirac and P. Zoller. “Quantum computations with cold trapped ions”. In: *Physical Review Letters* 74 (1995), pp. 4091–4094.

[17] F. Schmidt-Kaler et al. “Realization of the Cirac-Zoller controlled-NOT quantum gate”. In: *Nature* 422 (2003), pp. 408–11.

[18] C. J. Ballance et al. “High-Fidelity Quantum Logic Gates Using Trapped-Ion Hyperfine Qubits”. In: *Physical Review Letters* 117 (2016), p. 060504.

[19] R. Bowler et al. “Coherent diabatic ion transport and separation in a multizone trap array”. In: *Physical Review Letters* 109 (2012), p. 080502.

[20] A. Walther et al. “Controlling fast transport of cold trapped ions”. In: *Physical Review Letters* 109 (2012), p. 080501.

[21] K. Wright et al. “Reliable transport through a microfabricated X-junction surface-electrode ion trap”. In: *New Journal of Physics* 15 (2013), p. 033004.

[22] C. Monroe et al. “Large-scale modular quantum-computer architecture with atomic memory and photonic interconnects”. In: *Physical Review A* 89 (2014), p. 022317.

[23] M. Halder et al. “Entangling independent photons by time measurement”. In: *Nature Physics* 3 (2007), pp. 692–695.

[24] Ch. Simon and W. T. M. Irvine. “Robust Long-Distance Entanglement and a Loophole-Free Bell Test with Ions and Photons”. In: *Physical Review Letters* 91 (2003), p. 110405.

[25] D. L. Moehring et al. “Entanglement of single-atom quantum bits at a distance”. In: *Nature* 449 (2007), pp. 68–71.

[26] M. Saffman. “Quantum computing with atomic qubits and Rydberg interactions: Progress and challenges”. In: *Journal of Physics B* 49 (2016), p. 202001.

[27] P.S. Jessen and I.H. Deutsch. “Optical Lattices”. In: *Advances In Atomic, Molecular, and Optical Physics* 37 (1996), pp. 95–138.

[28] L. Guidoni and P. Verkerk. "Optical lattices: cold atoms ordered by light". In: *Journal of Optics B* 1 (1999), R23–R45.

[29] K. D. Nelson, X. Li, and D. S. Weiss. "Imaging single atoms in a three-dimensional array". In: *Nature Physics* 3 (2007), pp. 556–560.

[30] R. Grimm, M. Weidemüller, and Y. B. Ovchinnikov. "Optical dipole trap for neutral atoms". In: *Advances in Atomic Molecular and Optical Physics* 42 (2000), p. 95.

[31] S. Bergamini et al. "Holographic generation of micro-trap arrays for single atoms". In: *Journal of the Optical Society of America B* 21 (2004), pp. 1889–1894.

[32] F. Nogrette et al. "Single-Atom Trapping in Holographic 2D Arrays of Microtraps with Arbitrary Geometries". In: *Physical Review X* 4 (2014), p. 21034.

[33] E. Dennis et al. "Topological quantum memory Fault tolerance calculations for clocked quantum-dot cellular automata devices Topological quantum memory". In: *Journal of Mathematical Physics* 43 (2002), p. 4452.

[34] A. G. Fowler et al. "Surface codes: Towards practical large-scale quantum computation". In: *Physical Review A* 86 (2012), p. 032324.

[35] S. Kuhr et al. "Analysis of dephasing mechanisms in a standing-wave dipole trap". In: *Physical Review A* 72 (2005), p. 023406.

[36] Y. O. Dudin, L. Li, and A. Kuzmich. "Light storage on the time scale of a minute". In: *Physical Review A* 87 (2013), p. 031801.

[37] A. Fuhrmanek et al. "Free-space lossless state detection of a single trapped atom". In: *Physical Review Letters* 106 (2011), p. 133003.

[38] M. J. Gibbons et al. "Nondestructive fluorescent state detection of single neutral atom qubits". In: *Physical Review Letters* 106 (2011), p. 133002.

[39] E. Knill et al. "Randomized benchmarking of quantum gates". In: *Physical Review A* 77 (2008), p. 012307.

[40] K. Gillen-Christandl et al. "Comparison of Gaussian and super Gaussian laser beams for addressing atomic qubits". In: *Applied Physics B* 122 (2016), p. 131.

[41] D. Schrader et al. "Neutral atom quantum register". In: *Physical Review Letters* 93 (2004), p. 150501.

[42] S. Olmschenk et al. "Randomized benchmarking of atomic qubits in an optical lattice". In: *New Journal of Physics* 12 (2010), p. 113007.

[43] C. Knoernschild et al. “Independent individual addressing of multiple neutral atom qubits with a micromirror-based beam steering system”. In: *Applied Physics Letters* 97 (2010), p. 134101.

[44] D. D. Yavuz et al. “Fast ground state manipulation of neutral atoms in microscopic optical traps”. In: *Physical Review Letters* 96 (2006), p. 063001.

[45] T. Xia et al. “Randomized benchmarking of single-qubit gates in a 2D array of neutral-atom qubits”. In: *Physical Review Letters* 114 (2015), p. 100503.

[46] Y. Wang et al. “Coherent Addressing of Individual Neutral Atoms in a 3D Optical Lattice”. In: *Physical Review Letters* 115 (2015), p. 1562.

[47] Y. Wang et al. “Single-qubit gates based on targeted phase shifts in a 3D neutral atom array”. In: *Science* 352 (2016), pp. 1562–1565.

[48] I. Dotsenko et al. “Application of electro-optically generated light fields for Raman spectroscopy of trapped cesium atoms”. In: *Applied Physics B* 78 (2004), pp. 711–717.

[49] J. H. Lee et al. “Robust site-resolvable quantum gates in an optical lattice via inhomogeneous control”. In: *Nature Communications* 4 (2013), p. 2027.

[50] E. Hagley et al. “Generation of Einstein-Podolsky-Rosen Pairs of Atoms”. In: *Physical Review Letters* 79 (1997), pp. 1–5.

[51] O. Mandel et al. “Controlled collisions for multi- particle entanglement of optically trapped atoms”. In: *Nature* 425 (2003), pp. 937–940.

[52] M. Anderlini et al. “Controlled exchange interaction between pairs of neutral atoms in an optical lattice”. In: *Nature* 448 (2007), pp. 452–456.

[53] A. M. Kaufman et al. “Entangling two transportable neutral atoms via local spin exchange”. In: *Nature* 527 (2015), pp. 208–211.

[54] D. Jaksch et al. “Fast Quantum Gates for Neutral Atoms”. In: *Physical Review Letters* 85 (2000), p. 2208.

[55] M. Müller et al. “Mesoscopic rydberg gate based on electromagnetically induced transparency”. In: *Physical Review Letters* 102 (2009), p. 170502.

[56] L. Isenhower et al. “Demonstration of a neutral atom controlled-nOT quantum gate”. In: *Physical Review Letters* 104 (2010), pp. 8–11.

[57] X. L. Zhang et al. “Deterministic entanglement of two neutral atoms via Rydberg blockade”. In: *Physical Review A* 82 (2010), p. 030306.

[58] T. Wilk et al. "Entanglement of two individual neutral atoms using rydberg blockade". In: *Physical Review Letters* 104 (2010), p. 010502.

[59] K. M. Maller et al. "Rydberg-blockade controlled- not gate and entanglement in a two-dimensional array of neutral-atom qubits". In: *Physical Review A* 92 (2015), p. 022336.

[60] Y. Y. Jau et al. "Entangling atomic spins with a Rydberg-dressed spin-flip blockade". In: *Nature Physics* 12 (2016), pp. 71–74.

[61] M. J. Piotrowicz et al. "Two-dimensional lattice of blue-detuned atom traps using a projected Gaussian beam array". In: *Physical Review A* 88 (2013), p. 013420.

[62] Ch. Weitenberg et al. "Single-spin addressing in an atomic Mott insulator". In: *Nature* 471 (2011), pp. 319–324.

[63] W. Lee, H. Kim, and J. Ahn. "Three-dimensional rearrangement of single atoms using actively controlled optical microtraps". In: *Optics Express* 24 (2016), p. 9816.

[64] J. Lee et al. "Scalable cavity-QED-based scheme of generating entanglement of atoms and of cavity fields". In: *Physical Review A* 77 (2008), p. 032327.

[65] A. Datta, S. T. Flammia, and C. M. Caves. "Entanglement and the power of one qubit". In: *Physical Review A* 72 (2005), p. 042316.

[66] E. Knill and R. Laflamme. "Power of One Bit of Quantum Information". In: *Physical Review Letters* 81 (1998), p. 5672.

[67] B. P. Lanyon et al. "Experimental quantum computing without entanglement". In: *Physical Review Letters* 101 (2008), p. 200501.

[68] B. P. Lanyon et al. "Simplifying quantum logic using higher-dimensional Hilbert spaces". In: *Nature Physics* 5 (2009), pp. 134–140.

[69] K. Modi et al. "Quantum Correlations in Mixed-State Metrology". In: *Physical Review X* 1 (2011), p. 21022.

[70] C. W. Mansell and S. Bergamini. "A cold-atoms based processor for deterministic quantum computation with one qubit in intractably large Hilbert spaces". In: *New Journal of Physics* 16 (2014), p. 053045.

[71] G. Passante et al. "Experimental approximation of the jones polynomial with one quantum bit". In: *Physical Review Letters* 103 (2009), p. 250501.

[72] D. Tong et al. "Local Blockade of Rydberg Excitation in an Ultracold Gas". In: *Physical Review Letters* 93 (2004), p. 063001.

[73] K. Singer et al. “Suppression of Excitation and Spectral Broadening Induced by Interactions in a Cold Gas of Rydberg Atoms”. In: *Physical Review Letters* 93 (2004), p. 163001.

[74] E. Urban et al. “Observation of Rydberg blockade between two atoms”. In: *Nature Physics* 5 (2009), pp. 110–114.

[75] D. Barredo et al. “Demonstration of a strong rydberg blockade in three-atom systems with anisotropic interactions”. In: *Physical Review Letters* 112 (2014), p. 183002.

[76] M. Ebert et al. “Coherence and Rydberg Blockade of Atomic Ensemble Qubits”. In: *Physical Review Letters* 115 (2015), p. 093601.

[77] Y. R . P. Sortais et al. “Diffraction-limited optics for single-atom manipulation”. In: *Physical Review A* 75 (2007), p. 013406.

[78] T. Grünzweig et al. “Near-deterministic preparation of a single atom in an optical microtrap”. In: *Nature Physics* 6 (2010), pp. 951–954.

[79] N. Schlosser et al. “Sub-poissonian loading of single atoms in a microscopic dipole trap.” In: *Nature* 411 (2001), pp. 1024–1027.

[80] D. P. Divincenzo and D. Loss. “Quantum computers and quantum coherence”. In: *Journal of Magnetism and Magnetic Materials* 200 (1999), pp. 202–218.

[81] Ch. H. Bennett and G. Brassard. “Quantum Cryptography: Public Key Distribution and Coin Tossing”. In: *Theoretical Computer Science* 560 (2014), pp. 7–11.

[82] D. A. Meyer. “Quantum strategies”. In: *Physical Review Letters* 82 (1999), p. 1052.

[83] J. Eisert, M. Wilkens, and M Lewenstein. “Quantum games and quantum strategies”. In: *Physical Review Letters* 83 (1999), p. 3077.

[84] L. Goldenberg, L. Vaidman, and S. Wiesner. “Quantum gambling”. In: *Physical Review Letters* 82 (1999), p. 3356.

[85] A. M. Steane and Wim Dam. “Physicists Triumph at Guess my Number”. In: *Physics Today* 53 (2000), pp. 35–39.

[86] D. P. DiVincenzo. “The Physical Implementation of Quantum Computation”. In: *Fortschritte der Physik* 48 (2000), pp. 771–783.

[87] S. Hill and W. K. Wootters. “Entanglement of a Pair of Quantum Bits”. In: *Physical Review Letters* 78 (1997), pp. 5022–5025.

[88] John von Neumann. *Mathematical foundations of quantum mechanics*. Ed. by Eugene P Wigner and Robert Hofstadter. Princeton: Princeton University Press, 1955.

[89] R. Horodecki et al. "Quantum entanglement". In: *Reviews of Modern Physics* 81 (2009), pp. 865–942.

[90] Necia Grant Cooper, ed. *Los Alamos Science: Information, Science, and Technology in a Quantum World*. Vol. 27. 2002.

[91] I. Johansson. "Spectra of the alkali metals in the lead-sulphide region". In: *Arkiv för Fysik* 20 (1961).

[92] S. Goldsmith et al. "Spectrum and energy levels of eight-times ionized rubidium (Rb Ix)". In: *Journal of the Optical Society of America B* 1 (1984), pp. 631–634.

[93] P. Zeeman. "The Effect of Magnetisation on the Nature of Light Emitted by a Substance : Abstract : Nature". In: *Nature* 55 (1897), p. 347.

[94] E. Arimondo, M. Inguscio, and P. Violino. "Experimental determinations of the hyperfine structure in the alkali atoms". In: *Reviews of Modern Physics* 49 (1977), pp. 31–75.

[95] S. Bize et al. "High-accuracy measurement of the 87 Rb ground-state hyperfine splitting in an atomic fountain". In: *Europhysics Letters* 45 (1999), pp. 558–564.

[96] G. P. Barwood, P. Gill, and W. R. C. Rowley. "Frequency measurements on optically narrowed Rb-stabilised laser diodes at 780 nm and 795 nm". In: *Applied Physics B* 53 (1991), pp. 142–147.

[97] J. Ye et al. "Hyperfine structure and absolute frequency of the Rb87 3/2 state". In: *Optics Letters* 21 (1996), p. 1280.

[98] W. Li et al. "Millimeter-Wave Spectroscopy of Cold Rb Rydberg Atoms in a Magneto-Optical Trap: Quantum Defects of the ns, np, and nd Series". In: *Physical Review A* 67 (2003), p. 52502.

[99] B. Sanguinetti et al. "Precision measurements of quantum defects in the nP3/2 Rydberg states of 85Rb". In: *Journal of Physics B* 42 (2009), p. 165004.

[100] L. A. M. Johnson et al. "Absolute frequency measurements of 85RbnF7/2 Rydberg states using purely optical detection". In: *New Journal of Physics* 12 (2010), p. 063028.

[101] M. Mack et al. "Measurement of absolute transition frequencies of 87Rb nS and nD Rydberg states by means of electromagnetically induced transparency". In: *Physical Review A* 83 (2011), p. 52515.

[102] Thomas F. Gallagher. *Rydberg atoms*. Ed. by A. Dalgarno et al. Cambridge: Cambridge University Press, 1994.

[103] T. G. Walker and M. Saffman. "Zeros of Rydberg–Rydberg Föster interactions". In: *Journal of Physics B* 38 (2005), S309–S319.

[104] M. Saffman, T. G. Walker, and K. M??lmer. "Quantum information with Rydberg atoms". In: *Reviews of Modern Physics* 82 (2010), pp. 2313–2363.

[105] J. Dalibard and C. Cohen-Tannoudji. "Dressed-atom approach to atomic motion in laser light: the dipole force revisited". In: *Journal of the Optical Society of America B* 2 (1985), p. 1707.

[106] Rodney Loudon. *The quantum theory of light*. 3rd ed. Oxford: Oxford University Press, 2000.

[107] Benoît Darquié. "Manipulation d'atomes dans des pièges dipolaires microscopiques et émission contrôlée de photons par une atome unique". PhD thesis. Université Paris-Sud XI, 2005.

[108] M. Fleischhauer and J. P. Marangos. "Electromagnetically induced transparency: Optics in coherent media". In: *Reviews of Modern Physics* 77 (2005), pp. 633–673.

[109] O. A. Kocharovskaya and Y. I. Khanin. "Coherent amplification of an ultrashort pulse in a 3-level medium without a population-inversion". In: *JETP Letters* 48 (1988), pp. 630–634.

[110] S. E. Harris. "Lasers without inversion: Interference of lifetime-broadened resonances". In: *Physical Review Letters* 62 (1989), p. 1033.

[111] Anna Urszula Kowalczyk. "Manipulation and control of ultra-cold rubidium Atoms". PhD thesis. The Open University, 2013.

[112] M. D. Lukin et al. "Dipole blockade and quantum information processing in mesoscopic atomic ensembles." In: *Physical Review Letters* 87 (2001), p. 037901.

[113] J. T. Barreiro et al. "Experimental multiparticle entanglement dynamics induced by decoherence". In: *Nature Physics* 6 (2010), pp. 943–946.

[114] I. I. Beterov et al. "Deterministic single-atom excitation via adiabatic passage and Rydberg blockade". In: *Physical Review A* 84 (2011), p. 023413.

[115] T. W. Hänsch and A. L. Schawlow. "Cooling of gases by laser radiation". In: *Optics Communications* 13 (1975), pp. 68–69.

[116] S. Chu et al. "Experimental observation of optically trapped atoms". In: *Physical Review Letters* 57 (1986), pp. 314–317.

[117] W. D. Phillips and H. Metcalf. "Laser deceleration of an atomic beam". In: *Physical Review Letters* 48 (1982), pp. 596–599.

[118] E. L. Raab et al. "Trapping of Neutral Sodium Atoms with Radiation Pressure". In: *Physical Review Letters* 59 (1987), pp. 2631–2634.

[119] W. D. Phillips, P. L. Gould, and P. D. Lett. "Cooling, Stopping, and Trapping Atoms". In: *Science* 235 (1988), pp. 877–883.

[120] P. D. Lett et al. "Observation of atoms laser cooled below the doppler limit". In: *Physical Review Letters* 61 (1988), pp. 169–172.

[121] J. Dalibard and C. Cohen-Tannoudji. "Laser cooling below the Doppler limit by polarization gradients: simple theoretical models". In: *Journal of the Optical Society of America B* 6 (1989), p. 2023.

[122] P. Jeffrey Ungar et al. "Optical molasses and multilevel atoms: theory". In: *Journal of the Optical Society of America B* 6 (1989), p. 2072.

[123] M. Prentiss et al. "Atomic-density-dependent losses in an optical trap". In: *Optics Letters* 13 (1988), p. 452.

[124] A. M. Steane, M Chowdhury, and C. J. Foot. "Radiation Force in the Magneto-Optical Trap". In: *Journal of the Optical Society of America B* 9 (1992), p. 2142.

[125] C. G. Townsend et al. "Phase-space density in the magneto-optical trap". In: *Physical Review A* 52 (1995), pp. 1423–1440.

[126] D. Haubrich et al. "Observation of individual neutral atoms in magnetic and magneto-optical traps". In: *Europhysics Letters* 34 (1996), pp. 663–668.

[127] H. J. Metcalf and P. van der Straten. "Laser cooling and trapping of atoms". In: *Journal of Optical Society of America* 20 (2003), pp. 887–908.

[128] M. Talavera O. et al. "Accurate absolute measurement of trapped Cs atoms in a MOT". In: *Revista Mexicana de Fisica* 53 (2007), pp. 358–365.

[129] M. Haw et al. “Magneto-optical trap loading rate dependence on trap depth and vapor density”. In: *Journal of the Optical Society of America B* 29 (2012), p. 475.

[130] R. Chang et al. “Three-dimensional laser cooling at the Doppler limit”. In: *Physical Review A* 90 (2014), p. 063407.

[131] R. Romain et al. “Measuring the reabsorption cross section of a magneto-optical trap”. In: *Physical Review A* 89 (2014), p. 053425.

[132] R. Romain et al. “Spatial instabilities in a cloud of cold atoms”. In: *Physical Review E* 94 (2016), p. 5.

[133] D. Steck. “Rubidium 87 D line data”. Available online at http://steck.us/alkalidata, (version 2.1.5, 2015).

[134] T. W. Hansch and B. Couillaud. “Laser frequency stabilization by polarization spectroscopy of a reflecting reference cavity”. In: *Optics Communications* 35 (1980), pp. 441–444.

[135] G. C. Bjorklund. “Frequency-modulation spectroscopy: a new method for measuring weak absorptions and dispersions”. In: *Optics Letters* 5 (1980), pp. 15–17.

[136] G. A. Sanders, M. G. Prentiss, and S. Ezekiel. “Passive ring resonator method for sensitive inertial rotation measurements in geophysics and relativity”. In: *Optics Letters* 6 (1981), p. 569.

[137] R. W. P. Drever et al. “Laser phase and frequency stabilization using an optical resonator”. In: *Applied Physics B* 31 (1983), pp. 97–105.

[138] J. L. Hall et al. “Optical heterodyne saturation spectroscopy”. In: *Applied Physics Letters* 39 (1981), pp. 680–682.

[139] G. C. Bjorklund et al. “Frequency modulation (FM) spectroscopy”. In: *Applied Physics B* 32 (1983), pp. 145–152.

[140] J. W. Crowe and R. M. Craig. “SMALL-SIGNAL AMPLIFICATION IN GaAs LASERS”. In: *Applied Physics Letters* 4 (1964), pp. 57–58.

[141] A. S. Arnold, J. S. Wilson, and M. G. Boshier. “A simple extended-cavity diode laser”. In: *Review of Scientific Instruments* 69 (1998), pp. 1236–1239.

[142] E. A. Donley et al. “Double-pass acousto-optic modulator system”. In: *Review of Scientific Instruments* 76 (2005), p. 063112.

[143] T. Arpornthip, C. A. Sackett, and K. J. Hughes. "Vacuum-pressure measurement using a magneto-optical trap". In: *Physical Review A* 85 (2012), p. 033420.

[144] A. Fuhrmanek et al. "Imaging a single atom in a time-of-flight experiment". In: *New Journal of Physics* 12 (2010), p. 053028.

[145] L. Russell et al. "Measurements on release-recapture of cold 85Rb atoms using an optical nanofibre in a magneto-optical trap". In: *Optics Communications* 309 (2013), pp. 313–317.

[146] Silvia Bergamini. "Intrappolamento magneto-ottico per il potassio fermionico". Master thesis. Universita degli Studi di Firenze, 1997.

[147] J. E. Bjorkholm. "Collision-limited lifetimes of atom traps". In: *Physical Review A* 38 (1988), pp. 1599–1600.

[148] A. L. Migdall et al. "First Observation of Magnetically Trapped Neutral Atoms". In: *Physical Review Letters* 54 (1985), pp. 2596–2599.

[149] L. Torralbo-Campo et al. "Light-induced atomic desorption in a compact system for ultracold atoms". In: *Scientific Reports* 5 (2015), p. 14729.

[150] D. R. Scherer, D. B. Fenner, and J. M. Hensley. "Characterization of alkali metal dispensers and non-evaporable getter pumps in ultrahigh vacuum systems for cold atomic sensors". In: *Journal of Vacuum Science & Technology A: Vacuum, Surfaces, and Films* 30 (2012), p. 061602.

[151] R. W. G. Moore et al. "Measurement of Vacuum Pressure with a Magneto-Optical Trap: a Pressure-Rise Method". In: *Review of Scientific Instruments* 86 (2015), p. 093108.

[152] David Bates and Benjamin Bederson, eds. *Advances in Atomic and Molecular Physics*. Vol. 13. New York: Academic Press, 1977.

[153] Lucas Beguin. "Direct Measurement of the van der Waals Interaction between Two Rydberg Atoms". PhD thesis. Institut d'Optique Graduate School, 2013.

[154] ZEMAX. *Optical Design Program, User's Manual*. Tech. rep. 2011.

[155] J. M. Liu and L. Gomelsky. "Vectorial beam propagation method". In: *Journal of the Optical Society of America A* 9 (1992), p. 1574.

[156] A. Ciattoni, B. Crosignani, and P. Di Porto. "Vectorial free-space optical propagation: a simple approach for generating all-order nonparaxial corrections". In: *Optics Communications* 177 (2000), pp. 9–13.

[157] J.G. Wangüemert-Pérez, I. Molina-Fernández, and M.A. Luque-Nieto. "A novel Fourier based 3D full-vectorial beam propagation method". In: *Optical and Quantum Electronics* 36 (2004), pp. 285–301.

[158] Salah Obayya. *Computational Photonics*. 1st ed. Chichester, UK: Wiley, 2010. Chap. 2, pp. 9–24.

[159] Y. Suzaki and A. Tachibana. "Measurement of the μm sized radius of Gaussian laser beam using the scanning knife-edge". In: *Applied Optics* 14 (1975), p. 2809.

[160] M. Sheikh and N.A. Riza. "Demonstration of Pinhole Laser Beam Profiling Using a Digital Micromirror Device". In: *IEEE Photonics Technology Letters* 21 (2009), pp. 666–668.

[161] G. A. Askar'yan. "Effects of the Gradient of a Strong Electromagnetic Beam on Electrons and Atoms". In: *Soviet Physics. Journal of Experimental and Theoretical Physics* 15 (1962), pp. 1988–1090.

[162] V. S. Letokhov. "Doppler line narrowing in a standing light wave". In: *Soviet Physics. Journal of Experimental and Theoretical Physics* 7 (1968), pp. 272–274.

[163] A. Ashkin. "Acceleration and Trapping of Particles by Radiation Pressure". In: *Physical Review Letters* 24 (1970), pp. 156–159.

[164] A. Ashkin. "Trapping of atoms by resonance radiation pressure". In: *Physical Review Letters* 40 (1978), pp. 729–732.

[165] J. E. Bjorkholm et al. "Observation of Focusing of Neutral Atoms by the Dipole Forces of Resonance-Radiation Pressure". In: *Physical Review Letters* 41 (1978), pp. 1361–1364.

[166] Ch. S. Adams et al. "Evaporative cooling in a crossed dipole trap". In: *Physical Review Letters* 74 (1995), pp. 3577–3580.

[167] N. Davidson et al. "Long atomic coherence times in an optical dipole trap". In: *Physical Review Letters* 74 (1995), pp. 1311–1314.

[168] J. Kruse et al. "Reconfigurable site-selective manipulation of atomic quantum systems in two-dimensional arrays of dipole traps". In: *Physical Review A* 81 (2010), p. 060308.

[169] S. J. M. Kuppens et al. "Loading an optical dipole trap". In: *Physical Review A* 62 (2000), p. 013406.

[170] P. Kulatunga, T. Blum, and D. Olek. "Loading characteristics of a microscopic optical dipole trap". In: *arXiv* 1009.2544 (2010).

[171] S. Gensemer et al. "Trap-loss collisions of Rb85 and Rb87: Dependence on trap parameters". In: *Physical Review A* 56 (1997), pp. 4055–4063.

[172] O. Luiten, M. Reynolds, and J. Walraven. "Kinetic theory of the evaporative cooling of a trapped gas". In: *Physical Review A* 53 (1996), pp. 381–389.

[173] T. M. Brzozowski et al. "Time-of-flight measurement of the temperature of cold atoms for short trap-probe beam distances". In: *Journal of Optics B* 4 (2002), pp. 62–66.

[174] C. Tuchendler et al. "Energy distribution and cooling of a single atom in an optical tweezer". In: *Physical Review A* 78 (1008), p. 033425.

[175] S. D. Gensemer et al. "Ultracold 87Rb ground-state hyperfine-changing collisions in the presence and absence of laser light". In: *Physical Review A* 62 (2000), p. 030702.

[176] Paul F. Griffin. "Laser Cooling and Loading of Rb into A Large Period, Quasi-Electrostatic, Optical Lattice". PhD thesis. Durham University, 2005.

[177] Andreas Fuhrmanek. "From Single To Many Atoms in a Microscopic Optical Dipole Tra". PhD thesis. Université Paris-Sud XI, 2011.

[178] A. Gallagher and D. E. Pritchard. "Exoergic collisions of cold Na-Na". In: *Physical Review Letters* 63 (1989), pp. 957–960.

[179] G. Telles et al. "Inelastic cold collisions of a Na/Rb mixture in a magneto-optical trap". In: *Physical Review A* 59 (1999), R23–R26.

[180] A. R. Gorges et al. "Light-assisted collisional loss in a Rb 85/87 ultracold optical trap". In: *Physical Review A* 78 (2008), p. 033420.

[181] A. Fuhrmanek et al. "Light-assisted collisions between a few cold atoms in a microscopic dipole trap". In: *Physical Review A* 85 (2012), p. 062708.

[182] P. Sompet et al. "Dynamics of two atoms undergoing light-assisted collisions in an optical microtrap". In: *Physical Review A* 88 (2013), p. 051401.

[183] N. Schlosser, G. Reymond, and P. Grangier. "Collisional blockade in microscopic optical dipole traps." In: *Physical review letters* 89 (2002), p. 023005.

[184] A. J. Hilliard et al. "In-trap fluorescence detection of atoms in a microscopic dipole trap". In: *Physical Review A* 91 (2015), p. 053414.

[185] P. S. Julienne and Jacques Vigue. “Cold collisions oIr ground- and excited-state alkali-metal atoms”. In: *Physical Review A* 44 (1991), pp. 4464–4485.

[186] T. G. Tiecke et al. “High-flux two-dimensional magneto-optical-trap source for cold lithium atoms”. In: *Physical Review A* 80 (2009), p. 013409.

[187] W. D. Phillips and H. Metcalf. “Laser Deceleration of an Atomic Beam”. In: *Physical Review Letters* 48 (1982), pp. 596–599.

[188] Max Born and Emil Wolf. *Principles of Optics, Electromagnetic Theory of Propagation, Interference and Diffraction of Light*. 6th ed. Oxford: Pergamon Press, 1980.

[189] Joseph W. Goodman. *Introduction to Fourier Optics*. Ed. by Hubert Heffner and A. E. Siegman. San Francisco: McGraw-Hill, 1968.

[190] Isomet. *Acousto-Optic Scanning and Deflection*. Tech. rep. 2004.